# Facets of Proterozoic Sedimentation against the backdrop of a carbonate-siliciclastic transition: Examples from parts of the Vindhyan Supergroup, Central India

THESIS SUBMITTED FOR THE DEGREE OF
DOCTOR OF PHILOSOPHY (SCIENCE)
OF
JADAVPUR UNIVERSITY
(2022)

BY
SABYASACHI MANDAL
Index No: 19/17/Geol. Sc./25
DEPARTMENT OF GEOLOGICAL SCIENCES
JADAVPUR UNIVERSITY
KOLKATA-700032

যাদবপুর বিশ্ববিদ্যালয়
কলকাতা-৭০০০৩২, ভারত

JADAVPUR UNIVERSITY
KOLKATA-700032, INDIA

FACULTY OF SCIENCE : DEPARTMENT OF GEOLOGICAL SCIENCES

## CERTIFICATE FROM THE SUPERVISOR(S)

This is to certify that the thesis entitled "**Facets of Proterozoic Sedimentation against the backdrop of a carbonate-siliciclastic transition: Examples from parts of the Vindhyan Supergroup, Central India**" Submitted by Shri. Sabyasachi Mandal who got his name registered on **02/05/2017** for the award of Ph. D. (Science) Degree of Jadavpur University, is absolutely based upon his own work under the supervision of **Prof. Subir Sarkar and Prof. Pulak Sengupta** and that neither this thesis nor any part of it has been submitted for either any degree / diploma or any other academic award anywhere before.

Subir Sarkar 27.7.2022

Dr. Subir Sarkar
Professor
Department of Geological Sciences
Jadavpur University
Kolkata - 700 032

Pulak Sengupta 27/7/2022

Dr. Pulak Sengupta
Professor
Department of Geological Sciences
Jadavpur University, Kolkata-700032

(Signature of the Supervisor(s) date with official seal)

দূরভাষ : ২৪১৪-৬৬৬৬/প্রসারণ : ২২৬৮
Website : www.jadavpur.edu
E-mail : hod_geological@jdvu.ac.in
Phone : 2414 6666/Extn. 2268

**DEDICATED TO**

**MY FAMAILY** (Birendranath Mandal, Milu Rani Kar Mandal,
Dr. Souvik Mandal and Soma Mondal),

**FRIENDS and TEACHERS**

ACKNOWLEDGEMENT

I would like to express all of gratitude to my parents, brother, sister and all of family members. Their invariable inspiration and faith were my only belongings to motivate myself and follow myself.

I would also like to express my special thanks of gratitude to my supervisors, Prof. Subir Sarkar and Prof. Pulak Sengupta for their able guidance and support in completing my PhD thesis. They have always been a constant source of encouragement all throughout my stay in Jadavpur University. They were not only inspiring but also critical at times, which kept me stimulated throughout my fieldwork and manuscript preparation. I am extremely thankful for their endurance and the warmth they showered upon which provided me the strength and courage to come this far.

I am also deeply indebted to Prof. Pradip K. Bose, Prof. Santanu Banerjee and Prof. Partha Pratim Chakraborty for many of their fruitful suggestions, kind help and co-operation during the entire tenure. Without their guidance, criticisms and thought-provoking discussions this thesis work would not have been meaningful.

I express my sincere indebtedness to my alma mater, Jadavpur University, for providing all sorts of infrastructural help in pursuance of this work. I would also like to express gratitude to the teachers of Department of Geological Sciences, J.U.

I convey my thanks to UGC for providing me the financial assistance to carry out this work. I am also thankful to Department of Earth Sciences, IIT Bombay; IISER Kolkata; IIT Kanpur, for providing instrumental facilities. I am also grateful to all the people of Madhya Pradesh for their kind help and support during my fieldwork.

I express my humble thanks to all the members of JUSEDMENTOLOGYLAB, especially- Dr. Soumik Mukhopadhuay, Dr. Pradip Samanta, Dr. Sunipa Mandal, Dr. Nivedita Chakraborty, Dr. Anudeb Mandal, Dr. Adrita Choudhuri, Dr. Amlan Koner, Neeti Di, Anushka Di, Agnidipto Da, Swagata Di, Aniket Da, Saradindu Da, Arpan Da, Indrani, Shilpa, Rohan, Subhajit (Pandey), Arunava (Sagar), Sayak, Avik, Aditi, Souryadip for their support, constructive suggestions and care.

My special thanks to Dr. Vandana Prasad, Director, BSIP for her encouragement and inspiration. I am also thankful to Dr. Abha Singh, Dr. Prem Raj Uddandan, Dr. Shreya

Mishra, Dr. Anurag Kumar, Dr. Mayank Shekhar, Dr. Ranveer Singh Negi, Dr. Suman Sarkar, Dr. Divya Kumari Mishra, Sanjay Kumar Singh Gahlaud, Mahi and Shalini for their constant encouragement for submitting my Ph.D. thesis.

I am thankful to my friends, seniors, junior and classmates: Hirak Da, Mehmub Da, Sayantan Da, Subhasis Da, Giri Da, Deepjoy Da, Anindita Di, Bala Di, Joyjeet, Nandan, Sutanu, Banibrata, Amlan, Sukanya, Nita, Ranita, Asmita, Deedhiti Di, Arimita, Priyanka, Puja, Ekota, Madhuchanda, Prabhati, Somdipta, Aynagshu, Prithis, Kapil, Vikas, Moumita Di, Anirban (Manna), Sourav (Bedo), Sujatra, Ratul, Avik, Mousumi, Sudip (Bapu), Pratusha, Koustav, Saikat, Deba, Mahadeb for their good wishes, closeness and to receive warmth and affection livelong.

I also like to extend my thankful to members of Jadavpur University Main Hostel, $A_2$ block, Room no 68: Shibasis Da, Sayantan Da, Anupam Da, Manas (Maity), Gora, Utaplandu (Jeet), Susovon, Sandipan, Tapas, Nilay, Pronobesh, Indrajit, Sudeb, Biswajit and Subhankar.

Sabyasachi Mandal

---

Sabyasachi Mandal

## Abstract

The present thesis delves into sedimentalogical characteristics, both physical and chemical, of some parts of the Mesoproterozoic Rohtas Formation and lower part of the Kaimur Formation of the Vindhyan Supergroup in central India. Detailed state-of-art facies analysis of the aforementioned formations creates the broad frame for the present deliberation. A special emphasis has been laid on shallow water glauconitization in the epeiric sea in which the said formations were deposited. The process of chertification of the Rohtas Limestone and calculation of the then earth's surface temperature are the other two major issues that have been brought under focus. In the light of the latter a modified model of the Precambrian paleoclimate has been presented. The Rohtas Limestone Member of the Rohtas Formation is constituted by two distinct facies associations (I and II) and detail sedimentological analysis infers a restricted (Association I) to open marine (Association II) paleogeography for the limestone deposition. The basal ~12 m thick sandstone of the Kaimur Formation overlies an unconformity present above the Rohtas Limestone. The sandstone was also deposited in a tide dominated marine setting with frequent storm intervention. The Lower Quartzite (LQ) above the unconformity is claimed earlier to have been deposited in a localized area in the eastern sector of the basin. However, the present investigation carried out over a 120 km strike-parallel stretch reveals that the formation maintains the same lithological similarity refuting its local occurrences. Numerous soft-sediment deformation features present within Rohtas limestone have been analysed for their respective genesis. Adjudging their genetic implications in their respective facies (depositional) background helped to unravel their respective triggering mechanisms and to identify the triggering agents involved.

The discontinuous, but significant chert horizon present above the uppermost portion of the Rohtas limestone, just beneath the unconformity, has been studied in depth and its origin has been inferred. The then earth's surface temperature has been calculated with the help of recently developed triple oxygen isotopic studies. The present study suggests that earth's surface temperature during the Mesoproterozoic time was no different from that of the modern times (around ~25ºC). The result contradicts the existing claim for considerably higher contemporary earth temperature and attributes to overestimation of ancient ocean. In another way of mass balance calculation proposes a new window to estimate the paleo-temperature in relation with chertification process and replacement model during the present endeavour. Chert form by replacement of dolostone (Rohtas

Limestone) by mass change of (Tmass) of 2.12 at constant volume. Mass balance calculation of studied chert infer that initially carbonate was deposited in a marine setting at 10$^{o}$C temperature in equilibrium of modern sea where chert form at 0.8 F/R (Fluid/Rock) interaction. The triple oxygen isotope recorded within chert may be a transformation of later diagenesis of 25$^{o}$C to 300$^{o}$C fluid at F/R of 1 to 0.

An integrated sedimentological, petrographical and geochemical investigation of the LQ and the Lower Bhander Sandstone (LBS) of the Vindhyan Supergroup reveals a shallow marine sub-oxic depositional setting for the glauconite formation. The mineralogical and chemical analyses indicate enrichment of the glauconite in $K_2O$, MgO and $Al_2O_3$, and depletion in $Fe_2O_3$(total), compared to the Phanerozoic variety. Detailed sequence stratigraphic analysis suggests their association within transgressive systems tract (TST) deposit, which is capped by the maximum flooding zone (MFZ). The occurrence of glauconite within the LBS and LQ has been discussed at length to throw light on the glauconitization process within the overall shallow epeiric marine depositional setting. Intermittent subsidence and/or marine transgression of the depositional basin, associated with an event of major marine flooding eventually created a condition conducive for glauconitization of sediment.

## CONTENTS

**CHAPTER 7:** Revisiting the Boundary of the Upper and Lower Vindhyan Group in Son Valley Vindhyan, Central India

**CHAPTER 8:** Origin and Sequence Stratigraphic implication of High-Alumina Glauconite within the Lower Quartzite, Vindhyan Supergroup

**CHAPTER 9:** Shallow marine glauconitization during the Proterozoic in response to intrabasinal tectonics: a study from the Proterozoic Lower Bhander Sandstone, Central India

**PART-III: Compendium**

**CHAPTER 10:** Summary and Conclusion

# CHAPTER 1
# INTRODUCTION

## 1.1. Introduction

The Proterozoic Rohtas Limestone (RLM), Lower Quartzite (LQ) and Lower Bhander Sandstone (LBS) of the Vindhyan Supergroup in Central India is the mainstay of this thesis. The purpose is to recheck and strengthen certain conclusions that have emerged primarily from the studied sediment succession. The procedure also enhances the observations of certain ancient geological signature (specifically during Proterozoic) of the ancient earth- (a) enlighten the interpretation in sedimentation pattern and dynamics in epeiric sea, (b) role of tectonic in epeiric sea sediment dynamics and paleogeographic shift, (c) glauconitization in Precambrian time, role of sea water chemistry and basin dynamics on glauconitization, (d) detect the paleoclimate in Proterozoic earth and understand the chertification process by replacing earlier deposits.

The prime focus on the Vindhyan succession is prompted by rare application of state-of art sedimentological and geochemical analysis. Even the basic need of process and paleogeography related to facies analysis is rarely satisfied in parts of the Vindhyan Supergroup (Bose et al., 2001; Sarkar and Banerjee, 2020). A number of study of course has revealed the depositional environment and sequence building pattern of Vindhyan succession (Bose and Choudhuri, 1990; Bose et al., 2001; Sarkar et al., 2002, Chakraborty, 2006; Kumar and Sharma, 2011; Bose et al., 2015; Singh and Chakraborty, 2020; Sarkar and Banerjee, 2020) and interpreted a rift to sag basin transition with time. But, the change of sediment dynamics below and above the unconformity is not well studied. Stratigraphy is unnecessarily complex in absence of systematic regional study, without any effort given to laterally traced stratigraphic bounding surfaces of various ranks. The general quality of rock exposures and lateral facies variability over time and space create confusion, but excellent observations by some authors of lateral facies variation deserve to mention (Bose et al., 2001; Sarkar et al., 2002; Chakraborty, 2006; Singh and Chakraborty, 2020). Although, the soft sediment deformation structures are not unusual over time and space (Sarkar et al., 1995, 2014; Bose et al.,1997; Singh and Chakraborty, 2020) but, the record of *seismites* in carbonate rock is relatively rare (Sarkar et al., 2014). The carbonate succession (RLM) of the Vindhyan Supergroup provide a scope to escalate the view with recognition of deformations of widely variable scale and origin. Seismic deformations are separated from deformations related with casual sediment deposition. Geochemistry of shale and carbonate of the entire Vindhyan Supergroup carried out (Banerjee and

Jeevkumar, 2005; Banerjee et al., 2006, 2009; Chakrabarti et al., 2007; Singh et al., 2018; Basu et al., 2019; Basu et al., 2021; Singh and Chakraborty, 2021) and the interpretation regrading paleo-salinity, paleo-redox and paleo-environment has been put forward.

Besides the facies analysis, the studied Members of Vindhyan Supergroup potentially preserve authigenic sediments-glauconite and chert (silica). Between them, record of glauconite in the Proterozoic Vindhyan succession is very less recorded (Banerjee et al., 2008; Mandal et al., 2020, 2022), and gives an exceptional opportunity to study them during the present endeavor. The genesis of glauconite in Lower Quartzite and Lower Bhander Sandstone not only help to understand different scenarios during Precambrian time but also, the role of sea water, basin dynamics on different composition of glauconite has been explored. However, most of the cases of glauconitization are common in maximum flooding surface (MFS) but this study shows how sea level fluctuations and basin tectonic can control glauconitization. The study of chert reveals the gap of knowledge on origin of chert by replacing earlier carbonate rock by simple mixing of meteoric water/ ground water and sea water. This study suggests the role of source of silica, pH of silica super-saturated fluid, temperature of fluid and precipitation. Triple oxygen isotope data sets of this study and collection of data sets over geological time and space tried to explain the evolution of hydrosphere since Archean to recent. Temperature dependent oxygen isotope distribution also calculated the temperature during Mesoproterozoic.

## 1.2. Geological Background

The Vindhyan basin, the world's 2$^{nd}$ largest *Purana* basin has widely distributed along the NW-SE stretch of central India, with an average thickness of 4500 m (Ahmad, 1971). It is widely distributed in a different state of India like Bihar, Jharkhand, Uttar Pradesh, Madhya Pradesh, and Rajasthan (Fig. 1.1). These exposures cover an area of about 1,00,000 km$^2$, though it is not the actual exposure area, almost 70,000 km$^2$ has concealed under Deccan traps (Auden, 1933; Krishnan and Swaminath, 1959). Along with these the recent alluvium sediment of Yamuna, Ganga, and Son rivers has covered a considered huge area of Vindhyan succession in central India.

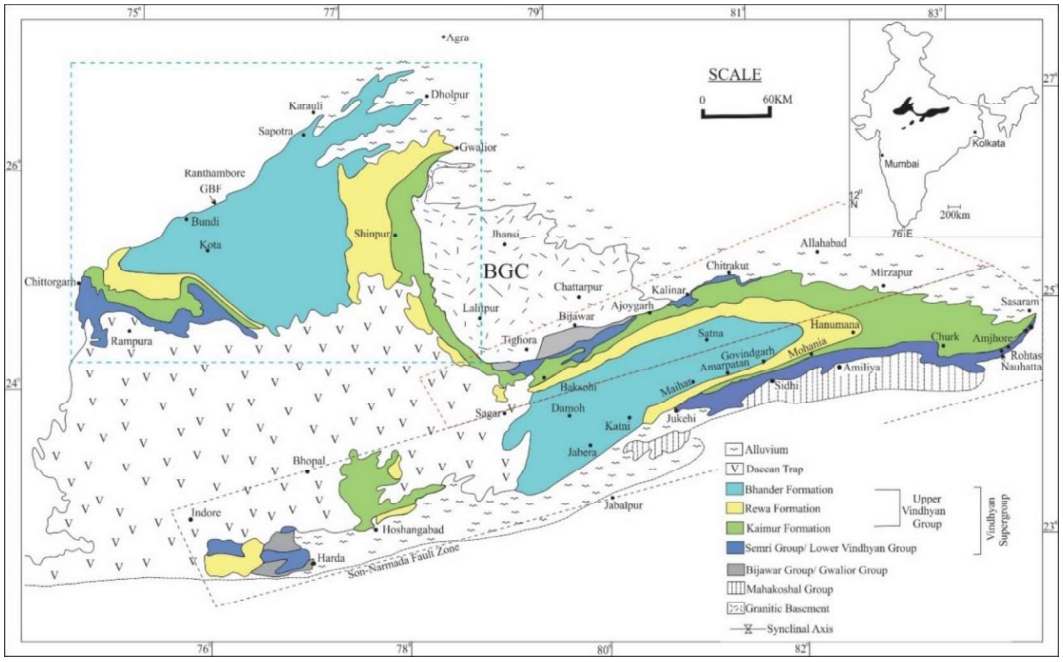


Fig. 1.1. Lithological map of Vindhyan basin (modified after Sarkar and Banerjee, 2020). Entire succession has divided into three Sectors-Rajasthan sector (marked by blue dotted line), Bundelkhand sector (red dotted line) and Son valley sector (black dotted line).

The Vindhyan sediment succession which covers a huge area of India has divided into three sectors depending on the differential distribution of basement rocks, lithology (Fig. 1.1). These are, the Rajasthan sector which is restricted in the Rajasthan and another two Bundelkhand sector and Son valley sector distributed in central India (Fig. 1.1; Madhya Pradesh, Uttar Pradesh, Bihar, Chhattisgarh).

Together the Son valley and Bundelkhand Vindhyan deposits look like a syncline fold with E-W elongation and closure in the east (Fig. 1.2). The beds are dipping towards the center of the syncline. The younger members are present at the core and older are in the flanks. Exposures of the Lower/Semri Group are asymmetrical on the both limb of syncline. In the Bundelkhand sector the stratigraphic units are discontinuous and in small patches, whereas in the Son valley sector beds are more extensive in comparison. But in upper Vindhyan the stratigraphic units are very extensive and uniformly distributed on both the limb of syncline Vindhyan deposit. The dip of the younger beds (i.e. Upper Vindhyan) are very gentle upto 4° whereas dip of the older beds i.e. Semri Group vary from 15° to 30°.

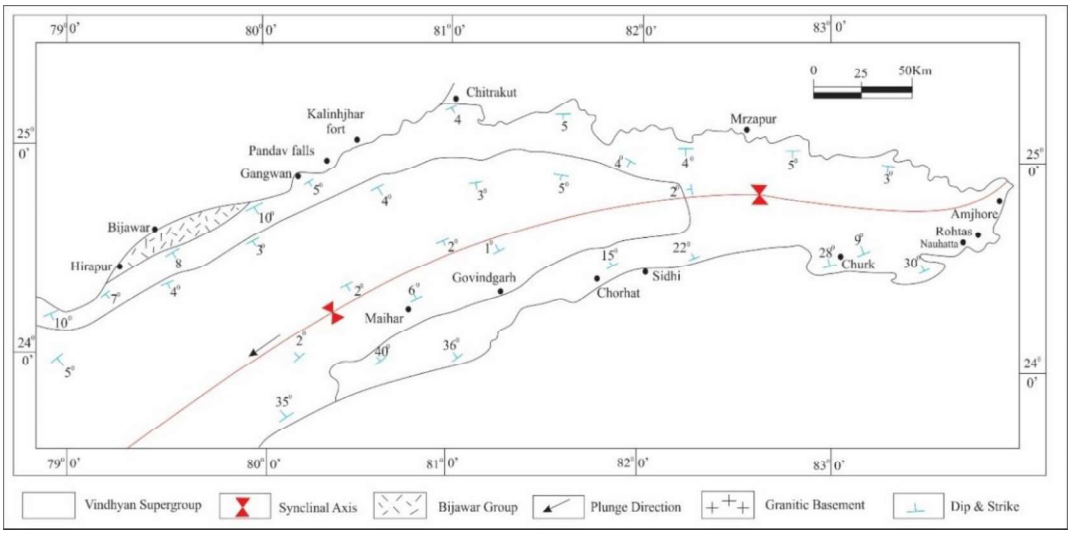


Fig. 1.2. Structural map of Vindhyan succession (modified after Sarkar and Banerjee, 2020).

### 1.2.1. Vindhyan Stratigraphy and Age Constrain

Being a thick sedimentary basin (ca. 4.5 km) classification of the entire stratigraphic succession to one scale is not so easy. Most of the workers put forwards their stratigraphic classifications. However, there are several classifications of Vindhyan stratigraphy but the initial one was proposed by Medlicott (1859). After Medlicott (1859) the stratigraphy of the Vindhyan basin has evolved by Mallet (1869), Oldham et al. (1910), Vredenburg (1910), Auden (1933), Banerjee (1974), Rao and Neelakantam (1978), Bhattacharyya (1996), Chakraborty (2006), Chakraborty et al. (2010), Kumar and Sharma (2011) and Sarkar and Banerjee (2020). The Vindhyan Supergroup is divided into two tire classification on the presence an unconformity in-between lower and upper Vindhyan Group which it laterally correlatable with a correlative conformity (Fig. 1.3; Chanda and Bhattacharya, 1982; Chakraborty, 1996; Bose et al., 2001). The lower Vindhyan is also known as Semri Group whereas the upper Vindhyan has no such formal name. Along with this formal name difference, the lower and upper Vindhyan has a significant difference in lithological distribution as well (Fig. 1.3). The lower Vindhyan has more carbonate and dolomites deposits compare to the upper Vindhyan. Except the carbonate and dolomite distribution, the volcanic are dominantly present in the lower Vindhyan, whereas in upper Vindhyan has only one carbonate unit (Chakraborty et al., 1996; Chakraborty, 2006). On the basis of the lithostratigraphic boundaries and the change of lithological distribution the lower Vindhyan classified into five Formations viz. Deoland sandstone, Kajrahat limestone, Denor Porcellanite, Kheinjua, and Rohtas in order to superposition (Fig. 1.3;

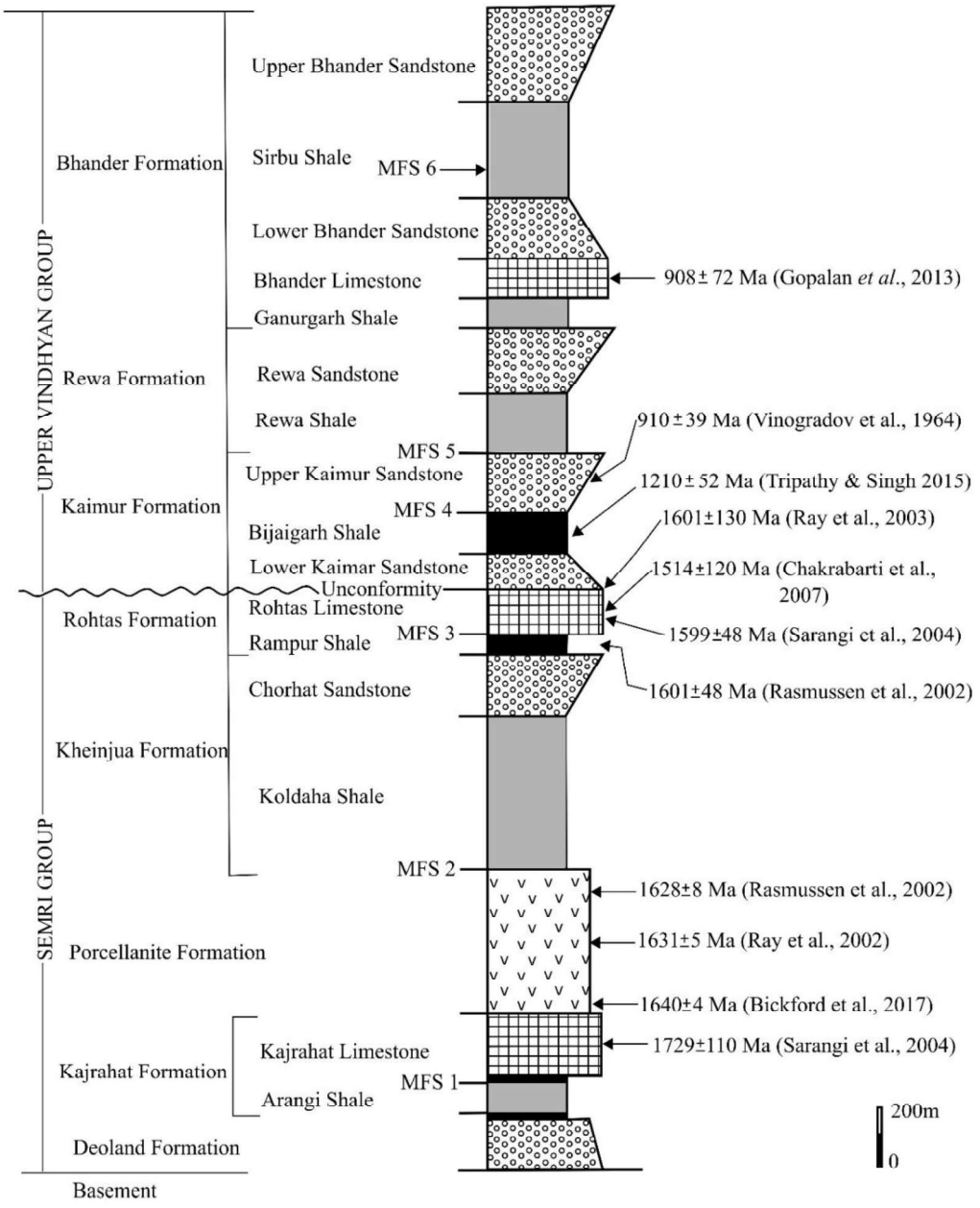


Fig. 1.3. Graphical log of Vindhyan succession (modified after Sarkar and Banerjee, 2020). Note the pronounced depositional age for this suitable sedimentary unit.

Table-1.1). The Deoland Formation is the basal deposit of Vindhyan succession which is directly overlying on the basement Mahakosal Group of rocks. It is entirely made up of sandy materials with some local patches of conglomerate (Prakas and Dalela, 1982). The differential lithological distribution in Kajrahat Formation has sub-divided this Formation

into two Members viz. Arangi Shale and Kajrahat Limestone. The Agrangi Shale consists of dark-grey carbonaceous shale with patches of carbonate deposit. The Kajrahat Limestone is immediately overlying on the Arangi Shale, consisting of limestone and dolostones with different sets of stromatolites (Rao and Neelakantam, 1978). The sedimentary succession consisting of silicified shale, pyroclastics, and volcanic tuffs is named as Porcellanite Formation which is overlain on Kajrahat Limestone. This volcano-clastic sediment deposit passes into shale, sandstone, limestone, and intraformational conglomerate (Auden, 1933; Rao and Neelakantam, 1978; Prakash and Dalela, 1982). This Formation is named as Kheinjua Formation and has been divided into two Members viz. Koldaha Shale and Chorhat Sandstone. The Kheinjua Formation is covered by Rohtas Formation with two Members. The Rampur Shale, the lower part of Rohtas Formation consists of black shale with some grey shale and sandstone intercalation in the basal part. The Rohtas limestone lies at the topmost part of lower Vindhyan overlying on Rampur shale composed of limestone.

The deposition of upper Vindhyan starts just above the unconformity between the lower and upper Vindhyan group. The upper Vindhyan Group consists of three Formation viz. Kaimur, Rewa and Bhander Formation (Fig. 1.3; Table-1.1). The upper Vindhyan Group is mainly consisting of shale and sandstone except one limestone deposit namely Bhander Limestone. The Kaimur Formation consists of five Members viz. Lower Quartzite/ Sasaram sandstone, Bhagwar Shale/ Silicified Shale, Upper Quartzite/ Markundi Sandstone, Bijaigarh Shale, Mangesar Sandstone/ Scarp Sandstone and Dhandraul Quartzite. Together the Lower Quartzite/ Sasaram Sandstone, Bhagwar Shale/ Silicified shale, Upper Quartzite/ Markundi sandstone, Bijaigarh Shale is known as lower Kaimur and Mangesar Sandstone/ Scarp Sandstone and Dhandraul Quartzite in together is known as upper Kaimur. However, the lower Kaimur consists of four Member but each of the stratigraphic unit is not traceable throughout the Son valley sector (Chakraborty, 2006). The Rewa Formation is overlying on Kaimur Formation with thin persistent transgressive lag (Bose et al., 2001). The Rewa Formation is composed of two members viz. Rewa Shale and Rewa Sandstone mainly. The Bhander Formation overlies on Rewa Formation, which consists of Ganurgarh Shale, Bhander Limestone, Lower Bhander Sandstone, Sirbu Shale and Upper Bhander sandstone Members.

Table-1.1. Stratigraphy distribution of Vindhyan Supergroup (modified after Mandal et al., 2019).

| | Group | Formation | Members |
|---|---|---|---|
| Vindhyan Supergroup | Upper Vindhyan Group | Bhander | Upper Bhander Sandstone |
| | | | Sirbu Shale |
| | | | Lower Bhander Sandstone |
| | | | Bhander Limestone |
| | | | Ganurgarh Shale |
| | | Rewa | Rewa Sandstone |
| | | | Rewa Sandstone |
| | | Kaimur | Dhandraul Quartzite |
| | | | Mangesar Sandstone/ Scarp Sandstone |
| | | | Bijaigarh Shale |
| | | | Upper Quartzite/ Markundi Sandstone |
| | | | Silicified Shale/ Bhagwar Shale |
| | | | Lower Quartzite/ Sasaram sandstone |
| | Unconformity | | |
| | Lower Vindhyan Group | Rohtas | Rohtas Limestone |
| | | | Rampur Shale |
| | | | Chorhat Sandstone |
| | | | Koldaha Shale |
| | | Porcellanite | |
| | | Khenjua | Kajrahat Limestone |
| | | | Arangi Shale |
| | | Deoland Sandstone | |

| Table-1.2. Depositional age of different stratigraphic unit in order to stratigraphic distribution of Vindhyan Supergroup in Son valley (modified after Sarkar and Banerjee, 2020) | | | |
|---|---|---|---|
| Stratigraphic Unit | Methods | Age | Authors |
| Upper Bhander Sandstone | K/ Ar | 550 Ma | Crawford and Compstone, 1970 |
| Sirbu shale | F-T | 625±25 Ma | Srivastava and Rajagopalan, 1988 |
| Lower Bhander sandstone | $^{87}Sr/^{86}Sr$ | 600 Ma | Ray et al. 2002 |
| Bhander Limestone | Pb-Pb<br>$^{87}Sr/^{86}Sr$<br>Pb-Pb | 908±72 Ma<br>750-650 Ma<br>1075-900 Ma | Ray et al. 2002<br>Ray et al. 2003<br>Goplalan et al. 2013 |
| Upper Kaimur (from majhgawan kimberlite) | Ar-Ar | 1073.5±13.7 Ma | Laura et al. 2006 |
| Bijaigarh Shale | Re-Os | 1210±51 Ma | Tripathy and Singh, 2015 |
| Rohtas Limestone | Pb-Pb<br>U-Pb<br>Pb-Pb | 1599±8 Ma<br>1631±1 Ma<br>1514±120 Ma | Sarangi et al. 2004<br>Ray et al. 2002<br>Chakraborty et al. 2007 |
| Rampur Shale | SHRIMP<br>SHRIMP | 1593±12 Ma<br>1602±10 Ma | Rasmussen et al. 2002<br>Rasmussen et al. 2002 |
| Porcellinite | SHRIMP<br>SHRIMP<br>U-Pb<br>$^{207}Pb/^{206}Pb$<br>$^{207}Pb/^{206}Pb$ | 1628±8Ma<br>1631.2±5.4 Ma<br>1630.7±0.4 Ma<br>1640±4 Ma<br>1647±18 Ma | Rasmussen et al. 2002<br>Ray et al. 2002<br>Ray et al. 2002<br>Bickford et al. 2017<br>Mishra et al. 2018 |
| Kajrahat Limestone | U-Pb<br>Pb-Pb | 1631±5 Ma<br>1729±110 Ma | Ray et al. 2002<br>Sarangi et al., 2004 |
| Basement-Mahakoshal (Jhiragadandi Granite) | U-Pb | 1753±9 Ma | Bora et al. 2013 |

The age of the Vindhyan Supergroup has been a matter of debate for over the last hundred years. Based on both radiometric dating and palaeobiological evidences, The Vindhyan Supergroup is considered to be of Meso- to Neoproterozoic age (Bose et al., 2001). Stromatolites from the Lower Vindhyan and Upper Vindhyan represents a age range from 1400-600 Ma (Prasad, 1980, 1984). Recent U-Pb, Pb-Pb geochronology from magmatic and detrital zircon have proved that the Vindhyan basin perhaps opened before ~1700 Ma and sedimentation closed nearly ca 1000Ma (Ray et al., 2002;Rasmussen et al., 2002; Sarangi et al., 2004; Chakrabarty et al., 2007; Malone et al., 2008; Bengston et al., 2009; Meert et al., 2010; Pradhan et al., 2010; Turner et al., 2010; Davies et al., 2011; Bora et al., 2013; Gopalan et al., 2013; Venkateswaralu and Rao, 2013; Basu and Bickford, 2014; Bickford et al., 2017). These reliable radiometric ages have put forward with respect to the age of Vindhyan Supergroup, particularly from the Lower Vindhyans (Table 1.2). Although, the unconformity between lower and upper Vindhyan is well known but missing of such reliable dating materials unable to ditect time period for no sedimentatioz. Recently Tripathy and Singh (2015) detect the age of Bijaigarh shale by Re-Os method and proposed that after lower Vindhyan sedimentation basin was exposed for 400 Ma (Fig. 1.3).

### 1.2.2. Lithological distribution and Paleogeography-Paleoclimate

Since from 1933 (Auden) there have been several attempts to visualize the depositional environment and paleogeography of Vindhyan successions. The several attempts have interpreted the different stratigraphic units as barrier bar, lagoon, tidal flat and beach deposition (Banerjee, 1964; Rao and Neelakantam, 1978; Chanda and Bhattacharya, 1982; Prakash and Dalela, 1982; Singh 1985; Soni et al., 1987; Prasad and Verma, 1991; Akhtar, 1996; Bose et al., 1999, 2001; Sarkar et al., 2002a, b, 2004). Though there are several depositional environments but a broad consensus suggests that the Vindhyan Supergroup is of largely shallow marine i.e. epeiric sea (Singh, 1980, 1985; Chanda and Bhattachrya, 1982; Bose et al., 1999, 2001; Sarkar et al., 1996) with some terrestrial input in-between (Bose and Chakraborty, 1994; Sarkar et al., 1996, 2011; Bose et al., 1999, 2001).

The Vindhyan Supergroup is mainly composed of sandstone, shale and carbonate sediments. In earlier sections, we have discussed that the Vindhyan Supergroup has divided into two Groups viz. lower and upper Vindhyan. Although volumetrically lower Vindhyan has higher carbonate and volcano-clastic sediment deposits, but except these there is not

much lithological difference between lower and upper Vindhyan Group, so we can't expect a huge difference in paleogeography in upper and lower Vindhyan.

As maintioned in earlier section the lower Vindhyan Group is consisting of Deoland, Kajrahat, Porcellinite, Kheinjua and Rohtas Formation. The Deoland is entirely composed of sandstone with some local patches of conglomerates. The Deoland sandstone was inferred as a glacier deposit (Dubey and Chaudhury, 1952; Ahmad, 1955; 1958; Mathur, 1954, 1960, 1981), while Singh (1973) inferred this deposit as high gradient coastal rivers deposits and Banerjee (1974) inferred it as mainland beach. But the study of the recent works infers this stratigraphic succession as shelf environment (Bose et al., 2001; Banerjee et al., 2008) and this deposit gradationally pass into Arangi shale of Kajrahat Formation. The overall fining upward sequence from Deoland Sandstone to Arangi Shale has been interpreted as a transgressive system tract deposit (Banerjee et al., 2008). The Arangi Shale is a shelf deposit (Bose et al., 2001), however lagoon and shallow marginal lagoon has also been inferred (Singh, 1973; Banerjee, 1974). The Arangi Shale deposit has pass into a limestone and dolomite succession which is known as Kajrahat Limestone. The kajrahat Limestone is consisting of limestone, dolomites with various types of stromatolites and this depositional environment is considered as tidal flat by Singh (1973), Banerjee (1974), Bose et al. (2001), Sarkar and Banerjee (2020), whereas Banerjee (1997) interpreted this deposit as a shallow marine product. The Kajrahat Limestone represents a shallowing upward succession from it's bottom to top. The volcanic tuff, pyroclastic surge and flow deposits above Kajrahat Limestone make Porcellinite succession which has interpreted as shallow marine deposition (Bose et al., 2001). Whereas Srivastava (1997), Banerjee (1997) recognized frequent subaerial deposit within sub-aqueous deposition. This volcano-clastic sediment succession gradationally passes into basal Member of Khenjua Formation, Koldaha Shale. Few pyroclastic layers are also associated with the sand free dark shale, grey shale with intercalation of sand, silt and thick texturally immature sandstone. This Koldaha Shale has inferred as shelf deposit with some deltaic- fluvial input, and the pyroclastic layers has been interpreted as reworked sediment of earlier deposit (Bose et al., 2001; Banerjee and Jeevankumar, 2005). Even, the granular lag within it has represented as a transgressive lag (Sarkar and Banerjee, 2020). The Koldaha Shale gradationally pass into Chorhat Sandstone which has been deposited in four non-recurring successions. The Chorhat sandstone consists of shale, intercalation of shale and fine sand, siltstone and stone. The deposition of this sedimentary unit has been interpreted as a

shallow marine deposit (Bose et al., 2001), whereas Sarkar et al. (2006, 2014) has interpreted this deposition as subtidal to intertidal to supratidal. The Rampur Shale of Rohtas Formation overlies on this tidal flat deposit. The Rampur shale is entirely composed of black shale with sand-shale intercalation in basal and shale-limestone intercalation in top. The deposition of Rampur Shale has interpreted as tidal flat environment (Singh, 1973; Banerjee, 1974), while Bose et al. (2001) interpreted this deposition as shelf deposit (Sarkar et al., 2002a). The Rampur shale gradationally pass into thick limestone deposit named as Rohtas Limestone. The Rohtas Limestone deposit has interpreted as Shelf environments whereas the flat pebble and edgewise conglomerate within it has been interpreted as gas degradation and storm surge (Banerjee et al., 2009; Sarkar et al., 2018).

The Kaimur, Rewa and Bhander are the three Formations composed within upper Vindhyan Group. The upper Vindhyan is well studied compare to the lower one. The upper Vindhyan is mostly comprise of shale-sandstone intercalations. The lower Kaimur comprises of Lower Quartzite/ Sasaram Sandstone, Bhagwar Shale/ Silicified shale, Upper Quartzite/ Markundind Upper Quartzite/ Markundi Sandstone Sandstone and Bijaigarh Shale. The lower Kaimur has started its deposition with a granular lag and followed by sandstone, shale repetitively. The Lower Quartzite consists of sandstone and shale which has been interpreted as tidal bars (Chakraborty and Bose, 1990). This sandstone deposit passes into Bhagwar shale/ Silicified Shale which is composed of volcano-clastic sediments in SW part and Sandstone-shale intercalation in NE part and followed by upper Quartzite/ Murkundi Sandstone and Bijaigah Shale which are mainly restricted in NE part mainly (Chakraborty, 1993, 1995, 2006; Bose et al., 2001). The sand free organic rich and pyrite bearing Bijaigarh Shale inferred as deep offshore product (Chakraborty, 1993, 1995; Banerjee et al., 2006; Sur et al., 2006; Schieber et al., 2007). The Bhagwar Shale has been interpreted as reworked product of volcanic sediments (Sarkar and Banerjee, 2020; Choudhuri et al., 2020). The lower part of upper Kaimur starts its deposition with a thick sandstone deposit, Scarp sandstone which has been interpreted as shallow shelf deposition and it transits to a fluvial-aeolian environment named as Dhandrual Quartzite (Chakraborty, 1993; Bose et al., 2001). However, Quasim et al. (2019) interpreted the Scarp Sandstone and Dhandrual Quartzite as tidal flat and tidally influenced fluvial channel deposit. The Rewa Formation starts its deposition with a thin granular lag which has been inferred as initiation of a transgression (i.e. transgressive lag) after deposition of Kaimur deposit (Bose et al., 2001). The transgressive lag has cover by an alternative sandstone, shale deposit which has transit to

shale with storm sandstone and this deposit is named as Rewa Shale (Chakraborty et al., 1996; Chakraborty and Sarkar, 2005; Sarkar and Banerjee, 2020). The deposition of Rewa Shale has inferred as storm dominated shelf (Chakraborty et al., 1996; Bose et al., 2001; Sarkar and Banerjee, 2020). Along with these, Rewa formation has contained some kimberlite pipes and some volcano-clastic conglomerate (Chakraborty et al., 1996; Bose et al. 2001). The Coarsening upward Rewa Sandstone is overlying on the Rewa Shale which has been interpreted as shallow marine-tidal flat deposit to fluvial-aeolian transition (Bose and Chakraborty, 1994; Bose et al., 2001). The Bhander Formation, the youngest Formation of upper Vindhyan comprises of Ganurgarh Shale, Bhander Limestone, Upper Bhander Sandstone, Sirbu Shale and Lower Bhander Sandstone. The Ganurgarh Shale consists of wave dominated reddish grey coloured alternative sandstone and shale and interpreted as chenier environment (Bose et al., 2001, Chakraborty et al., 1998). Followed by shale-limestone intercalation grading upward into Bhander Limestone. This Bhander limestone has been inferred as shallow marine with partely developed lagoon in-between (Bose et al., 2001; Sarkar et al., 1996, 2014). Here, the carbonate depositional setting has inferred as an open ramp setting (Sarkar et al., 1996; Sarkar and Banerjee, 2020). The Lower Bhander Sandstone overlies on Bhander Limestone, consists of red mudstone and fine-grained sandstone and interpreted as coastal playa deposition (Bose and Chaudhuri, 1990; Chakraborty et al., 1998; Bose et al., 2001; Sarkar and Banerjee, 2020). In the transition from Lower Bhander Sandstone to Sirbu Shale a stromatolite patch, oolitic bars are present and this is considered as the lower part of Sirbu Shale. The lagoonal environment has been inferred as its depositional environment (Singh, 1973; Bose et al., 2001, Sarkar et al., 2002). The upper part of Sirbu Shale consists of shale in some intercalation sandstone beds and the number and thickness of sandstone increase upward. Gradationally this shale sandstone intercalation passes into a thick sandstone deposit named Upper Bhander Sandstone. The upper of Sirbu Shale has interpreted as a storm-dominating shelf (Bose et al., 2001; Sarkar et al., 2002) and the Upper Bhander sandstone inferred as Fluvio-aeolian and marginal marine i.e. terrestrial deposit (Bose et al., 2001; Sarkar et al., 2004, 2011; Sarkar and Banerjee, 2020). Lithological distribution and their corresponding depositional environment has represented in Table-1.3.

Table 1.3. Lithological distribution, depositional environment and sequence stratigraphic system tracks of each member present in Upper Vindhyan and Lower Vindhyan Group (N.B. TST-Transgressive system track, HST-High-stand system track, MFS-Maximum flooding surface, modified after Bose et al., 2001)

| Group | Formation | Members | Lithology | Depositional Environment | System Track |
|---|---|---|---|---|---|
| Upper Vindhyan Group | Bhander Formation | Upper Bhander Sandstone | Well sorted sandstone with wave features, current crescents at the lower part and the upper part has very well sorted sandstone with translatent cross-stratifications, adhesion ripples. | Fluvio-aeolian and marginal marine | HST |
| | | Sirbu Shale | Sirbu shale has two different lithology. Basal part is dominating of Stromatolite and carbonate deposit. Upper part is dominating of grey shale with some sandstone layers. | Shelf-lagoon | TST |
| | | Lower Bhander sandstone | Sandstone-mudstone inter-bedding, thin conglomerate with dominating wave and storm features. Mudstone is mainly reddish in color. Abundance of salt pseudomorphs. | Coastal playa | |
| | | Bhander Limestone | Dominating in micritic, oolitic and Stromatolitic limestone with tidal- emergence features. Laterally continuous soft-sediment deformation structures. | Shallow marine | |
| | | Ganurgarh Shale | Mudstone-sandstone inter-bedding with abundance wave and emergence features. | Chenier | |
| | Rewa Formation | Rewa Sandstone | Medium to well sorted sandstone with bimodal cross-stratification, mud draping at basal part and upper part consists of ill-sorted sandstone unimodal trough cross-stratifications, compound cross-stratification. | Tidal-Fluvio-aeoline | HST |
| | | Rewa Shale | Sandstone-shale inter-beds with wave and sole features. | Shelf | TST |
| | Kaimur Formation | Dhandrual Quartzite | Large scale cross-stratified thick sandstone with inbetween well sorted aeolian sediments. | Shelf to fluvio-aeolian | HST |
| | | Scarp Sandstone | Well sandstone with thin mudstone, quartz rich, large scale cross-stratified. | | |

| | | | | | |
|---|---|---|---|---|---|
| | | Bijaigarh Shale | Black shale with some intercalation of volcano-clastic sediments | Intertidal to shelf | TST |
| | | Upper Quartzite | Medium grain sandstone with the wave and tide features. | | |
| | | Bhagwar Shale | Reworked volcanoclastic materials. | | |
| | | Lower Quartzite | Sandstone with siltstone, shale in-between. Sandstone contains dominating tidal features. | | |
| Lower Vindhyan Group | Rohtas Formation | Rohtas Limestone | Black shale- limestone intercalation transit to pure limestone and dolomite deposit. The limestone contains abundant wave features. | Shelf | HST |
| | | Rampur shale | Black Shales with few volcano-clastic layers in-between and basal part is sandstone-grey shale intercalation with few wave features followed by shale and gutter sandstone. | Shelf | TST |
| | Khenjua Formation | Chorhat Sandstone | Well sorted sandstone and mudstone inter-beds. Sandstone is full of wave features and MISS structures. Mudstone is reddish in color. | Shallow marine | HST |
| | | Koldaha Shale | Sandstone-shale inter-beds with waves and sole features. Local poorly sorted sandstone intervals with emergence features. | Shelf, deltaic fluvial | |
| | Porcellinite | | Volcanic ash, pyroclastic flow/ surge deposits, locally large bombs. | Shallow marine | TST |
| | Kajrahat formation | Kajrahat Limestone | Dominating in dolomitic limestone with different sets of Stromatolite and desiccation cracks on top. Few volcano-clastic and siliciclastic beds have also interbedded in-between. | Subtidal to peritidal | HST |
| | | Arangi Shale | Composed of grey shales. | shelf | TST |
| | Deoland | | Well sorted sandstone, bimodal-bipolar cross-stratification. Local patches of conglomerate. It has a fining upward deposition. | Shallow Shelf | |

### 1.2.3. Tectonic Setting and Sedimentation

As mentioned earlier the Vindhyan basin is one of the largest Purana basins in the world and covered 100000 $km^2$ area. The Vindhyan sediments were distributed from Rajasthan to Madhya Pradesh, Uttar Pradesh, Bihar, and Chhattisgarh (Fig. 1.1). This sediment distribution is bounded by the Son-Narmada lineament in the southern margin and Great Boundary Fault in the northern margin. The Son-Narmada lineament is continuously present along 1200 km in the Indian sub-continent and separates the boundaries of Aravalli-Bundelkhand and Dharwar Province (Mazumder et al., 2000; Achyaryya, 2003). Along with a series of southerly dipping reverse faults (Kaila et al., 1985), this lineament is directed along the NNE-SSW direction in central India and periodically reactive during Precambrian (Choubey, 1971). The deep seismic study infers that this lineament is extended up-to-the Moho discontinuity boundary in the inner earth (West, 1962; Kaila et al., 1985, 1989; Archaryya, 2003). The western margin i.e. Rajasthan sector the Great Boundary fault is dipping in NW direction along with the NE-SW trend (Tewari, 1968; Naqvi and Rogers, 1987; Narain, 1987; Verma, 1991; Srivastava and Sahay, 2003). The Great Boundary Fault separates the Vindhyan basin from the folded metasedimentary Aravalli Supergroup, the Delhi Supergroup, and Bhilwara Supergroup (Fig. 1.4).

The Vindhyan basin was initiated its sedimentation with a wide range of basement and that is Bundelkhand-Aravalli Province (Erriksson et al., 1999; Mazumder et al., 2000). The variety of Precambrian basement rocks are Bundelkhand granite, Mahakoshal Group of rocks, Bijawar Group of rock, Gwalior Group of rock, Banded Gneissic Complex (BGC) and Chhotanagpur Granitic Complex (Fig. 1.4; CGC). The Bundelkhand Gneissic Granite Complex present in the north western margin of the crescent shaped Vindhyan basin central India and it separates the entire Vindhyan basin from Rajasthan area to central India Vindhyan deposit (Fig. 1.4). The Bundelkhand Granite Gneiss Complex is dominated by Tonalitic-Trondhjemite-Granodiorite and some K-rich granite emplacement within these (Rogers, 1968; Bandhyopadhya et al., 1995; Eriksson et al., 1999; Mazumder et al., 2000). The Mahakosal Group is present in the southern and eastern margin of crescent shaped central India Vindhyan basin (Das et al., 1990; Roy and Bandyopadhyay, 1990; Nair et al., 1995). Bijawar Group restricted on the northern and northeastern margin of the crescent shaped Vindhyan, central India (Das et al., 1990; Roy and Bandyopadhyay, 1990). The

Chottonagpur Gneissic Complex is at the basement of the Vindhyan in southeastern part and it consists of gneisses, granite and granodiorite (Singh et al., 2001). The Banded Gneissic complex and Gowalier Group are present as the basement of Rajasthan sector Vindhyan.

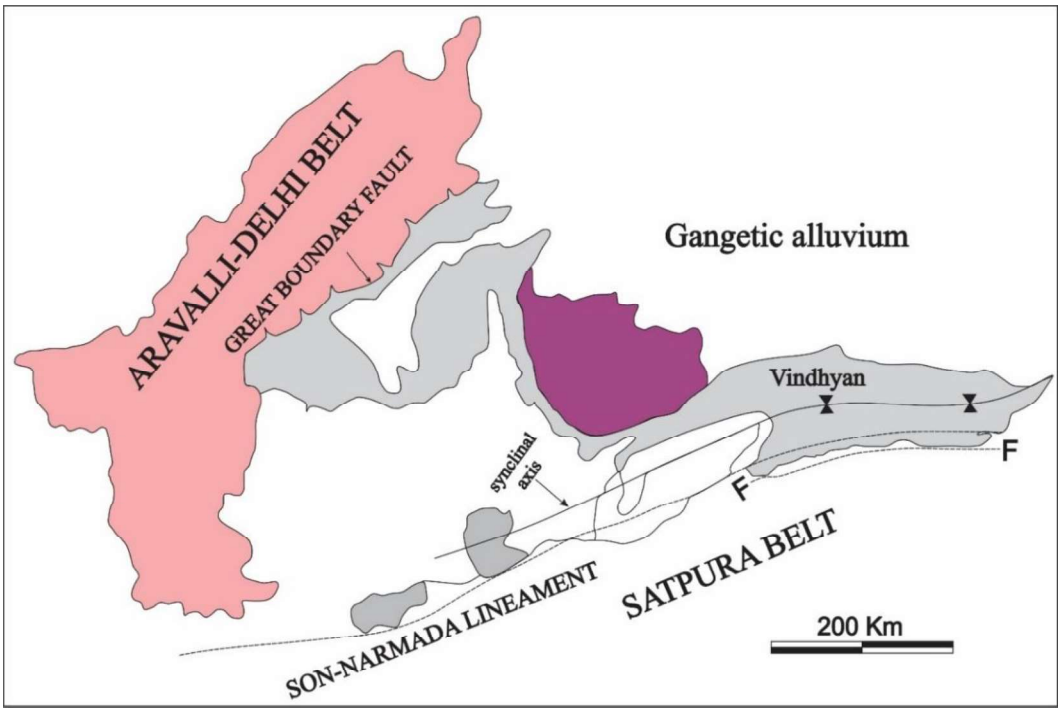


Fig. 1.4. Structural map of Vindhyan Supergroup (modified after Sarkar and Banerjee, 2020).

There have been different ideas about the tectonic setting of Vindhyan basin (Table 1.4). The presence of the Aravalli, Delhi, Satpura orogenic belt at the boarder of the Vindhyan basin infer that The Vindyan basin was formed as a periphetral foreland basin related to southernly diping subduction before the collision of Bhandara and Bundelkhand cratons (Auden, 1933; Chakraborty and Bhattacharyya, 1996; Raza and Casshyp, 1996; Chakraborti et al., 2007). The concept of foreland basin was also supported by the Nd isotope study of clastic and non-clastic sediment deposit within the basin (Chakraborti et al., 2007). The sediment was verging either north (Charkroborti and Bhattacharyya, 1996) or south (Chakraborti et al., 2007) direction. However, some workers have proposed this basin as strike-slip fault basin (Crawford and Compston, 1970; Crawford, 1978). Except these two concepts, a different view has suggested by most of the workers (Table-1.4) where the Vindyan basin has been considered as intracratonic rift basin (Choubey, 1971; Naqni and Rogers, 1987; Kaila et al., 1989; Verma and Banerjee, 1992; Sarkar et al., 1995; Ram et al., 1996; Bose et al., 1997). Along with these, the observation of Bose et al. (1997,

2001) i.e. the overall fine grain size and high textural and mineralogical maturity of sandstone advocated that this basin is a transition of an intracratonic rift to sag basin.

Table-1.4. Tectonic models proposed by previous workers

| Tectonic models | Authors |
|---|---|
| Foreland basin | Auden (1933); Chakraborty and Bhattacharyya (1996); Raza and Casshyap (1996); Chakraborti et al. (2007) |
| Strike-slip basin | Crawford (1978) |
| Syncline | Chanda and Bhattacahrya (1991); Chaudhuri and Chanda (1991); Prakash and Dalela (1982) |
| Rift basin | Choubey (1971); Naqvi and rogers (1987); Kaila et al. (1989); Verma and Banerjee (1992); Ram et al. (1996) |
| Intracontinental platform | Valdiya (1982) |
| Rift to sag basin | Bose et al. (2001) |

The intracratonic Vindhyan sediments were deposited in E-W direction with westernly opening basin (Chanda and Bhattacharyya, 1982; Chaudhuri and Chanda, 1991; Sarkar et al., 2004; Chakraborty et al., 2012) have recorded the evolution of initial rift during deposition of Lower Vindhyan and that converted to sag during Upper Vindhyan deposition (Bose et al., 2001; 2015). The intracratonic north-south rifting with a dextral shear at the initial and sag at subsequent stage has revealed after extensive studies of multiple fronts (Bose et al., 1997, 2001; Sarkar et al., 2002b). However, NW-SE orientation of several rides has identified in E-W elongated main Vindhyan basin but in upper Vindhyan these segments was removed at sag stage (Bose et al., 2001).

### 1.2.4. Paleocurrent distributions

Since from the Auden (1933) many workers have collected the paleocurrent data from the different part of Vindhyan basin (Banerjee, 1964, 1974; Misra and Awasthi, 1962 and many more). All the paleocurrent study convey that the average paleocurrent direction is in north-west. The average paleo-slope was remained more or less constant throughout the Vindhyan sedimentation. The paleocurrent in central and eastern part of the basin is dominating in north-western direction. The same paleo-current direction i.e. NW is also following in southern and northern boundary. However, the paleo-current direction of the

basal sandstone and conglomerate in Deoland Formation is directed along southerly (Bose et al., 1997).

Along the southern boundary of the basin noted north-easterly direction (Misra, 1969). For the western and northwestern part of the basin paleo-current data are too meagre to yield a reasonable regional pattern. The paleo-current data obtained by Jafar et al. (1966) from the Kaimur Group at Chunar and Bhander Group at the Fatehpur Sikri appear to be extremely significant, as these two locations occur in the northern boundary of the basin. A NW to NNW and E to ENE paleo-current directions at Chunar and Fatehpur Sikri respectively indicates that the deeper parts of the basin should exist northwest of Chunar and east or ENE of Fatepur Sikri. Furthermore, Jafar et al. (1966) suggested that the Lower Vindhyan sea did not extend much beyond the present northern limit, but in the following Kaimur time the sea extended far beyond submerging the Bundelkhand massif.

It appeared that the suggestions made by Jafar et al. (1966) and Banerjee (1964) are more or less identical. Whereas Jafar et al. (1966) conceived of northward regression of the southern shoreline, Banerjee (1974) on the basis on his paleo-current data coupled with isopach data suggested that the zone of maximum accumulation of sediments in the eastern part of the basin shifted towards the northern part with time. The regional paleo-slope was north-westerly in the Son valley and Bundelkhand sector (Bose et al., 2001) and westerly in Rajasthan sector.

### 1.2.5. Vindhyan biotas

The un-metamorphosed and mildly un-deformed Vindhyan basin deposit consists of wide variety of ancient life forms. The fossils are mainly organo-sedimentary structures, carbonaceous mega-fossils, micro-fossils, Ediacara fossils and several trace and body fossils (Table-1.5, 1.6, 1.7). However, some of the fossils provide the age of the deposition associated with fossils but some the ages conflict with the deposition of Vindhyan Supergroup.

| Table 1.5. Stromatolite reported from the Vindhyan Supergroup and its age implication | | | |
|---|---|---|---|
| Name of the Members | Stromatolites | Authors | Age |
| Sirbu Shale | Colleniabiacalica, Colleniacolumnari, Colleniaburiatica, Colleniabaicalica | Prasad and Ramaswamy (1980); Prasad (1984) | Middle to upper Riphean |
| Bhander Limestone | Colleniasymmetrica, Baicaliabaicalica, Maihariamaiharensis, Colleniaundusa, Tungussia, Boxonia | Rao et al. (1977); Kumar (1967a); Sarkar (1974); Kumar (1982) | Upper Riphean (900-600 Ma) |
| Rohtas Limestone | Colleniakusiensis, Colleniacolumnaris, Conophytoncylindricus, Colleniabaicalica | Sharma (1996); Singh and Banerjee (1980) | Middle Ripjean |
| Koldaha Shale | Collenia cylindrical, Colonellacolumnaris, Colleniaclappii | Kumar (1976b) | Lower Riphean |
| Kajrahat limestone | Conophytoncylindricus, Colleniakusiensis, Cryptozonoccidentale, Colonnella sp., Colleniafrequence, Conophytoninclinatum, Kussiellakusiensis, Kussiella, Colonnella | Prasad (1980) Prasad (1984) Kumar (1982) Kumar and Gupta (2002) | Lower Riphean |

The organo-sedimentary structures represent Stromatolite and microbilites. The Stromatolite and microbialites are the organo-sedimentary infer the interaction between benthic microbial communities and detrital or chemical sediments. However, the stromatolites and other organo-sedimentary structured has used as bio-stratigraphic profile though some of them are time and space constrain (Raaben, 1969, 2005; Kumar, 1978, 1980; Raha and Sastri, 1982). The stratigraphic units of Vindhyan Supergroup contain some specific species (Table-1.5). The Lower Vindhyan Group is constricted with *Conophyton, Colonnella and Kussiella* species whereas Upper Vindhyan Group is dominating with *Baicalia* and *Tungussia*. In comparison between Lower and Upper

Vindhyan species the *Conophyton* was entirely absent in Upper Vindhyan. Based on the age of species the Lower Vindhyan is restricted in Late to Middle Riphean age (1600-1400 Ma and 1400-1000 Ma) whereas workers proposed Middle to Upper Riphean age (1400-1000 Ma and 1000-650 Ma) for the Upper Vindhyan Group (Kumar, 1984; Kumar et al., 2005). However, some of the species are restricted in Precambrian but some of them are still found in modern sea like Conophyton is only found in Precambrian record but Cryptozon also present in modern intertidal sea (Logan, 1961). Along with the age specification, some of the species are used to identify the depositional environment. But some of the workers has questioned on the bio-stratigraphic application based stromatolite (Davaud et al., 1994; Altermann, 2002, 2004).

Along with the identification of wide varieties organo-sedimentary structures, Stromatolite, carbonaceous mega-fossils a large number of microfossils also have been reported from both argillaceous and carbonates deposit of Vindhyan Supergroup. However, most of the microfossils are belong to cyanobacterial group but few eukaryotic acritarch is also found in Vindhyan Supergroup. The microfossils reported from the Vindhyan Supergroup infer that the Semri Group was deposited during Mesoproterozoic and the Upper Vindhyan was deposited in Neoproterozoic.

With all of the fossils some Ediacara fossils has reported from the Vindhyan Supergroup though there is confusion about its originality i.e. these may not true Ediacara. The Ediacara fossils which are reported from Vindhyan Supergroup are *Ediacara flindersi, Cyclomedusa davidi, Medusinites, Medusinites asteroids, Dickinsonia* and *Beltanelliformis brunsae*. Kathal (2000) reported an Ediacara genus and compared with *Spriggina floundersi*. However, Kumar (2001) suggested these are as weathering features. After that fossils have reported as problematic Ediacara fossils by Schmidt (2003) and De (2003). The recent radiometric dating has been questioned on all of these reported fossils and they have compared with microbial mat related structures (Seilacher, 1997; Banerjee et al., 2010; Sarkar et al., 2006, 2014, 2018; Sarkar and Banerjee, 2020; Choudhuri et al., 2020).

| Table-1.6. Carbonaceous fossil reports from the Vindhyan Supergroup | | | |
|---|---|---|---|
| Stratigraphic horizon | Carbonaceous mega-fossils | Authors | Remarks |
| Sirbu Shale | Fermoria like structures | Misra and Awasthi (1962) | Uncertain |
| Bhander Limestone and Sirbu shale | Chuariacircularis, Tawuiadalensis | Kumar and Srivastava (1997) | |
| Rewa Shale | Chuariacircularis, Tawuiadalensis | Rai et al. (1997), Srivastava (2004) | |
| Suket Shale | Vidhyanellajonesi, Fermoria minima | Sahni (1936) | Revised as Chuariacircularis |
| Suket Shale | Circular to semi ovoid carbonaceous disc | Misra and Dube (1952) | Chuariacircularis |
| Suket Shale | Circular form Fermoriaspbrodely ovoid form | Misra (1969) | Chuariacircularis |
| Suket Shale | Disc-like remain type 1-6 | Maithy and Shukla (1977) | Chuariacircularis |
| Suket Shale | Vavosphaeridiumreticulatum, Vavosphaeridiumvindhyanesi, Kildinellasuketensis, Tasmanitesvindhyanesis | Maithy and Shukla (1977) | Revised as Chuariacircularis |
| Suket Shale | Chuariacircularis, Tawuiasuketensis, Vindhyaniajonesii | Marthur (1982) | Vindhyaniajonesii is similar to Krishnania acuminate |
| Suket Shale | Chuariacircularis, Chuariafermorei, Twauiasuketenis, Tawuiarampuranesis | Marthur (1982) | Revised as Chuariacircularis and Tawuiadalensis |
| Suket Shale | Chauriacircularis | Maithy and Shukla (1984) | |

| | | | |
|---|---|---|---|
| Suket Shale | Tyrasotaenia sp. | Shukla and Sharma (1990) | |
| Suket shale-Rampur Shale | Carbonaceous disc described as Obolella/ Operculam of Hyolithella | Jones (1909) | Revised as Chuariacircularis |
| Suket shale-Rampur Shale | Fermoria minima, Fermoria granulosa, Fermoriacapsella, Protobolellajonesidescribed primitive brachiopod or eurypterids | Champmann (1935) | Revised as Chuariacircularis |
| Rohtas Limestone | Spiral impression described as impression of coiled worm | Beer (1919) | Revised as Grypaniaspiralis |
| Rohtas Limestone | Carboneceousdics and algal dust | Misra and Bhatnagar (1950) | Revised as Amjhorearohtasae |
| Rohtas Limestone | Katniasinghi classified under Annelida | Tendon and Kumar (1977) | Similar to Grypania |
| Rohtas Limestone | Chuaria minima, Tawuadalensis | Maithy and Babu (1988) | |
| Rohtas Limestone | Krishnania acuminate, Krishshnaniamultistriata | Maithy (1991) | Krishnania possibly represents oldest benthic algal forms |
| Rohtas Limestone | Chuariacircularis, Grypania sp. | Kumar (1995) | |
| Rohtas Limestone | Chuariacircularis, chuariagigantia, chuariamelanocentrics, Grypaniaspiralis, Grapania sp., Phylloniabistaria | Rai and Gautam (1998) | Chuariagigantia and Chuariamelanocentric are the synonymy of Chuariacircularis |
| Rohtas limestone | Chuariacircularis, Tawuiadalensis | Srivastava (2004) | |

| Table-1.7. Microfossil reported from Vindhyan Supergroup | | | | |
|---|---|---|---|---|
| Formation | Member | Evidence | Authors | Proposed age |
| Bhander | Upper Bhander Sandstone | | | |
| | Sirbu Shale | *Archaeorestis sp., Spaerophucuspervum, Myxoccoidespsilata,Protosphaeridiumdesum,* | Maithy and Mandal(1983) | Late Proterozoic |
| | | | Maithy and Meena (1989) | Late Proterozoic |
| | Lower Bhander Sandstone | | | |
| | Bhander Limestone | *Biocatenoidessphaerula,Sphaerophycusparvum* | Maithy and Gupta (1983) | Late Proterozoic |
| | Ganurgarh Shale | | | |
| Rewa | Rewa Sandstone | | | |
| | Rewa Shale | *Myxoccoidespsilata,Nanococcus vulgaris* | Maithy and Mandal (1983) | Late proterozoic |
| Kaimur | | | | |
| Rohtas | Rohtas Limestone | *Myxoccoides globose,Palaeonacystissuketensis* | Maithy and shukla (1977) | Late Riphean |
| | | Misraeapsilata | Maithy and Babu (1988) | 1200-940 Ma |
| | | Leisphaeridiadensum | Nautiyal (1986) | 1000-900 Ma |
| kheinjua | Chorhat sandstone | Eomycetopsis septate | | |
| | Koldaha Shale (Fawn Limestone) | Sphaerophycusparvum,Bontophysalisbelcherensis, Oscillatorioppsisbreviconvera | Kumar and Srivastava (1995) | 1200 Ma |
| | | Myxoccoides minor, | McMenamin et al. (1983) | 1200 Ma |
| | | Tetraphycus congregates | | |
| | | Kildinellaaff. | Nautiyal (1983) | 1200-900 Ma |
| Porcelllinite | | | | |
| Kajrahat | | Palaeoanacystissuketensis | Nautiyal (1983) | 1200-900 Ma |

Except these fossils some trace fossils have also been reported from Vindhyan deposit (Kumar, 1978; Kulkari and Boarkar, 1996a). However, these trace fossils have clarified as cracks, synerasics cracks on mat induced sandy beds (Banerjee, 1997; Seilacher et al., 1998; Seilcher, 1997, 2004; Singh and Sinha, 2001; Sarkar et al., 2004). Like these Seilacher (1997) infer gas escape structures and impression of algae and microbial mat which was earlier reported as burrow by Kulkarni and Borkar (1996b). Diverse trace fossils like things are reported by Sarkar et al. (1996) and Seilacher et al. (1998), and metazoan life by Rasmussen et al. (2002, 2004) have questatied on Precambrian life and metazoan evolution.

### 1.3. Scope of Works

The objective of the present thesis is to deal with the sedimentalogical and geochemical aspects of some of the units across the boundary between Lower and upper Vindhyan. The major focus of the thesis is the Rohtas Limestone, confined between the unconformity and Rampur Shale. The Lower Quartzite/ Sasaram sandstone, basal deposit of Lower Kaimur rest on the unconformity surface and not reported so far from this part of the studied area has been discussed. Though these two members has been studied in detailed but the author has also considered the Lower Bhander Sandstone member of the Upper Vindhyan Group to theorize the formation of glauconite apparently in a shallow water condition in epeiric sea. Detailed field works were carried out to understand sedimentation dynamics and sequence building pattern within the studied Rohtas Limestone, Lower Quartzite (Fig. 1. 5) and Lower Bhander Sandstone. Classification of different facies and their associations has carried out on the basis of lithology, primary sedimentary structures, body geometry and lateral and vertical continuity, their contacts with the surrounding bodies. Depositional mechanism, paleogeography and the sequence building pattern have emerged from all these primary studies. Pictorial representation of the paleocurrent data and their interpretation strengthen the paleogeographic contention. The study of facies and facies association of Lower Quartzite in lateral and vertical continuity revels similar stratigraphy throughout Vindhyan for upper Vindhyan. The sedimentation on unconformity infer reinitiating basin after a long hiatus. Dealing with the facies and soft sediment deformation structures afforms a good opportunity to identify the actual triggering agents which play a major role on the soft sediment deformation structures.

Potential preservation of glauconite in Lower Quartzite and Lower Bhander Sandstone not only documentation of abundance glauconite during Proterozoic, in opposition of less abundance glauconite in Precambrian time also deal with the genesis of glauconite. The origin of glauconite interprets about the sea water chemistry and paleo-redox condition in Proterozoic time. The sub-oxide condition in favor of glauconitization discuss how sea level fluctuation and basin subsidence, phenomena of epeiric sea play important role on glauconite formation.

Extensive geochemical analysis XRF, ICP-MS of chert layer on top of Rohtas Limestone deals with the chertification process. The present approach on chertification pointed out the importance of silica source, pH of fluid and temperature of fluid where earlier believe was sea water and meteoric water interaction can form chert. The newly developed triple oxygen isotope study to estimate the paleotemperature and ancient hydrosphere in studied chert suggest about paleotemperature as modern earth. Considering an extensive literature survey a likely model of chertification process and paleotemperature during the Mesoproterozoic time has been inferred in the present deliberation.

## 1.4. Materials and Methods

The fieldwork and geochemistry of the samples are the mainstay of this work. In course to facilitate this field work the essential equipments are geological hammer (East Wing, USA made, length 35 cm), chisel, magnet, hand lens, diagonal scale, permanent rock marker, knife, measuring tape, clinometers, brunton compass, abney level, camera, GPS (MAP76CSX with PC interface cable and accessories), rock cleaning brush, acid (for carbonate testing) etc. Numerous rock samples were collected and packed within zipped plastic satchel for petrographic study under microscope. From the collected rock samples, thin sections preparations were also implemented in the sedimentology laboratory, Department of Geological Sciences, Jadavpur University. Petrographic analysis including modal proportions and grain-size analysis were performed in computerized transmitted light petrographic microscope (Leica DM LP with 1.6X, 4X, 10X, 20X 50X & 100X magnifications specially attached Leica DC 320 image analyzer and point counting system with CVS PETROG software) placed in the Sedimentology Laboratory and facilitated the work enormously. Vertical litho-logs, different types of maps, models, rose-diagrams, figures and sketches and geochemical plots were erected. Computer software like Adobe Photoshop CS4, CorelDraw X5, Open rose, Microsoft Office 2007, PCPDFWIN and

Google Earth were used for these reconstructions and data processing. Systematically collected and processed samples of rock specimens along with glauconites and chert (silica) went through different types of geochemical analysis in different national and international academic institutions and international professional laboratories. Samples were analyzed at IISER Kolkata for XRF, IIT Bombay for major element oxide concentration (EPMA), IIT Kanpur for REE and trace element concentration and chert chemistry (triple oxygen isotope) study respectively. All the instruments specifications and analytical processes are described below:

### 1.8.1. X-Ray Fluorescence analysis

Samples were analyzed using the Wavelength Dispersive X-ray Fluorescence (WDXRF) S8 Tiger (4Kw) from Bruker-AXS, Germany at the Indian Institute of Science Education and Research Kolkata and 4 grams of fine grained (less than -200 mesh size) ground sample was measured and it was mixed with the help of mortar with binder Boric acid in 4:1 ratio. This mixture was mixed thoroughly and then was carried within aluminum cups to be pressed under 15-ton hydraulic pressure for 20seconds. Two standard reference materials, MESS-3 (Certified Reference Material, CRM) certified by National Research Council of Canada (NRC - CNRC) and USGS geochemical reference material SDC-1, were analyzed with each batch of unknown samples to determine accuracy of analyses.

### 1.8.2. Electron Probe Micro Analyzer (EPMA)

Major element concentrations of glauconite were estimated in thin sections using a Camera SX 5 Electron Probe Micro Analyzer at Department of Earth Sciences, Indian Institute of Technology Bombay, with following specifications: accelerating voltage 15 kV, specimen current of 40 nA and beam diameter of 1μm (peak: 10–20s and background counting: 5–10s) and analytical error less than 1%. Standards include both synthetic and mineral phases. Glauconite pellets were separated from the lightly crushed rocks using Zeiss Stemi 2000 stereo zoom microscope for geochemical and mineralogical analysis. About 0.1 gm of glauconite pellets was powdered and ultrasonicated for the preparation of smear mounts. These smear mounts were scanned from 1° to 70° (step size–0.026° 2θ), using the nickel filter copper radiation at a scan speed of 96 secs/step in an Empyrean X-Ray Diffractometer with Pixel 3D detector at Department of Earth Sciences, Indian Institute

of Technology Bombay. The $Fe^{+2}/Fe^{+3}$ ratio of glauconite pellets was measured by the titration process (cf. Kelly and Webb, 1999).

### 1.8.3. Inductively Coupled Plasma-Mass Spectroscopy (ICP-MS)

The trace element and REE concentration in each powdered samples were analyzed by ICP-MS at Department of Earth Sciences Indian Institute of Technology, Kanpur. Approximately 0.25 gm of powdered samples was digested in pre-cleaned Teflon beakers at 130 ± $5^0$C using a mixture of trace element grade HF (3 parts) and $HNO_3$ (1 part) for 48 hours. Each digested samples were dried and re-dissolved in concentrated 2 ml of aqua regia. Concentrated $HNO_3$ was used for complete digestion of the residual organic matter. Trace element concentrations were determined at ~200 ppm total dissolved solid solutions. Three procedural blanks, Reference Materials SBC-1 and SCO-1 (shale), SRM-2704 (river sediment), and SRM 2709a (soil) from US Geological Survey (USGS) and WGB-1 (Gabbro) rock standard from Canadian Certified Reference Material Project were also digested following the same procedures. Multi elemental standard solution diluted to 7 appropriate concentrations was used to construct the calibration curve, and trace element concentrations were determined based on the calibration curve. All the samples and standards were spiked by ~5 ppb Rhodium solution, and rhodium was used as an internal standard. The instrument (8900 Triple Quadrupole ICP-MS) was run both in standard and He Kinetic Energy Discrimination mode to optimize the separation of measured isotopes from interfering polyatomic interferences. The final concentrations were blank – corrected using the average procedural blank concentrations and matrix effect was corrected by in normalization. The measured trace element concentration of reference materials agrees well with the USGS certified values.

### 1.8.4. Oxygen isotope analysis by Laser Fluorination

The oxygen isotope composition of chert samples was measured by laser fluorination (Sharp, 1990) in combination with gas chromatography and gas source mass spectrometry. Details regarding the current system were described in (Pack et al., 2016). Samples were treated with 10% HCl in order to remove carbonates, which constitute a major contaminant in some of the samples. San Carlos olivine (Pack et al., 2016; Sharp et al., 2016; Wostbrock et al., 2020) and Gore Mountain garnet (UWG-2 (Valley et al., 1995))

were used as standards. The uncertainty (obtained from the 1 S.D. external reproducibility of the olivine and garnet standards) was 0.3 ‰ or better for $\delta^{18}O$ and 0.01‰ for $\Delta'^{17}O$.

### 1.8.5. Isotope notation

In this study, we summarize the triple oxygen isotope notations as follow. Isotopic abundance ratio is reported here in both standard and linear notations. The standard denotation is defined as (McKinney et al., 1950):

$$\delta^{X}O = \left( \frac{\left(\frac{O^{X}}{O^{16}}\right)_{sample}}{\left(\frac{O^{X}}{O^{16}}\right)_{standard}} - 1 \right) * 1000 \text{---------- equation 1.1}$$

Where $^{X}$ is the heavier isotope (18 or 17). We calculate chert oxygen isotopes ($\delta^{18}O$ and $\delta^{17}O$) relative to the VSMOW and SLAP, two important standards created by International Atomic Energy Agency, Vienna (IAEA) for reporting oxygen isotope ratios. The equilibrium fractional (α) relation between $^{17}O$ and $^{17}O$ by (Sharp et al., 2016):

$$\alpha^{\frac{O^{17}}{O^{16}}}_{silica-water} = (\alpha^{\frac{O^{18}}{O^{16}}}_{silica-water})^{\theta_{silica-water}} \text{----------equation 1.2}$$

$$\ln(\alpha^{17}_{silica-water}) = \theta_{silica-water} * \ln(\alpha^{18}_{silica-water}) \text{---------- equation 1.3}$$

where

$$\left[ \alpha^{\frac{O^{18}}{O^{16}}}_{silica-water} = \frac{(\frac{O^{18}}{O^{16}})_{silica}}{(\frac{O^{18}}{O^{16}})_{water}} \right]$$

The θ is the isotope effect of $^{18}O$ compared to $^{17}O$ for a specific reaction. θ≈0.5 for equilibrium and kinetic reactions (Craig, 1957), and at this value the $\delta^{17}O$ vs. $\delta^{18}O$ plot shows a nearly linear relationship (Clayton, 2003; Rumble et al., 2007). Recasting the $\delta^{17}O$ and $\delta^{18}O$ variation express by (Miller, 2002):

$$\delta'^{X}O = 1000 * \ln\left(\frac{\delta^{X}O}{1000} + 1\right) \text{---------- ----------equation 1.4}$$

where x is either 17 or 18 (as in $^{17}O$ or $^{18}O$). In linearized notation the equilibrium fractionation equation between two phases (silica and water) is:

$$1000\ln(\alpha^{X}_{silica-water}) = \delta'^{X}O_{silica} - \delta'^{X}O_{water}$$-------equation 1.5

We define θ for triple oxygen isotope calculation as (Sharp et al., 2016):

$$\theta_{silica-water} = \frac{\delta'^{17}O_{silica} - \delta'^{17}O_{water}}{\delta'^{18}O_{silica} - \delta'^{18}O_{water}}$$ ---------- equation 1.6

The Δ'17O is denoted as (Sharp et al., 2016):

$$\Delta'^{17}O = \delta'^{17}O - \lambda_{RL} * \delta'^{18}O + \gamma$$---------- equation 1.7

Where RL is the reference line, $\lambda_{RL}$ is expression of reference line slope and γ is the y-intercept. The we define small deviations from the reference line in form of $\Delta'^{17}O$, using the data $\lambda_{RL}$=0.528 and γ=0 (Sengupta et al., 2020; see details in Materials and Methods) to.

$$\Delta'^{17}O^{sample}_{\lambda=0.528} = 10^3 * \ln\left(\frac{\delta^{17}O^{sample}_{VSMOW}}{1000} + 1\right) - 0.528 \times 10^3 \times \ln\left(\frac{\delta^{18}O^{sample}_{VSMOW}}{1000} + 1\right)$$--equation 1.8

The fractionation $^{18}O/^{16}O$ between silica and water has summarized by equation 9 (Sharp et al., 2016):

$$1000 * \ln\alpha^{\frac{O^{18}}{O^{16}}}_{silica-water} = \frac{4.28\times10^6}{T^2} - \frac{3.5\times10^3}{T}$$ ---------- equation 1.9

Sharp et al. (2016) expressed the temperature dependence θ to:

$$\theta^{equilibrium}_{silica-water} = \frac{-(1.85\mp0.04)}{T} + 0.5305$$---------- equation 1.10

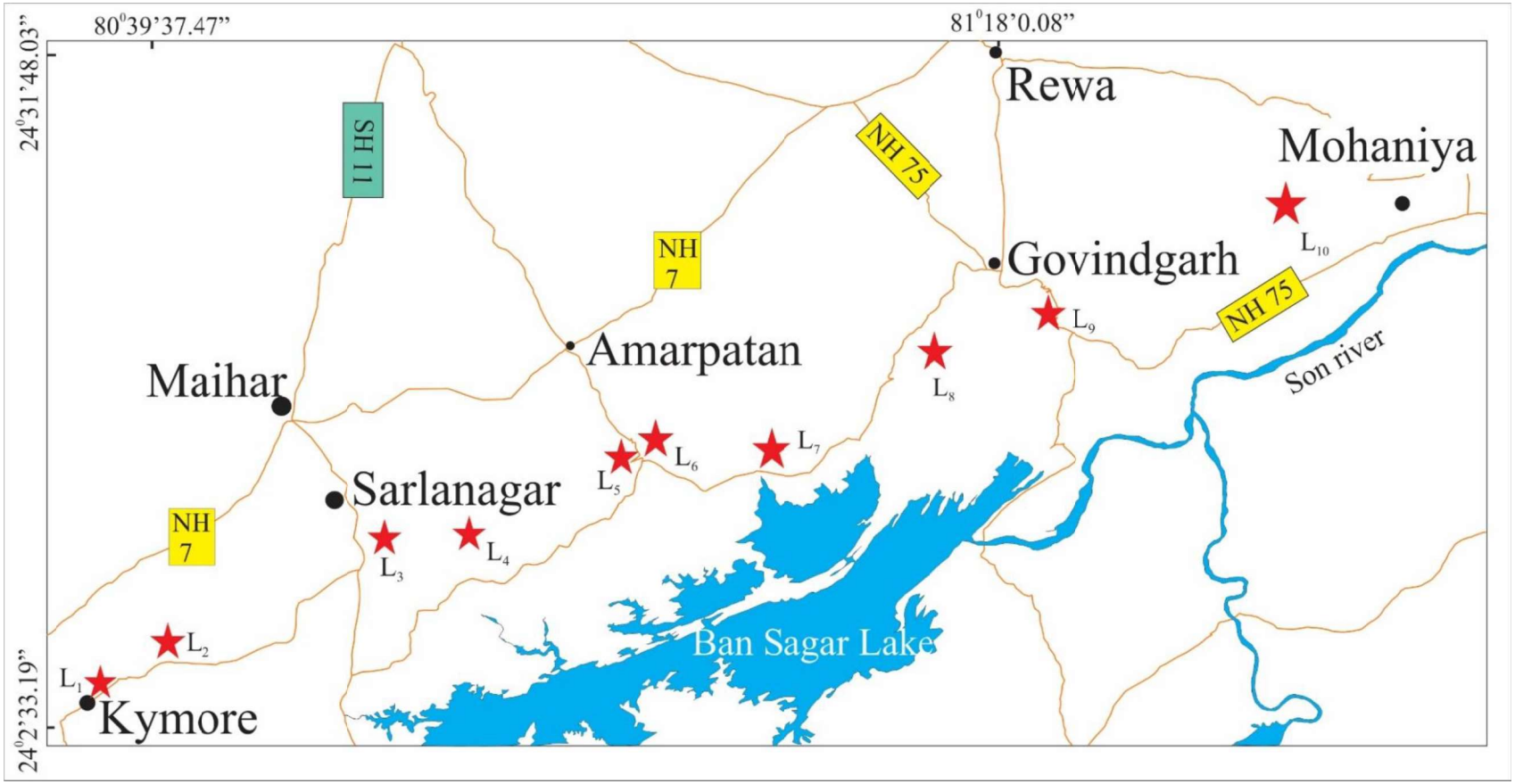


Fig. 1.5. Location map of study areas in Son valley Vindhyan, central India. Studied section has marked by the red stars. Note each location $L_1$ to $L_{10}$ are most suitable for study the Lower Quartzite/ Sasaram Sandstone (LQ). Although top part of Rohtas Limestone (RLM) is exposed all the study section, but for details study we have mainly concentrated on $L_3$, $L_7$, $L_8$, and $L_9$. Chertified layer is best exposed in $L_{10}$.

## 1.5. Organization

The organization of this dissertation follows the scope of works that have been outlined above. The present chapter has introduced the geological information of the Vindhyan Supergroup (i.e. tectonic setup, stratigraphy, age, paleogeography, paleoclimate, paleocurrent, and biotas), goal of this thesis with scope of works and materials and materials in more emphasis of the Rohtas Limestone, Lower Quartzite/ Sasaram Sandstone and the unconformity between Upper and Lower Vindhyan. The entire work of this dissertation has been discussed in three parts. In Part-I, I have discussed the detailed facies, facies association and depositional environment including the previous work done by earlier workers. In this part from Chapter-2 to Chapter-3, facies and facies associations have emphasized in the following order Rohtas Limestone, and Lower Quartzite/ Sasaram Sandstone. The special interests of the studied sedimentary units have detailed in the Part-II i.e. from chapter-4 to chapter-9. The summary and conclusion of this dissertation have been discussed in Part-III, chapter-10.

# PART-I

# Facies analysis and Depositional environment in parts of Rohtas limestone and Lower Quartzite

# CHAPTER 2

# Facies analysis and Depositional environment of Rohtas Limestone

## 2.1. Introduction

Rohtas Limestone Member, the top most stratigraphic unit of the Lower Vindhyan is entirely composed of carbonate rocks. This stratigraphic unit overlies on the Rampur Shale (basal member of Rohtas Formation) and underlies by an unconformity which demarcate the boundary between the upper and lower Vindhyan. The U/Pb dating from the Rohtas Limestone infer that the limestone was deposited during 1599±48 Ma (Rasmussen et al., 2002; Ray et al., 2002, 2003; Sarangi et al., 2004; also see Table 1.2). The contact between Rohtas Limestone and Rampur Shale is gradational (Bose et al., 2001; Banerjee et al., 2005, 2006; Banerjee and kumar, 2007; Sarkar and Banerjee, 2020). The uppermost 1m. of the Rohtas Limestone is chertified followed by the unconformity (Chakraborty and Bose, 1990; Bose et al., 2001; Chakraborty, 2007; Mandal et al., 2019, 2020; Sarkar and Banerjee, 2020). Although, a number of studies has been carried out on the Rohtas Limestone (Chakraborty et al., 1996; Bose et al., 2001; Banerjee et al., 2005, 2006; Banerjee and kumar, 2007; Sarkar et al., 2018; Sarkar and Banerjee, 2020) but state-of art facies analysis is still pending. Thus interpretation of depositional environment is a puzzle. Chakraborty et al. (1996) interpreted the depositional of Rohtas limestone as deep marine origin but shelf to inner shelf depositional environment has also been proposed (Bose et al., 2001; Banerjee et al., 2005, 2006; Banerjee and Kumar, 2007). The oxygen and carbon isotopic study from the Rohtas Limestone also support the shallow marine origin (Banerjee et al., 2005). Keeping these views in mind a 57 km. stretch of Rohtas Limestone extending from Bhadanpur to Bhagwar, M.P. has been chosen for the present study (Fig. 1.5 in the locality of $L_3$, $L_7$, $L_8$ and $L_9$). Both temporal and spatial variations have been considered to get a better view regarding the depositional environment and related issues.

## 2.2. Facies and Facies association

The Rohtas Limestone is well exposed in the studied stretch between Bhadanpur and Bhagwar (ca 57 km). Detailed state -of -art facies analysis considering the spatial and temporal variations revel two dominating facies association in the studied stretch of Rohtas limestone. Each of the facies association also consists of numbers of facies (Fig. 2.1). Description and interpretation of each facies within facies association is as follows.

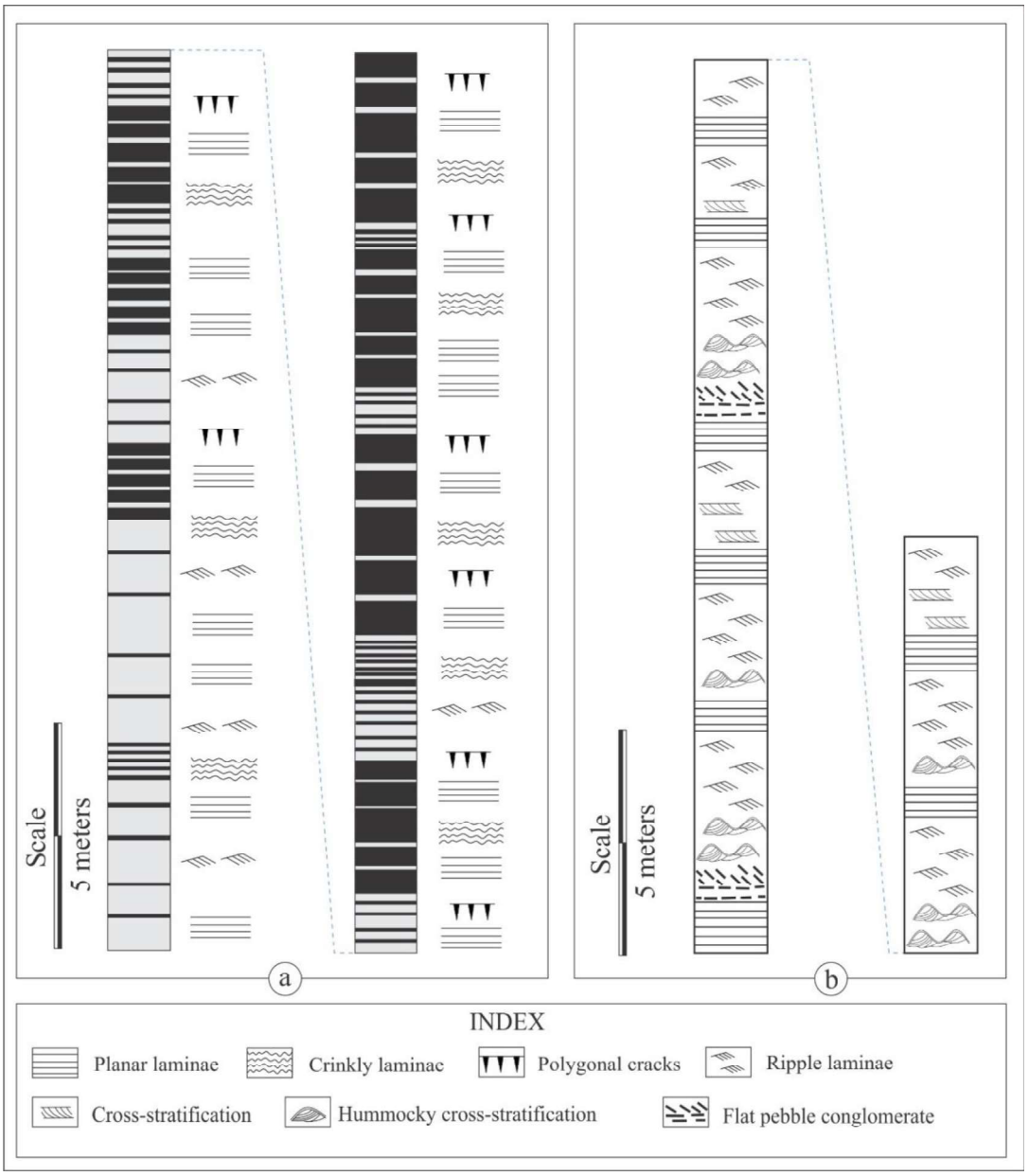


Fig. 2.1. Lithological log of Rohtas limestone. Note the characteristic primary sedimentary structures associated with facies association I (a) and II (b).

### 2.2.1. Facies association I (Restricted shelf):

This facies association is constricted in the basal part (ca. lower 40m) of Rohtas Limestone. Although, limestone starts to deposit with alternation of grey/black shale of the underlying Rampur shale, we have not consider the black shale in the present study. This facies association is constituting of the facies namely rhythmic alternation of dark and light planar laminations, crinkly lamination, ripple laminations and edgewise conglomerate (Fig. 2.1a). Description and interpretation of each facies as follows.

### 2.2.1.1. Alternating dark and light color planar laminated facies ($FI_1$)

Rhythmic alternation of mm scale planar laminated dark and light layer is the major characteristics of this facies with numerous pockets of breccia (Fig. 2.2a). This facies is entirely composed of micrite. The thickness of the layers is generally uniform though closer scrutiny reveals that there are minute variations. Some small scale scour marks are observed occasionally at the base of light layers (Fig. 2.2b). Usually, planar lamination dominates but occasionally small scale ripples are also observed within these light layers. Sharp bases of the lighter strata often selectively bear minor irregularities in the form of load features (Fig. 2.2c). Internally, the lighter layers commonly bear sub-millimeter thick planar and wavy laminae, but small-scale cross-laminae are also present locally. The dark layers, in contrast, appear massive or crinkly laminated, both in field and under microscope. Under the microscope, the dark layers appear micritic, while the lighter layers are made up of microsparite. The contacts between dark and light layers are sharp but under microscope it reveals that the upper contact of the lighter layer gradationally passes into the dark layers. The domes like structures are common appearance at the top of the dark layers (Fig. 2.2d, e). Some cracks are also associated with this facies (Fig. 2.2f, g). The cracks are varying in length between 15 to 25 cm having their maximum depth ca. 2cm. They never cross cut each other. Within the dark layers, abundant of cubic isotropic minerals have observed (Fig. 2.2h). The EDS data confirms the isotropic minerals are pyrites. Different types of Microbial mat related structures (MRS or MISS) viz., wrinkle structure, elephant skin structure, pustules, domes and Astropolithon, are associated with these dark layers (2.3a. b, c, d). The Raman Spectroscopic data show high kerogen content within these dark layers (see Sarkar et al., 2018).

**Interpretation:**

The rhythmic alternation of dark and light laminations infers very calm and quite environment (Sarkar et al., 2014; 2018). The preservation of wavy crinkly laminations suggests the microbial mat growth during this deposition, within photic zone and very low sedimentation rate. The cubic pyrite grains in association of this also supports calm and quite deposition and, suggest an anoxic condition generation in this environment. The sharp and erosional scale scour at the boundary of lighter layer suggest higher energy flow compare to darker one. The mound like structures on the bedding plane has compared to gas dome structures (Bouougari et al., 2007; Bottjer and Hagadorn, 2007). These bulbous

structures are compared to gas escape as microbial mat growth in dark layers generate this gas due to degradation of microbial mat structures (Bouougari et al., 2007; Bottjer and Hagadorn, 2007). The desiccation cracks on bedding surface infer exposure of the depositional site. The non-cyclic alternation of dark and light layer discard tidal influence during deposition.

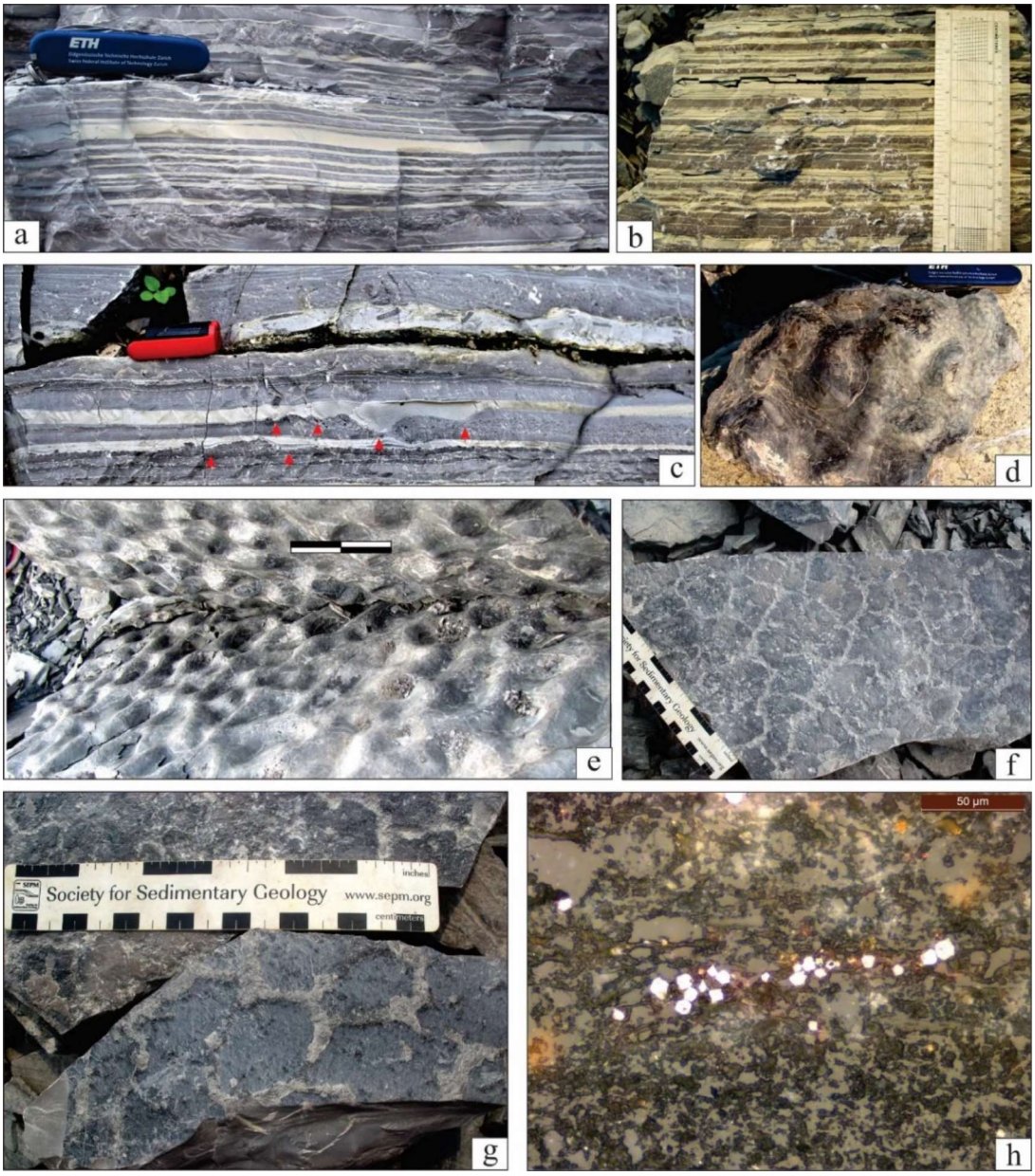


Fig. 2.2. Rhythmic alternation of dark and light planar laminated facies (a, b; length of knife 8 cm and scale length 15 cm; note the sharp boundary of light layer on top of dark layer), gas dome structure on bedding surface of alternative dark and light layer (d, e; knife length 8 cm, bar length 10 cm), light layers consisting of load structures on dark layer (c, length of marker cap 5 cm), desiccation cracks on bedding surface (f, g; scale length 15 cm), cubic pyrite grains under microscope (h).

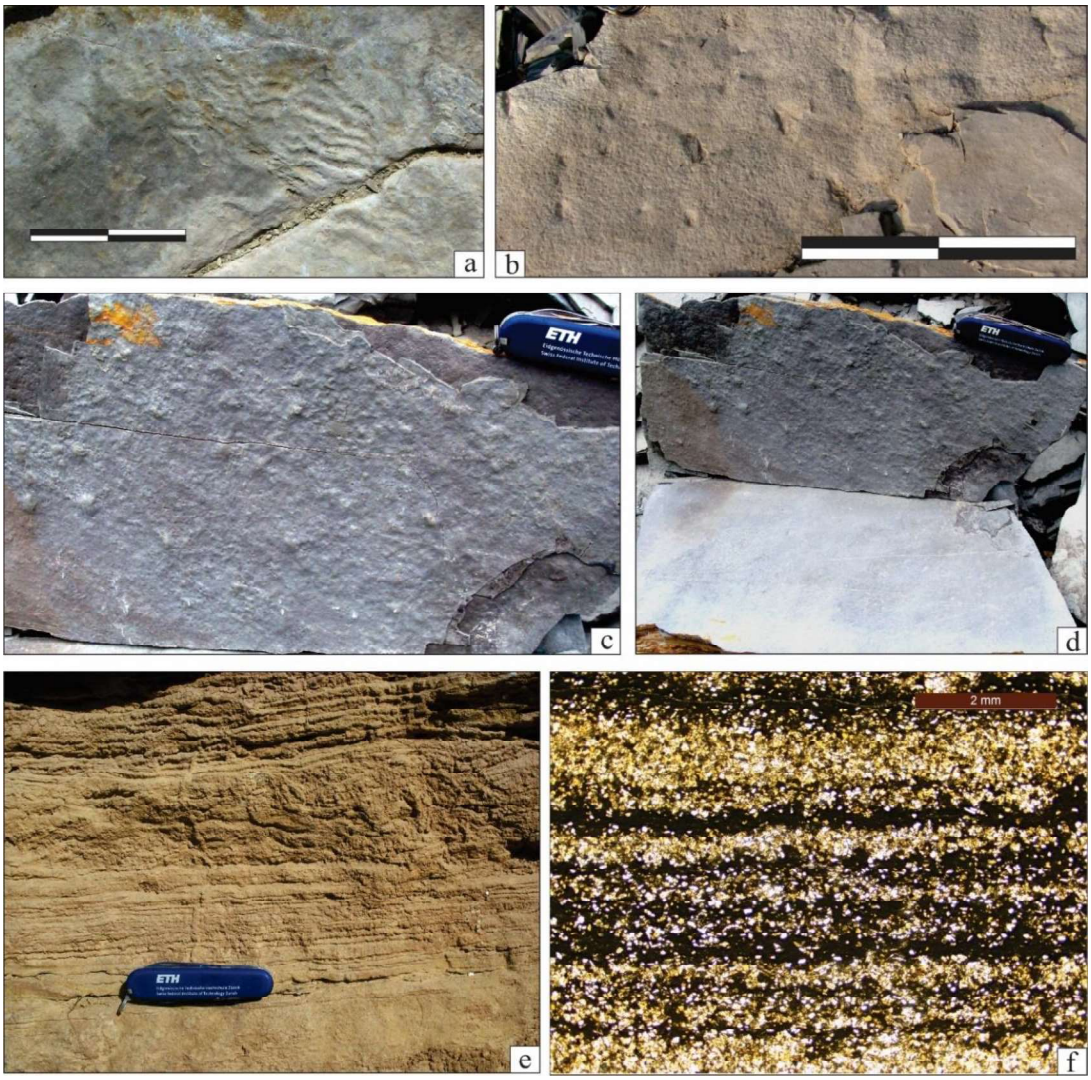


Fig. 2.3. Crinkly lamination on the bedding surface of alternative dark and light layer (a, b; bar length 15 cm), pustules on bedding surface and prized open surface as well (c, d; length of knife 8 cm), crinkly lamination (e, knife length 8 cm), divergence and convergence pattern in crinkly lamination (f).

### 2.2.1.2. Crinkly laminated facies ($FI_2$)

The crinkly lamination facies are grey to buff in coloured and tabular in geometry. The Crinkly laminated fine-grained with occasional clusters of up-building are the next dominating facies present in this association (Fig. 2.3e). Maximum thickness of the facies is 20 cm. This facies is characterized by mm thick crinkle laminations. Laminations are dark in color composed of fine-grained carbonate mud. Both divergent and convergent pattern of thin dark laminae is observed under microscope (Fig. 2.3f). Pyrite grains are frequently observed in these facies as well. In a lateral continuity these facies has changed into the intraclastic breccia facies (discussed later).

**Interpretation:**

The crinkly lamination infers the intact microbial mat layers (Banerjee et al., 2007). Microbial mat growth suggests the depth of deposition within photic zone. Very fine grain deposition indicates suspension deposition in absence of any strong current. The presence of pyrite grains suggests anoxic deposition and support lack of agitation.

### 2.2.1.3. Flake Conglomerate facies ($FI_3$)

These intraclastic conglomerate beds have appeared in lenticular fashion, shows flake like carbonate intraclasts (Fig. 2.4; Tucker, 1982; Sepkoski, 1982). The constituent clasts are internally planar laminated, tabular in shape and generally have beveled edges. The average maximum clast length is about 17 cm. The thinner beds are broadly lenticular, whereas beds thicker than about 20 cm show strong lenticular geometry with flat bases and irregular convex upward tops. Steeply inclined clasts, often stacked up in clusters, laterally give way to gently inclined clast assemblages (Fig. 2.4a; Banerjee et al., 2005). They are either clast or matrix-supported (Fig. 2.4). This facies is associated with alternating dark and light planar lamination and crinkly laminated facies. In a lateral transition this facies transit to their associated facies. The intraclasts are vertical to sub-vertical in orientation (Fig. 2.5a, b, c, d, e, f; Sarkar et al., 2018).


Fig. 2.4. Flake conglomerate beds with wedge shaped geometry (a, bar length 15 cm; b, bar length 35 cm; c, scale length 15 cm). Note the transition of conglomerate to alternative dark and light layer. Also note vertical to bed parallel orientation of platy clasts.

**Interpretation:**

Highly angularity of the clasts and similar composition of clasts and matrix infer they have not transported much. The miss-match boundaries of clasts support very less transportation or its origin position. The association of $FI_1$ and FI, lateral transition to $FI_1$ and $FI_2$ and similar type of clasts as $FI_1$ infer that these beds have formed from either $FI_1$ or $FI_2$. However, this sorts of clasts arrangement suggests fluid expulsion by storm pounding/wave pounding, seismic jerks, slope failure and sea level fluctuations (Mount and Kidder, 1993; Myrow et al., 2004; Chen et al., 2009, 2011; Van Loon et al., 2013). The chaotic nature and vertical to sub-vertical orientation of the intraclasts suggest the collision between intraclasts shearing, rotational movement (Mount and Kidder, 1993), but the association of this facies deny to accept this processes. The formation of these beds may generate because of the gas expulsion process (Sarkar et al., 2018) as the $FI_1$ and $FI_2$ facies contain huge amount of microbial mat and due to degradation of the microbial (Bouougari et al., 2007; Bottjer and Hagadorn, 2007). The orientation of vertical to sub-vertical can also explained by gas expulsion path.

**2.2.1.4. Ripple laminated facies ($FI_4$)**

This facies is characterized by asymmetric ripple laminations with preserved ripple forms on bed surface (Fig. 2.5g, h). They are straight crested, broadly sinuous and locally bifurcated. Few flat crested ripple has also identified. The thickness of the ripple laminations varies. It is composed of calc-arenite. The average wavelength and amplitude of ripple is ca. 3 cm and 5 mm. The basal part of the ripples is very irregular and some small scours have also observed. Lateral discontinuity of these ripples have identified as starved ripple (Fig. 2.5h).

**Interpretation:**

The different sets of ripple, bifurcating ripple crests and bimodal cross-stratification infer wave influence in the depositional site. Flat crested ripples indicate strong shear action within the flow and very shallow water deposition. This facies likely to be deposited in a shallow water condition under the wave influence. Starved nature of ripples suggest limited sediment supply.

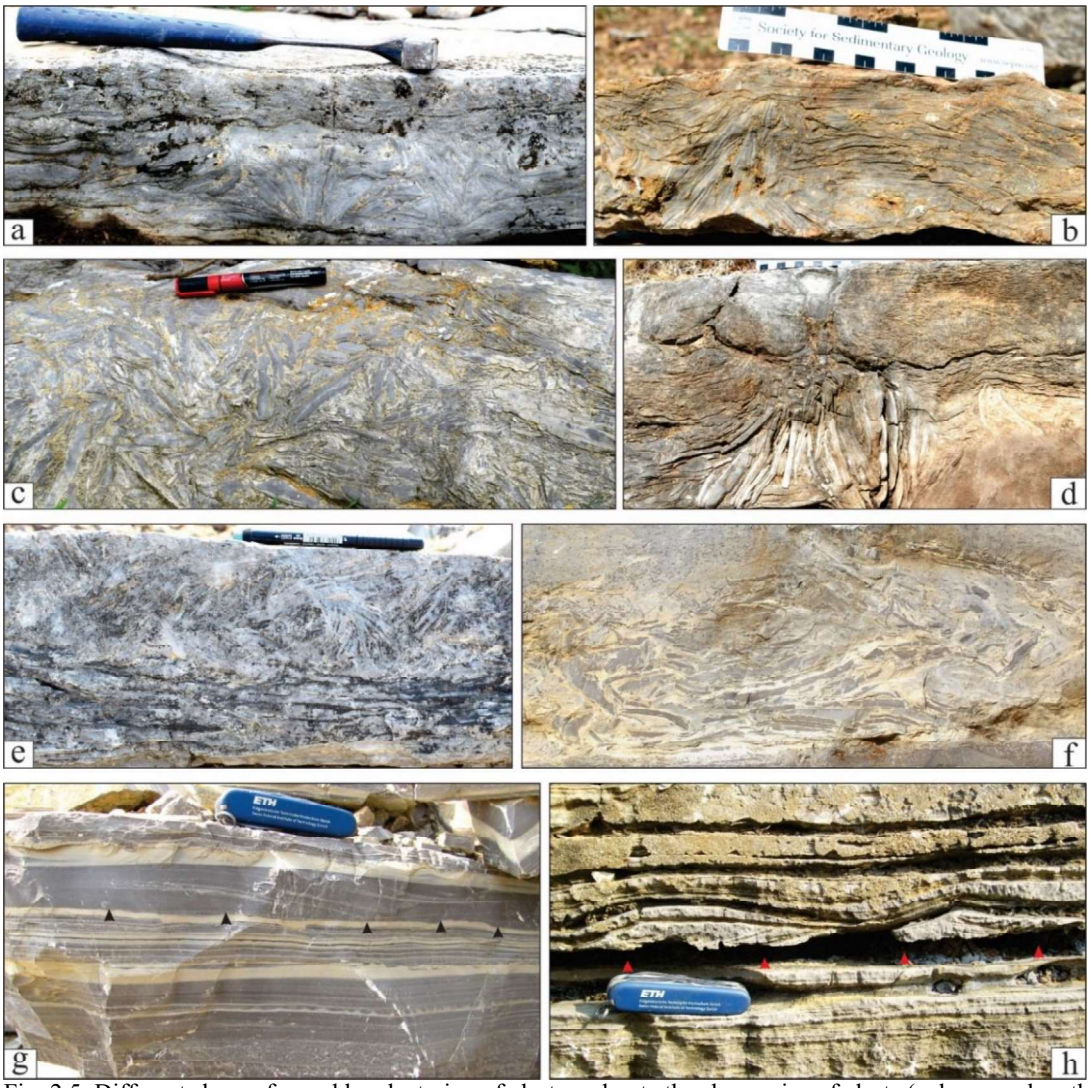


Fig. 2.5. Different shapes formed by clustering of clasts and note the shape, size of clasts (a, hammer length 35 cm; b, scale length 15 cm; c, marker length 15 cm; d, scale length 15 cm; e, marker length 15 cm; f, bar length 15 cm), symmetric wave ripple (g, h, scale length 8 cm).

### 2.2.2. Facies association II (Open shelf):

The facies association II lying above the Facies association I is entirely different with respect to sediment characteristics and primary structures. However, in between Facies association I and II there is a laterally continuous soft sediment deformation layer (discussed later). The facies association is consist of the following facies:

#### 2.2.2.1. Hummocky cross-stratification facies ($FII_1$):

This facies is entirely composed of calc-arenite with hummocky cross-stratifications (Fig. 2.6). The amplitude and wavelengths of the hummocks are, on average, 8.5 cm and 21 cm respectively. The bases of the calc-arenites are invariably sharp while

their tops are less sharp or even gradational (Fig. 2.6a). These beds have concave/ flat base and convex-upward top with erosional structures at the base (Fig. 2.6a, e). Sole of the beds are characterized by small scale gutters, flute casts, prod marks (Fig. 2.7a). Occasionally some clastic beds are present at the basal part of the facies (Fig. 2.6a, 2.7b). The average thickness of this facies is ca. 50 cm. Hummocky cross stratifications are overlying/underlying planar laminae and ripples at the top part also observed (Fig. 2.6b, d).

**Interpretation:**

Preservation of hummocky cross-stratifications indicates deposition under the influence of oscillatory flow possibly during storm surges (Walker and Plint, 1992; Harms et al., 1975). The basal scour, flute casts at base have formed when storm build up approach the peak stage. Gradual transition from hummocky cross-stratification facies to ripple lamination or planar lamination facies suggests waning of storm surges.


Fig. 2.6. Field photographs of hummocky cross-stratified facies. Symmetric nature of hummocks and its appearance on flat pebble conglomerate (a, hammer length 35 cm), appearance of hummock facies with sharp and erosional base on planar laminated facies (b, hammer length 35 cm), cross-cutting of hummocky by another (c, knife length 8 cm), asymmetric hummocky (d, hammer length 35 cm), amalgamated nature of hummocks (e, hammer length 35 cm).

### 2.2.2.2. Flat pebble conglomerate facies ($FII_2$):

This facies forms isolated bodies restricted within some stratigraphic interval (Fig. 2.1). They are persistent compare to the flake conglomerate facies associated with facies association I. The constituent clasts are internally planar laminated, tabular in shape and generally have beveled edges (Fig. 2.7c, d, e, f). The clasts generally lie bed-parallel, with few occasional imbrication (Fig. 2.7c, d). The beds generally have their bases planar and sharp locally loaded and in some other cases erosional, concave upward. The conglomerates are both clast and matrix-supported (Fig. 2.7c, d, e, f). Occasional normal grading is noticed in some beds. The most striking aspect of the thick beds is edgewise clast fabric in chaotic as well as fan shaped arrangement in some conglomerates (Fig. 2.7f). This facies is graded to massive calc-arenite facies or hummocky cross-stratified facies (Fig. 2.6a, 2.7a).

**Interpretation:**

Compositional similarity between clasts and matrix infer that this conglomerate beds formed by intrabasinal sediments. Sharp, erosional base of this bed suggest high energy flow. Bed parallel orientation of high matrix strength within flow, whereas imbrication of clasts corroborates strong flow. Matrix supported to clastic supported conglomerates are the indication the flow transition. This facies grading to hummocky cross-stratification and/ or massive beds infer storm pounding on earlier deposit and pick up the clasts from se floor.

### 2.2.2.3. Massive calc-arenite facies ($FII_3$):

Absence of any primary sedimentary structures, coarse grain has differentiated these facies from the other facies present in this association (Fig. 2.7c, d, e, f). Basal part of this facies is very irregular and sharp compare to its upper part. Gutters, bipolar prod marks and flutes are present at the sole of this facies (Fig. 2.7g, 2.8a). The massive beds often grade upward into planar laminated beds followed by cross-stratifications. Occasionally this facies grades into either hummocky cross-stratification or ripple laminated facies. Conglomerate beds are common at the base of the massive beds as well as along the cross stratifications The average thickness of the facies is ca 22cm.

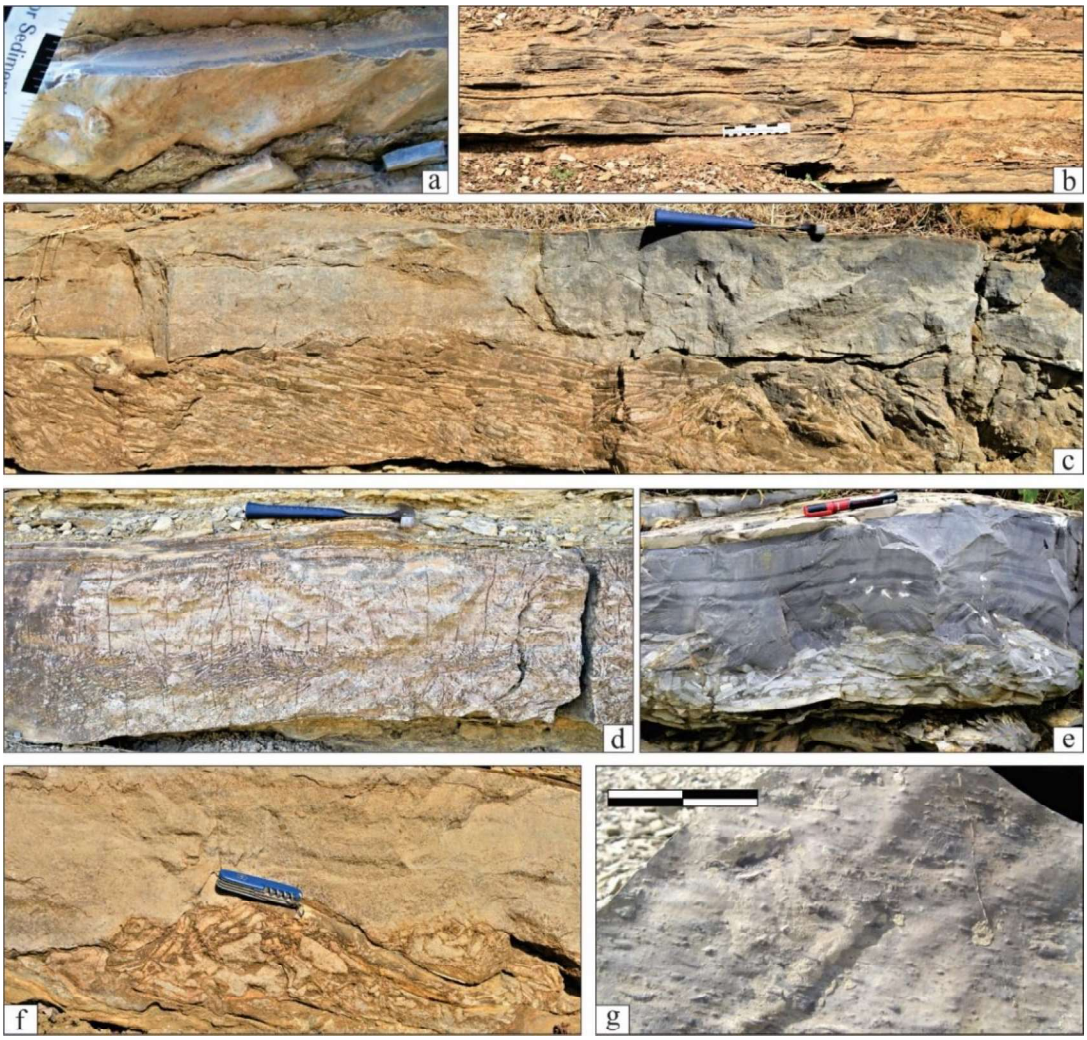


Fig. 2.7. Conglomerate bed at base of hummocky beds and transition to ripple (a, scale length 15 cm), flute and tool marks at the sole of these beds (b, scale length 5 cm), flat pebble conglomerate at base and massive beds on top with sharp and erosional base (c, d, hammer length 35 cm; e, hammer length 15 cm), protrusion of clasts on massive bed (f, knife length 8 cm), numerous tool marks at the sole of massive bed (g, bar length 10 cm).

**Interpretation:**

Preservation of massive beds infer very rapid rate of sedimentation. Amalgamation of these beds suggests the high-density flow The sharp erosional base and sole marks indicates higher energy flow. All of these characteristics and the associated bed infer episodic storm surge deposition.

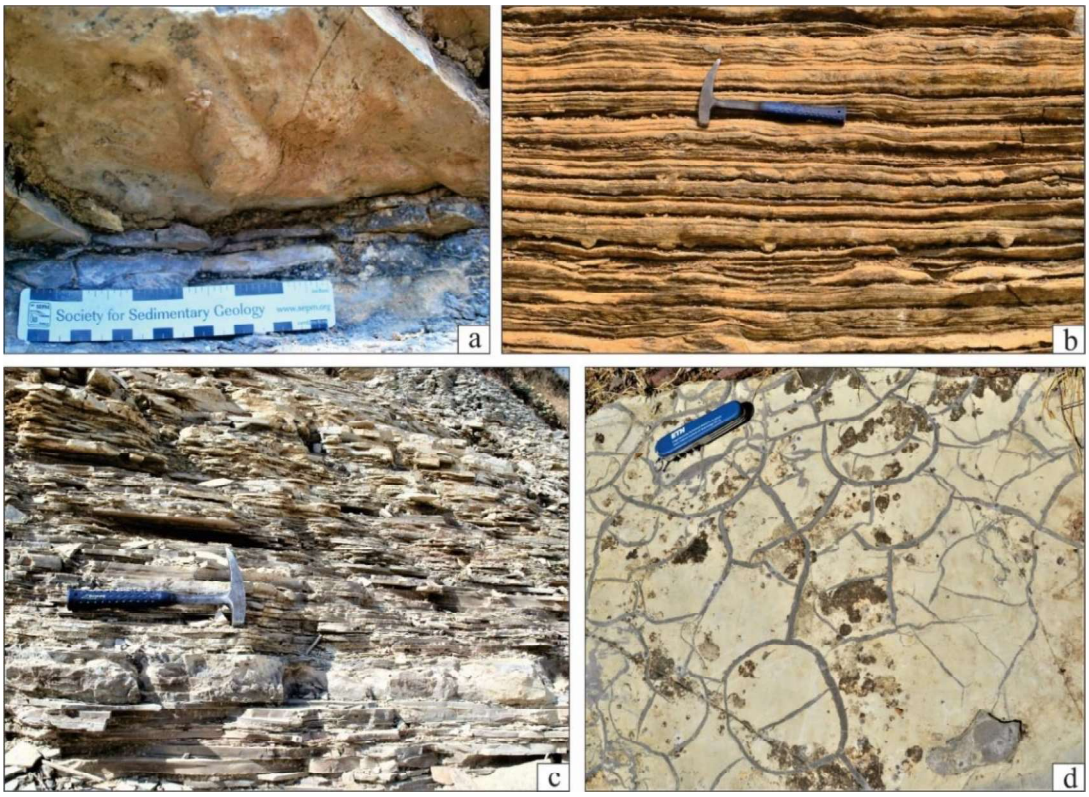


Fig. 2.8. Flute casts at the sole of massive bed (a, scale length 15 cm), small scale cross-stratification (b, hammer length 35 cm), planar laminated facies (c, hammer length 35 cm), desiccation cracks on the bedding surface of planar laminated beds (d, knife length 8 cm).

### 2.2.2.4. Ripple lamination facies ($FII_4$):

This facies is composed calc-siliciclastic to micritic grain and cm scale cross-stratification with preserved ripple form on the bed surfaces (Fig. 2.8b). The average height and spacing of these ripples are 4cm and 12cm respectively. The ripples have their crests straight or broadly sinuous and locally bifurcated. Basal part of ripples has preserved some small erosional evidence. This facies is present at top part of hummocky cross-stratification and massive calc-arenite facies.

**Interpretation:**

Bimodal distribution of cross-lamination and crest bifurcation infer that the deposition took place in a wave dominated environment. Its appearance on top of hummocky cross stratification or massive calc-arenite facies indicates winging of flow.

### 2.2.2.5. Planar laminated facies ($FII_5$)

The facies is characterized by calc-arenite lithology and dominated by plane laminations (Fig. 2.8b). The maximum thickness of the facies is ca. 1 m. This facies grades from massive facies or hummocky cross-stratified or ripple laminated facies (Fig. 2.8c). Bedding surface of this facies consists of numerous dissication cracks (Fig. 2.8d).

**Interpretation:**

This facies infer low energy suspension deposition. Dissication cracks on bedding surfaces indicates frequent subaerial expose. Depositional of this facies on high energy storm suggest that this planar lamination facies may have deposited as waning flow of flow.

### 2.3. Depositional environment and Paleogeography

Abundance of micrite deposition in this facies association infers that depositional site was dominated by suspension load deposition in a tranquil environment. However, minor scour at the basal part and small-scale ripple preservation within the light color planar laminated limestone facies signify presence of traction current domination during the deposition of the facies. The presence of flake conglomerate with edgewise arrangement of the clasts suggests erosive storm-driven combined flow is the most likely agent to produce the edgewise conglomerate beds in the marine Rohtas Limestone (Mount and Kidder, 1993, Banerjee et al., 2005). The straight crested and bifurcated ripple laminations present at the bed tops infer presence of wave within the depositional system. But the lateral discontinuities of ripples infer the low rate of sediment supply in the depositional site. The abundance of pyrite grains within the alternating dark and light planar laminated and crinkly laminated facies infers that depositional site prevailed anoxic condition. The crinkly laminations and kerogen content in dark laminas supports the microbial mat domination in the depositional site (Sarkar et al., 2018). The cyclic deposition of organic rich dark laminae in an alternation with light laminae infers cyclic change of depositional process. The desiccation cracks on the bedding surface of alternate dark and light planar laminated facies interpret subsequent exposer of depositional site. All the facies present in this association indicate that they were plausibly deposited in a restricted shelf which exposed intermittently and wave, however, feeble it is occasionally reworked the sediment within this restricted shelf. Beside the depositional sites also interfered by storm currents occasionally.

Most of the facies distributed in this Facies association indicate that the they are likely to be deposited in an open marine wave agitated condition. Abundant distribution of calc-arenite with cross stratification, and intraclastic beds convey deposition took place both by traction and suspension load. The calc-arenitic carbonate deposits encased within calc-micrite and calcisiltite seems to have been laid down by episodic storm originated wave-cum-current combined flow (Dott and Bourgeois, 1982, Sarkar et al., 1996, Banerjee et al., 2006), although determination of grain types is difficult at times due to pervasive recrystallization. Bedding is characterized by planar lamination, hummocky cross-stratification, wavy-bedding, and ripple and cross-bedding. Hummocks have wavelengths of up to meter scale indicate deposition open marine setting, within storm wave base (Dibenedetto and Grotzinger, 2005; Banerjee et al., 2005; Sarkar et al., 1996). The presence of hummocky cross-stratification with erosional base and abundant sole structures indicates substantial storm activity within the depositional basin. The flat pebble conglomerate facies with erosional base below these facies also supports the conclusion. The presence of massive beds in association of these two facies indicate high rate of sedimentation during the high energy events. The plane laminated facies appear to be product of sheet flow under high energy depositional regime. The ripple laminated facies present on top of hummocky cross-stratification or massive beds respectively signify deposition from the wanning stages of the storm events. The facies are composed of calc-arenite and micrite also support that they are the product during waning stage of the storm flows. The edgewise conglomerates have a striking similarity with those reported from high energy environment (Dionne, 1971). The clast-supported, platy, intra-clast grainstones and pack-stones occur as sheet-like beds or as isolated lenses with flat bases and mounded tops, showing polygonal packing of clasts. These features indicate deposition under oscillatory flow conditions preserving the deceleration and changing of direction of the wave orbit (Mount and Kidder, 1993). Considering all the facies distributed within this association it can be inferred that the Facies association II likely to be deposited in a storm dominated open shelf.

# CHAPTER 3

# Facies analysis and Depositional environment of Lower Quartzite

## 3.1. Introduction

The Lower Quartzite (also named as Sasaram Sandstone in the part) is the basal member of Kaimur Formation. It is bounded above and below by Bhagwar shale and the unconformity respectively. The unconformity also demarcates the boundary between upper and lower Vindhyan (Chakraborty and Bose, 1990; Bose et al., 2001, Mandal et al., 2019). This sediment succession of the Lower Quartzite is composed of sandstone deposit with - some silt layers in between. However, thickness of the sandstone deposit varies from place to place but on an average the thickness of sandstone deposit is 12 m (Fig. 3.1). The boundary between the Rohtas Limestone and the overlying Sandstone is sharp, erosional and demarcated by a thin (~10 cm) sheet-like granular lag containing pebbles of chertified limestone (av. clast size 5cm) at several places in the study area (Fig. 3.2a).

## 3.2. Facies and Facies association

This sheet-like pebble bearing unit is followed upward by a laterally persistent sandstone unit (max thickness 12 meter) along ~ 150 Km East–West stretch of the study area (Fig. 1.5). The overall grain size of this sandstone varies from coarse to fine sand. Considering the primary sedimentary structures, sediment composition and bed geometry the sandstone can be subdivided into two facies associations - (a) Facies Association I and (b) Facies Association II (Fig. 3.1). The constituting facies of association I is in general of fine to medium grained sandstone and also rich in mud compared to that of Facies Association II. Following are the detailed description and interpretations for each Facies Association of the sandstone.

### 3.2.1 Facies Association I

Facies Association I is distinctly different from the facies association II with respect to grain size (varying from medium to fine sand) and mud content. This Facies Association I is dominantly cross-stratified and consists of following four facies.

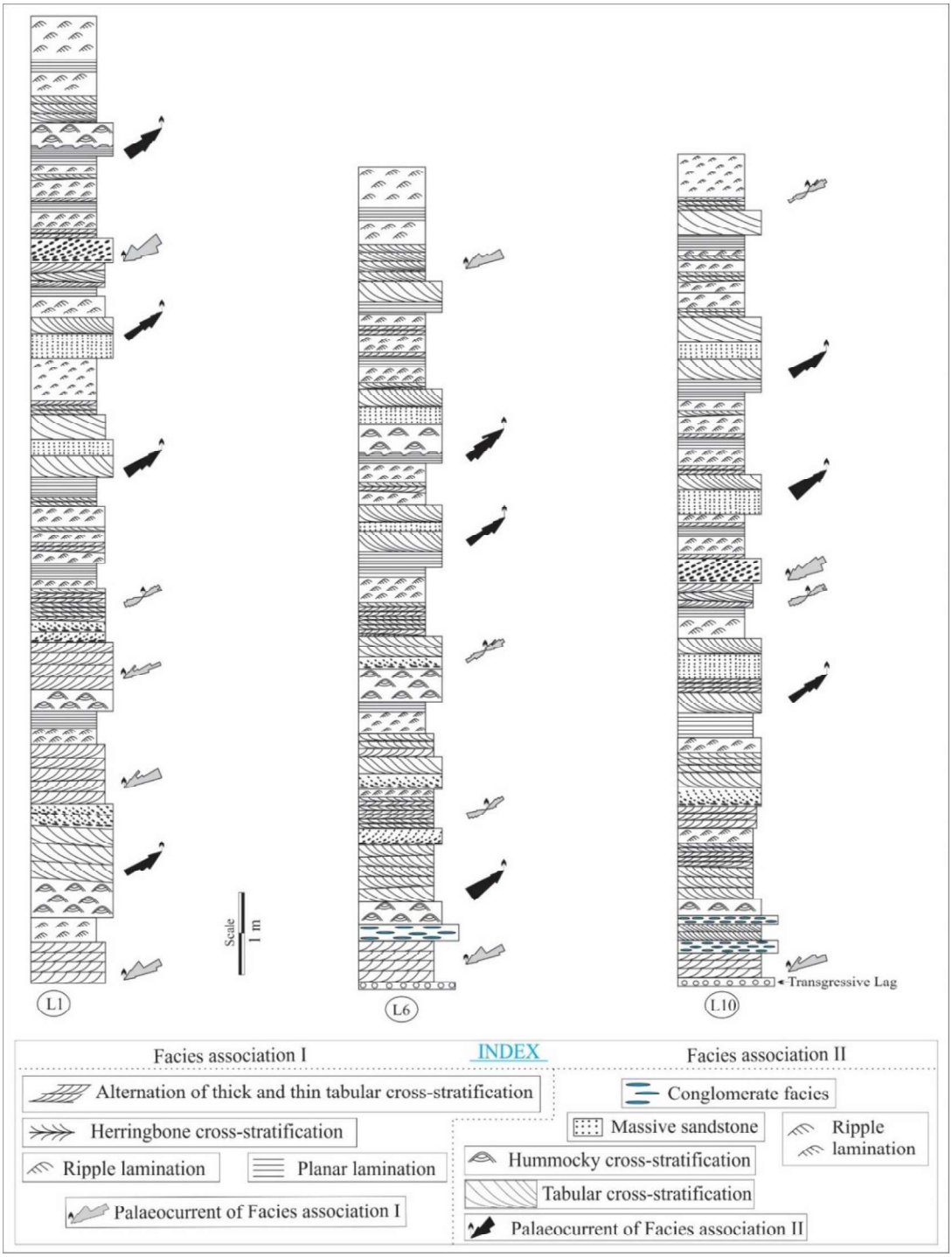


Fig. 3.1. Distribution of facies association along with paleocurrent direction for two facies association in three best exposed localities.

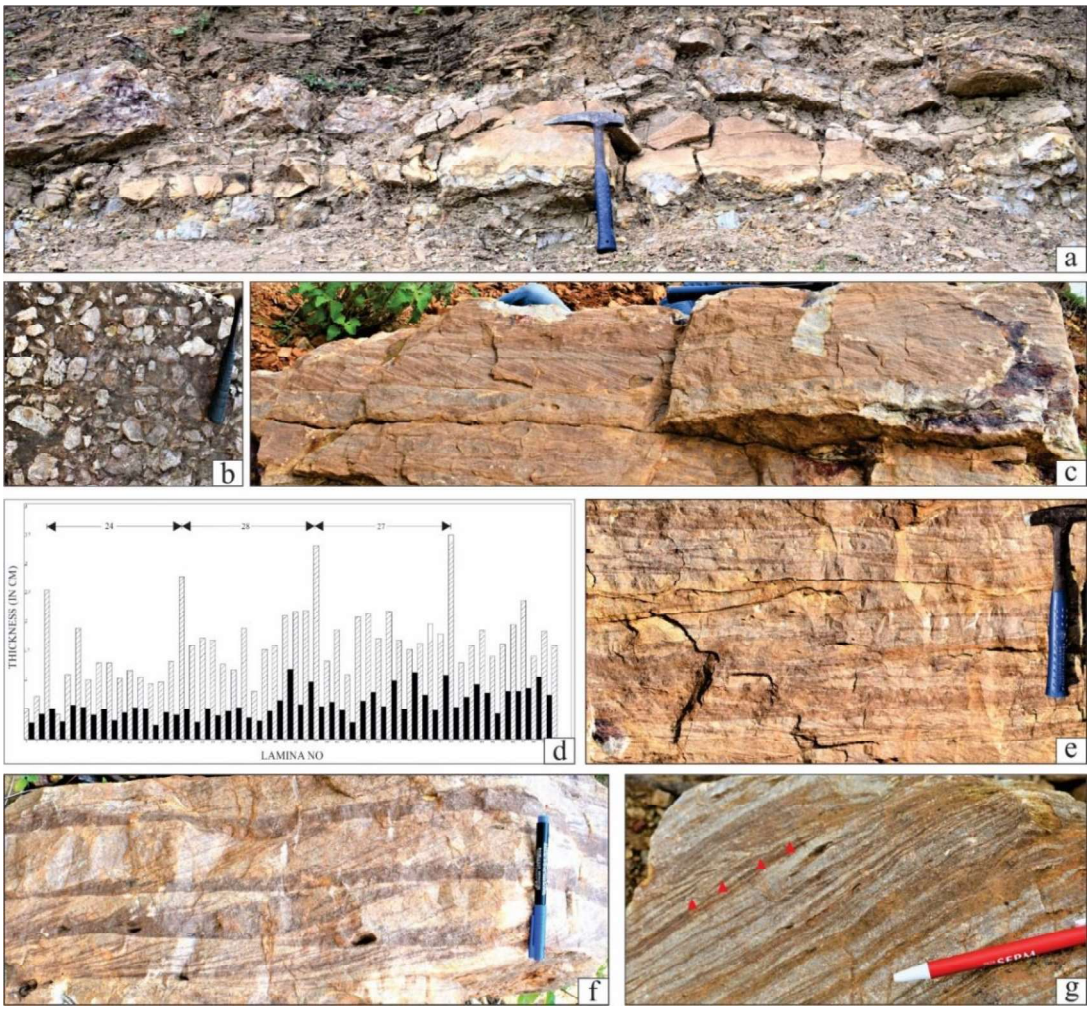


Fig. 3.2. Transgressive lag at the basal part of Lower Quartzite (a, hammer length 35 cm), transgressive surface defining by chert clasts (b, hammer length 35 cm), amalgamated alternative thick-thin cross-stratified sandstone facies (c, hammer length 35 cm), cycle in alternative thick-thin laminas (d), mud drape defining the surfaces alternative thick-thin cross stratification facies (e, f, hammer length 35 cm, marker length 15 cm), opposite direction of small scale cross-stratification with respect to large cross-stratification (marked by red arrows, g, pen length 15 cm).

### 3.2.1.1. Alternation of thick and thin tabular cross-stratified sandstone facies ($FI_1$)

This facies comprises medium to fine-grained sandstone exhibiting unidirectional cross-stratification. It is present at the basal part of the sandstone and lies exactly on top of the basal thin and sheet-like pebble bearing unit (Fig. 3.2a, b). The average thickness of the facies is 15 cm. Internally the cross-stratifications are characterized by an alternation of thick and thin planar tabular cross-strata (Fig. 3.2c), the foresets bundles are separated by mudstone partings (Fig. 3.2c). The thickness of the individual foresets varies between 0.5cm and 3.2 cm, whereas the mudstone laminae are sub-millimeter in thickness. The thickness measurement of cross-set bundles reveals a nearly symmetrical pattern of cyclicity (Fig. 3.2d, e). A maximum of 28 laminae occurs between two successive peaks of

the thick laminae (Fig. 3.2d). Usually, foresets dip decreases from the highest peak to the trough of the sinuous curve. The dips of cross-sets decrease down current from ca. 30º to ca. 15º and laterally pass over into compound cross-stratification at times (Fig. 3.2f, g; Rouse, 1961; Bose et al., 1997). Some of the foresets are defined by mud clasts. At places thick mud drapes (up to 2 cm) occur within cross-lamina set (Fig. 3.2f). Small-scale cross-lamina (ca 3 cm thick) dipping oppositely is occasionally present within the larger foresets of the cross-bedding (Fig. 3.2g).

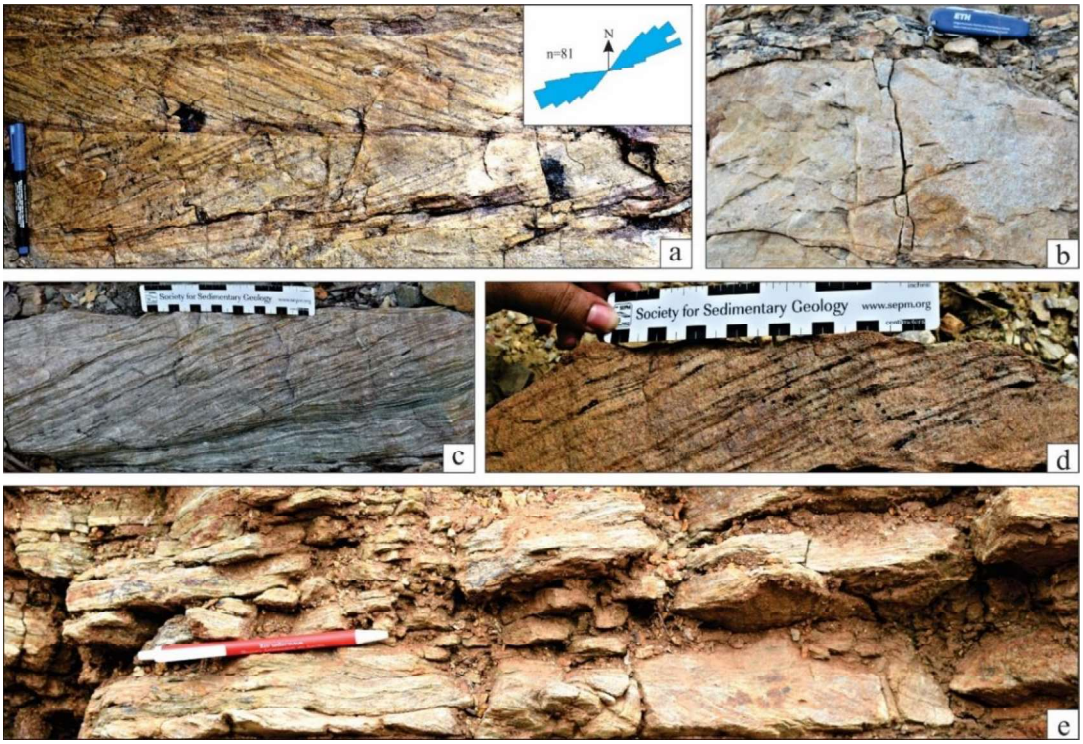


Fig. 3.3: Reactivation surface in alternative thick-thin cross-stratification facies (a, marked by yellow arrows, bar length 15 cm), herring bone cross-stratification (b, marker length 15 cm, note the bipolar paleocurrent direction within), mud clasts defining the herringbone cross-stratification (c, knife length 15 cm), double mud drape (d, e, scale length 15 cm), small scale cross-stratification in ripple sandstone (f, pen length 15 cm).

### 3.2.1.2. Herringbone cross-stratified sandstone facies ($FI_2$)

Two sets of oppositely dipping cross-strata separated by a gently inclined, planar erosional surface constituting a herring-bone pattern is a characteristic feature of this association (Fig. 3.3a, b). The average thickness of this facies is 30 cm. The orientation of herringbone cross-strata shows distinct bi-polar and bi-modal palaeocurrent direction all over the studied stretch (Fig. 3.3a). Double mud drape is a characteristic feature of the foresets (Fig. 3.3c, d). Mud clasts are present along the boundary between two differently oriented sets of cross-stratification at places (Fig. 3.3b).

### 3.2.1.3. Small-scale ripple laminated sandstone facies ($FI_3$)

This facies is characterized by small-scale ripple laminated sandstone and is commonly associated with the facies $FI_2$ and $FI_4$ (Fig. 3.1). Mud is present at the trough of some of the ripples. The maximum thickness of the ripple foresets is 5cm. Thick mud partings occur at the ripple set boundaries (Fig. 3.3e, 3.4a). Ripple cross-lamina exhibit sigmoidal pattern at places (Fig. 3.3e).

### 3.2.1.4. Planar laminated sandstone facies ($FI_4$)

Parallel laminated sandstone with intermittent mud laminae defines $FI_4$ facies (Fig. 3.4b). The average thickness of the facies is 20 cm. The facies exhibits vertical variations in lamina thickness (ca. 2 cm for sand lamina and 0.3 cm for mud lamina) (Fig. 3.4b). However, limited exposure does not permit measurement of the thickness of sufficient numbers of laminae.

### 3.2.2. Facies association II

This association occasionally interferes with the Facies Association I. However, Facies Association II, characteristically contains less mud compared to Facies Association I. Facies Association II primarily consists of coarse to fine-grained sandstone. Five facies comprising of the Facies Association II are discussed as follows:

### 3.2.2.1. Conglomerate facies ($FII_1$)

This facies occurs locally and is characterized by a matrix-supported conglomerate unit having wedge-shaped geometry with a maximum thickness of ~40 cm. The base of the facies is invariably sharp and scoured (Fig. 3.4c). The compositions of clasts include chertified limestone, vein quartz and sandstone (Fig. 3.4c, d, e). The maximum size of the clasts is 11 cm. The interstitial spaces between the clasts of the conglomerate are filled up by coarse-grained sandy matrix (Fig. 3.4c, d). This conglomerate facies often grades into massive sandstone laterally and vertically (Fig. 3.4e).

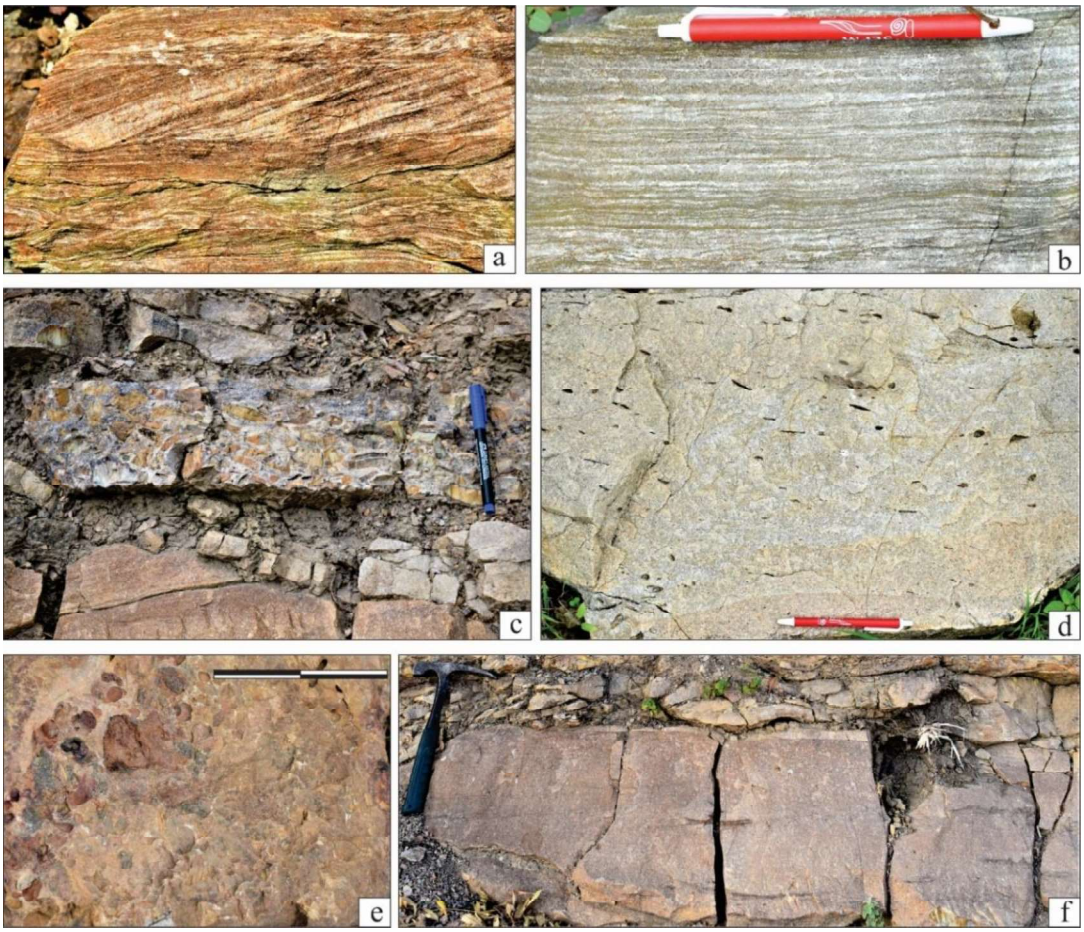


Fig. 3.4. Alternation on alternative thick-thin cross-stratification and ripple lamination facies (a, bar length 15 cm), planar laminated sandstone (b, pen length 15 cm), abundance syneresis crack on bedding surface of planar laminated sandstone bed (c, scale length 15 cm), conglomerate (d, clasts are defining by chert clasts, marker length 15 cm), conglomerate (e, clasts are composed of mud, pen length 15 cm), conglomerate (f, clasts are fragment of sandstone, bar length 15 cm).

### 3.2.2.2. Massive sandstone facies ($FII_2$)

This facies is characterized by massive, coarse to medium-grained sandstone beds (thickness of the facies is ~ 20cm) (Fig. 3.4f). The base of the facies is sharp than its top. Gutters, bipolar prod marks and locally flutes are present at the sole of this facies. The massive sandstone often grades upward into planar laminated beds followed by cross-stratifications (Fig. 3.5a). Though massive in general but occasionally the grain size of the facies decreases upward. Mud clasts are common at the base of the massive beds as well as along the cross-stratifications. Style of cross-stratification within a set changes laterally but non-cyclically. The brink point of the cross-stratifications maintains nearly the same distance from the base (Fig. 3.5b). The top of the sandstone beds is invariably wave rippled (Fig. 3.5c).

### 3.2.2.3. Tabular cross-stratified amalgamated sandstone facies ($FII_3$)

This facies is characterized by amalgamated sandstone beds (Fig. 3.5d, e). The maximum thickness of the individual bed is ca. 32cm but amalgamation may contribute a thickness up to 1 m. Internal tabular cross-stratifications define the amalgamated sand beds (Fig. 3.5d). Palaeo-current direction measured from this tabular cross-strata is directed towards WSW direction (Fig. 3.1). It is commonly associated with massive to feebly graded sandstone facies and hummocky cross-stratified sandstone facies (Fig. 3.1). The bases of the facies are sharp while their tops are gradational with the occasional presence of wave-ripple laminations.

### 3.2.2.4. Hummocky cross-stratified sandstone facies ($FII_4$)

This facies is characteristically medium grained, moderately sorted sandstone with broadly lenticular to tabular beds and convex-up tops (Fig. 3.5f). It is overlain by wave ripple laminated facies (Fig. 3.1) with less sharp contact. Hummocks and swales are frequently observed with maximum height and wavelength ca. 8 cm and 35 cm respectively. Bases of such beds generally replicate the underlying bed surface. Hence the bases are sharp but non-erosional whereas the top of the beds is less sharp. This facies is commonly associated with the top part of the Massive sandstone facies. Overall normal gradation is observed within the facies.

### 3.2.2.5. Ripple laminated sandstone facies ($FII_5$)

This ripple laminated sandstone facies generally overlies the top of the preceding facies (Fig. 3.5g). Ripple crests are straight and show bifurcations on the bedding plane. Syneresis cracks are abundantly present on the bed surfaces of these beds at different levels (Fig. 3.5h). Overall orientations of these cracks are fairly consistent but vary widely between beds (Pratt, 2002).

## 3.3. Paleogeography and Depositional environment

The presence of a thin lag between the Rohtas Limestone and the sandstone unit possibly represents a transgressive lag (Catuneanu, 2006; Mandal et al., 2016). The presence of the transgressive lag along the boundary of the Rohtas Limestone and this sandstone indicate a fresh episode of sedimentation after the completion of lower Vindhyan

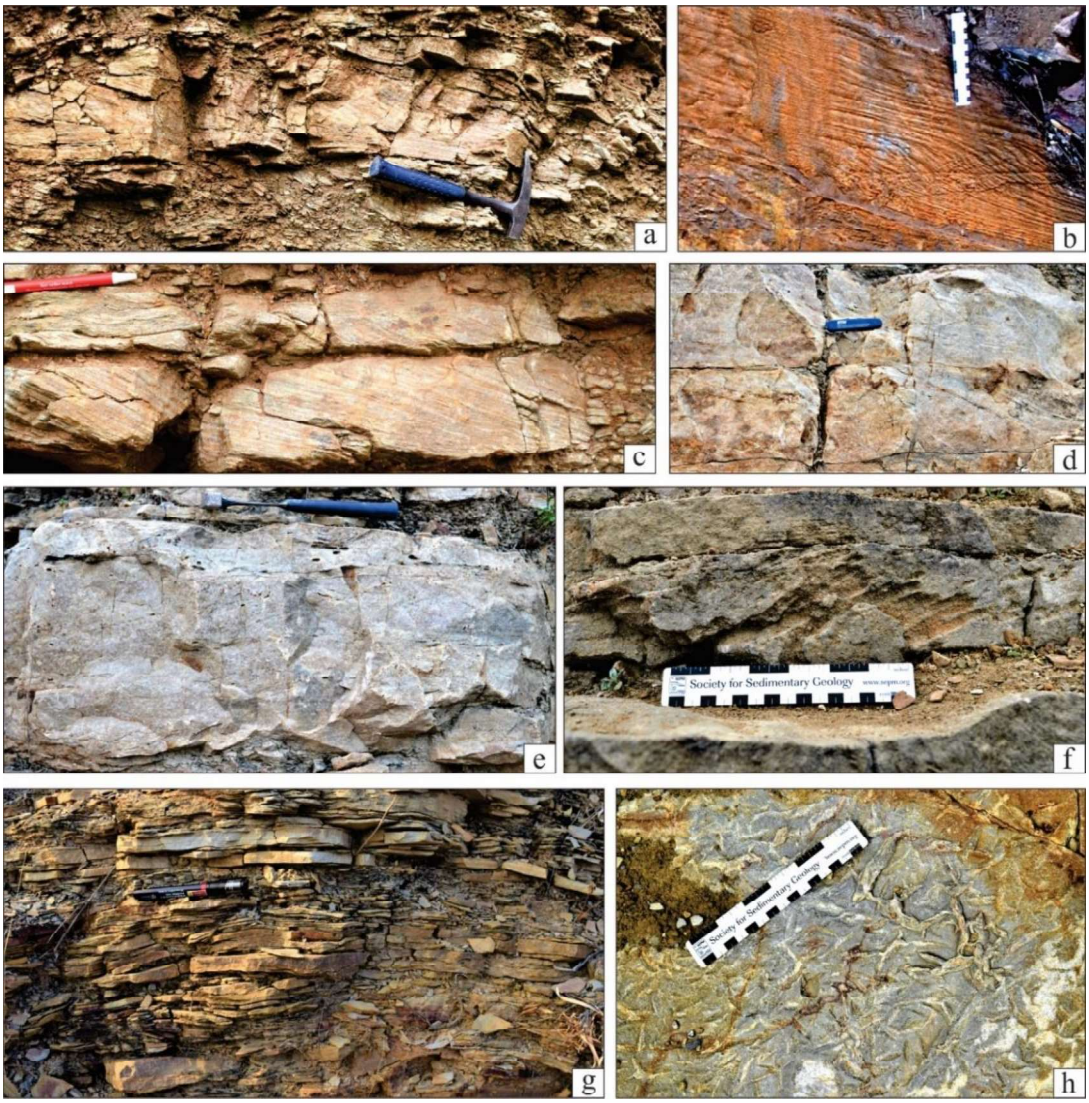


Fig. 3.5. Massive bed (a, hammer length 35 cm), later transition of massive to cross-stratification (b, hammer length 35 cm), bring pint shifting (c, scale length 15 cm), large scale cross-stratification bed (d, pen length 15 cm), amalgamation of cross-stratification beds (e, knife length 8 cm), mud clasts alignment along cross-stratification (f, hammer length 35 cm), hummocky cross-stratified sandstone bed (g, scale length 15 cm), ripple laminated facies (h, marker length 15 cm).

sedimentation. The internal structures of sandstone, cyclicity in laminae thickness and high concentration of mud within all the constituting facies of the facies association I indicate tide-dominated depositional setting. The bed load movement under the influence of dominant unidirectional current during the tidal regime is inferred. The alternations between thick-thin foresets strongly support tidal actions. Bipolar and bimodal palaeocurrent direction of herring-bone patterned cross-stratified sandstone facies corroborates tidal actions (DeBoer et al., 1989, Bose et al., 1997). Presences of double mud drapes within this facies (Fig. 3.3c, d) indicate a subtidal environment (Bose et al., 1997; Eriksson and Simpson, 2004, Kohseik and Terwindt, 1981). The larger cycle, measured

from alternating thick-thin laminae (Fig. 3.2), is very much compatible with the lunar bi-monthly (spring to spring) cycle. This can readily be attributed to semidiurnal tides. The intra-set cyclic variations along with grain size indicate repeated waxing and waning of the water flow. In contrast to the bidirectional palaeocurrent pattern, alternating thick-thin tabular cross-stratified sandstone facies ($FI_1$) is unidirectional (Fig. 3.1), indicating flow reversal during abandoning phase of tidal sand-waves (Nio and Young, 1991; Bose et al., 1997). In places mud laminae within the constituting facies are very thick (Fig. 3.2f). Such thick mud drapes in between the sand layers rarely form at any stage of tidal cycle (McCave, 1985; Chakraborty and Bose, 1990). However, thick mud can be introduced to any tidal system from outside by a process which is able to disperse mud in suspension load from the shoreline environments, possibly by a super-storm event (Allen, 1988; Chakraborty and Bose, 1990). High suspended sediment concentration may lead to deposition of thick mud layer during the neap period as well (Schieber, 1986).

The stacking pattern of beds within the facies of this association reveals occasional interruptions by high energy events like storms within a tide-dominated environment. The massive sandstone facies indicates rapid dumping of the sediments. Massive character suggests deposition from short-lived, high-density flows. The high rate of sedimentation prevents the sorting process to operate (Kneller and Branney, 1995; Magalhães et al., 2015). The vertical and lateral transition of conglomerate facies to massive sandstone indicates the deposition of both the component from a single flow. The scoured base of the conglomerate beds (Fig. 3.4c) at places indicates the presence of turbulence within the flow. The flow must have enough capacity to pick-up chertified limestone clasts from the topmost part of the Rohtas Limestone. The occurrence of amalgamated sandstone beds within Facies Association II, juxtaposed one above other suggests rapid recurrence of event flow, possibly storm surges, in a high flow regime (Sarkar et al., 2004). The individual sandstone bed comprising amalgamated sandstone facies indicates the product of a single depositional continuum over a relatively short time. Sharp irregular base with sole features also supports the high energy events responsible for the deposition of the beds and supercritical nature of the initial flow (Sarkar et al., 2012). The cross-stratification having the brink points at the same height from base suggests the high rate of sand fall-out from suspension possibly during the periods of a heavy storm. The steady upward decline in both grain-size and flow regime suggests a gradual waning of the high energy events (Bose and Sarkar, 1991). Preserved wave ripple forms on the bedding surface and hummocky cross-stratified

sandstone facies reflect deposition under the influence of oscillatory flow possibly during storm surges. Asymmetry in the ripple profiles indicates the simultaneous presence of a tractive force within the flow. Deposition from the storm-generated combined, wave-cum-current, flow is thus inferred. Syneresis cracks present on the bed-surfaces of wave ripple laminated sandstone facies possibly originate through dewatering of the sandy beds due to the rapid deposition of the overlying sediment (Kidder, 1990). Increased pore-water pressure because of storm wave action (Cowan and James, 1992, Harazim et al., 2013; McMahon et al., 2017) may be responsible for the generation of syneresis cracks.

# PART II

# Aspect of Special Interests

# CHAPTER 4

# Depositional facies vis a vis triggering agents of soft sediment deformation structures: a case study from Mesoproterozoic Rohtas Limestone Member, Vindhyan Supergroup, central India

## 4. 1. Introduction

Soft-sediment deformation structures (SSDS) are formed by liquefaction and concomitant fluidization processes within the unconsolidated sediments induced by both exogenic and endogenic triggers (Owen and Moretti, 2011; Owen et al., 2011; Moretti and Ronchi, 2011; Moretti and Van Loon, 2014; Sarkar et al., 2014; Shanmugam, 2016). The analysis of liquefaction-induced SSDS comprises of two aspects viz. triggering mechanism and triggering agents. The identification of the triggering agent is always difficult as morphology of SSDS are independent of triggering agent i.e., similar types of SSDS are formed by both exogenic and endogenic triggers (Owen and Moretti, 2011; Owen et al., 2011; Moretti and Ronchi, 2011). Even the lateral persistency, vertical repetition and change-over of SSDS through lateral continuity which are considered as diagnostic features for exogenic triggers has failed to assure that these characters can't be corrosponds to endogenic triggers (Owen et al., 2011). However, identification of actual triggering agents is very important because they are co-relatable with the basin evolution process. Keeping this in view, a relatively new method has been adopted in this paper to identify the SSDS and their respective triggering agents which ultimately helps to recognize the scenario of the basin evolution.

To measure the accuracy of the newly adopted method we have examined the Rohtas limestone succession of Vindhyan Supergroup, Son valley, central India over a stretch of 57 km from Vadanpur to Mohania (Fig. 1.5; $L_3$, $L_7$, $L_8$ and $L_9$) where SSDS are abundantly present. The temporal and the spatial variation of the constituting facies and their associations have broadened the scope of the study. Some of SSDS present within the limestone are laterally persistent, vertically repetitive in nature. However, the preferential occurrence of SSDS with distinctive facies association helps to identify the systematic variation in triggering mechanism as well as the triggering agents. This also help to reveal the basin evolution history of the Rohtas Limestone.

## 4.2. Geological setting

This study addresses ~110 m thick Rohtas Limestone Member (RLM) of the Vindhyan Supergroup exposed along a transect from Vadanpur to Mohania in central India

(Fig. 1.5). The RLM itself is considered as of marine origin (Bose et al., 2001; Banerjee et al., 2009; Sarkar et al., 2019). It is underlain by Rampur Shale and overlain by a basin wide unconformity (Mandal et al., 2019), which divides the Vindhyan Supergroup into two Groups, the Lower Vindhyan/Semri and the Upper Vindhyan Group (Fig. 1.3). The Upper Vindhyan Group above the unconformity starts with the Lower Quartzite representing a hiatus of about 400 MY (Tripathy and Singh, 2015) and changes in depositional facies from carbonate to siliciclastic. (Bose et al., 2001; Sarkar et al., 2002, 2004, 2005; Choudhuri et al., 2020). The RLM is completely devoid of skeletal remains suggests that the SSDS have no relation towards biogenic origin. The pyroclastic occurring at the basal part of the Rampur Shale, the underlying member of the Rohtas limestone have been dated to 1599±8 Ma by the U/Pb SHRIMP technique (Fig. 1.3; Rasmussen et al., 2002; Ray et al., 2002, 2003). The RLM is dated 1599 ± 48 Ma on the basis of Pb-Pb isotope ratio (Fig. 1.3; Sarangi et al., 2004). The limestone was deposited in an intracratonic rift basin (Bose et al., 1997).

### 4.3. Facies analysis of the studied stretch

The studied stretch of the RLM consists of two facies associations, with a four stacked intensely deformed and laterally continuous zone in between. This zone is almost devoid of primary structures and is not considered for facies analysis. The two facies associations are present below and above these deformed zone having contrasting characters, including the primary sedimentary structures present within them. The facies analysis study was conducted with a goal to identify the depositional setting of the sediments that underwent deformation. During the present study four detailed sections were measured along 57 km stretch from Vadanpur to Bhagwar (Fig. 4.1). The facies constituents of these two facies associations are described and interpreted below.

#### 4.3.1. Facies association I (FA I)

Facies association I present below the intensely deformed layer (Fig. 4.1), is composed of intra-clastic and muddy carbonate sediments and comprises of four facies. See details of facies in section 2.2.1.

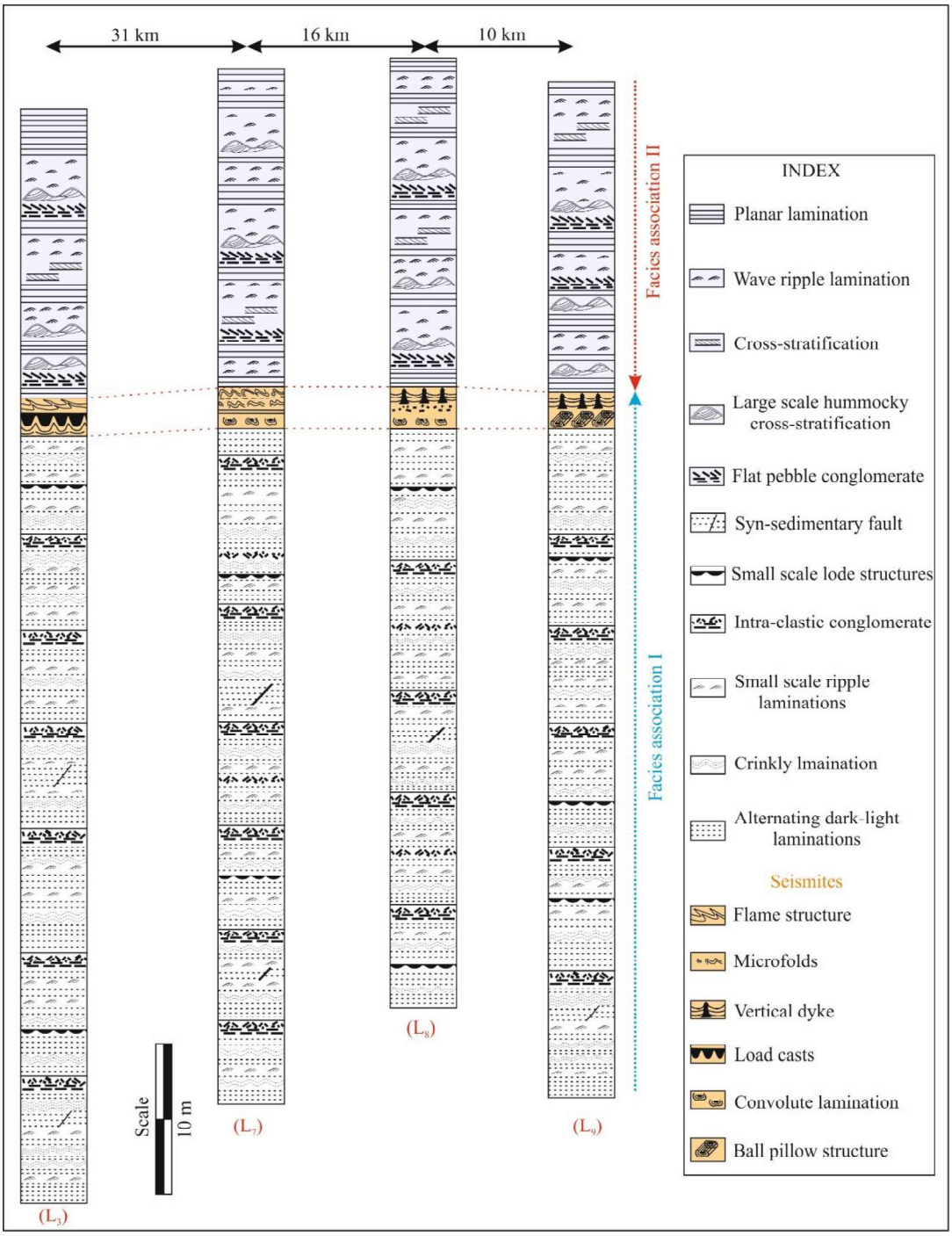


Fig. 4.1. Facies succession in several vertical logs, with their characteristics. Note the different character of the two facies associations (FA I- below the *seismite*; FA II- above the seismites). The SSDS in the seismite interval are much larger than in the rest of the successions.

### 4.3.2. Facies association II (FA II)

Facies association II lays above the Facies association I with the deformed four layers stacked zone in between. The average thickness of the association is ca. 30 m. This association is entirely different from the previous association with respect to their lithology

(mostly calc-arenite), primary sedimentary structures and the size of the constituting bedform. Description and interpretation of facies is in section 2.2.2.

### 4.4. Soft sediment deformation structures (SSDS) present within the RLM

Both the facies associations described above contain various types of soft sediment deformation structures (SSDS). Many of them are complicated in nature. Some of the SSDs are present within a specific facies association and some of them are shared by both the facies association. Noteworthy to mention that there is a 3 to 4 m thick zone in between FA I and FAII which comprises four stacked deformed layers. This four-stacked deformed zone is 57 km laterally persistent. This deformation zone contains different varieties of SSDS some of which are exclusive to this deformed zone while some of them are shared by overlying FA II. As the prime objective of the present paper is to identify the triggering mechanisms of the SSDs, the individual SSDS are grouped into three morphological categories- brittle, contorted and intruded structures (Table-4.1; Fig. 4.2, 4.3, 4,4, 4.5). Their detailed descriptions and plausible mechanisms are provided in Table-4.1.

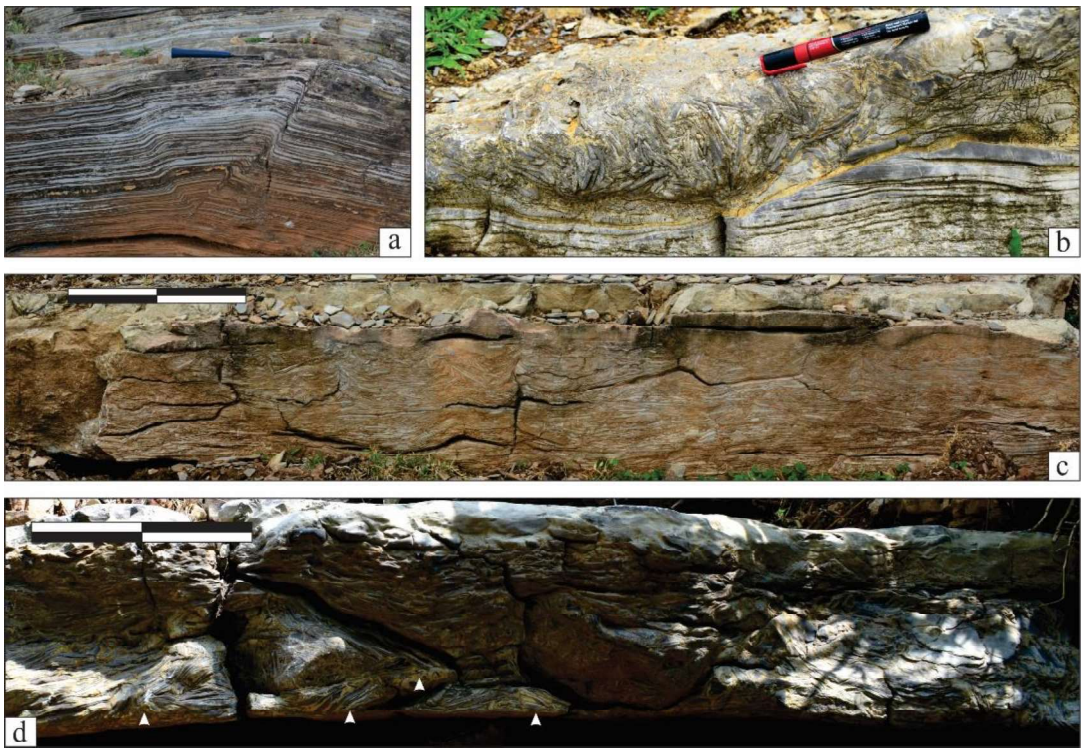


Fig. 4.2. SSDS in FA I: syn-sedimentary faults and folds (a; hammer length 35 cm), slide plane defined by intraclastic bed (b; marker length 15 cm), vertical to sub-vertical orientation of intraclasts of breccia bed (c; bar length 15 cm), folded clasts within breccia bed (c; marker length 15 cm; note folded clasts are marked by white arrows).

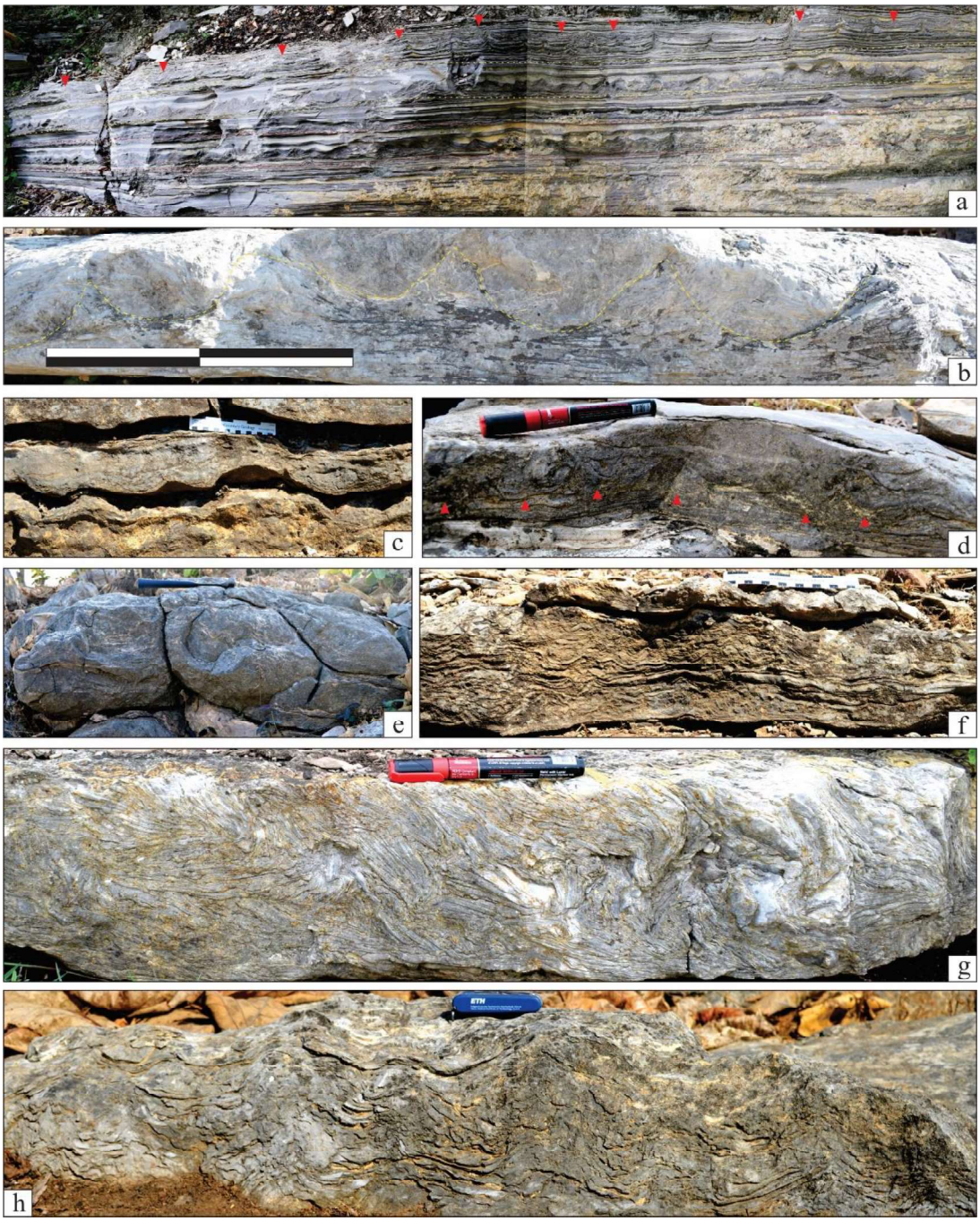


Fig. 4.3. SSDS in seismite: alternating load casts and flame structure bearing beds (a, b: hammer length 35 cm, bar length 15 cm), convolute lamination (c, d and e; marker length 15 cm, scale length 15 cm, hammer length 15 cm; note symmetric and asymmetric natures), micro-folds (f; scale length 15 cm; note up-warped laminas i.e. fluid escaping path), breccia with folded clasts (g; marker length 15 cm; note alternating antiform and synform nature of folded clasts), conduits (h; knife length 8 cm; note conduits are massive nature).

Table 4.1. Description, similarities and difference of SSDS present in studied sections

| Type of structure | Name of SSDS | Association of SSDS | Description of SSDS | Differences of similar SSDS if present other association as well |
|---|---|---|---|---|
| Brittle structures | (a) Syn-sedimentary fault | FA-I; commonly associated with $FI_A$ facies | Present at few stratigraphic levels without any periodic repetition (Fig. 4.2a); laterally impersistent, maximum extension is ca.10 m; thickness of the faulted layer varies between 4 cm and 15 cm; fault plane orientation is bipolar (Fig. 4.2a); laminae at the downthrown side are thickened. | Strictly restricted in FA I |
| | (b) Slide planes | FA I (Fig. 4.2b) and FA II (Fig. 4.3b, c, d), but more common with FA II association, In FA I associated with $FI_A$ facies whereas in FA II, it is mostly associated with $FII_C$ facies | Lystric in nature; maximum dip amount of the slide plane is ca. 15˚ but it decreases downward; downslope is occupied by breccia (Fig. 4.2b, 4.4b, c, d); planar lamination structures are preserved as clasts in both cases (Fig. 4.2b, 4.4e); ripple laminates are also preserved as clasts in FA II (Fig. 4.4f) | FA I: bed is persistence upto 10 m.<br>FA II: bed is persistence in Km; maximum length of clasts is 1.5 m (Fig. 4.5a, b); in-between planar laminated beds are preserved in length of 1-5 m (Fig. 4.4b, 4.5b). |
| Contorted structures | (a) Syn-sedimentary folds | Rare in FA I (Fig. 4.2a, d); also present abundantly within the four stacked deformed zone between FA I and FA II (Fig. 4.2g) | Small scale in nature and terminate against undeformed beds; intense deformation is restricted within the three stacked layer and scale is larger than those present in FA I. Folds have asymmetric limbs with differential inclination (Fig. 4.2a, 4.4 g). | In case of in-between FA I and II series of antiform and synform observe, whereas in case of FA I suddenly appear as clasts in intraclastic bed |
| | (b) Load casts and flame structures | FA II ( Fig. 4.4a), also within four stacked deformed zone between FA I and FA II ( Fig. 4.3a, b) | Light coloured calc-arenite layers are loaded within dark calcareous muddy sediment (Fig. 4.3a, 4.4a); load casts are asymmetric in nature (Fig. 4.3a, 4.4a); in between load casts, flame structures are also present (Fig. 4.3a, 4.4a); the | In case of FA II, loaded beds disappeared in hundred meters whereas it's continuous km after km for in-between FA I and II |

| | | | | |
|---|---|---|---|---|
| | | | tips of the flames are pointed towards SW direction. | |
| | (c) Convolute laminations | Deformed zone between FA I and FA II | Distorted stratification forms alternate convex and concave upward morphologies; laterally persistent zone is observed (Fig. 4.3b, c, d, e); convolutes are of different size (max height and width 5 cm and 15 cm respectively); the convolute lobes are both symmetric and asymmetric in nature (Fig. 4.3b, c); also single and multiple lobate nature of convolutes are present; degree of deformation gradationally defuses downward and passes into undisturbed laminae. | Specified within deform zone between FA I and FA II |
| | (d) Micro-folds | Deformed zone between FA I and FAII | Highly distorted stratification; characterised by mm-scale folded laminae with series of small anticline and syncline form (Fig. 4.3f) or irregular morphology and forms; it is present within alternate calc-arenite and calcareous mud; they are laterally continuous with discontinuity of laminas by folded/ torn lamina and vertical to sub-vertical project (Fig. 4.3f ); vertically grades into undeformed laminae. | Restricted in seismite zone |
| | (e) Folded Breccia | FA I (Fig.4.2d), in-between FA I and FA II (Fig. 4.3g), and FA II (Fig. 4.5c, d) | These breccia bodies do not have any definite shape. However, series of antiform and synform made up of clasts characterise this feature; they are laterally persistent; synform part is more preserved than antiform; average thickness of this SSDs is 30 cm; the top surface is highly distorted in nature. | In FA I and II, folding nature in preserved only as clasts. In association II, clasts have retained planar lamination.<br>In case of deform zone between FA I and II bed in continuous. |

| | | | | |
|---|---|---|---|---|
| | | | In FA II, besides clastic nature of laminas; clasts are restricted within breccia beds; in some cases these are at base of base and followed by massive bed; somewhere in protruded within underlying deposit. | |
| Intruded structures | (a) Conduits | Deformed zone between FA I and FAII | Characterised by series of vertical to steeply inclined conduits (Fig. 4.3h) that sharply intruding the overlying strata; filling material of the conduits are relatively coarser calc-arenite and internally massive in nature; their basal edges are attached to the underlying sediment sources and laminae are bent towards the conduits (Fig. 4.3h); height of the conduits varies laterally ( max 15 cm); on the bedding plane, they appear as dome shape. | Restricted in seismite zone. |

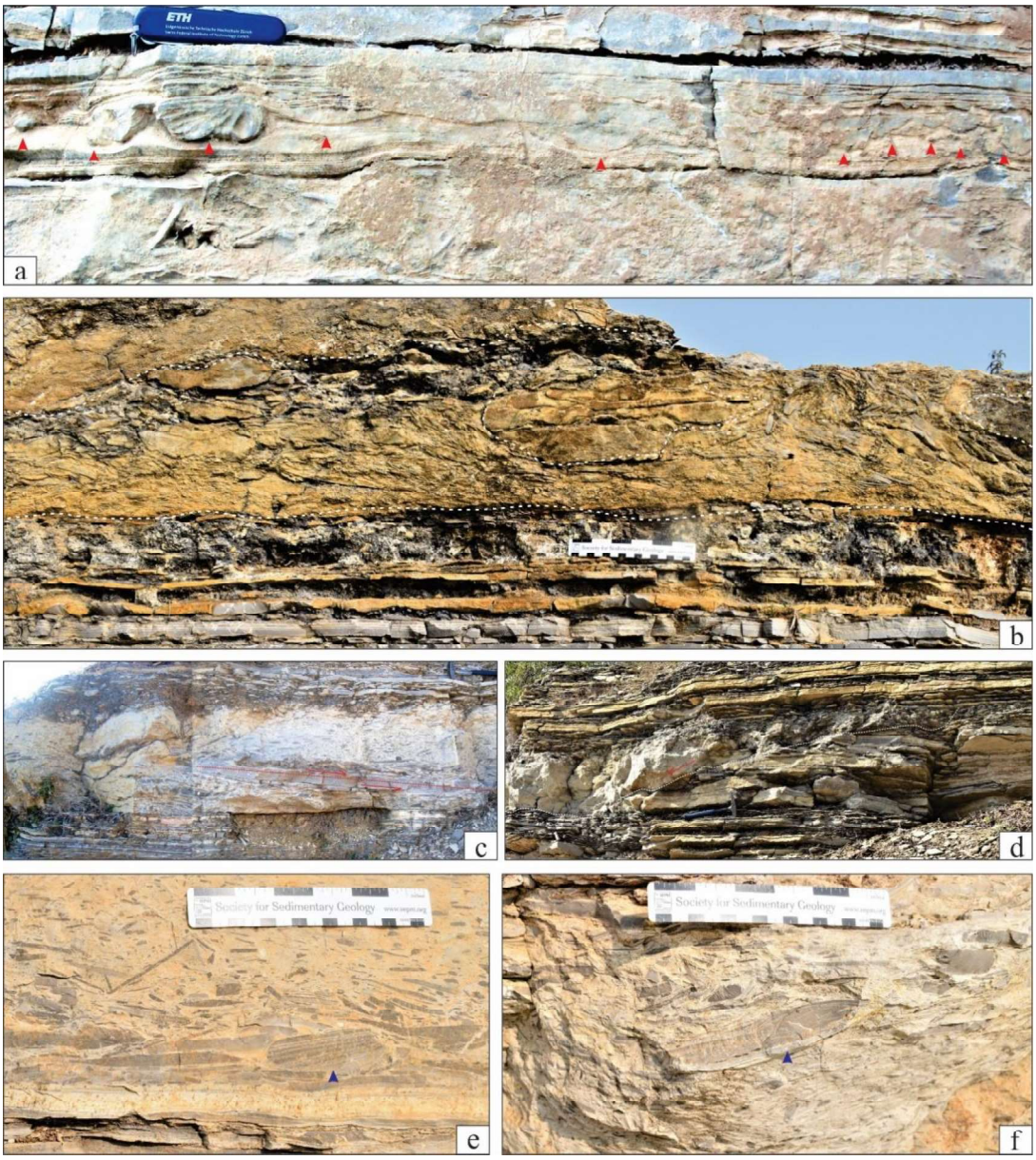


Fig. 4.4. SSDS in FA II: multi-loads (a; knife length 8 cm; note loads are marked by red arrows), intraclastic breccia defining slide plane (b; scale length 15 cm; note planar laminated parent beds within bed), well define slide plane in an angle of ~$15^0$ (c, d; hammer length 35 cm; note the thickness variation and its transition to undeform planar laminated bed, marked by dotted lines), planar lamination as intraclasts (c; scale length 15 cm; marked by blue arrow), cm-scale ripple cross-stratification as intraclasts (d; Scale length 15 cm).

## 4.5. Discussion

### 4.5.1. Mechanism of SSDS formation

Faults and slide planes are attributed to brittle deformation and therefore points to differential compaction (Rossetti, 1999). Differential compaction may have some role in different rate of stress which in turn may influence the varying pore pressure within the

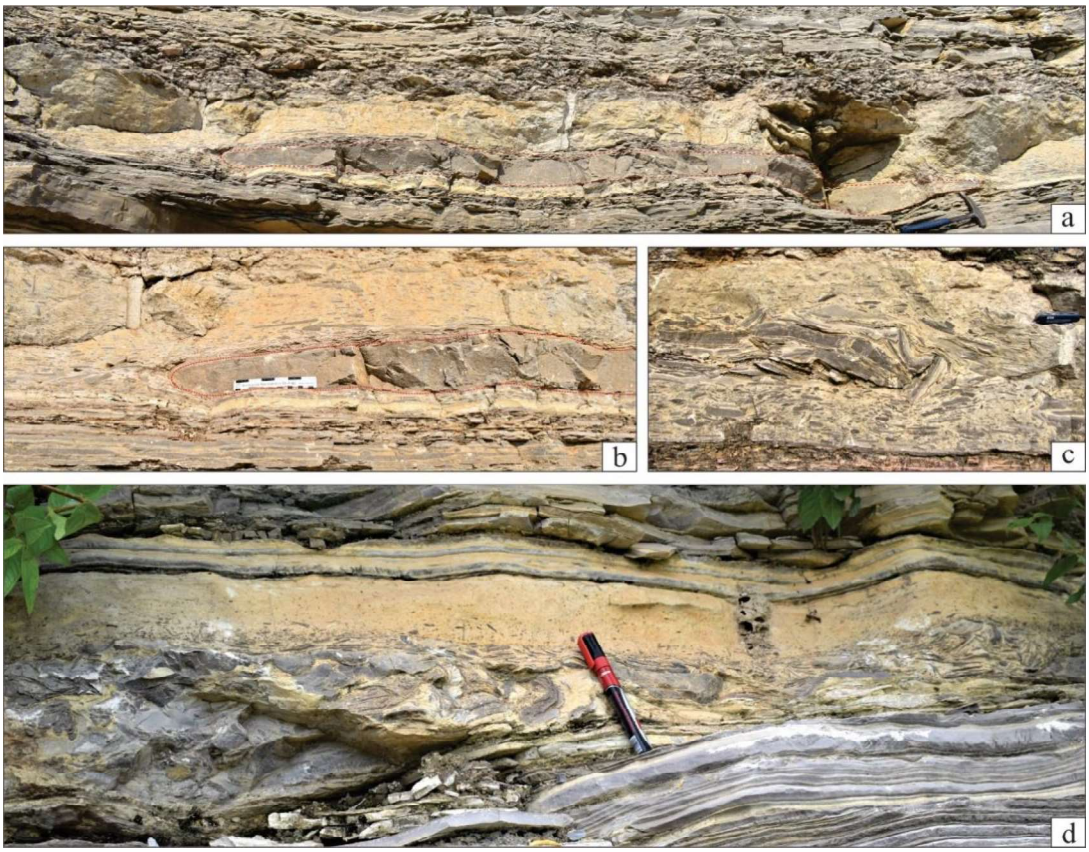


Fig. 4.5. SSDS in FA II: large clasts about 1.5 m in length (a; hammer length 35 cm; clasts are marked by red dotted line), thin planar laminated limestone beds on top of the clasts (b; scale length 15 cm; clast is marked by red dotted line; note small clasts alignment at base of large clast), folded-bended clasts protruded within matrix of breccia (c; marker length 15 cm), breccia bed (e; marker length 15 cm; note folded clasts at base followed by massive bed transition).

sediment (Anand and Jain, 1987). Thickness variation of the strata along the faults point to higher sediment deposition on the downthrown side of the fault in response to increase subsidence as the faulted block moved progressively. Association with slide planes and other contorted SSDs e.g. syn-sedimentary folds indicate that the faulting took place when the sediment was still in an unconsolidated to semi-consolidated nature (Rossetti, 1999). Laterally impersistent natureof the syn-sedimentary fault and slide planes indicate that deformed laminae were frozen in an embryonic stage. It indicates that these brittle SSDs were caused by instantaneous shocks. As the syn-sedimentary faults are restricted at a particular stratigraphic interval without any repetition also corroborates their origin related to instantaneous shock (Rossetti, 1999). Preferred clasts orientation of the breccias present on the downthrown side of the slide planes in FAI indicates escape of pore fluids along the slide planes. Lensoid nature of the breccias on the downthrown side of the slide planes imply that origin of slide planes are also due to instantaneous shocks. On the other hand,

the breccias associated with slide planes present within FAII indicate the shocks causing slide planes generation were more persistent in nature than that of FA I.

Contorted structures suggest reverse density loading might have been an important deformation process. Convolute folds are extremely complex forms of load structures produced when a high-density layer overlies a lower density layer (Anketell et al., 1970; Mills, 1983; Rossetti, 1999). Thixotropic or liquefaction processes reduce the shear strength and promote the gravitational collapse of higher density layers and the rise of less dense layers. Presence of load structures and associated flame structures corroborate this contention. Reverse density loading is mainly facilitated by rapid deposition of calcarenite onto calcareous muds with high water content (Potter and Pettijohn, 1977; Scott and Price, 1988); partial liquefaction/ fluidisation can generate gravitational instability and density contrast between more fluidized and less fluidized sediments, resulting into contorted SSDS (Nichols et al., 1994; Owen, 1996). Convolute folds were probably formed when less liquefied sediment sank down to replace the underlying more liquified sediment moving upward due to fluidisation. As deformation became more intense, convolutes may develop lobes – single or multiple. More chaotic and probably more intense deformation results into asymmetric lobated convolute folds. For syn-sedimentary fold, micro-folds and folded breccia, several other processes may act together rather playing isolated role during deformation (Nichols, 1995). Subsidence of beds was probably accompanied by simultaneous upward flow of sediment-water mixture. Syn-sedimentary folds, micro-folds imply some degree of compression along with subsidence, fluidisation and liquefaction.

Dykes are widely interpreted to represent flow paths with fluidised sediments being injected from surrounding strata as a result of increasing interstitial pore pressure (Rossetti, 1999). Series of conduits of vertical to sub-vertical nature in Rohtas Limestone indicate fluid along with sediments escaped rapidly from multiple points and the structures freeze at different points after rupture (Nichols et al., 1994). The concave-up nature of the underlying laminae at the base of the conduits are attributed to sediment fluidization and upward flow motion (Lowe, 1975, 1976; Rossetti, 1999).

### 4.5.2. Triggering agents- seismic or aseismic

Our field evidence shows that three types of SSDs- brittle, contorted and intruded, were formed within the Rohtas Limestone mainly by liquefaction and/or fluidization

processes within alternatingly deposited coarse-grained calc-arenite and fine-grained calcareous mud. The liquefaction and fluidisation processes responsible for SSDs can be related to several natural trigger mechanisms. However, differentiating the SSDs – which one is seismic and which one is aseismic, often seems quite difficult because similar kinds of SSDs can be generated by both seisimic and aseismic processes (Mills, 1983; Jones and Omoto, 2000; Moretti and Sabato, 2007). Also, more than one process may operate together, so identification of triggering mechanism is often difficult. Aseismic triggering mechanisms include storm/wave pounding, sediment overloading, unequal loading related to glacier, bioturbation causing deformations, slope failures, rapid sedimentation, different degree of compaction resulting into pore fluid over pressuring (Moretti and Sabatto, 2007; Sarkar et al., 2014, 2019; Choudhuri, 2020). The Mesoproterozoic Rohtas Limestone devoid of any skeletal organisms omits the possibility of biota induced SSDs. Convolute laminae and intruded structures, as noticed in the studied section (Table-4.1), may also be formed due to unequal loading along the margin of an ice cover, but no other evidence of the presence of glacier has been observed and thus glaciogenic triggering mechanisms can be excluded. The laminae are in general flat lying in nature, and there is no substantial evidence of slope failure (e.g. slump folds) in the study area which can be accounted for three types of SSDs. The commonly used criteria to identify the seismic triggering agents as proposed by Jones and Omoto (2000) are-(a) depositional setting, (b) the extent of the deformation units; (c) absence of evidence relating to aseismic triggering agents; (d) whether evidence of aseismic SSDs are present within the other stratigraphic sections which are otherwise undeformed in nature. The present study reveals that importance of determining paleoenvironment as it can help us to differentiate between the seismic and aseismic triggering agents.

The sedimentary facies analysis of the studied Rohtas Limestone indicates that there is a change of depositional setting. Initially the paleoenvironment was restricted and tranquil in nature (Choudhuri, 2020; Sarkar et al., 2019) at the lower part (FA I) of the studied section. Abundance of micrite deposition implies that suspension load was dominant. Occasional storms disrupting the otherwise calm environment is recorded by the presence of small-scale cross-laminae but their lateral discontinuity implies slow rate of sediment supply. On the other hand, the upper part of the studied section (FA II), represents an open marine wave agitated depositional condition. Hummocks ($FII_A$), massive beds ($FII_B$), intraclastic beds ($FII_C$) supports the interpretation. The boundary between FA I and

FA II is marked by the four-stacked intensely deformed zone which is 40…km laterally traceable. This deformed zone in between FA I and FA II can be correlated with earthquake shock which is responsible for the basin subsidence as well (Moretti and Van Loon, 2014). It is confirmed that, at this level, strongly deformed four-stacked layers were developed by an agent that had affected the sediments over an extensive area and the agent triggered at least three deformation phases one after another in the form of aftershocks of an earthquake. The four-stacked deformed zone containing several contorted type of SSDs (see Table-4.1) are confined to a particular stratigraphic interval and laterally traceable upto 57 Km and thus invokes to a seismogenic origin. The vertical transition from a restricted lagoon to an open marine wave agitated depositional condition implies a rapid transgression of the sea either due to rapid sea-level rise or due to rapid subsidence. No such features supporting rapid sea-level rise have been found elsewhere as well. Thus rapid subsidence of the basin is the only option to explain the sudden transition from a low-energy environment (FA I) to an open, wave-agitated shelf environment (FA II). This transition is not only reflected by the ripple index observed in the two facies associations but also by presence of hummocky cross-stratification ($FII_A$) massive beds ($FII_B$) and intraclastic conglomerates ($FII_C$). The combination of laterally extensive four-stacked deformed layers in between two facies associations and the evidence of a sudden rise of sea-level can be explained only by tectonic activity that started very intensely and ultimately led to rapid subsidence of the depositional site (Sarkar et al., 2014). FA II had also experienced high rate of sediment supply compared to FA I.

The association of both brittle type and contorted type of SSDs in the study area supports the seismic activity in the studied Rohtas Limestone as observed in several Pleistocene and Quaternary deposits around the world (Anand and Jain, 1987; Mohindra and Bagati, 1996; Demoulin, 1996). Syn-sedimentary faults and slide planes (see Table-4.1) in which dip changes and becomes flat laterally also indicate seismic origin of the SSDs (Seilacher, 1969). In addition, intruded type SSDs (vertical to sub-vertical dykes in series) must be produced by instantaneous shocks contemporaneous to sediment deposition. They also indicate seismic activity at the transition between FA I and FA II (Tasgin et al., 2011). Several SSDs of contorted type (Table-4.1) however involves liquefaction and fluidisation processes generated due to reverse density gradient. This can be triggered due to rapid sedimentation (Owen, 2003). This can be of two reasons- either due to seismic shock or due to cyclic build-up of pore pressure generated due to storm/wave

pounding (Owen, 2003; Tasgin et al., 2011). Load casts and flame structures present within the four stacked *seismite* can therefore be correlated with the instantaneous shocks by earthquake whereas those present within the open, wave agitated marine environment (FA II) were formed due to cyclic build-up of pore fluid pressure. Syn-sedimentary folds, micro folds and folded breccia point to combination of several processes and points to pore fluid overpressure generated due to differential compaction (Sarkar et al., 2019). Subsidence of beds due to seismic activity was accompanied by simultaneous upward flow of sediment-water mixture (Nichols, 1995). Also, some degree of compression along with subsidence played some role to liquefaction and fluidization.

The SSDS associated in the Rohtas Limestone can be subdivided into four discreate segments. The structure associated with the FA I may be of aseismic origin because they are restricted and rare in occurrence. Pore-water pressure or even occasion storm introduction within the overall clam and quiet depositional regime may generate these structures as well. Micro-seismicity before the generation of the laterally persistent layers over kilometres may be also responsible. However, restricted occurrences always inevitable for the SSDs present within FA I. The association of open marine storm deposits and the SSDs present within them can be easily correlated with the storm pounding which is one of major triggering mechanism for complete liquefaction. High instantaneous storm sedimentation increase sedimentation rate can be responsible for this sort of liquefaction of a water saturated soft-sediment substratum (Moretti and Ronchi, 2011). The four stacked deformed zone (though facies analysis is not possible because of intense deformation) may be top part of the FA I and affected by strong seismic shock, which not only deformed the upper part to a large extent but was held responsible for basin subsidence as well. The four stacked layers at the boundary between the two facies associations (FA I and FA II are deformed over their entire lateral extent. Fluidisation and liquefaction played a major role in their genesis, suggesting exposure to a shock wave. In combination with the size of the deformations, which are much larger than those elsewhere in the succession, and in combination with the sudden tectonic activity, these four layers are interpreted as seismites.

### 4.6. Conclusion

Considering the sediment dynamics and associated soft sediment deform structured beds, we draw the following conclusion to identify the seismites from other exogenic triggering agent.

(a) Detail facies analysis suggest that the facies association I was deposited in a restricted shelf whereas facies association II in an open shelf condition.

(b) The sharp change of the depositional milieu from facies association I to II is likely to be the resultant of basin subsidence. The subsidence possibly because of some seismic events which affected the top part of the underlying facies association I. The seismites present at the top part bearing tell-tale evidence of seismicity.

(c) The SSDS in facies association I was under some sediment cover. Here, the liquefaction and fluidization was formed by local scale subsidence. The SSDS in facies association II has formed by storm pounding.

(d) The present study reveal that Facies analysis of sedimentary rock may be helpful to recognize triggering agents.

# CHAPTER 5

# Triple oxygen isotope: evidence of low temperature earth surface during Mesoproterozoic and its trend of high to low temperature earth over 4 billion years

## 5.1. Introduction

The high $\delta^{18}O$ record from Hadean Zircon have dated back the earth's surface ocean since ~4.4 Ga ago (Peck et al., 2001; Wilde et al., 2001), whereas oldest water-lain sediment has recovered from Archean (~3.85 Ga; Nutman et al., 1997). Temperature dependent oxygen isotope distribution in water lain chemical sediment hold the significant paleoclimate-paleoenvironment conditions (Urey, 1947). Although there are numbers of water-lain sediments (like carbonate, chert, phosphate) directly precipitate from water and record oxygen isotope, but chert (silica) is the best substrate not only because of its minimum diagenetic modification, also for its abundance since Archean (Knauth and Epstein, 1976; Wostbrock and Sharp, 2021). Although the physico-chemical condition of Phanerozoic ocean is well constrained, but knowledge is limited regarding earliest ocean (Precambrian) and its evolution to modern ocean. Water on earth surface at the time of "faint young sun" implies high concentration of greenhouse gas and warm climate (Kasting, 1987; Feulner, 2012; Georg, 2012), where rare evidence of ice before 3 Ga also this support. Although, warming in influence of greenhouse effect prevent the early Earth from frozen, but hot ocean temperature around ~200ºC (Hardardottir, 2011; Zarkhov and Bidemann, 2019; Zakharov et al., 2021) estimated from triple oxygen (3-O) isotope of chert is too much hot.

Oxygen isotope analysis ($\delta^{18}O$) unveils a gradual drop of temperature from 80ºC to 20ºC from Archean to present (Fig. 5.1; Robert and Chaussidon, 2006), but recently scientists unfold error in temperatures estimates by analyzing $\delta^{18}O$ alone, and propose to consider both $\delta^{18}O$ and $\delta^{17}O$ for the purpose (Pack and Herwatz, 2014, 2015; Herwartz et al., 2015; Sharp et al., 2016, 2018; Bindeman et al., 2018; Sengupta and Pack, 2018; Miller and Pack, 2021). 3-O data sets recorded so far (Levin et al., 2014; Sengupta and Pack, 2018; Hayles et al., 2019; Sengupta et al., 2020; Liljestrand et al., 2020; Lown et al., 2020; Wostbrock and Sharp, 2021; Zakharov et al., 2021; McGunnigle et al., 2022) show that oxygen isotope is gradually decreasing since Archean to recent. Compare to Phanerozoic, Precambrian data sets have very low $\delta^{18}O$ and high $\Delta'^{17}O$. Temperature calculation manifest that Archean ocean temperature was around ~100ºC (Zakharov and Bindeman, 2019; Liljestrand et al., 2020; Zakharov et al., 2021; McGunnigle et al., 2022). The low

$\delta^{18}O$-high temperature Archean ocean and its evolution to modern sea has modelled as- (a) hot primitive ocean (Knauth and Lowe, 1978, 2003; Shemesh et al., 1983, 1988, 1992; Karhu and Epstein, 1986; Jean-Bapstiste et al., 1997; Muehlenbachs, 1968; Robert and Chaussidon, 2006; Sengupta and Pack, 2018; Lowe et al., 2020; McGunnigle et al., 2022); (b) change in ocean composition over time (Jaffres et al., 2007); (c) isotopic exchange between sea-water and meteoric water during diagenesis (Degens and Epstein, 1962; Marin-Carbonne et al., 2013, 2014; Taylor, 1978, Sharp et al., 2016; Liljestrand et al., 2020; Sengupta et al., 2020); (d) intense carbonization and silicification of oceanic crust at high flux of $CO_2$ is the result of low $\delta^{18}O$ early ocean (Herwartz et al., 2021). But offset of 3-O isotope data sets from silica-water equilibrium ($\delta^{18}O \approx -1‰$ and $\Delta'^{17}O \approx 0‰$) can't presume how does the oxygen isotope composition of the ocean over Geological time vary. Therefore, scientists proposed high temperature alternation ($F_{HT}$), low temperature alternation ($F_{LT}$), continental weathering ($F_{CW}$), continental growth ($F_{CG}$) and mantle recycling ($F_{MR}$) influence primary isotope modification/ evolution (Muehlenbachs, 1998; Wallmann, 2001; Kasting et al., 2006; Pack and Herwartz, 2014; Sharp et al., 2016, 2018; Sengupta and Pack, 2018; Hayles et al., 2019; Sengupta et al., 2020; Wostbrock and Sharp, 2021; Zakharov et al., 2021; McGunnigle et al., 2022), but still temperature, composition of hydrosphere and its evolution over time is enigmatic.

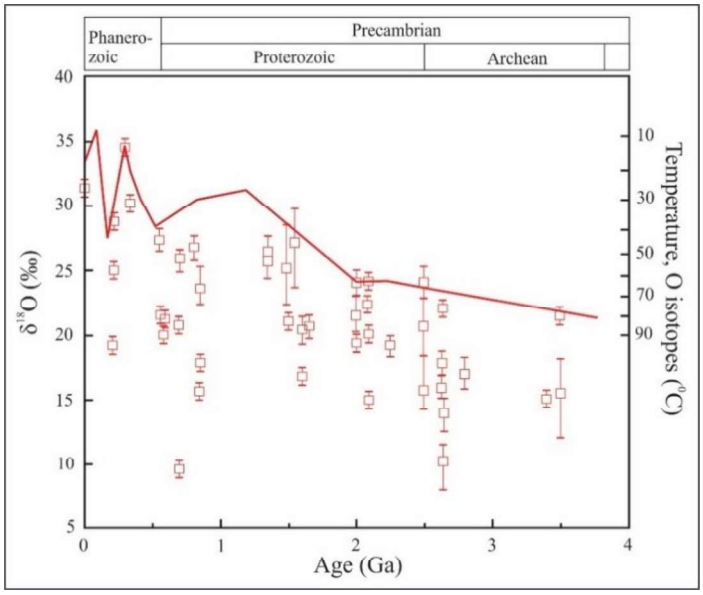


Fig. 5.1. Variation in chert $\delta^{18}O$ values with geological age. Error bars correspond to 1σ error on the mean of three to five analyses per sample. The solid line (referred to in the text as $\delta^{18}O_{KL}$ (Knauth and Lown, 1978)), shows the highest $\delta^{18}O$ value found in cherts at a given age. Considering that the ice caps were absent-that is, $\delta^{18}O_{sea\ water} = -1‰$ variation in $\delta^{18}O_{KL}$ with time may reflect seawater temperature variations between about 70°C in the early Archaean and about 30°C in the late Proterozoic (modified after Robert and Chaussidon, 2006).

In the present study we expand 3-O isotope record of Precambrian by analyzing the Mesoproterozoic chert of Vindhyan Supergroup, India. Triple oxygen data set of this ancient chert equilibrate with silica-meteoric water system enlighten the earth surface

temperature during Mesoproterozoic. The availability of published triple oxygen isotope calibration (Levin et al., 2014; Liljestrand et al., 2020; Sengupta and pack, 2020; Lown et al., 2020), offered an opportunity to take close look on the secular trend of $\delta^{18}O$ and $\delta^{17}O$ over geological time, its relation with volume of oceanic and continental crust. Consequentially combined data sets offer to calculate modification of triple oxygen data sets by high and temperature fluid rock interaction. Integrated study of all of these allows us to explain the necessity of some advanced explanation to estimate the evolution of hydrosphere and temperature since Archean to recent.

## 5.2. Material and Methods

### 5.2.1. Sample suits

During the present study, we have collected chert samples from a 70 cm thick chert layer. The chert layer is present along the unconformity of the Vindhyan Supergroup, present in-between the upper and lower Vindhyan Group (Mandal et al., 2019, 2020). With the thickness variation from 2 m to 50 cm, the chert layer is also laterally discontinuous upto 2 km. The chert clasts are also present in the transgressive lag present at the base of Upper Vindhyan present at places (see Mandal et al., 2019, 2020).

To estimate the change of oxygen isotope composition of chert over geological time (since Archean to recent) to evaluate the evolution of hydrosphere and temperature, we have reviewed a numbers of triple oxygen isotope paper published so and numbers of data sets have collected. All of these data sets have plotted in different diagram of silica-water system.

### 5.2.2. Physico-chemical analysis

Detailed field study was carried out on exposed succession along the unconformity surface of lower and upper Vindhyan. Fresh samples of chert was collected. Petrographic investigation was carried on Leica DM2700P polarizing microscope attached Leica DFC550 camera in Department of Geological Sciences, Jadavpur University.

The $\delta^{17}O$ and $\delta^{18}O$ of the $SiO_2$ samples were measured by laser fluorination (Sharp, 1990) at Georg-August-Universität in combination with gas chromatography and gas source mass spectrometry (for details see Pack et al., 2016). In the preprocessing each powdered samples were treated with 10% HCl in order to remove carbonates, which constitute a major contaminant in some of the samples. The insoluble residual of $SiO_2$ has

analyzed from triple oxygen isotope. San Carlos olivine (Pack et al., 2016; Sharp et al., 2016; Wostbrock et al., 2020) and Gore Mountain garnet (UWG-2; Valley et al., 1995) were used as standards. The error was 0.3% or better in $\delta^{18}O$ and 0.01 for $\Delta'^{17}O$.

**5.2.3. Isotope notation:** See details in section 1.8.5.

## 5.3. Result

### 5.3.1. Petrography of present chert

The studied chert samples are consisting of grey, fine-grained microquartz (<20µm) with modal percentage of microquartz ranges from 80 to 90 wt% (Fig. 5.2a, b). Individual microquartz are commonly varies from 3 to 5 µm with crenulated, irregular boundaries and undulose extinction. Except these, some mesoquartz (>20 µm; same texture as microquartz) and megaquartz (>20 µm; more regular boundaries and no undulose extinction) are present within vug (Fig. 5.2c). Few chert samples are consisting of ooids, peloids and intraclasts structures with distorted laminas (Fig. 5.2d). Both radiating and concentric rim of ooids and, composite ooids are well preserved.

Table-5.1. Triple oxygen isotope value of chert samples in Rohtas Limestone

| | Ch8a | Ch8b | Ch8X | Ch9b | Ch11 | Ch12 | Ch12a | Ch14a | Ch14b |
|---|---|---|---|---|---|---|---|---|---|
| $\delta^{17}O$ | 13.999 | 13.881 | 13.840 | 13.949 | 13.683 | 13.297 | 13.568 | 13.462 | 13.625 |
| $\delta^{18}O$ | 26.891 | 26.660 | 26.579 | 26.779 | 26.263 | 25.511 | 26.046 | 25.858 | 26.152 |
| $\Delta'^{17}O$ | 0.109 | 0.106 | 0.105 | 0.101 | 0.097 | 0.092 | 0.100 | 0.107 | 0.098 |

### 5.3.2. Triple oxygen isotope distribution of present chert

The triple oxygen isotope composition of the Rohtas Limestone chert is listed in Table 5.1. The $\delta^{18}O$ and $\delta^{17}O$ range from 26.15 to 26.90‰ (avg. 26.30‰) and 13.30 to 14.00‰ (avg. 13.70‰). The corresponding $\Delta'^{17}O$ varies from -0.098 to -0.109‰ (avg. -0.10). No such 3-O isotope values variation is observed laterally and vertically.

### 5.3.3. Distribution of triple oxygen isotope over geological time

To understand the change of oxygen isotope composition over geological time 3-O isotope data sets have been plotted against geological time ($\delta'^{18}O$ vs. geological time and $\delta'^{17}O$ vs. geological time; Fig. 5.3). Although the exact nature of the change in $\delta^{18}O$ and $\delta^{17}O$ through time is debatable, progressive increase of $\delta^{18}O$ and $\delta^{17}O$ is clear. Trend capture in $\delta^{18}O$ vs. time and $\delta^{17}O$ vs. time also satisfy the equation 1.2.

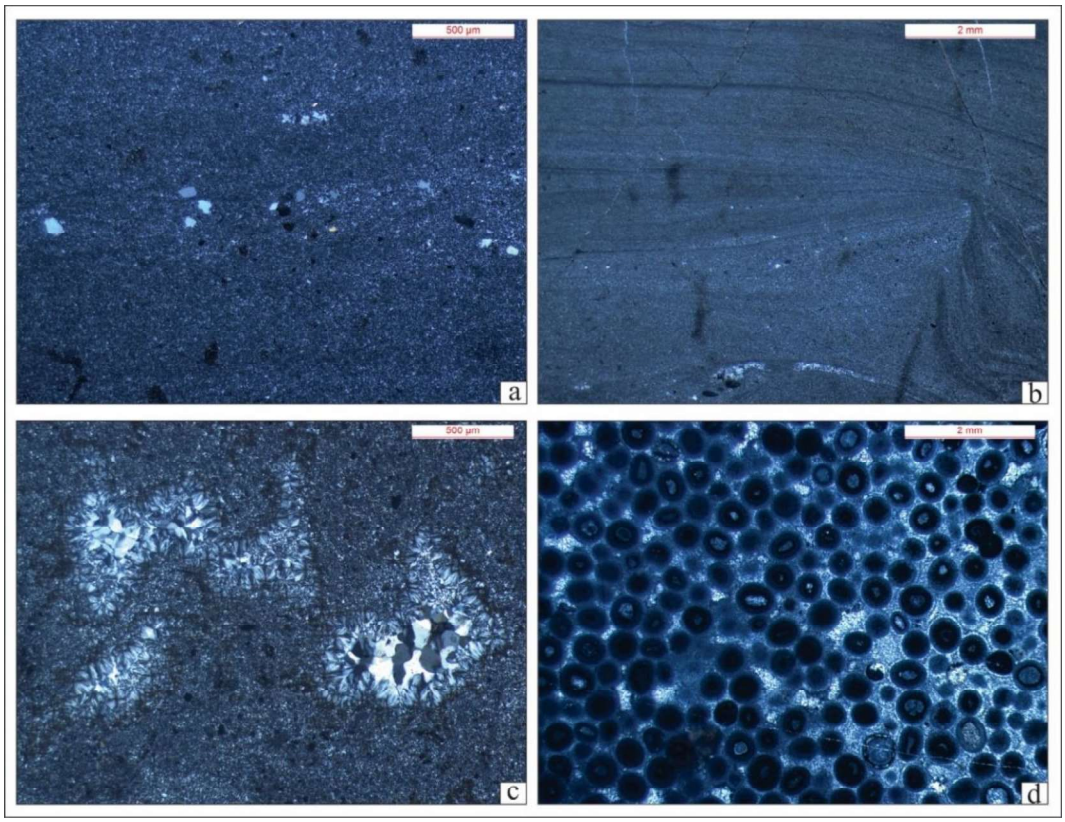


Fig. 5.2. Microscopic photographs of chert: microcrystalline quartz with few detrital quartz (a), partially preserved laminations within microcrystalline quartz field (b), chalcedony and megaquartz growth (c), ooids-peloids pseudomorphs (d).

### 5.3.4. Time barrier on triple oxygen isotope distribution

Although, our measurement in Fig. 5.3 capture increasing trend of $\delta^{18}O$ and $\delta^{17}O$ over time (since Archean to modern) but this diagram unable to capture whether there is any converse field between geological Era. So, we have look through the triple oxygen isotope distribution with geological Era as well Triple oxygen isotope is distributed as follows:

Archean Era: $\delta'^{18}O\approx$ 22. 25 to 13.24‰; $\delta'^{17}O\approx$ 11.60 to 6.90‰ and $\Delta'^{17}O\approx$-0.15‰ to -0.03‰

Proterozoic Era: $\delta'^{18}O\approx$ 32.50 to 13.24‰; $\delta'^{17}O\approx$ 17.01 to 6.89‰ and $\Delta'^{17}O\approx$ -0.19 to -0.06‰

Phanerozoic Era: $\delta'^{18}O\approx$34.08 to 29.94‰; $\delta'^{17}O\approx$ 17.81 to 15.66‰ and $\Delta'^{17}O\approx$ 0.15 to 0.03‰

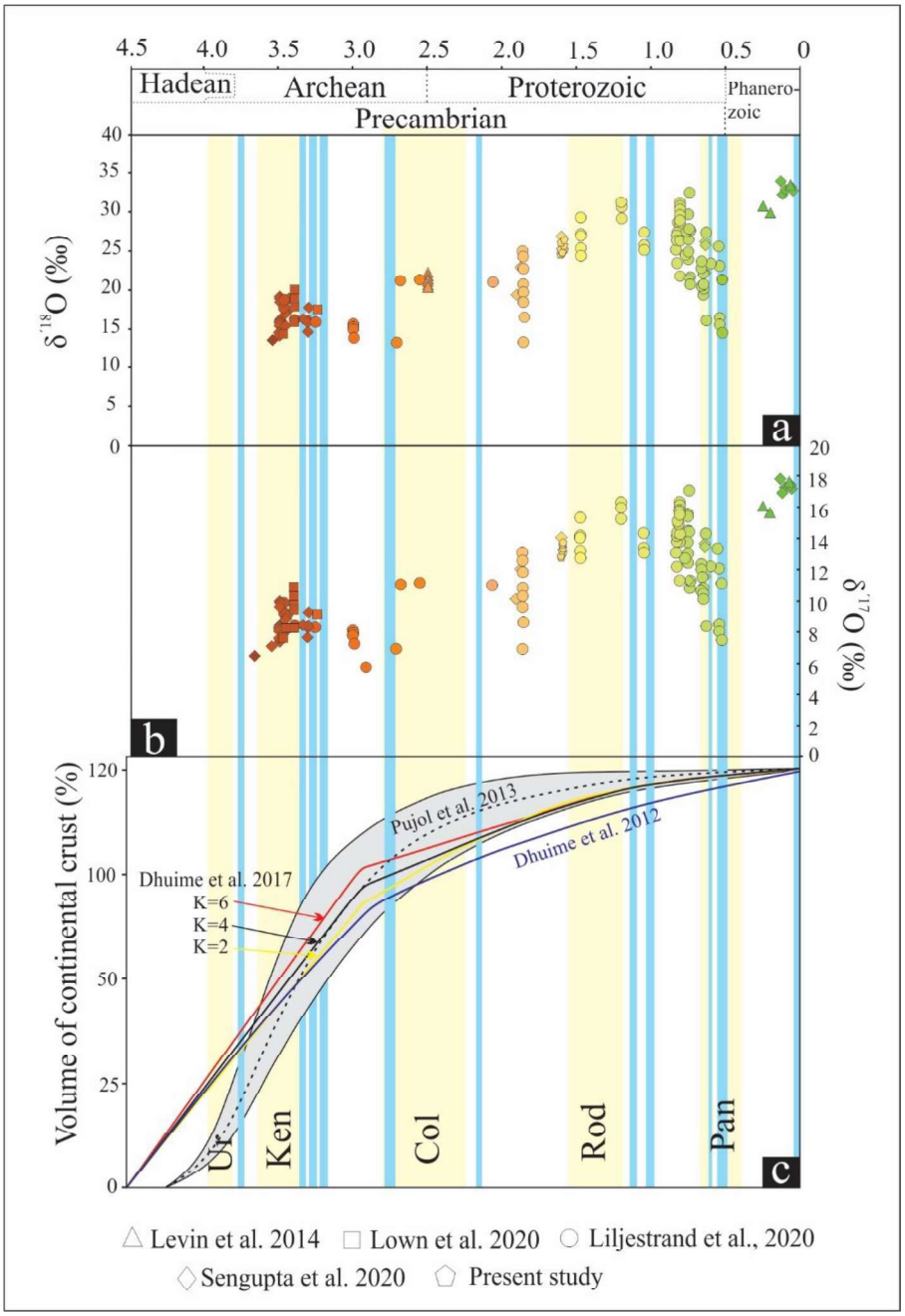


Fig. 5.3. δ'$^{18}$O variation over geological time (a), δ'$^{17}$O variation over geological time (b), Selected crustal growth curves suggesting that 60-80% of the present volume of the continental crust had been generated by 3 Ga, compared with the present day proportions of juvenile continental crust (c; modified after Hawkesworth et al., 2020). Note the glaciation and supercontinent have marked by blue and yellowish colour (modified after Young, 2012).

Time barrier oxygen isotope composition show that both Archean and Proterozoic data sets and Proterozoic and Phanerozoic data sets has convergence zone (Fig. 5.4).

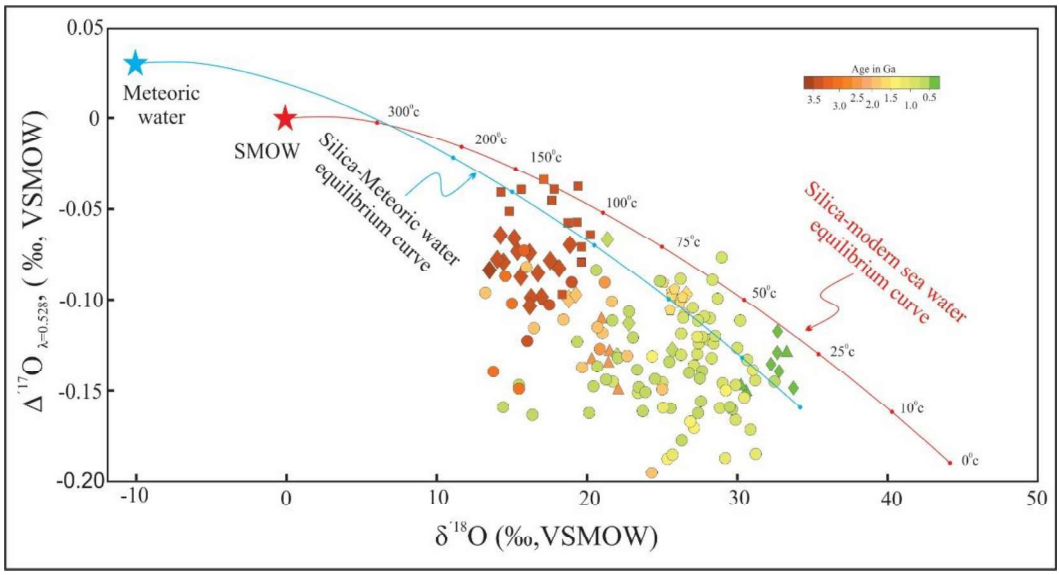


Fig. 5.4. Plot of $\Delta'^{17}O$ vs. $\delta'^{18}O$ over geological time. Red solid line represents silica-sea water equilibrium curve (Sharp et al., 2016). Blue solid line represents silica-meteoric water ($\delta^{18}O \approx -10‰$ and $\Delta'^{17}O \approx 0.03$) equilibrium curve. Note none of triple oxygen data sets are corresponds with SMOW as well as meteoric water.

## 5.4. Discussion

### 5.4.1. Paleokarstified chertification and record of earth surface temperature

Studied chert consists of pseudomorphs of ooids (both radiating and concentric rim preserved alternatively), peloids and intraclasts infer that this chert layer has formed by replacement of carbonate (Kenney and Knauth, 1992). Chertification along the fracture plane of ooids, peloids grains indicate the chertification took place after solidification of rock. Restriction of this chert layer along unconformity surface also explain that chert has formed as paleokarst by dissolution of carbonate (see details in Kenney and Knauth, 1992).

Analyzed triple oxygen data sets of studied chert show that none of these value is equilibrium with silica-modern ocean (Fig. 5.5). Sharp et al. (2016, 2018) also demonstrates silica can also precipitate in equilibrium from meteoric water. The studied chert samples well fit with the silica-meteoric water ($\delta^{18}O \approx -10‰$ and $\Delta'^{17}O \approx 0.03$; Fig. 5.5). The $\delta'^{18}O$ and $\Delta'^{17}O$ trajectory in $\delta'^{18}O$ and $\Delta'^{17}O$ space diagram infer that silica was precipitated around 25ºC. The newly generated data set of our study extrapolates a low temperature system chertification.

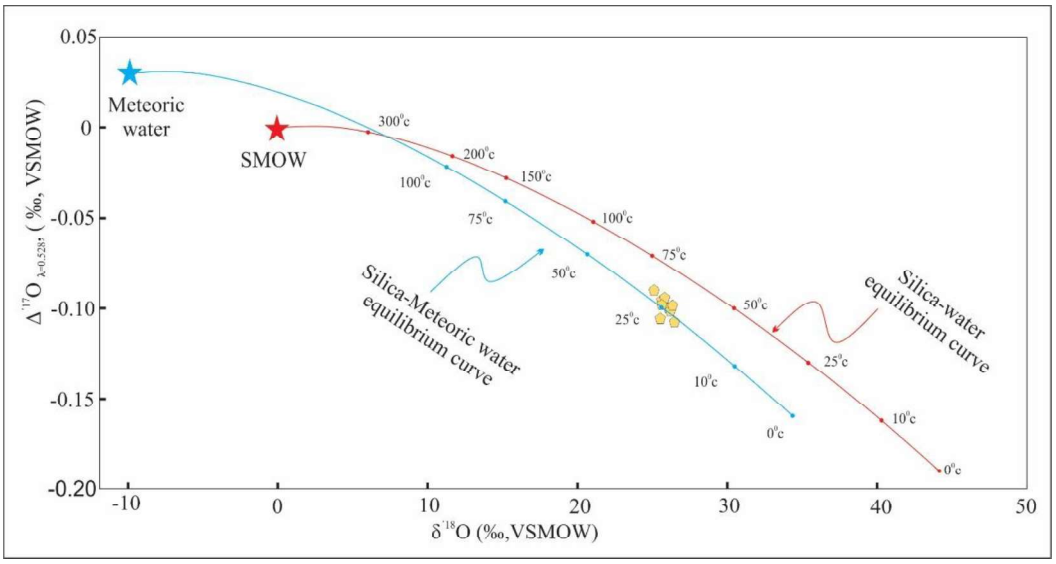


Fig. 5.5. Plot of $\Delta'^{17}O$ vs. $\delta'^{18}O$ for present studied samples. Red solid line represents silica-sea water equilibrium curve (Sharp et al., 2016). Blue solid line represents silica-meteoric water ($\delta^{18}O\approx$-10‰ and $\Delta'^{17}O\approx$+0.03‰) equilibrium curve. Note studied chert is equilibrated with silica- meteoric water ($\delta^{18}O\approx$-10‰ and $\Delta'^{17}O\approx$+0.03‰) equilibrium curve at 25°C temperature.

### 5.4.2. Testify the pre-existing hypothesis in the light of $\Delta'^{17}O$

As calculated in earlier section studied chert was precipitated at around ~25°C in equilibrium with water (meteoric water; $\delta^{18}O\approx$-10‰ and $\Delta'^{17}O\approx$0.03). Even though silica precipitation from low $\delta^{18}O$ hot seawater has proposed so far, its evolution to modern ocean in assumption of flux was different in deep time and alternation of primary record is still required to explanation. Collective data sets from earlier works and present data sets has verified earlier hypothesis.

#### 5.4.2.1. A warm primitive sea cool to low temperature ocean

This hypothesis explain that ancient ocean had similar $\delta^{18}O$ and $\Delta'^{17}O$ as modern ice-free ocean and ocean temperature much higher than present (Sengupta et al., 2020; Lown et al., 2020). Triple oxygen isotope value, a function of temperature equilibrium $SiO_2$-$H_2O$ fraction curve moves downward (Sharp et al., 2016) in corresponding to the ice free ocean ($\delta^{18}O\approx$ -1.2‰, $\Delta'^{17}O\approx$ -0.005‰; Sengupta and Pack, 2018; Zakharov et al., 2019). In this circumstances, $\delta^{18}O$ value corresponds to the hot Precambrian ocean (180°C to 120°C for Archean; 80°C to 125°C for Proterozoic and 38°C for Phanerozoic; Sengupta and Pack, 2018; Liljestrand et al., 2020; Sengupta et al., 2020). Measured triple oxygen of 3.4 Ga Bartson Greenstone Belt samples (Lowe et al., 2020) equilibrate $\delta^{18}O\approx$ -1‰ $SiO_2$-$H_2O$ curve and estimate silica precipitation ocean temperature ~120°C. Recently,

McGunnigle et al. (2022) suggest ocean temperature in Archean ranges from 77ºC to 100ºC. Temperature calculation from Si isotope estimates >70ºC as well (Robert and Chaussidon, 2006) and gradually evolve to modern climate with decreasing of temperature.

The classical argument for constant $\delta^{18}O$ of the ocean is derived from the almost constant $\delta^{18}O$ value of oceanic crust through time (Gregory, 2003), but the "faint young sun" can't corroborate with early hot ocean (Herwartz et al., 2021). $\Delta'^{17}O$, a unique measurement in triple oxygen isotope also don't corresponds to the $SiO_2$-$H_2O$ (modern ocean) equilibrium curve (Fig. 5.4). In this puzzle, Herwartz et al. (2021) propose intense carbonization and silica precipitation at high $pCO_2$ atmosphere led Archean ocean (specifically >3 Ga) lower $\delta^{18}O$ without effecting $\Delta'^{17}O$ and temperature recorded from chert are overestimation. Greenhouse at high $pCO_2$ balance the low luminosity of the faint young sun and higher temperature in place of frozen earth (Kasting, 1987; Lown and Tice, 2004; Feulner, 2012). Segduction tectonics, less continents, high thermal gradient and effective $CO_2$ corroborates with Archean climate and slightly modified ocean composition.

Proterozoic ocean has assumed like modern ocean with decreasing of intensity of carbonization and silica precipitation around ~3 Ga, modern plate tectonic style, thick continental crust (Herwartz et al., 2021). Combining data sets of Proterozoic triple oxygen isotope show similar value as Archean and offsets from $SiO_2$-$H_2O$ fraction curve (Fig. 5.4). In consequence of offsets 3-O isotope data from silica-modern ocean system, we support the variable ocean composition for different period of geological time, may be not that much hot as estimated earlier.

Phanerozoic chert, slightly reflected from the modern ocean-silica equilibrium curve also confuse to estimate the paleotemperature (Fig. 5.4). It's least offset of $\Delta'^{17}O$ infer that silica dissolution and reprecipitation in influence of fresh water (Knauth, 1979; Sengupta et al., 2020). Composition of mixed water is $\delta^{18}O \approx -3‰$, $\Delta'^{17}O \approx +0.01‰$ (blue star in Fig. 5.6), a common process of chert nodule extrapolate that these chert was precipitated at 20ºC to 30ºC, $F/R \approx 3/2$ (Fig. 5.6; Sengupta et al., 2020). It is very less convincing whether temperature has decreased from Archean to recent!

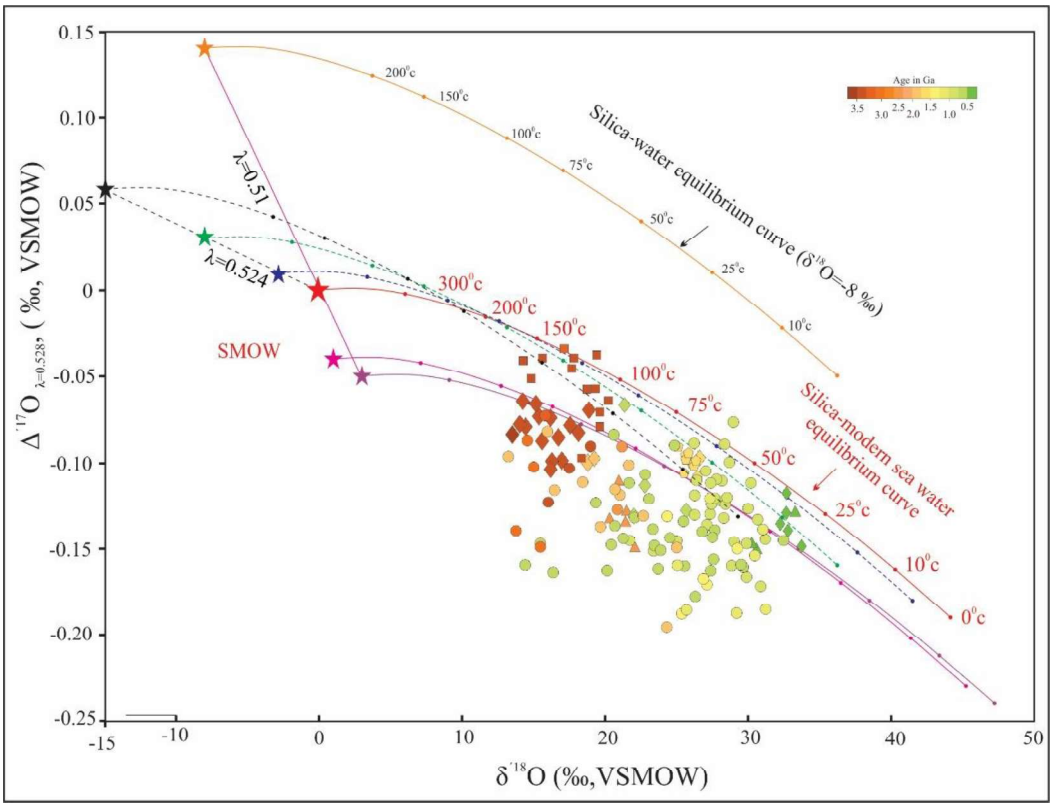


Fig. 5.6. Various sea-water composition from where chert has precipitated in past. Triple oxygen isotope data sets are not equilibrated with low δ'$^{18}$O Archean ocean (orange star), δ$^{18}$O and δ$^{17}$O of sea-water response at the trend λ=0.51 (modified after Sengupta and Pack, 2018; orange solid line). A possible high temperature alternation (may be hydrothermal activity) of modern high δ$^{18}$O ocean (magenta and purple star) during Precambrian. Composition of chert forming fluid is δ$^{18}$O≈+3‰ with λ≈0.51 (Johnson and Wing, 2020; purple dotted line) and, δ$^{18}$O≈+1‰ with λ≈ 0.521 (Sengupta et al., 2020; Zakharov et al., 2021; magenta dotted line) respectively. Another possible explanation for low δ$^{18}$O Precambrian ocean is low temperature alternation. Chert precipitating water composition has modified at alternation rate of 0.524 and proposed δ$^{18}$O≈-15‰ for Archean (black star; black dotted line) and δ$^{18}$O≈-8‰ for Proterozoic (green star; green dotted line) respectively (Liljestrand et al., 2020). Meteoric water influence triple oxygen isotope modification of Phanerozoic data sets (Sengupta et al., 2020; blue star; blue dotted line).

### 5.4.2.2. Evolution of seawater composition over geological time from low δ$^{18}$O early ocean

As discussed above, 3-O isotope of chert is an overestimation in equilibrium of silica-modern ocean system, so another assumption has made that ocean composition is evolving since Archean where chert register the compositional change. The reflection of δ$^{18}$O in chert is the secular variation of ocean composition (Perry, 1967; Wallmann, 2001; Kasting et al., 2006; Galili et al., 2019; Vérard and Veizer, 2019) in influence of $F_{HT}$, $F_{LT}$, $F_{CW}$, $F_{CG}$ and $F_{MR}$ (Sengupta and Pack, 2018; Hayles et al., 2019; Sengupta et al., 2020; Wostbrock and Sharp, 2021; Zakharov et al., 2021; Herwartz et al., 2021; McGunnigle et al., 2022). The change of δ$^{18}$O and Δ′$^{17}$O of seawater is mainly govern by $F_{CW}$, and $F_{HT}$ during sea floor spreading (Muehlenbachs and Clayton, 1976; Muehlenbachs, 1998;

Sengupta and Pack, 2018; Sengupta et al., 2020; McGunnigle et al., 2022). At high temperature, $\delta^{18}O$ and $\Delta'^{17}O$ of seawater modify its value to higher $\delta^{18}O$ and lower $\Delta'^{17}O$ in interaction with mid oceanic ridge and deep oceanic crustal rocks (Sengupta and Pack, 2018; Johnson and Wing, 2020; Zakharov et al., 2021; McGunnigle et al., 2022). At low temperature, this exchange is related to weathering of continental crust and upper oceanic crusts (Sengupta and Pack, 2018; Liljestrand et al., 2020; Zakharov et al., 2021; McGunnigle et al., 2022).

In the contribution of oxygen isotope of $F_{HT}$, $F_{LT}$, $F_{CW}$, $F_{CG}$ and $F_{MR}$; Sengupta et al. (2018) modelled the change of ocean composition changes at alternation rate of $\lambda \approx 0.51$ (Fig. 5.7). This model reconstructs that how ocean composition changeed at a fixed temperature (Fig. 5.7; see details in Sengupta et al., 2018; Wostbrock and Sharp, 2021). Sengupta et al. (2018) proposed $\delta^{18}O \approx -8‰$ for Archean ocean in influence of $F_{HT}$ hydrothermal substrates. But later on that Johnson and Wing (2020), Sengupta et al. (2020), Zakharov et al. (2021) show due to less abundance of continental crust sea water composition shift towards higher $\delta^{18}O$ along $\lambda \approx 0.51$ (Fig. 5.6, 5.7). Johnson and Wing (2020) suggest $\delta^{18}O \approx +3‰$ with $\lambda \approx 0.51$ (purple star in Fig. 5.6) and triple oxygen data distribution suggest ~175°C to 85°C temperature for Archean and ~150°C to 50°C temperature for Proterozoic Ocean. Sengupta et al. (2020) and Zakharov et al. (2021) proposed modified $\lambda$ value of 0.521, $\delta^{18}O \approx +1‰$ (orange star in Fig. 5.6) and suggest silica precipitation at ~250°C to 75°C for Archean and ~220°C to 50°C for Proterozoic. McGunnigle et al. (2022) suggest around 100°C ocean temperature for $SiO_2$-$H_2O$ equilibrium system. Collective 3-O isotope data sets don't synchronize altogather with this modified ocean (Fig. 5.6), and so question remain at same point, how much different was ancient ocean? Is it a special or temporal variation?

In another assumption, Liljestrand et al. (2020) more concentrated on $F_{LT}$, $F_{CW}$. They suggest $\lambda$ value of 0.524 for low temperature seafloor alternation and show evolution of modern ocean from low $\delta^{18}O$ Archean ocean (Fig. 5.6). In order of this sea water composition has assumed $\delta^{18}O \approx -15‰$ (black star at Fig. 5.6) for Archean and $\delta^{18}O \approx -8‰$ (green star in Fig. 5.6) for Proterozoic at $\lambda \sim 0.524$. Silica and this highly negative $\delta^{18}O$ ocean equilibrium system estimate that temperature of ocean during Archean and Proterozoic was around 30°C with maximum value of 50°C (Fig. 5.6).

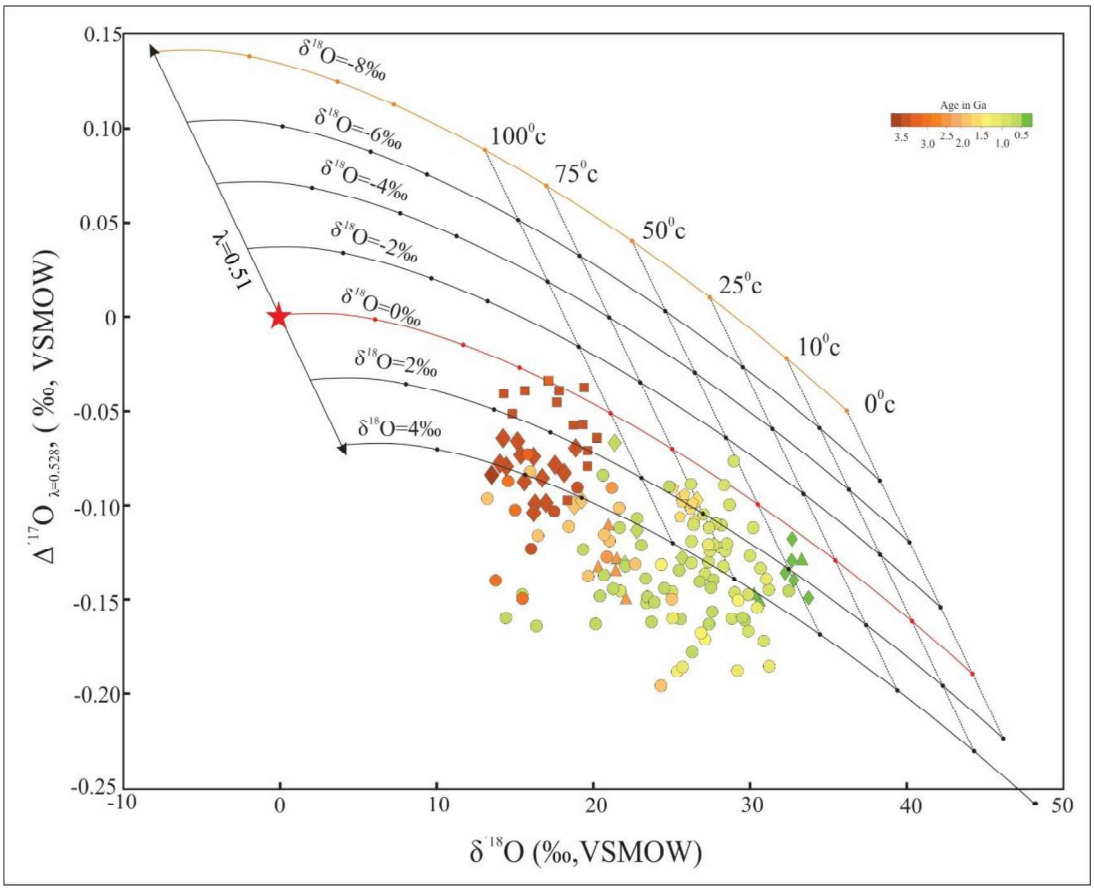


Fig. 5.7. $\Delta'^{17}O$ vs. $\delta'^{18}O$ diagram of changing sea-water composition (modified after Sengupta and Pack, 2018; Wostbrock and Sharp, 2021). Sea-water composition is changing at $\lambda$=0.51 with high to low temperature alternation rate (Sengupta and Pack, 2018). Note, for similar temperature triple oxygen isotope of chert increase $\Delta^{17}O$ with decreasing of $\delta^{18}O$ than modern ocean. For similar temperature triple oxygen isotope of chert decrease $\Delta^{17}O$ with increasing of $\delta^{18}O$ than modern ocean.

Although, $F_{HT}$ influence corroborates with high hydrothermal activity, high geothermal gradient and less continent crust-less weathering (Bindeman et al., 2018; Sengupta et al., 2020; Johnson and Wing, 2020; Zakharov et al., 2021), but Hawkesworth et al. (2019, 2020) clearly shows almost similar volume of continental crust as today since 3.0 Ga (Fig. 5.3). Therefore, it is questionable whether $F_{HT}$ was everywhere or restricted in special distribution. Thereafter, $F_{LT}$, $F_{CW}$ best fit with ocean composition evolution (Fig. 5.6). Less continent during 4.5 to 3.0 Ga can't satisfy the very low $\delta^{18}O$ ocean during that time (Fig. 5.6). Although, recently Herwartz et al. (2021) has great proposal that high $pCO_2$ during that time shift negative $\delta^{18}O$ without effecting $\Delta'^{17}O$. Besides this, $F_{LT}$, $F_{CW}$ has no such variation on 3-O isotope distribution during supercontinent formation and glaciation events (Fig. 5.3). In the relevance of high rate of weathering during supercontinent and low rate of weathering during glaciation, it is not unreasonable to point out that maximum effect

of low temperate continental weathering is observed during glaciation. But, ocean composition recorded so far does not coincide with geological phenomena. We agree with Liljestrand et al. (2020) and conclude that a single equilibrium process will not capture the geological record of any specific Eon. It is more worth to find out the reason of $\Delta'^{17}O$ deflection in the silica-water equilibrium space diagram of $\delta^{18}O$ and $\Delta'^{17}O$.

### 5.4.2.3. Alternation of primary 3-O isotope

Whereas previous hypothesis explains the 3-O isotope of chert is a reflection of ocean composition, but offsets of triple oxygen isotope record in $\delta^{18}O$ and $\Delta'^{17}O$ trajectory put forward to model an alternation hypothesis of reproduction of primary signal. In depict of this, diagenetic modification of primary record has proposed (Sengupta and Pack, 2018; Hayles et al., 2019; Liljestrand et al., 2020; Sengupta et al., 2020; Zakharov et al., 2021; Wostbrock and Sharp, 2021; McGunnigle et al., 2022). Diagenetic modification is controlled by temperature of fluid, oxygen composition of fluid and degree of alternation (fluid: rock ratio) (Sengupta and Pack, 2018; Hayles et al., 2019; Liljestrand et al., 2020; Wostbrock and Sharp, 2021). In focus of lower $\delta^{18}O$ and higher $\Delta'^{17}O$ change, we have mainly concentrated on low temperature diagenesis as low temperature diagenesis/ metamorphism simply re-equilibrate oxygen isotope with carbonate, iron mineral and clay mineral.

The effect of diagenetic modification is calculated from initial rock and water composition with simple mass-balance equation (Sengupta and Pack, 2018; Hayles et al., 2019; Sengupta et al., 2020; Wostbrock and Sharp, 2021; McGunnigle et al., 2022). A primary fluid of meteoric water ($\delta^{18}O \approx -10‰$ and $\Delta'^{17}O \approx +0.03‰$) has assumed as diagenetic fluid (Fig. 5.8). The bulk composition of system is calculated by a numbers of calculation (see details in Sengupta and Pack, 2018; Sengupta et al., 2020; Wostbrock and Sharp, 2021) and final composition is expressed by (Wostbrock and Sharp, 2021):

$$\delta^{x}O_{\text{rock final}} = \frac{1000X+\alpha(X.\delta^{x}O_{\text{rock initial}}-X.\delta^{x}O_{\text{water initial}}-\delta^{x}O_{\text{rock initial}}-1000X)}{\alpha X-\alpha-X} \quad \text{----equation 5.1}$$

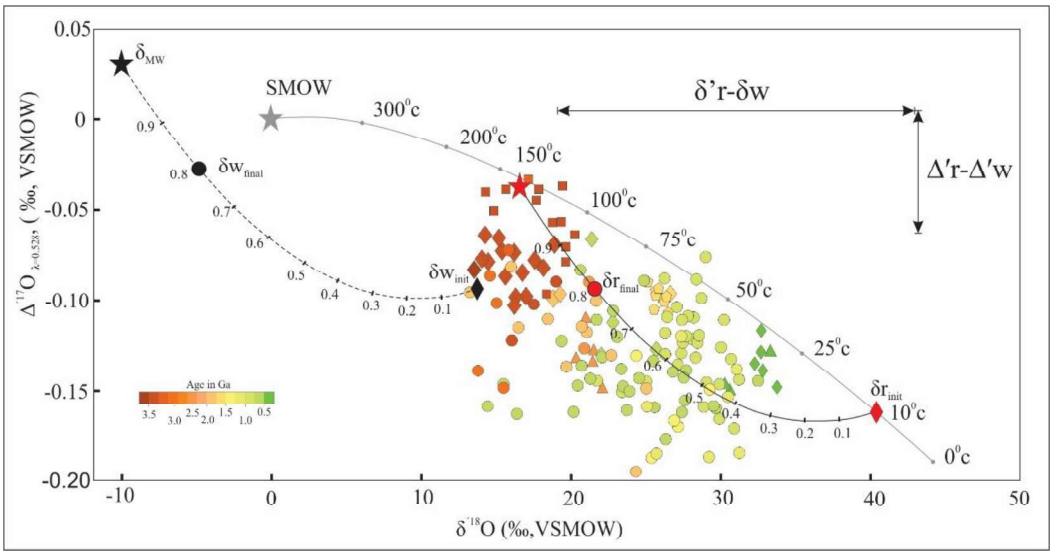


Fig. 5.8. Alternation trajectory of triple oxygen isotope in $\Delta'^{17}O$-$\delta'^{18}O$ space diagram (modified after Wostbrock and Sharp, 2021). The chert precipitated at certain triple oxygen isotope value ($\delta r_{init}$) moves along solid curve with increasing of fluid/rock (F/R). The infiltrating fluid has a composition at $\delta_{MW}$ (black star), equilibrates with rock and has a composition $\delta w_{init}$ (black romb). The re-equilibrated water follows the dotted curved path from $\delta w_{init}$ towards lower $\delta^{18}O$ and higher $\Delta'^{17}O$ values as the F/R ratio increases. The final rock and water compositions in this example correspond to an *X*water value of 0.8, resulting in the $dw_{final}$ (black circle) and $dr_{final}$ (red circle) The equilibrium oxygen isotope fractionations at 100ºC are shown by the doubled arrow lines.

A typical pathway 100ºC temperature diagenetic water ($\delta^{18}O \approx -10‰$ and $\Delta'^{17}O \approx +0.03‰$) trajectory (Fig. 5.8) show that if a chert was initially precipitated at 10ºC temperature ($\delta^{18}O \approx -40.3‰$ and $\Delta'^{17}O \approx -0.16‰$) with silica-modern ocean equilibrium and after diagenetic alternation at degree of alternation rate (F/R) ~0.8, rock composition shifts to $\delta^{18}O \approx 21.5‰$ and $\Delta'^{17}O \approx -0.095‰$. The final composition shifts to low $\delta^{18}O$ and high $\Delta'^{17}O$ composition (Fig. 5.8). With the variable concentration of fluid, compositional of final rock vary (Fig. 5.8; the black solid and dotted curve). Although oxygen isotope composition is equal to that meteoric water for Fig. 5.8, but meteoric water composition and its temperature also may vary. With the change of this diagenetic fluid composition and temperature alternation pathway also changes (Wostbrock and Sharp, 2021; McGunnigle et al., 2022). In compresence of this, we have assumed fluid temperature from 30ºC (blue line), 50ºC (green line) and 100ºC (orange line) and their composition vary from $\delta^{18}O \approx -10‰$ (solid line) to -6‰ (dotted line) (Fig. 5.9). The $\delta'^{18}O$ vs. $\Delta'^{17}O$ diagram show that all of the triple oxygen composition of ancient chert are the resultant of variable F/R ratio, fluid composition $\delta^{18}O \approx -10‰$ to -6‰ (Fig. 5.9). This diagenetic alternation also show that initial silica was precipitated from modern sea water composition range from 30ºC to 8ºC (Fig. 5.9). Archean records are result of high to moderate F/R ratio and initially these chert was precipitated at temperature maximum temperature of 30ºC. Proterozoic

chert was initially precipitated 20ºC, lower temperature than 30ºC (Fig. 5.9), while Phanerozoic chert was precipitated around 10ºC (Fig. 5.9).

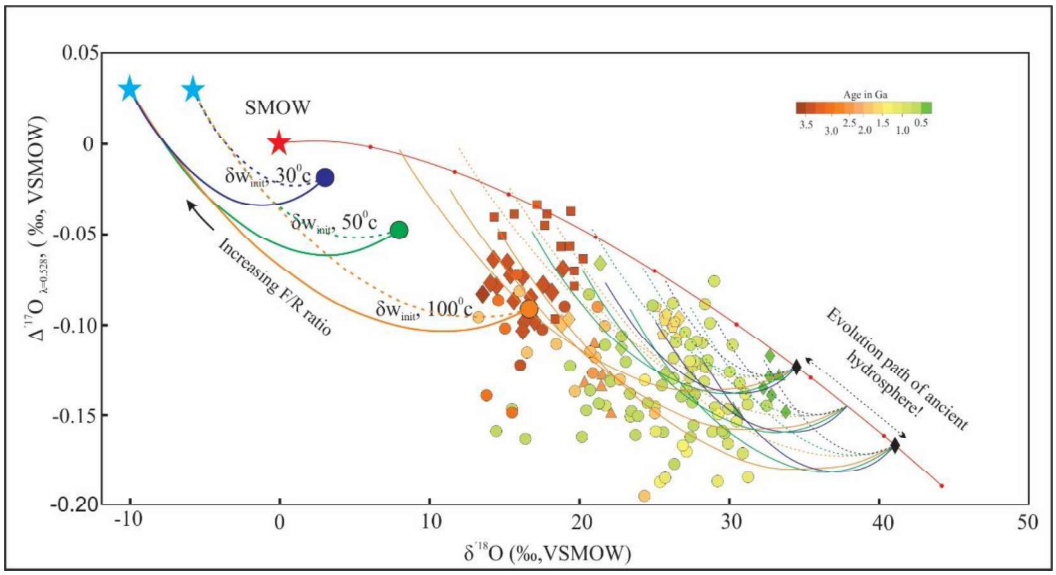


Fig. 5.9. Alteration trajectories for a rock starting with a $\delta'^{18}O$-$\Delta'^{17}O$ of $dr_{init}$. Dashed and solid lines are for interaction with an infiltrating meteoric water ($\delta_{MW}$) with $\delta'^{18}O$ values of -10‰ and -6‰, respectively and $\Delta'^{17}O$ values of 0.03‰. The rock trajectories are thick curves; fluids are thin curves. Temperature of fluid is 100ºC (orange), 50ºC (green) and 30ºC (blue) respectively. The rock trajectory starts from circle and rock trajectory from diamond. Possibly ancient sea-water composition was around 30ºC to 8ºC temperature equilibrated triple oxygen isotope (marked by black dotted line on silica-SMOW equilibrated line).

### 5.4.3. Understanding of the triple oxygen isotope distribution over time

Although, any one of three principle hypothesis can't solely extrapolate ancient temperature and ocean composition, but among these diagenetic alternation provides most satisfactory answer to explain all the data sets registered so far. Diagenesis alternation support the pioneer works that ancient ocean was not so much hot (Fig. 5.8, 5.9; Sengupta and Pack, 2018; Liljestrand et al., 2020; Wostbrock and Sharp, 2021). Present calculation estimates that ocean temperature was ranging from 30ºC to 8ºC over space and time. This diagenetic change provides an uncertainty to predict the ancient climate and ocean composition as isotopic change can proceed in early phase (i.e. during or soon after deposition) or late phase (i.e. after lithification). It's on question mark whether is our evaluation of ancient ocean temperature and composition acceptable or overestimated? Although, Herwartz et al. (2021) established overestimation of temperature and proposed 3-O isotopes are result of $F_{CO2+H2O}$, but timing of silicification, source of silica, pH of fluid and temperature of silica bearing fluid after 3.0 Ga stands on wild assumption.

Almost similar 3-O isotope value of silica saturated hydrothermal vent fluid and ancient chert (Shanks, 2001; DeRonde et al., 1997; Farber et al., 2015; Zakharov and Bindeman 2019; Zakharov et al. 2019b; Zakharov et al., 2021; McGunnigle et al., 2022) sort out the source of silica. Estimated chert formation fluid temperature around ~180ºC-190ºC (Hardardottir, 2011; Zarkhov and Bidemann, 2019; Zakharov et al., 2021) solve silica bearing fluid temperature. Formation of bedded chert in alternating band of BIF (banded iron formation) by influenced of warm/hot bottom brines or hydrothermal fluid also support the context (Liljestrand et al., 2020; Sengupta et al., 2020; Zakharov et al., 2021; Herwartz et al. 2021). Spatial and temporal restriction of these silica source and heat source of hydrothermal activity question, are these temperatures calculated from 3-O isotope useful for throughout globe or an overestimation? Although one can conclude that temperature estimation from these 3-O isotopes in deep time is an overestimation as Herwartz et al. (2021) suggested, but there is a gap in knowledge.

Dring the present study a model has been proposed which inidicates that initially a carbonate rock was deposited on sea floor and later with interaction of hot silica rich fluid/ meteoric water and host carbonate replaced by silica precipitation. Although, Wostbrock and Sharp (2021) explains silica precipitation in a carbonate hosted rock by its replacement (see Fig. 19 in Wostbrock and Sharp, 2021), but they were restricted at a low temperature fluid. Whereas Mishra (2012) proposes that to form a chert layer solubility of silica in fluid will be much higher than normal fluid, and to carry so temperature of fluid must be high. Though chert precipitation is guided by a number of factors, but during the present study a range of silica rich fluid of 35ºC to 300ºC hot water has considered for replacing the lithified carbonate rock at different (0-1) F/R ratio (Fig. 5.10). One can argue regreading influence of 300ºC temperature, but theoretical and experimental study shows that 300ºC temperature is the maximum temperature of diagenesis (Tucker, 1983) and critical point of water where liquid phase still exists (Phillpotts and Ague, 2009). The quartz recrystallization in metamorphic process at ~300ºC in Mendon and Dresser Formations also support the present view (Marin-Carbonne et al., 2011; Zarkov et al., 2021).

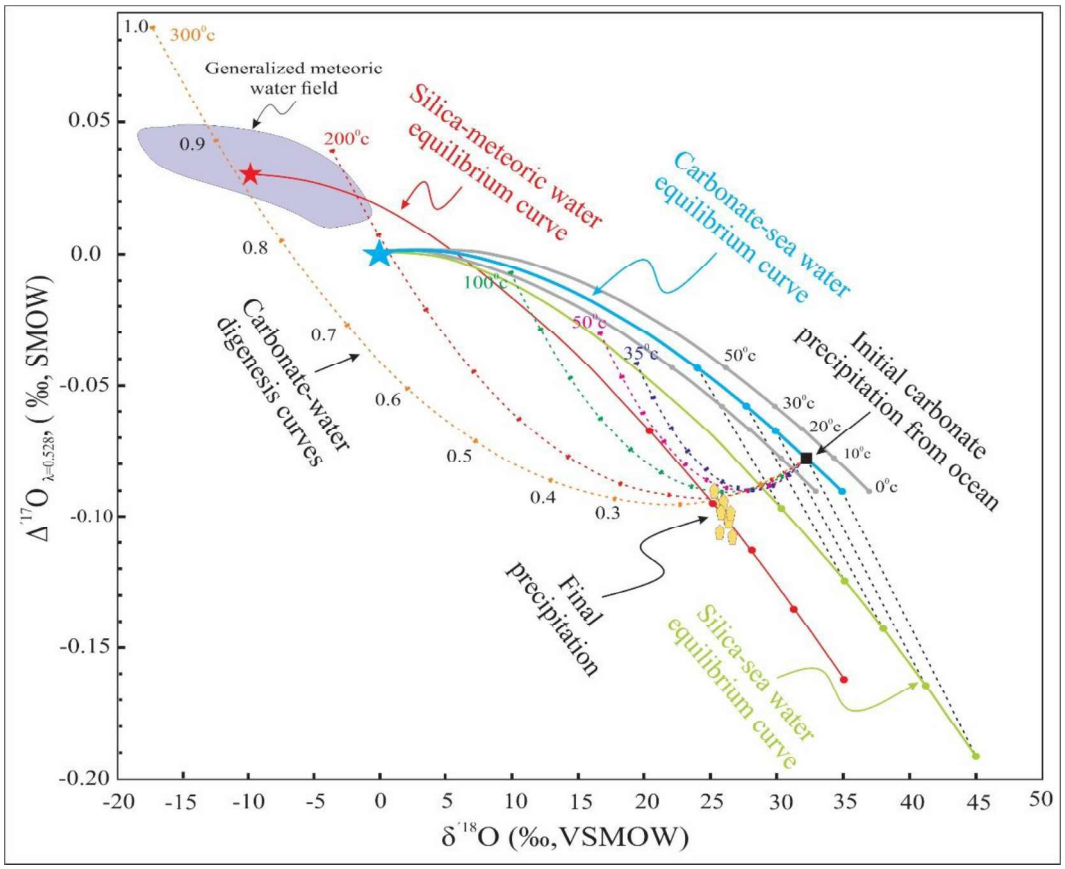


Fig. 5.10. Possible reaction sequence to explain the triple oxygen isotope value of carbonate hosted chert from the triple oxygen isotope data of present study. Carbonate was initially precipitating at 10ºC temperature with equilibrium of SMOW (black diamond). 300ºC hot silica rich pore fluid buffered the carbonate rock following the orange dotted line at orange diamond point. This fluid cooled and precipitated quartz at 25ºC, in equilibrium of silica-fluid composition ($\delta^{18}O \approx -10‰$ and $\Delta'^{17}O \approx +0.03‰$; red solid line). Possible ancient triple oxygen isotopes are result of a long range temperature fluid (35ºC to 300ºC) interaction with initial sedimentary rock (may be carbonate, shale, iron minerals, phosphates) at different F/R ratio. May be true ocean temperature was like present day i.e. modern ocean.

Propose model suggests that an ooidal carbonate rock was deposited at around 10ºC temperature ocean (Fig. 5.10). As soon as the carbonate rock was subaerially exposed, reacting with meteoric water started to dissolve the carbonate. With time meteoric water percolating through porosity-fractures of surrounding rocks, and collecting silica. In the process, oxygen isotope is also exchanging with these rock and modified oxygen isotope to low $\delta^{18}O$ and high $\Delta'^{17}O$ (Sengupta and Pack, 2018; Liljestrand et al., 2020; Sengupta et al., 2020; Wostbrock and Sharp, 2021; McGunnigle et al., 2022). Continuous processes produce siliceous fluid equilibrium with $\delta'^{18}O \approx -10‰$ and $\Delta'^{17}O \approx +0.03‰$, and increasing of depth and temperature of fluid may reach around 300ºC at burial heat and pressure. Continuous buffering dissolves carbonate and precipitate silica as chert. Decreasing of fluid temperature is an important criterion to precipitate silica, so this siliceous fluid must have come to surface or near the surface. Therefore, precipitation temperature of fluid must have

equilibrated with earth surface at around 25ºC. Though for the present silica was equilibrated with $\delta'^{18}O \approx -10‰$ and $\Delta'^{17}O \approx +0.03‰$ in the continental weathering (i.e. collection of silica) and 300ºC is burial temperature, but the fluid composition varies depending on the rock type from where silica is collecting. The temperature of fluid also varies with depth and hydrothermal activity.

In contrast of this scenario, we infer that low $\delta^{18}O$ records of Precambrian chert are the result of low to high fluid-rock interaction with hot silica rich fluid, replacing shale, sandstone, carbonate, iron mineral initially depositing in sea floor. Maximum temperature of ancient earth was around $30^0$c (Liljestrand et al., 2020; Sengupta et al., 2020) and most of the 3-O isotope records are an overestimation (Herwartz et al., 2021). Precambrian ocean might have slightly different from modern ocean in terms of temperature and composition. These variations of temperature and ocean composition are possibly because of variable the source of silica and temperature of silica bearing fluid. More advance study is required on how a meteoric water carrying high amount silica, source of silica, pathway of silica rich fluid follows, relation with pH-temperature-pressure to dissolve silica in fluid. This may simplify our understanding of regrading ancient climate and environment.

**5.5. Conclusion**

The triple oxygen isotope of chert demonstrates more precise information about paleoclimate compare to $\delta^{18}O$ alone. Compilation of triple oxygen of chert over time attributes low $\delta^{18}O$ and $\delta^{17}O$ to high $\delta^{18}O$ and $\delta^{17}O$ evolution from Archean to recent, but interpretation of this record is debatable. It is unreasonable to interpreat ancient chertification was in equilibrium with modern sea. The triple oxygen data sets may be the result of high temperature-low temperature alternation, diagenetic modification or replacement of earlier rock by meteoric water/ high temperature fluid.

Diagenetic alteration by variable fluid composition of different temperature dependent best fit curve with 3-O of chert over time, but it is not reseasonal that elevated seawater temperature of Archean and/ or Proterozoic cherts are result of high temperature alternation in presence of high hydrothermal flux. Present study only interpreat that ocean water composition may have evolved but there is no such fixed path, which can trace by $\lambda$ (alternation rate) of silica-water equilibrium curvature.

Present study suggests that earth surface during Mesoproterozoic (~1.6 Ga) was around 25ºC, and supported the views of Herwartz et al. (2021) that derivation of the then

paleotemperature from 3-O isotope data sets are an overestimation. Maximum temperature may reach upto 30$^{o}$C and ocean composition was frequently interrupted by silica source (continental weathering, hydrothermal activity). To draw a concrete conclusion regrading the ocan composition of past and modern days we have to concentrate more on chertification process and 3-O isotope in a single frame.

# CHAPTER 6

# Silicification of Carbonate bed in Mesoproterozoic Vindhyan basin, India: A revised model for the origin of chert in carbonate deposition and estimation of temperature

## 6. 1. Introduction

The structural, texture, and the chemical and isotopic composition of chert provide invaluable clues about the physicochemical conditions of the depositional and diagenesis environment of a sedimentary rock sequence in which the chertification go on. Furthermore, chemical and stable isotopic composition of the chert serves as a proxy to reconstruct the past climate (Robert and Chaussidon, 2006; Pack and Herwatz, 2014, 2015; Sharp et al., 2016, 2018; Knauth and Lowe, 1978, 2003).

Although records of the chemically precipitated silica, commonly in the form of chert, in the marine succession have been recorded from the Archean to recent time, the distribution of chert shows a non-uniform distribution (Maliva et al., 2005). A number of models have proposed on the origin of chert. Some important mechanism includes (a) direct precipitation from seawater (Gao and Land, 1991; Murray et al., 1992; Lawrence, 1993), (b) hydrothermal fluid (Jacobsen and Pimentel-Kolse, 1988a, 1988b; Derry and Jacobsen, 1990; Klein and Beukes, 1992), (c) biogenic silica (Knauth, 1979; Malavi et al., 1989; Kidder and Erwin, 2001; Kidder and Munna, 2003), (d) replacement of carbonate (Knauth, 1979; Hesse, 1989; Kenny and Knauth, 1992; Knauth 1994). It is commonly invoked that the silica required for the chert formation during the Phanerozoic were derived from dissolution of diatom, radiolarian, and siliceous sponge (Knauth, 1979; Malavi et al., 1989; Matyszkiewicz, 1989, 1996; Tréguer et al., 1995; Kidder and Erwin, 2001; Tréguer and Rocha, 2013; Kidder and Munna, 2003), but non-/ sparse availability of such silica secreting organism in the Precambrian (Rigby, 1991; Racki and Cordey, 2000; Falkowski et al., 2004) require alternative source of silica. Two major hypothesis for the source of silica are proposed for the Precambrian chert. These are - (a) direct precipitation from seawater (Rasmussen et al., 2019) and (b) precipitation from the hydrothermal fluid (Hofmann and Harris, 2008; Shen et al., 2018). Recently triple oxygen isotope of Precambrian chert also support hydrothermal fluid influence chert formation (Sharp et al., 2016, 2018; Sengupta and Pack, 2018; Bindeman et al., 2018; Hayles et al., 2018; Liljestrand et al., 2020; Sengupta et al., 2020; Lown et al., 2020; Miller et al., 2020; Miller and Pack, 2021; Wostbrock and Sharp, 2021; Zakharov et al., 2021). Even triple oxygen

(3-O) isotope in bedded chert formation in alternative layer of banded iron formation (BIF) also support the context (Gregory, 2003; Knauth, 2005; Liljestrand et al., 2020; Sengupta et al., 2020; Zakharov et al., 2021). Low $\delta^{18}O$ ocean and elevated ocean temperature calculated from 3-O isotope, has alternatively explained as an isotopic exchange between iron phase (low $\delta^{18}O_{FeOx}$) and silica phase (high $\delta^{18}O_{silica}$) (Levin et al., 2014). But there is a gap in knowledge how can we estimate true ancient temperature and ocean composite from these 3-O isotope data sets.

Chert commonly replaces marine carbonates, limestone and dolostone, typically occurs as (a) nodules form and (b) laterally continuous beds (for several tens of meters) and/ or layer in limestone and dolomites (Maliva et al., 2005). This replacement has explained by replacement of carbonate by silica rich water that was supersaturated with $SiO_2$ during diagenesis (Knauth, 1979; Kenny and Knauth, 1992). It is commonly presumed that the mixing of meteoric-marine system, silica supersaturated diagenetic fluid dissolve the carbonate and precipitate silica (Banks, 1970; Knauth, 1979). Dissolution of siliceous organism and mix up with interstitial fluid produce silica supersaturated fluid.

Inspite of large volume of publications many aspect of the genesis of chert by replacement earlier sediment remain unanswered. These include - (a) source of large silica that are required for the large scale chertification of carbonate as solubility of quartz in common natural water is very low (17.74 ppm; Mishra, 2004), (b) pH<9.82 unable to carry silica (Mishra, 2004), (c) temperature for silica saturation, (d) silica transportation and precipitation, (d) mass balance with precursors and chert. In order of this, pressure dissolution quartz and/ or feldspar (Banks, 1970; Hesse, 1987; Meyers, 1977), volcanic rock (McBride, 1988; Adachi et al., 1986; Keheila and El-Ayyat, 1992) has proposed as a source of silica, but robust mass balance calculation for the chertification process has been attempted in a few studies (Hofmann and Harris, 2008). Silica precipitation in response of colling mechanism has proposed (Alexandre et al., 2004; Thiry et al., 2015a, 2015b; Thiry and Milnes, 2017). Whereas near surface colling can be useful for paleoclimate estimation (Khalaf et al., 2020), but this process can also occur in subsurface as well. In comprehensive of these four parameter, chertification by replacement of carbonate is still enigmatic. Also there is very few study (Wostbrock and Sharp, 2021) to estimate temperature via 3-O isotope in deep time.

In this backdrop an attempt has been made to understand the genesis of the bedded chert that is present as top most bed of the carbonate (dolostone) of Rohtas limestone and clasts in the sandstone bed of Lower quartzite of the lower Vindhyan, deposited around ~1.59 to 1.21 Ga.

## 6. 2. Geological background

The chert studied herein is in the sediment sequence of Vindhyan basin, mildly deformed and unmetamorphosed Vindhyan succession, world 2nd largest *purana* basin. The entire Vindhyan succession divided into two group-lower Vindhyan/ Semri Group and upper Vindhyan with an unconformity surface in-between (Bose et al., 2001; Mandal et al., 2019; Sarkar and Banerjee, 2020). Each of these group consisting of numbers of Formation and members respectively. Semri/ lower Vindhyan group is further subdivided into five major Formation- Deoland sandstone Fm., Kajrahat Fm., Porecellnite Fm., Kheinjua Fm. and Rohtas Fm. in ascending order (Bose et al., 2001; Mandal et al., 2019; Sarkar and Banerjee, 2020). Whereas upper Vindhyan is consisting three major formation-Kaimur Fm., Rewa Fm. and Bhander Fm. in ascending order (Bose et al., 2001; Mandal et al., 2019; Sarkar and Banerjee, 2020). All of these Formations is further divided into numbers of members with change of depositional environment and paleogeography from one to another. Although basin is dominating in shale, sandstone, carbonate, but there are few Members which are fully or partially composed of volcanic materials (Bose et al., 2001; Rasmussen et al., 2002; Ray et al., 2003; Sarangi et al., 2004; Chakraborty et al., 2007; Mandal et al., 2019; Mageswarri et al., 2019; Sarkar and Banerjee, 2020; Choudhuri et al., 2020). Magmatic layer is consisting numbers of unstable phases including pumice, tuff, glass, amorphous silica etc. Whereas most of the magmatic layer is constricted in Semri/lower Vindhyan, but recently Choudhuri et al. (2020) show reworking volcanic sediments deposition as Bhagwar shale. In lower Vindhyan, Porecellnite is entirely composed of volcanic material (Srivastava et al., 2003; Paikaray et al., 2008; Mishra et a., 2017a, b, c, 2018; Mageswarri et al., 2019). Except this, Rohtas limestone and Rampur shale (Members of Rohtas Formation) are also consisting of numbers of volcanic bed within (Rasmussen et al., 2002; Ray et al., 2003; Sarangi et al., 2004; Chakraborty et al., 2007). The unconformity boundary passes through between Rohtas and Kaimur Formation, more specifically between Rohtas limestone (RLM; top most member of Rohtas Fm. and lower Vindhyan) and Lower Quartzite (LQ; basal most deposit of Kaimur Fm. and upper Vindhyan). Although there was debate on the stratigraphic position of unconformity, but

recently Mandal et al. (2019) show that this unconformity boundary is present although the Vindhyan basin in-between RLM and LQ. Unconformity boundary is very irregular and erosional (Mandal et al., 2019). Sometime a chert layer is also present on top of RLM and these chert are also preserved within the transgressive lag and conglomerate of LQ (Mandal et al., 2019, 2020).

Although exact age when Vindhyan sedimentation was initiated is still unknown, but the radiometric dating of basement rock ~1.753 Ga (Jhiragadandi Granite of Mahakoshal Group of rocks underlying below Vindhyan succession; Bora et al., 2013) infer that Vindhyan sedimentation was initiated around 1.7 Ga. Sedimentation was continued around 1.0 Ga, with a long hiatus within (Sarkar and Banerjee, 2020). Whereas missing of radiometric materials in each of the member is unable to detect the time gap from one sedimentation unit to other but, radiometric dating of basal and upper sediment member suggests a sedimentation gap of ~400 My (Tripathy and Singh, 2015). Pb-Pb isochrones and U-Pb dating of the magmatic layers of RLM, below the unconformity suggest that this carbonate sedimentation going on around 1599±48 ma (Sarangi et al., 2004), 1514±120 Ma (Chakraborti et al., 2007) and 1631±1 Ma (Ray et al., 2002). Re-Os dating from Bijaigarh shale (thick black shale) overlying on LQ with two members (Silicified shale/ Bhagwar Shale and Upper Quartzite in-between; see Mandal et al., 2019) suggest that this unit was deposited ~1210±51 Ma (Tripathy and Singh, 2015). Therefore, lower Vindhyan/ Semri Group sediment succession was deposited from ~1.70 Ga to ~1.59 Ga. After lower Vindhyan sedimentation basin was exposed around 400 Ma, from ~1.59 Ga to ~1.2 Ga (Tripathy and Singh, 2015; Sarkar and Banerjee, 2020).

## 6. 3. Result

### 6.3.1. Field relationship and occurrence of chert

The sedimentary sequence hosting the chert layer is consisting of light brown and whitish colour carbonate beds at base (RLM; Fig. 6.1a) and brown colour siliciclastic sandstone (LQ; Fig. 6.1b, c). The basal unit exposed in rock wall is approximately 35 m. It is consisting of alternating hard dense calc-arenite (average thickness 45 cm) and micrite beds (average thickness 35 cm) (Fig. 6.2a). Calc-arenite beds have appeared on micrite bed with sharp and erosional base. The carbonate sandstone beds are consisting of cross-stratification, ripple laminations and intra-formation conglomerate (Fig. 6.2b, c, d). Scale

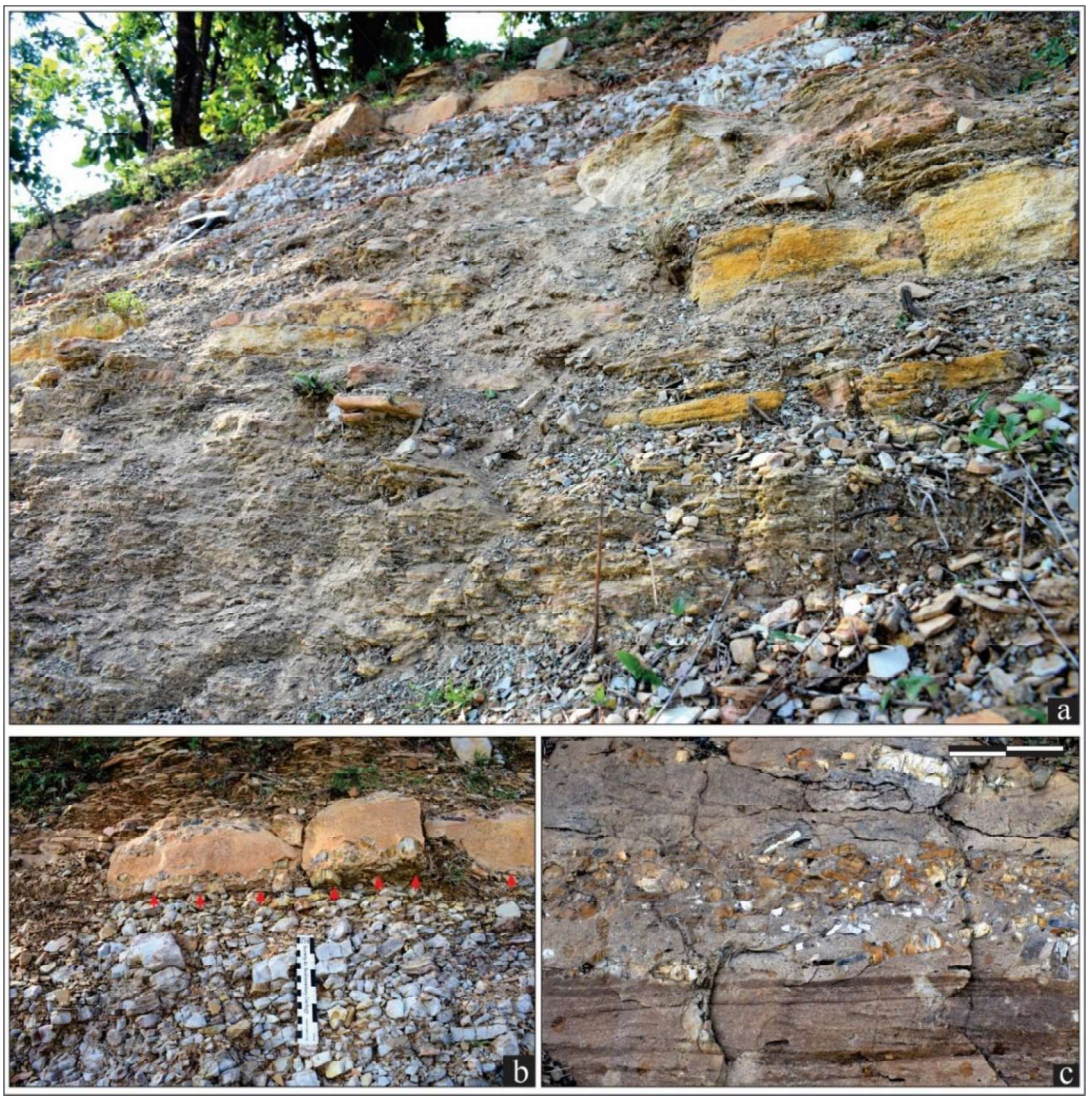


Fig. 6.1. Field photographs of studied area: laterally persistence chert layer (a; in-between red dotted line; hammer length 35 cm; note basal unit is RLM and upper unit is LQ), Sandstone (LQ) directly on chert layer (b; scale length 15 cm; note the transgressive lag defined by chert clasts marked by red arrows), chert clasts distribution with the conglomerate facies of LQ (c; bar length 15 cm).

of cross-stratification are varying bed to beds. Occasionally composite cross-stratifications are also observed within few beds. Both large and small scale cross-stratifications are oriented along same direction. Dip of small and large cross-strata is 2º-5º and 15º-20º respectively. Ripples are identified by cm-scale cross-stratifications in transverse section and bifurcated crest line on bedding surface (Fig. 6.2d). Ripple crest are straight to sinuous in nature with few cresset shape. Clasts composed of micrite are mostly chaotically arranged, with few alignments along cross-stratifications. Carbonate mud, micrite beds are composed of very fine grain, grey in color (Fig. 6.2a, e). These micrite beds are consisting of abundance planar laminations, with dissication cracks on bedding surface (Fig. 6.2e).

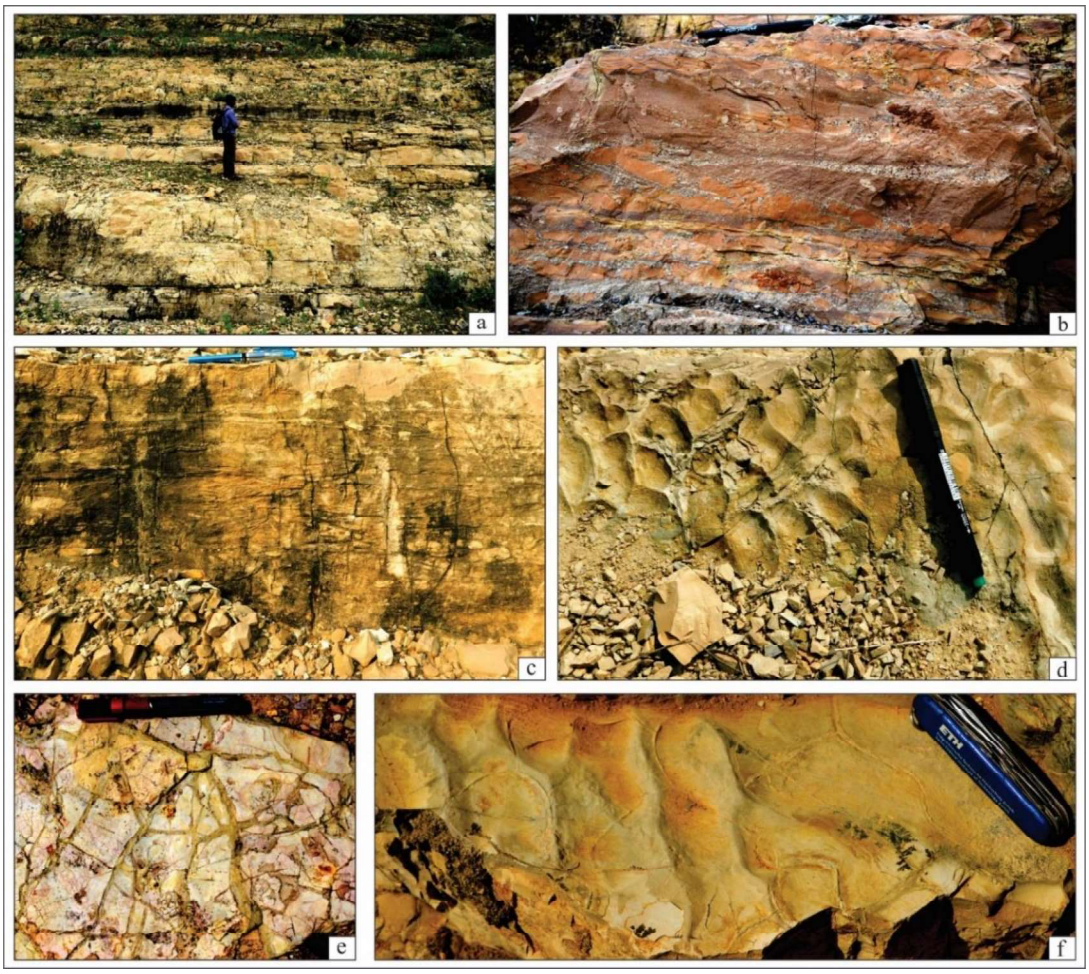


Fig. 6.2. Field photographs of RLM: alternation calc-arenite and carbonaceous mud beds (a; man height 1.5 m), cross-stratified facies within carbonate (b; marker length 15 cm; note clasts orientation along cross-stratification), cm scale symmetric cross-stratification (c; pen length 15 cm), ripple laminations (d; marker length 15 cm; note the interference nature), dissication cracks (e; marker length 15 cm), bifurcated ripple crest and manchuriphycus cracks on ripple through (f; knife length 8 cm).

Preciously chert layer is laying on a micrite bed with sharp contact like calc-arenite bed appear on micrite bed. Below this micrite bed, alternation calc-arenite and micrite bed going on. The upper unit, approximate exposed about 4 m is composed of siliciclastic sandstone (LQ; Fig. 6.1c). The chert layer is aligned like sedimentary bed, but the contact between basal carbonate bed and chert layer is uneven and irregular. The contact with upper sandstone bed is an irregular erosional surface marked by thin, discontinuous band of lag abundance of chert fragment (Fig. 6.1). This sandstone unite is consisting of numbers of tidal and storm facies (see details in Mandal et al., 2019, 2020).

Chert occurs as a continuous band that reach ~75 cm thickness and extended about ~1.0 km along the horizon that is slightly discordant to bedding. Chert layer is directly lying

on carbonate mud bed. The chert mostly massive (except few laminations) and dark to light grey in colour (Fig. 6.1). Except laterally persistence layer characteristics, these chert has also occurred as clasts within the transgressive lag and conglomerate facies of LQ (see details in Mandal et al., 2019, 2020).

### 6.3.2. Petrography of dolostone (RLM) and chert

The basal dolostone (RLM) section is consisting of carbonate sandstone and mud (Fig. 6.2a), petrography study also supports this context. Carbonate sandstone beds are dominating with ooids, peloids and intraclasts (Fig. 6.3). Also both broken and composites ooids also frequently observed. Ooids grains have distinctly preserved alternating concentric and rating rims (Fig. 6.3a). With haphazard orientation ooids-peloids are also aligned along cross-stratification (Fig. 6.3e). Ooids, peloids and intraclasts grains are binding materials. Intraclasts have variable shape and size, composed of micrite. From rounded to angular shape, length of these intraclasts varies from 0.5 µm to 2 mm (Fig. 6.3c, d). Carbonate mud beds are entirely composed of micrite with few laminas (Fig. 6.3b). Along these laminas some rhombic dolomite grain is frequently preserved (Fig. 6.3b, f). Apart from the radial sparite crystal in ooids, huge amount sparite has grown in the fenestra and vug structures of these calc-arenite rock (Fig. 6.4). These vug filling sparite are also within the carbonate mud layers (Fig. 6.4).

Under optical microscopic study, chert samples identify domination of fine grain silica with dark to light grey colour in planar polarized light and cross-polarized light respectively (Fig. 6.5a). Although these fine grain silica field are massive in character, but numbers of chert samples have preserved numerous ooids, peloids and intraclasts like structures (Fig. 6.5b, c, d). Ooids, peloids and intraclasts are entirely composed of silica. Ooids are has potentially preserved alternating radiating and concentric rim (Fig. 6.5b). Peloids and intraclasts have identified depending on their size, where smaller size is for peloids and larger size is for intraclasts (Fig. 6.5d). Besides their uniform colour and composition, peloids and intraclasts have preserved few quartz gains (Fig. 6.5d). These quartz gains are angular to sub-angular in shape with a distinct boundary (Fig. 6.5d). A bunch of ooids is surrounded by a boundary and suggest composite ooids. Apart from these carbonate grains, few primary laminae like structures are well recognized (Fig. 6.5c).

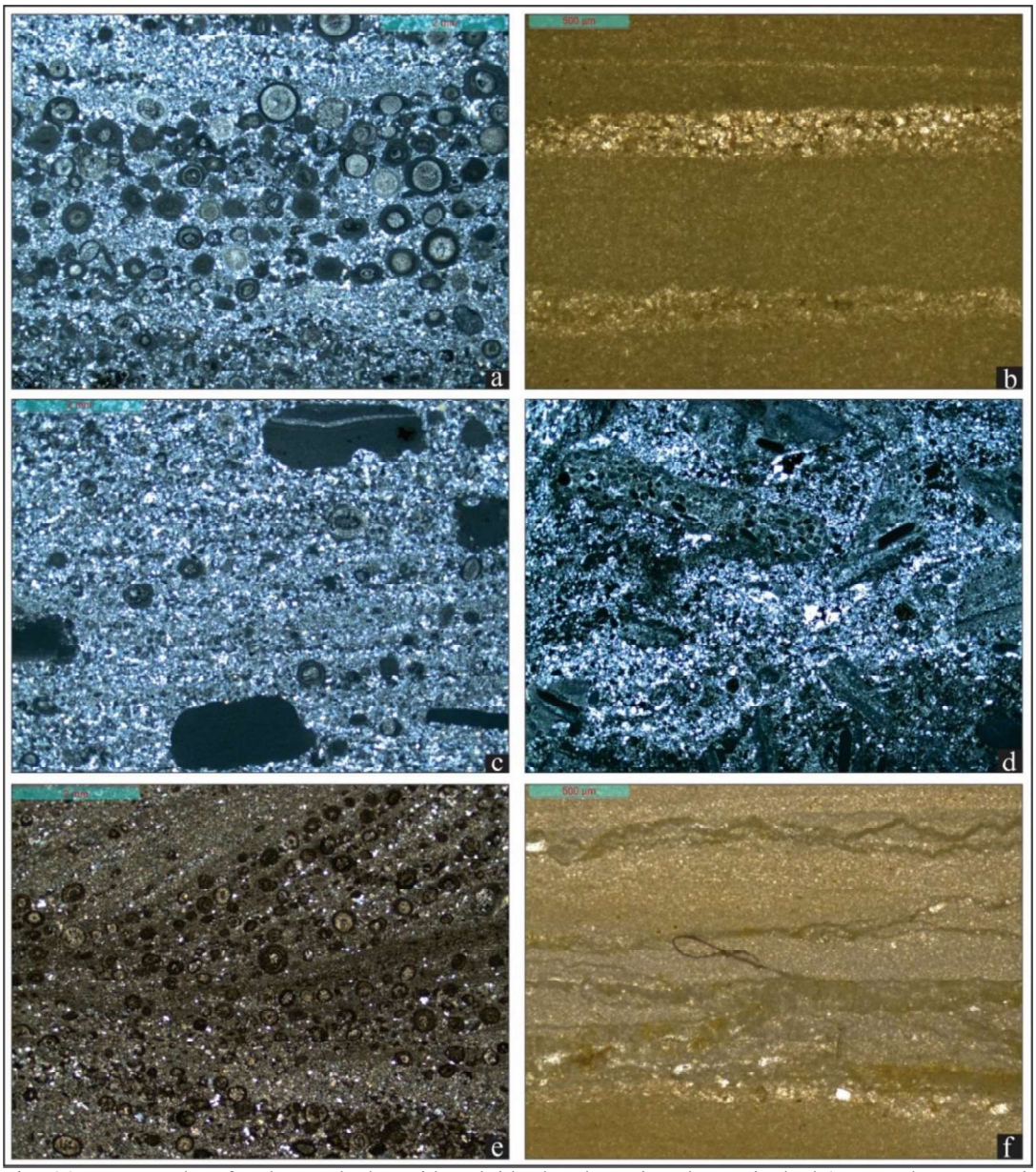


Fig. 6.3. Petrography of carbonate beds: ooids-peloids abundance in calc-arenite bed (a; note the concentric and radiating rim in ooids), micrite dominance in carbonate mud beds (b), micritic intraclasts with variable size and shape (c), composite ooids (d), ooids-peloids alignment along cross-stratification (e), dolomite romb along micrite laminas (f).

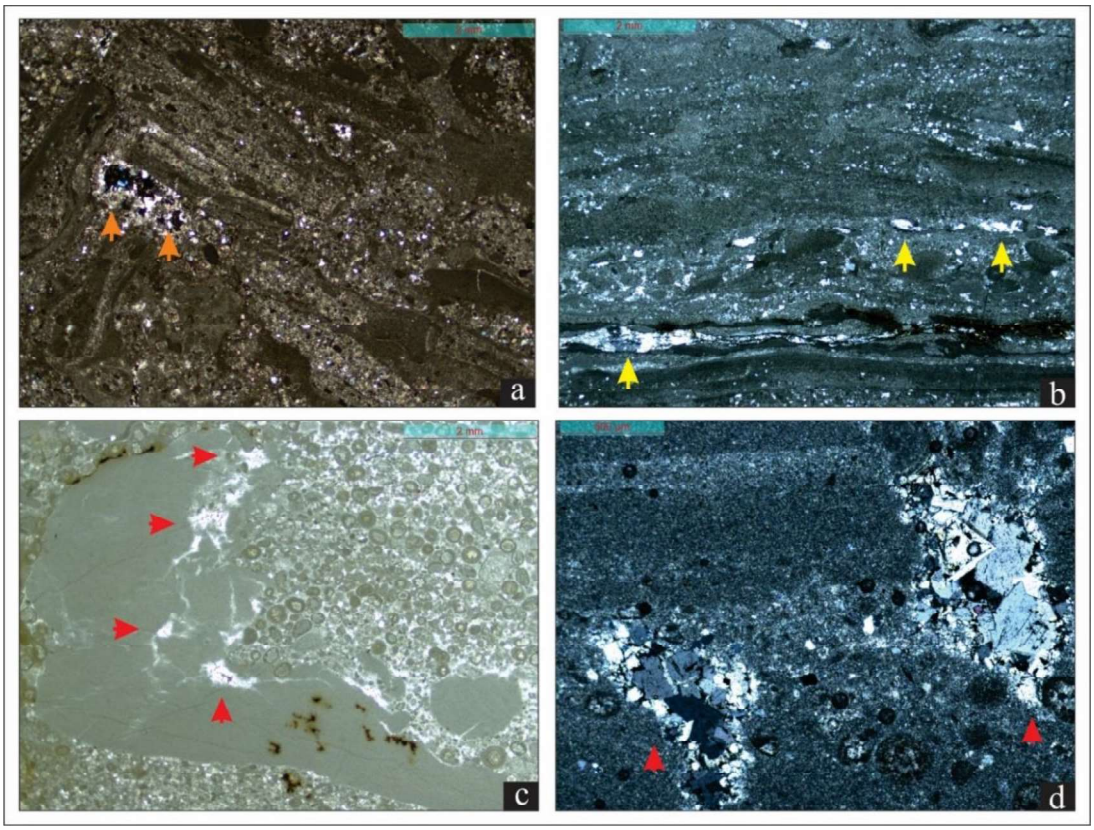


Fig. 6.4. Vug filling sparite cement growth in both calc-arenite and micrite beds.

With these pseudo structures of silica, three main silica polymorphs have recognized under optical microscopy include microcrystalline quartz, chalcedony and mega quartz (Fig. 6.5). Few fractures also distinguished, and these fractures have pass through the ooids, peloids without any displacement. These fractures paths are filled up with megaquartz. Microcrystalline quartz is most abundant silica polymorphs and commonly occurs as subeuhedral to xenomorphic mosaics of randomly oriented crystal, <20 µm in size, undulatory extinction (Fig. 6.5a). Dominances of microcrystalline quartz are mostly homogeneous without any primary structures. Chalcedony commonly forms botryoidal or mammillary wall lining (upto 1 mm thick) of cavities and consists of micro-laminated and juxtaposed and spherulitic. Chalcedony is strictly restricted within pore space of pseudo-ooids, peloids and intraclastic (Fig. 6.5b). Megaquartz crystals have a crystal size greater than 20 µm. Isometric and elongated crystals are the two main types, and both may be euhedral or xenomorphic. Most commonly these megaquartz are restricted in the cavities (Fig. 6.5b). Elongated megaquartz has grown at the boundaries, whereas isometric quartz has preferred in the center of vug.

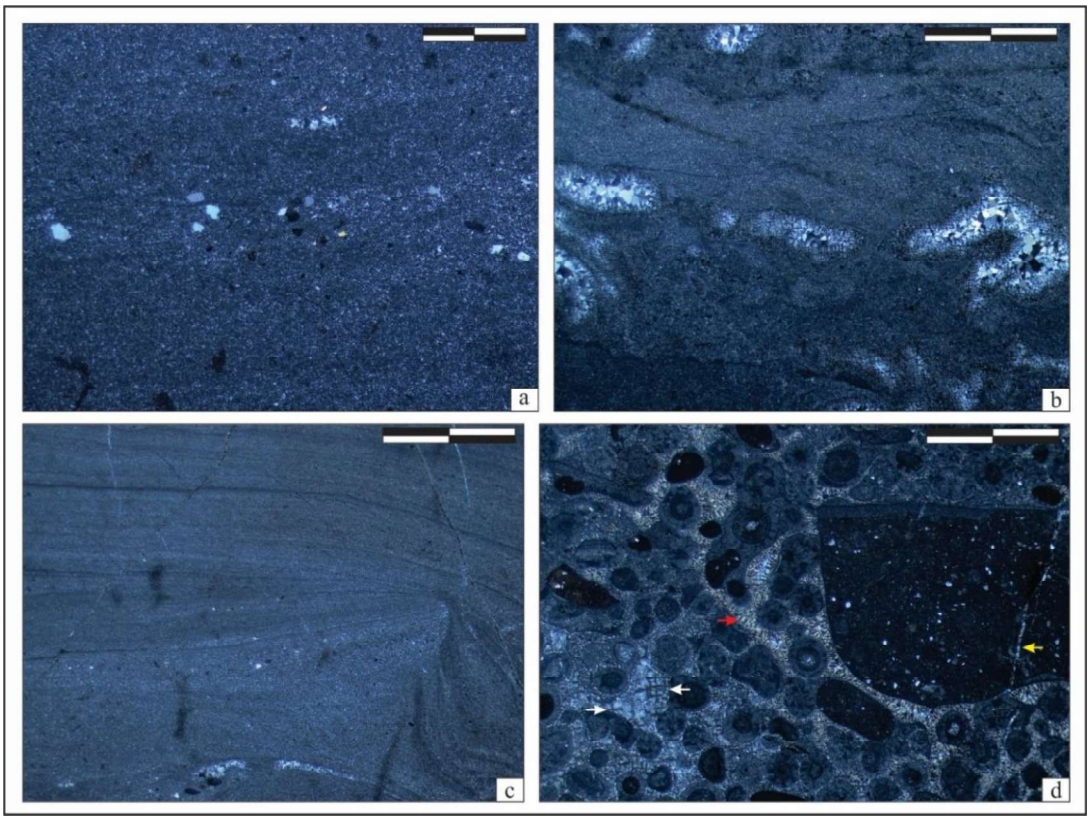


Fig. 6.5. Petrography of chert samples: microcrystalline quartz dominance (a; note inherited quartz fragments within; bar length 500µm), mega-quartz growth in vug (b; note acicular form at the boundary; bar length 500µm), distorted laminas within microcrystalline quartz (c; bar length 500µm), pseudo ooids-peloids-intraclasts (d; note chalcedony marked by red and white arrows; also observe fracture filling quartz cross-cutting ooids, peloids marked by yellow arrow; bar length 500µm).

### 6.3.3. Chemistry of dolostone

Major elements oxide concentration of Rohtas limestone show a variable concentration of CaO, MgO, $SiO_2$, $Al_2O_3$, $Fe_2O_3$, $K_2O$, MnO and $TiO_2$. Details concentration of the major element oxide concentration is in Table 6.1. Interestingly, CaO (avg. 24.76 wt.%): MgO (avg. 17.38 wt.%) is almost 1:1. This ~1:1 ratio of Ca: Mg infer that studied carbonate section is composed of dolostone. The average shale normalized REE (Fig. 6.6) of dolostone flat orientation of normalized REE and trace with positive Gd anomaly. The average shale normalized extended trace elements diagram (Fig. 6.7) exhibits opposite anomaly of Ba, Sr, Ti, V, Cr and Ni with respect to chert. All of them (Ba, Sr, Ti, V, Cr and Ni) show negative anomaly in dolostone whereas in chert these are positive (Fig. 6.8). The concentration average shale normalized REE (Fig. 6.6) and extended trace elements (Fig. 6.7) of dolostone show a variation 0.1 to 0.5.

### 6.3.4. Chemistry of chert

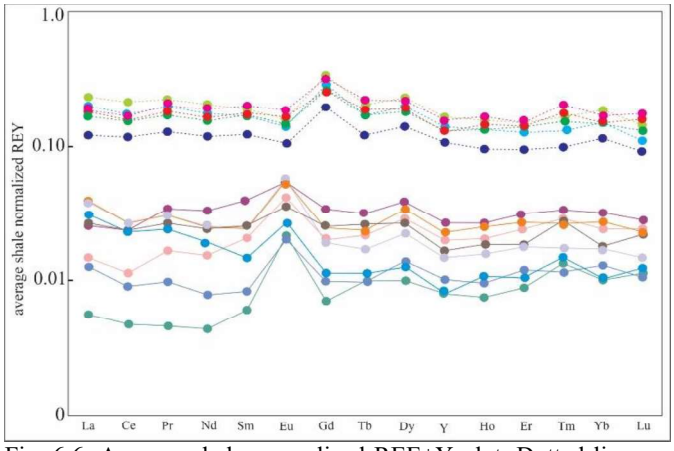


Fig. 6.6. Average shale normalized REE+Y plot. Dotted line are for dolostone samples and solid lines are for chert samples. Note the depletion of REE+Y for all the chert samples in compare to dolostone. Also note positive Eu anomaly in chert and Gd anomaly in dolostone.

The studied chert is dominated by $SiO_2$ (>94 wt.%; Table-6.1) with low concentration of $Al_2O_3$ (0.58-1.76 wt.%, avg. 0.87wt%). The concentrations of CaO, MgO, MnO, $TiO_2$, $K_2O$ and $Fe_2O_3$ are very low (sum of the concentrations of the species never exceeds 0.25 wt.%). Barring one sample (#Ch12a where 0.14 wt.% of $Fe_2O_3$ is recorded), concentrations of $Fe_2O_3$ and MnO in all other chert samples are close to zero. Fig. 6.6 (Only REE) and Fig. 6.7 (extended trace elements) show the average shale REE normalized concentration of the trace elements of the chert. With respect to average shale, trace elements of the studied chert show a marked depletion (ratio below or close to 0.1; Fig. 6.7). Nevertheless, a positive anomaly is recorded for U, Ba, Pb, Ni, Ti, and V whereas Th shows a negative anomaly. For most samples Sr does not show any anomaly. Barring Eu which shows a distinct positive anomaly, all other REE show nearly flat pattern (Fig. 6.7). Compared to the dolostone, the chert samples show marked enrichment in $SiO_2$ and depletion in (a) $Al_2O_3$, $Fe_2O_3$, CaO and MnO (Fig. 6.8) and (b) trace element concentrations (+REE) excepting Ba (enrichment), Pb (enrichment) and Ni (similar concentration). Though the total REE content of the chert samples are distinctly lower than the dolostone, the PAAS normalized REE pattern of both the rocks mimic each other barring Eu (Fig. 6.6, 6.7). The latter element shows distinct positive anomaly in the chert and a mild negative anomaly in the dolostone. U/Th is less than 1 in both the rocks though the chert samples show greater depletion Th with respect to U.

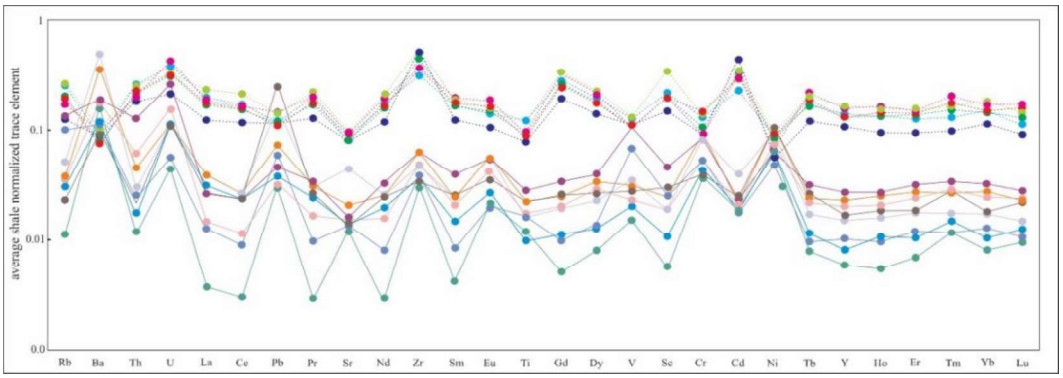


Fig. 6.7. Extended trace element diagram of chert samples and dolostone. Dotted line are for dolostone samples and solid lines are for chert samples. Note the depletion of trace and REE for all the chert samples in compare to dolostone.

## 6.4. Discussion

It is evident from the foregoing analysis that the studied chert layer is a record of diagenetic alternation of carbonate rock. Textural relation and compositional variation of the chert and carbonate provide clue of timing of silicification, nature of silicification process and earth surface temperature under the following heading.

### 6.4.1. Environment and timing of chertification

Textural similarity (i.e. ooids, peloids and intraclastic structures) between the dolostone (RLM) and chert layer infer that this chert layer has formed by replacement of carbonate rock which primarily deposit ooids, peloids like structures. This textural similarity can't confirm whether this is syngenetic origin (Keheila, 2000; Lindgreen and Jakobsen, 2012) or diagenetic origin (Snavely et al., 1979; Maliva and Siever, 1989a; Knauth, 1994; Lawrence, 1994; Abd El-Hameed et al., 1997; Genedi, 1998; McBride et al., 1999; James., 2000; Shaaban, 2004; Kwiatkowski, 2005; Bustillo et al., 2009; Madsen and Stemmerik, 2010). The field and petrography study reinforce the diagenetic alternation of carbonate rock- (a) preservation along the unconformity surface, (b) laterally persistence (upto 1 km) but irregular in nature, (c) no such distortion of ooids, peloids, (c) fracture filling silica across ooids, peloids without any deformation.

Superposition of the unconformity surface as a roof on RLM argue that this carbonate sequence has never deep buried and so there will not be effect of elevated pressure and temperature until overlying sandstone (LQ) deposition. Chronostratigraphy of Vindhyan succession infer the ~400 Ma (~1.59 Ga to 1.2 Ga; Tripathy and Singh, 2015) sedimentation gap in-between lower and upper Vindhyan i.e. lower Vindhyan was

subaerially exposed for this time interval. Chert layer on top of RLM insinuate that during this time chert layer has formed. As RLM was the top most deposit and expose on earth surface so, the chert layer on top of RLM must have formed on surface i.e. karstification process (Kenny and Knauth, 1992). Whereas because of lack of chemistry data sets, I can't extrapolate whether dolomitic character of RLM is an inherited property of Precambrian sea or a result diagenesis, but chert layer on top of RLM infer that chert precipitation must have equilibrium with atmospheric pressure and temperature. The field and microscopic pictorial view, I can't find out step by step process of mineralogical change from dolostone to chert but it is inferred that environment of chert precipitation is directly related to land surface pressure-temperature.

Although, anyone can argue that this chert has formed after complete of entire Vindhyan deposition (i.e. both lower and upper Vindhyan) and, initially this was a carbonate bed in place of chert layer and carbonate pebbles in transgressive lag and conglomerate of LQ. But angular shape of chert pebble discard the possibly as with long transportation carbonate pebble shape rounded. One-time appearance in-between RLM and LQ, no such effect on immediately below mud layer of chert recommend that chert was formed on the top most layer of RLM i.e. on the earth surface. Absence of this chertification effect in immediately below layer also infer that silica supersaturated fluid pass through as layer parallel. This chert layer was formed during hiatus event i.e. from 1.59 Ga to 1.21 Ga.

| Table 6.1. Oxide concentration of major elements in chert and limestone [Note: RL are the sample analyzed from limestone and Ch are chert sample] | | | | | | | | | | | | | | |
|---|---|---|---|---|---|---|---|---|---|---|---|---|---|---|
| Sample no | RL 1 | RL 2 | RL 3 | RL 4 | RL 5 | RL 6 | Ch8a | Ch8b | Ch9b | Ch11 | Ch12 | Ch12a | Ch14a | Ch14b |
| $Al_2O_3$ | 4.04 | 1.61 | 2.85 | 2.87 | 2.44 | 1.68 | 0.58 | 1.76 | 0.61 | 0.77 | 1.27 | 0.97 | 0.37 | 0.63 |
| CaO | 26.7 | 28.44 | 29.23 | 29.24 | 28.88 | 28.42 | 0.05 | 0.06 | 0.06 | 0.05 | 0.07 | 0.06 | 0.05 | 0.06 |
| $Fe_2O_3$ | 1.24 | 1.08 | 1.21 | 1.21 | 2.00 | 1.07 | 0.00 | 0.00 | 0.00 | 0.00 | 0.00 | 0.14 | 0.00 | 0.00 |
| $K_2O$ | 1.36 | 0.58 | 0.90 | 0.90 | 0.64 | 0.58 | 0.11 | 0.44 | 0.13 | 0.11 | 0.38 | 0.17 | 0.04 | 0.09 |
| MgO | 19.15 | 20.03 | 20.42 | 20.41 | 19.93 | 20.02 | 0.02 | 0.05 | 0.02 | 0.02 | 0.07 | 0.02 | 0.02 | 0.02 |
| $SiO_2$ | 20.78 | 20.75 | 17.66 | 17.5 | 17.57 | 20.78 | 97.58 | 94.93 | 97.54 | 96.09 | 97.18 | 95.90 | 98.09 | 96.76 |
| $TiO_2$ | 0.11 | 0.06 | 0.08 | 0.08 | 0.07 | 0.07 | 0.02 | 0.03 | 0.03 | 0.02 | 0.02 | 0.03 | 0.02 | 0.02 |
| MnO | 0.05 | 0.05 | 0.05 | 0.05 | 0.05 | 0.05 | 0.00 | 0.00 | 0.00 | 0.00 | 0.00 | 0.00 | 0.00 | 0.00 |
| Al/(Al+Fe+Mn) | - | - | - | - | - | - | 1.00 | 1.00 | 1.00 | 1.00 | 1.00 | 0.92 | 1.00 | 1.00 |
| Si/(Si+Ca+Mg) | - | - | - | - | - | - | 0.99 | 0.99 | 1.00 | 0.98 | 0.98 | 0.99 | 0.99 | 0.99 |

| Table 6.2. REY and trace element concentration in chert and limestone [Note: RL are the sample analyzed from limestone and CH are chert sample] | | | | | | | | | | | | | | |
|---|---|---|---|---|---|---|---|---|---|---|---|---|---|---|
| Sample | RL 1 | RL 2 | RL 3 | RL 4 | RL 5 | RL 6 | CH8a | CH8b | CH9b | CH11 | CH12 | CH12a | CH14a | CH14b |
| La | 9.31 | 7.95 | 7.09 | 6.73 | 7.27 | 4.88 | 0.59 | 1.02 | 1.57 | 1.25 | 0.50 | 1.53 | 0.15 | 1.06 |
| Ce | 20.36 | 16.39 | 14.87 | 14.48 | 15.88 | 11.08 | 1.08 | 2.23 | 2.58 | 2.18 | 0.86 | 2.55 | 0.29 | 2.24 |
| Pr | 2.16 | 1.89 | 1.75 | 1.65 | 1.93 | 1.24 | 0.16 | 0.33 | 0.30 | 0.23 | 0.09 | 0.30 | 0.03 | 0.26 |
| Nd | 8.02 | 6.86 | 6.36 | 5.99 | 7.29 | 4.64 | 0.60 | 1.28 | 0.97 | 0.75 | 0.31 | 0.98 | 0.11 | 0.95 |
| Sm | 1.39 | 1.22 | 1.27 | 1.23 | 1.45 | 0.90 | 0.15 | 0.29 | 0.18 | 0.11 | 0.06 | 0.18 | 0.03 | 0.19 |
| Eu | 0.25 | 0.22 | 0.26 | 0.23 | 0.30 | 0.17 | 0.07 | 0.09 | 0.09 | 0.04 | 0.03 | 0.09 | 0.03 | 0.06 |
| Gd | 2.34 | 2.01 | 1.83 | 1.82 | 2.25 | 1.36 | 0.14 | 0.24 | 0.17 | 0.08 | 0.07 | 0.13 | 0.04 | 0.18 |
| Tb | 0.24 | 0.20 | 0.23 | 0.20 | 0.27 | 0.14 | 0.03 | 0.04 | 0.03 | 0.01 | 0.01 | 0.02 | 0.01 | 0.03 |
| Dy | 1.28 | 1.08 | 1.05 | 1.00 | 1.20 | 0.77 | 0.16 | 0.21 | 0.18 | 0.07 | 0.08 | 0.12 | 0.04 | 0.15 |
| Y | 6.81 | 5.71 | 5.31 | 5.40 | 6.44 | 4.37 | 0.82 | 1.11 | 0.93 | 0.33 | 0.42 | 0.61 | 0.24 | 0.68 |
| Ho | 0.25 | 0.21 | 0.23 | 0.21 | 0.26 | 0.15 | 0.03 | 0.04 | 0.04 | 0.02 | 0.02 | 0.03 | 0.01 | 0.03 |
| Er | 0.59 | 0.49 | 0.55 | 0.54 | 0.58 | 0.37 | 0.09 | 0.12 | 0.11 | 0.04 | 0.05 | 0.07 | 0.03 | 0.07 |
| Tm | 0.10 | 0.08 | 0.11 | 0.09 | 0.12 | 0.06 | 0.02 | 0.02 | 0.02 | 0.01 | 0.01 | 0.01 | 0.01 | 0.02 |
| Yb | 0.68 | 0.55 | 0.55 | 0.54 | 0.63 | 0.42 | 0.09 | 0.12 | 0.10 | 0.04 | 0.05 | 0.06 | 0.03 | 0.07 |
| Lu | 0.10 | 0.08 | 0.11 | 0.09 | 0.12 | 0.06 | 0.02 | 0.02 | 0.02 | 0.01 | 0.01 | 0.01 | 0.01 | 0.02 |
| Rb | 37.22 | 17.53 | 23.70 | 28.07 | 28.94 | 35.96 | 4.79 | 18.44 | 5.10 | 4.05 | 13.94 | 6.94 | 1.52 | 3.14 |
| Ba | 58.28 | 51.68 | 57.36 | 41.58 | 43.90 | 51.8 | 101.8 | 109.3 | 201.56 | 68.50 | 65.10 | 281.9 | 94.3 | 54.8 |
| Th | 3.09 | 2.18 | 2.40 | 2.63 | 2.57 | 3.09 | 0.75 | 1.52 | 0.54 | 0.20 | 0.28 | 0.35 | 0.14 | 0.26 |

| | | | | | | | | | | | | | | |
|---|---|---|---|---|---|---|---|---|---|---|---|---|---|---|
| U | 1.20 | 0.80 | 1.58 | 1.19 | 1.18 | 1.39 | 0.58 | 0.96 | 0.42 | 0.34 | 0.21 | 0.42 | 0.16 | 0.40 |
| Pb | 2.83 | 2.29 | 2.92 | 2.17 | 2.34 | 2.37 | 0.64 | 0.92 | 1.45 | 0.76 | 1.20 | 3.11 | 0.61 | 5.27 |
| Sr | 28.56 | 23.43 | 27.58 | 26.53 | 24.48 | 24.09 | 4.64 | 4.82 | 6.18 | 4.08 | 4.12 | 13.28 | 3.59 | 4.09 |
| Zr | 84.94 | 87.91 | 57.79 | 56.35 | 70.85 | 49.95 | 7.62 | 10.07 | 9.92 | 5.86 | 6.28 | 7.41 | 4.72 | 5.46 |
| Ti | 549.6 | 356.6 | 425.8 | 398.4 | 422.7 | 556.3 | 80.16 | 129.97 | 102.68 | 45.26 | 75.24 | 73.56 | 55.84 | 37.76 |
| Sc | 5.83 | 2.50 | 3.36 | 3.40 | 3.38 | 3.69 | 0.32 | 0.78 | 0.42 | 0.18 | 0.43 | 0.32 | 0.09 | 0.51 |
| V | 16.79 | 4.32 | 13.76 | 13.89 | 14.18 | 16.70 | 2.99 | 13.46 | 4.06 | 2.61 | 8.71 | 4.49 | 1.96 | 3.59 |
| Cr | 11.87 | 4.30 | 8.43 | 13.20 | 9.50 | 11.75 | 4.79 | 7.47 | 8.48 | 3.95 | 4.79 | 7.60 | 3.29 | 3.55 |
| Ni | 6.37 | 3.85 | 4.52 | 5.76 | 5.67 | 5.99 | 4.97 | 4.32 | 6.58 | 4.41 | 3.28 | 6.26 | 4.47 | 7.25 |
| Cu | 1.80 | 1.24 | 1.75 | 7.20 | 6.04 | 8.37 | 1.95 | 3.74 | 4.68 | 0.79 | 1.85 | 4.44 | 0.77 | 3.33 |
| Zn | 7.60 | 5.68 | 10.97 | 9.17 | 7.72 | 9.52 | 3.32 | 4.02 | 8.27 | 8.73 | 4.06 | 4.74 | 3.22 | 18.07 |
| As | 4.05 | 2.82 | 1.17 | 1.90 | 1.46 | 1.81 | 1.94 | 1.55 | 3.62 | 0.88 | 0.86 | 9.97 | 1.78 | 2.16 |
| Mo | 0.52 | 0.42 | 0.78 | 0.56 | 0.39 | 0.28 | 0.28 | 0.18 | 0.31 | 0.18 | 0.13 | 0.49 | 0.38 | 0.31 |
| Cd | 0.29 | 0.36 | 0.25 | 0.24 | 0.26 | 0.18 | 0.02 | 0.02 | 0.02 | 0.02 | 0.01 | 0.03 | 0.01 | 0.02 |
| Sn | 1.34 | 0.77 | 1.02 | 1.13 | 1.15 | 1.19 | 0.58 | 0.97 | 0.62 | 0.59 | 0.78 | 0.86 | 0.84 | 0.53 |
| Sb | 0.73 | 0.26 | 0.40 | 0.34 | 0.26 | 0.32 | 0.80 | 2.23 | 0.82 | 0.36 | 0.37 | 1.23 | 0.59 | 0.54 |
| Pr/Pr* | 1.06 | 1.09 | 1.12 | 1.13 | 1.11 | 1.12 | 1.23 | 1.20 | 1.18 | 1.14 | 1.16 | 1.18 | 1.01 | 1.11 |
| Ce/Ce* | 0.89 | 0.85 | 0.79 | 0.79 | 0.82 | 0.80 | 0.65 | 0.68 | 0.75 | 0.79 | 0.77 | 0.74 | 0.98 | 0.82 |
| Eu/Eu* | 0.60 | 0.66 | 0.71 | 0.75 | 0.68 | 0.62 | 2.07 | 1.47 | 2.25 | 2.06 | 2.23 | 2.58 | 4.64 | 1.40 |
| La/La* | 0.91 | 0.83 | 0.81 | 0.82 | 0.83 | 0.85 | 0.78 | 0.71 | 0.93 | 0.93 | 0.92 | 0.92 | 1.17 | 0.86 |

### 6.4.2. Enrichment and depletion of chemical species: a mass balance approach

The apparent compositional difference that exist between the chert and its precursor dolostone does not necessarily signify that these chemical species behaved as mobile components unless the transformation process conserve the rock mass. Several studies have demonstrated that chemical transformation from one rock to the other rock is associated with significant mass change (Grant, 1986, 2005; Hofmann and Harris, 2012). In such a situation leads to residual enrichment, an evaluation of the mobility (or immobility) of the different chemical species requires an evaluation of the rock mass change that might be associated with replacement of the dolostone by chert. Ague (1994a, b) derived an equation that calculates the rock mass ($T_{mass}$) in terms of concentration of an immobile species that is present in the precursor and the replaced rock. The equation is,

$$T_{mass} = \frac{C_i^o}{C_i^{o\prime}} \quad \text{---------- (equation 6.1)}$$

$C^0_i$ and $C^{0\prime}_i$ being the concentration of the immobile species 'i' in precursor and replaced rock respectively. The concentrations can be expressed in any unit of relative mass (e.g. wt.%, ppm or ppb). Equation 6.1 is valid for all the mobile species. This then follows that the ratio $C^0_i/C^{0\prime}_i$ will be the same (or very close to so) for all the immobile species.

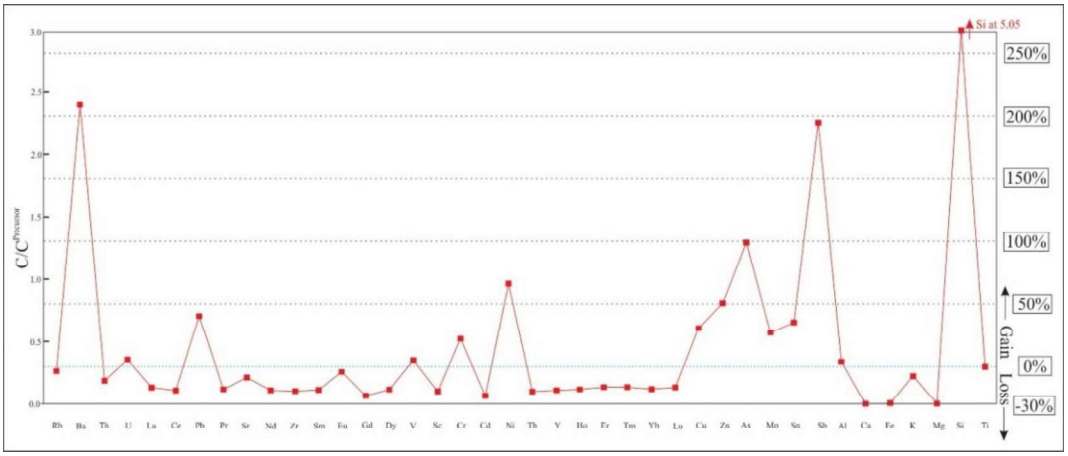


Fig. 6.8. $C^{o\prime}_{CH}/C^{o}_{DS}$ ($C/C_{Precursure}$) plot showing element mass loss and gain during replacement of dolostone by chert (silica).

The ratio of $C^{0'}_{CH}/C^{0}_{DS}$ has been plotted for the major and trace elements that are present in dolostone (DS) and Chert (CH, Fig. 6.8). The diagram Fig. 6.8 shows that the ratio $C^{0'}_{CH}/C^{0}_{DS}$ remain effectively constant for Al, Ti, U, and V (0.32±0.02). Following the rational outlined by Philpotts and Ague (2009), it is presumed that these four elements

remained effectively immobile during chertification of the dolostone. The value $C^{0'}_{CH}/C^{0}_{DS}$ = 0.32 yields a $T_{mass}$ = 2.12. This means the chertification process of the dolostone involves ~212% increase in rock mass. Such a large increase in rock mass explains why most of the major and trace elements show a drop in concentrations of the chert as compared to dolostone (Fig. 6.8). In diagram (Fig. 6.8), a horizontal line that intersect the $C^{0'}_{CH}/C^{0}_{DS}$axis at 0.32 has been drawn. Concentrations of elements that fall off this line are mobile species. This diagram shows a great loss (degree of depletion; points lie below the line) and gain (degree of enrichment; point lie above the line) of elements during chertification. A number of deductions can make from Fig. 6.8 as following-

(a) Barring, Eu, concentrations of all other REE, Th, Ca, Mg, Sr were leached out from the dolostone during the chertification process. Barring Eu, the degree of depletion of LREE and HREE remain virtually the same (0.24 ppm). This explains why the average shale normalized REE patterns of chert and dolostone samples are similar (Fig. 6.6). Leaching of REE from the dolostone by chert forming fluid (meteoric and hydrothermal) have been documented from many studies (Jacobsen and Pimentel-Kolse, 1988a, 1988b; Derry and Jacobsen, 1990; Klein and Beukes, 1992). The Ca, Mg, Sr being highly alkaline elements, these elements has savaged from source rock and dissolved into silica supersaturated fluid.

(b) As expected $SiO_2$ shows ~80 % increase followed by increase in concentrations of Ba (~58%), Sb (~55%), As (~22%), Pb (~42%) and Ni (~3%) during the certification process. Enrichment of these elements may be because of higher value in silica supersaturated fluid and precipitation with silica (chert).

(c) $TiO_2$ and $Al_2O_3$ behaved as immobile species. This is consistent with the fact that Al and Ti remain insoluble/nominally soluble over a range of fluid chemistry and physical conditions (Adachi et al., 1986; Yamamoto, 1987; Aitchison and Flood, 1990).

(d) Immobile behavior of U and Eu warrant an explanation. Studies have shown that these two elements with variable valency states responds differently during oxidation. While U is soluble in oxidizing environment, Eu (in its $^{+3}$ state) remain nominally soluble. Besides the oxidation state, low pH (<8) and the increased concentrations of $(CO_3)^{2-}$ and $(PO_4)^{3-}$ in the chert forming aqueous fluid likely to exert control on immobility of U. The acidic pH and the high concentrations of carbonate and phosphate ions in the aqueous fluid

also responsible for preferential leaching of Th (relative to U) by the chert forming fluid. Eu is mobile under reducing state (in $Eu^{2+}$). Depletion of Fe in chert suggest that iron was dominantly in the more soluble $Fe^{2+}$ species and was carried out of the system during fluid-carbonate interaction. Studies have shown that to convert $Eu^{3+}$ to $Eu^{2+}$ degree of reduction will be more than converting $Fe^{3+}$ to $Fe^{2+}$. It therefore seems likely that redox potential of the chert forming fluid was in between the equilibria $Eu^{3+}+e= Eu^{2+}$ and $Fe^{3+}+e= Fe^{2+}$.

### 6.4.3. Source and mode of transportation of silica by fluid

Mass balance calculations (Fig. 6.8) shows over fivefold, by weight, in $SiO_2$ in the chert relative to the precursor dolostone. It, therefore, stands to reason thatan internal reorganization of the inherited silica, irrespective of its form and solubility, cannot account for the bedded chert formation from the dolostone in the studied area. This then follows that for near complete replacement of dolostone by chert, silica has to be transported into the dolostone by an extraneous aqueous fluid. Studies have shown that solubility of silica in low temperature ($<300^0$C) aqueous fluids is a complex function of temperature, alkalinity, and alkali content of the fluid (Fleming and Crerar, 1982; Williams et al., 1985; Rimstidt, 1997; Utami et al., 2014; Crundwell, 2017). Although experimental data shows that silica content of a given low temperature fluid show positive correlation with these three parameters, its relative importance depends upon the physical and chemical composition of the fluid and nature of the substrate (the source of silica, Crundwell, 2017). Pressure does influence the silica solubility (positive correlation, Loucaides et al., 2012). However, published information does not suggest a stronger influence of pressure on solution/precipitation of silica in sedimentary early diagenetic condition. Published information puts following constraints on the dissolution of silica from the source rocks and transport in the aqueous fluids:

(a) Saturation of $SiO_2$ in aqueous fluid: keeping the influence of other parameters (temperature and chemical composition) the saturation value of $SiO_2$ in a given aqueous fluid depends upon the form of silica. At 25°C and varying pH of fluid, amorphous silica/opal, the likely precursor of the cryptocrystalline chert (Crundwell, 2017) has distinctly higher solubility (~117 ppm) than the quartz/chalcedony (~6ppm) that usually form cement in the chert (Mishra, 2012).

(b) pH has a marked influence on the solubility of silica (Fig. 6.9). At pH ≤9 (25ºC and 1 bar), solubility of silica in pure water does not depend upon the pH value irrespective of the form of silica (quartz/chalcedony or amorphous silica/opal). In this pH range $H_4SiO_4$, a neutral species, is virtually the only silica species in the aqueous fluid ($SiO_2+2H_2O= H_4SiO_4$). At higher pH, $H_4SiO_4$ dissociates by the reaction $H_4SiO_4= H^+ + (H_3SiO_4)^-$ (pH 9.8- 11.5) followed by the dissociation reaction $(H_3SiO_4)^-= H^+ + (H_2SiO_4)^-$ at pH ~11.5. For this reason, the solubility curve abruptly steepens in the pH range of 9 to 11 for ordered and disordered silica species (Fig. 6.9).

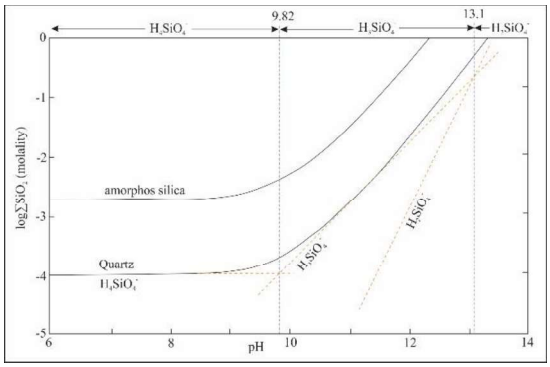


Fig. 6.9. calculated solubility of crystalline α-quartz and amorphous silica in pure water as a function of pH at 25$^0$c and 1bar. Note the solubility is constant up to about pH=9. Figure has modified after Mishra (2012).

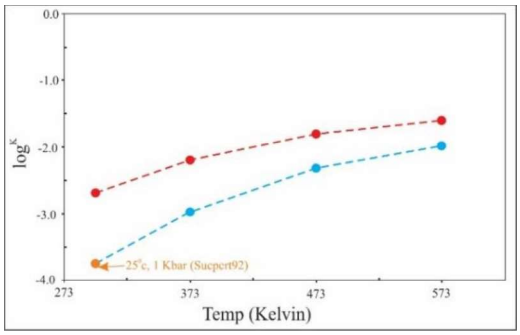


Fig. 6.10. Calculate solubility of amorphous silica in pure water as a function of temperature and pressure at pH>9. Note blue for 1 bar, cyan for 2 bar, green for 3 bar, red for 4 bar, magenta for 5 bar, purple for 6 bar, orange for 7 bar, pink for 8 bar, dark blue for 9 bar, power blue for 10 bar. Solubility of silica has calculated in SUPCRT92. Dotted line is the solubility of silica modified after Gunnarasson and Arnorsson (1999).

(c) Temperature enhances silica solubility, for both the amorphous silica and quartz, suggesting that dissolution process of silica is an overall endothermic process. The temperature dependence silica solubility equation of Gunnarsson and Arnorsson (1999) [valid up to pH =9, and 1 bar pressure] shows a significant drop of in solubility of amorphous silica (~100 ppm) in pure water if the temperature decrease from 100ºC to 25ºC (Fig. 6.10). Ignoring the small curvature of the solubility line, the pure water loses silica solubility (for the amorphous silica) in the tune of ~14 ppm per 10ºC decrease in temperature (Mishra, 2012; Thiry and Milnes, 2017). Owing to dilute concentration of $SiO_2$ in pure water at saturation (<1 mol $SiO_2$/kg of solution) at pH up to 11 (Fig. 6.9), the trapped water in the pore space of the precursor rock (even for an unrealistically high porosity of 60%) is unlikely to contribute significant $SiO_2$ in the chertification process.

(d) The kinetics of dissolution of silicates have been experimentally studied by many (Rimstidt and Barnes. 1980; Gunnarsson and Arnorsson, 1999). However, the exact

mechanism and the influencing factors on the reaction kinetics remain elusive. Nevertheless, there is a general consensus that other factors remaining constant, the rate of dissolution of silica from silicates with long rage disorder (such as glass or similar disordered form) is faster than highly ordered silicates (Fleming and Crerar, 1982; McBride, 1988; Bustillo, 2010). The dissolution process is further augmented by Na and K content of the fluid (Marshall and Warakomski, 1980; Thiry et al., 2006; Khalaf et al., 2020).

In this backdrop an attempt has been made to trace the source of silica that metasomatized and converted the dolostone to chert. Since, the natural waters seldom exceed pH>9 (Fleming and Crerar, 1982), it is reasonable to consider that the neutral species $H_4SiO_4$ (or $SiO_2aq$) was effectively the sole species in advective aqueous fluid. This then follows that temperature and nature of silica sink (ordered vs disordered form) controlled the silica content of the fluid. In view of the aforesaid points, role of pH of the fluid appears to be minimal in controlling tine silica content of the fluid. The Semri Group of rocks in and around the studied area has a thick porcellanite unit that is older than the Rohtas limestone. The studied area belongs to the upper part of Rohtas limestone (Fig. 6.1). Published information shows that the Porcellanite Bed is composed of volcanogenic and volcanoclastic materials akin to rhyolitic/rhyodacitic affinity (Srivastava et al., 2003; Paikaray et al., 2008; Basu and Brickford, 2014; Mishra et a., 2017a, b, c). This includes pumice, glass, lapilli, magmatic quartz and sanidine (Srivastava et al., 2003; Paikaray et al., 2008; Basu and Brickford, 2013; Mishra et al., 2013; Mishra et a., 2017a, b, c). In addition to these volcanogenic/volcanoclastic materials laterally persistent layers of green and gray opal are present in this unit (Srivastava et al., 2003; Paikaray et al., 2008; Basu and Brickford, 2013; Mishra et al., 2013; Mishra et a., 2017a, b, c). Studies also suggest that the among other features, the Porcellanite Bed is variably altered to illitic/smectitic clays and opal-rich pods and lenses (Mageswarii et al., 2019).

### 6.4.4. Hydrodynamics of chert forming fluid and mode of silica metasomatism:

In the previous section (section 6.4.3) it has been argued that the silica load of the chert forming fluid was likely to be sourced from the disordered and very unstable phases (glass, opal, sanidine) present in the Porcellanite Bed lying below the chertified dolostone (Rohtas limestone). However, availability of silica laden fluid is not the only factor to cause

extensive silica metasomatism of the studied dolostone. In the following para the roles of other critical factors that might play a crucial silica precipitation.

Time integrated fluid flux: The dolostone at the immediate contact with and presumably replaced by silica contains an average of 19 wt.% $SiO_2$. The silica in the dolostone occurs in different forms (quartz clasts; Fig. 6.3). A mass balance calculation is performed in a simple system to obtain a most conservative amount of silica that was deposited from the percolating fluid to transform the dolostone to chert. In this calculation 1 kg of chert is arbitrarily chosen. This amount of chert is formed from the dolostone precursor in the studied area. The chert for this calculation is considered to have 100% $SiO_2$. The density of quartz (2.65 gm/cc) at 25ºC and 1 bar yields a volume of 377cc for 1 kg of chert. Mass balance calculation (Fig. 6.8) suggest that chertification of dolostone required ~80.18 % increase in rock mass. This means 810 gm of silica was deposited from the fluid to produce 1 kg of chert. Considering, the maximum value of soluble $SiO_2$ in aqueous fluid at 25ºC (maximum 107 ppm when the substrate is amorphous silica, Gunnarsson and Arnórsson, 2000), a huge amount of fluid is required to pass through the dolostone for the formation of 1 kg chert. For the conservative estimate, of the quantitative fluid solubility value of aqueous fluid at 300ºC (just below the critical point of $H_2O$ at 1 bar) is used which is ~1500 ppm $SiO_2$ or ~1.5 gm of silica /kg of fluid. This means 540 kg of water was needed to produce per kg of chert. This translate to 540 liters (or 540000cc) of water assuming density of water to be 1gm/cc. It is to be noted that this is the most conservative estimate of fluid required to permeate through the dolostone to form 1 kg of chert.

Mode of silica precipitation: Studies have shown that up to a pH of ~9.82 (Fig. 6.9), solubility of silica remains virtually insensitive to pH of the aqueous fluid as $H_4SiO_4$ seems to be virtually the only soluble $SiO_2$ species. Natural waters including the sea water rarely exceed the pH 9.82. Fig. 6.10 shows the relation of temperature and the equilibrium constant of the two reactions:

- $SiO_2$(quartz) +$H_2O$ = $H_4SiO_4^0$(equilibrium constant $K_1$) ----------(equation 6.2)
- $SiO_2$ (amorphous silica) +$H_2O$ = $H_4SiO_4^0$(equilibrium constant $K_2$) -------(equation 6.3)

These diagrams are computed with the program SUCRT92 (revised and updated by Gunnarsson and Arnórsson, 1999) and the relations of Gunnarasson and Arnorsson (1999).

Both the methods show reasonable convergence (Fig. 6.10). Fig. 6.11 shows pressure dependence of silica solubility that is calculated using the updated program SUPCRT92 program. Solubility of silica in water does not appear to change up to the pressure difference of 2 Kbar (correspond to a crustal depth of ~6-8 km). The activities of the silica polymorphs and the water have taken as unit and owing to very low concentrations of $SiO_2$ in water over a range of temperature it is assumed that activity $SiO_2(aq.)=mSiO_2$ (aq.) (Mishra, 2012; Walther, 2009). Solubility of aqueous silica was then obtained from the equilibrium constant multiplying the K value with gram molecular wt. of $SiO_2$ and the amount was converted to ppm (Fig. 6.10). Two important features emerge from Fig. 6.10:

- If a fluid that was in equilibrium with amorphous silica or with very unstable (at near surface condition) silicate phases comes in contact with quartz, equation 6.2 will be operative and $K_1$ will be the equilibrium constant. Since $K_2>>K_1$ at any temperature and pressure, massive silica is expected to be deposited to achieve equilibrium.
- Other factors remaining constant, a drop in temperature also reduces silica solubility in eater and hence triggers the silica precipitation.

It is an established fact that owing to development of new surface of the product (positive surface energy) and that $\Delta G$ at the point of saturation at a given temperature and pressure is always positive (e.g. reviewed in Philpotts and Ague, 2009). This means no crystallization is possible at the point of saturation. To achieve significant crystallization of silica directly from the aqueous fluid, temperature must be lowered from the equilibrium (under cooling) till the $\Delta G$ of the reactions are sufficiently negative to allow homogeneous nucleation (eg. Direct precipitation from the fluid by equation 6.2 and/or 6.3). This then follows that the silica laden water can remain oversaturated without precipitation of silica till the $\Delta G$ of the silica-forming reaction to be sufficiently negative. The extent of undercooling is required to cause silica precipitation from the aqueous fluid in upper crustal conditions is not precisely known. Nevertheless, studies in magmatic system suggest several tens of degrees of under cooling for nucleation and growth. A significant reduction in the required undercooling for silica precipitation can be achieved if the rock in contact of the silica laden aqueous fluid contains some form of silica seed (e.g. quartz, chalcedony, amorphous silica etc.).

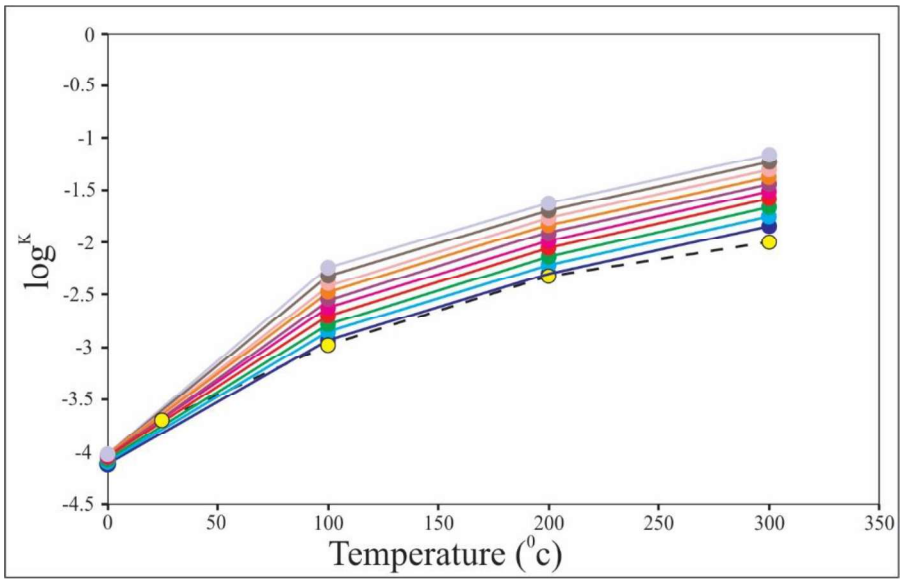


Fig. 6.11. Calculate solubility of amorphous silica in pure water as a function of temperature and pressure at pH>9. Note blue for 1 bar, cyan for 2 bar, green for 3 bar, red for 4 bar, magenta for 5 bar, purple for 6 bar, orange for 7 bar, pink for 8 bar, dark blue for 9 bar, power blue for 10 bar. Solubility of silica has calculated in SUPCRT92. Dotted line is the solubility of silica modified after Gunnarasson and Arnorsson (1999).

Integrating all the features it seems likely that a switch in equilibrium constants from $K_1$ to $K_2$ for silica precipitating reaction was caused by inherited quartz grains with or without a decrease in temperature. This phenomenon caused rapid and massive deposition of opal that eventually gave away to microcrystalline chert. The well-ordered macro quartz grain showing the cavity filling texture likely to have formed later than the opal (now microcrystalline chert) in view of low solubility of crystalline quartz (Fig. 6.11). Mixing with cold fluid and/or release of heat from the hot silica rich water to cold wall rock may cause cooling of the silica-bearing fluid at or near the surface and that can help precipitation of silica. However large scale mixing of hot and cold fluid (with lower $SiO_2$ content) might render a 'dilution effect' to the saturated, hot fluid and impede precipitation.

### 6.4.5. Mechanism of replacement of the dolostone by chert: a couple dissolution-precipitation

Replacement of a mineral or a rock by one or more minerals can be achieved chiefly by two mechanisms. These are diffusion (frame work of the mineral structure remains unaltered after replacement) and solution-precipitation (bonding of the mineral being replaced are completely destroyed during the replacement, reviewed in Vernon, 2004, Philpott and Ague, 2009). Considering the low values of diffusion coefficient of the elements over a range of physic chemical conditions, replacement via pure diffusion is

unlikely to operate beyond a few mm (reviewed in Putnis, 2002, 2009, Chowdhury et al., 2013, Talukdar et al., 2017). Furthermore, advective mass transport is considered to be the dominant, if not only, mode of mass transport that facilitate mineral replacement process through the solution-precipitation mechanism (Putnis, 2002, 2009; Putnis and Putnis, 2007; Hövelmann et al., 2010; Chowdhury et al., 2013). In the preceding section, it has been argued that for the extensive chertification of the studied dolostone required large flux of $SiO_2$ rich fluid. This together with (a) broadly layer parallel replacement of dolomite by chert that is traceable for more than km and, (b) a large difference in atomic structures in dolomite and any solid silica phases suggest that coupled solution-precipitation was the main process for chertification of the studied dolostone (Ruiz-Agudo et al., 2014). Textural features do suggest that the chert retains many features (like ooids, peloids) that are found in the dolostone and it replaced. These features suggest that the replacement was texturally non-destructive. In some places of chert, typical vug filling textures are noted. Here, acicular quartz/chalcedony are formed nearly perpendicular to the wall and pointing towards the aggregates of irregular mesoquartz (Fig. 6.5). This feature can be best explained by the sequence: dissolution of dolostone, formation of cavities, wall controlled crystallization of acicular quartz/chalcedony and formation of irregular meso-quartz at the center. Growth of the wall controlled acicular quartz/chalcedony suggest energetically favorable heterogeneous nucleation and growth over the direct precipitation of silica from the permeating fluid (homogeneous nucleation and growth, cf. McSween et al., 1987; Walther, 2009). Several experimental and theoretical studies have demonstrated that structurally non-destructive replacement in presence of fluid can be achieved by coupled solution-precipitation process in which (a) the replacement process occurs at the length scale of nanometers and, (b) the macroscopic volumes of the reactant and the product phases remain nearly constant (Putnis, 2002, 2009, Chowdhury et al., 2013, Ruiz Agudo et al., 2014, Renard et al., 2018). The published experimental studies on carbonate and non-carbonate substrate demonstrate that the controlling factors of coupled dissolution-precipitation are primarily dictated by difference of volumes, solubility and the rates dissolution and precipitation of reactant and the product phases (reviewed in Ruiz Agudo et al., 2014) and precipitating phases. The precipitation of the phases may be kinetic (heterogeneous nucleation and growth) or thermodynamic (super-saturation of the product phases is maximum in the region of higher dissolution of the reactant phases; Putnis, 2002; Ruiz Agudo et al., 2014). The textural destructive (vug filling) and nondestructive (preservation of ooids, peloids) replacement of the dolostone by chert are, therefore,

consistent with the experimentally determined coupled dissolution-precipitation process. The result of the experimental studies on coupled dissolution-precipitation also supports the view that inherited quartz in dolostone might trigger and facilitated the chertification process (McBride, 1988). This is because of the fact that the inherited quartz did the following:

- Helped the $SiO_2$ rich fluid, once equilibrium with disordered solid silica phase, to become supersaturated $K_1$ was the new equilibrium constant.
- Induced epitaxial growth and help the $SiO_2$ bearing fluid to overcome the activation energy barrier of amorphous silica precipitation.

However, direct application of the experimental results on dissolution-precipitation to the large scale chertification process is difficult. This is because of the fact that the reactant (dolomite) and the product (silica) phases have completely different compositions. Unlike what has been experimented, chertification of dolostone requires, besides precipitation of silica, removal of large amount of Ca, Mg, Fe and $CO_2$ from the chertified zone. As no secondary Ca-Mg-Fe bearing phases are noted within or adjoin dolostone layers of the chert, the fluid must have carried these elements out of the region of the present study. The liberated $CO_2$ should have no effect as $H_4SiO_4$ being the stable aqueous species at pH~10. Studies have shown that the coupled dissolution-precipitation occurs via a boundary fluid layer (cf. Renard et al., 2018). To achieve large scale chertification process and taking away the liberated Ca, Mg, Fe and $CO_2$, the reaction front must move deep into the dolostone along the permeable zones. Field features do not support any such zone in the adjoining dolostone. There is no evidence that the dolostone, now represented by chert layer, was highly permeable to induce large scale replacement process. One approach to resolve this problem could be the generation of secondary porosity during the replacement process (Putnis, 2002) or dissolution of carbonate by meteoric water diagenesis (Tucker, 1983). Several studies have demonstrated that the rate of dissolution, by and large, is faster than the rate of precipitation of new phases (reviewed in Putnis, 2002, Renard et al., 2018). If such a scenario developed during chertification of the dolostone, the reaction front could move through the open space it created. This mechanism has been established experimentally for a single mineral grain (Putnis, 2002) and can also be a viable process for km size replacement process. However, the flux of $SiO_2$ must be maintained across the reaction front during the entire period of the chertification process. More studies are

required to properly understand the large scale replacement process at nearly constant volume.

### 6.4.6. Model for route map of chertification by replacing dolostone in Rohtas Limestone

Collecting all the evidences and experiment data the following processes are envisaged for the present study of chert formation by replacement of carbonate rock (Fig. 6.12).

- Rohtas limestone exposed subaerially as soon as Lower Vindhyan sedimentation completed/ stopped by some reason. Rain fall (meteoric water) percolating into RLM through porosity and dissolving the carbonate.
- This meteoric water also penetrated deep up to the Porcellanite Formation (or even deeper).
- The fluid leached $SiO_2$ from the disordered silica sinks including glass, pumice, opal from pyroclastic beds (Porcellanite Fm., Rampur Shale, Rohtas Limestone) and became $SiO_2$ rich.
- If the elevated thermal structure prevailed during the fluid-rock interaction, temperature could further augment the silica leaching process by increasing the silica solubility and aiding the kinetics of silica dissolution. Alteration of the unstable and disordered sanidine to illite might enrich the fluid with $K^+$ which in turn increases the kinetics of dissolution. Evidence of alteration of Porcellanite Bed by hot water is recorded (McBride, 1988).
- The silica enriched fluid move through porosity and moves to younger direction, cooled down and acted as the source of silica for the chertification process.

### 6.4.7. Estimate the chert precipitating temperature and revise the paleotemperature of 1.6 Ga hydrosphere-atmosphere

Although silica precipitation from solution by colling process question on paleoclimate investigation as cooling can proceed in subsurface, but for the present study chertification at or near the surface realms that for the present study paleoclimate holds the signature of earth surface. Temperature dependence triple oxygen isotope data sets of studied chert samples has plotted in the $\Delta'^{17}O$ vs. $\delta'^{18}O$ space diagram (Fig. 6.13). The non-equilibrium relation of triple oxygen data sets with silica-sea water equilibrium curve also

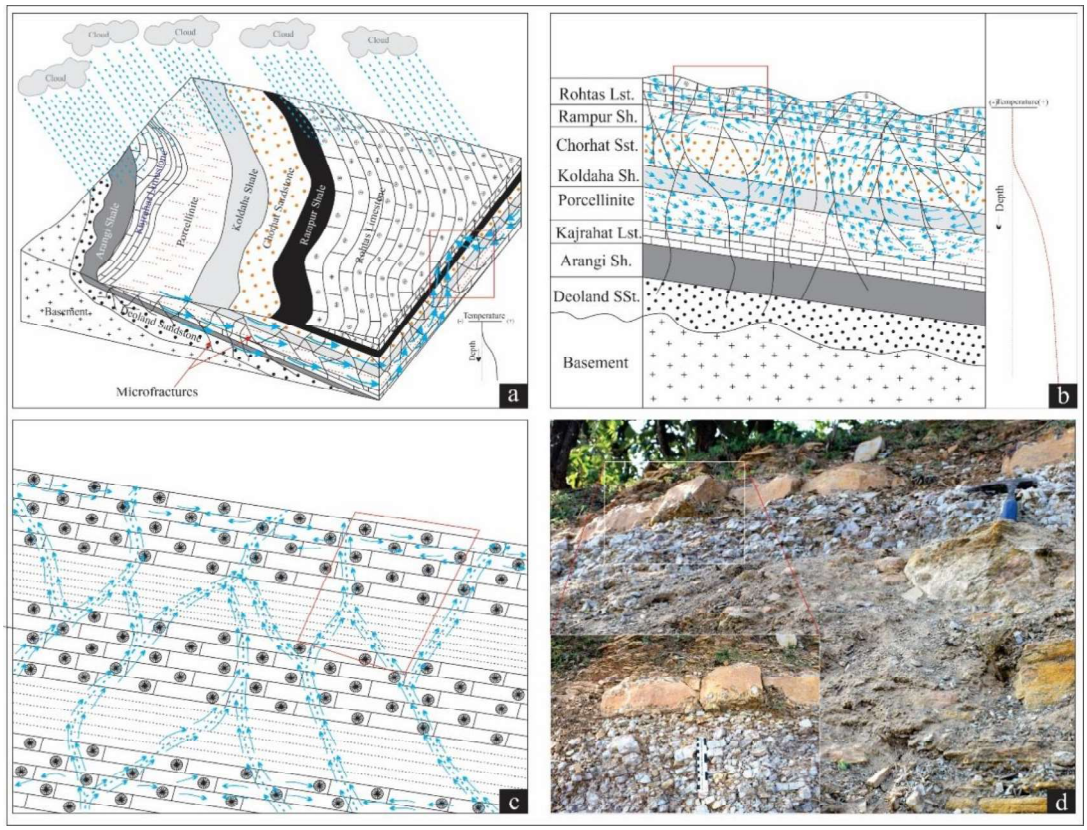


Fig. 6.12. Schematic diagram of chert formation by replacement of Rohtas Limestone. Percolation of rain water (meteoric water) through porosity-permeability-fractures and meteoric water is warming as it perceleting through deep rock in influence geothermal gradient (a; note geothermal gradient iset), enlarge view of marked zone of Fig. 6.12a (b; note the fluid movement in convection cycle in inflences of geothermal gradient; also note fluid is enriching in silica as porcellanite beds is suppling silica from unstable phases like glass, pumice, sanidine), enlarge view of marked area in Fig. 6.12b (c; note the fracture path formed by dissolution of dolostone due to meteoric water percolation and hot silica supersaturated fluid is also easily percolating through this paths, and precipitationg the chert along this paths as temperature drop by replacing the dolostone), field photographs related with enlarged view of Fig. 6.12b marked by red dooted rectangle (d; hammer length 35 cm; note the enlarge view with).

support the context of meteoric water chert formation not directly from sea-water (Fig. 6.13). As discussed in section 5.4.1 and 5.4.3, meteoric water ($\Delta'^{17}O \approx +0.03‰$ and $\delta'^{18}O \approx -10‰$)-silica equilibrium curve estimates the temperature of 25°C. This then the temperature is the earth surface temperature as it cooled down in land surface.

In previous chapter 5, it has already discussed that the chert form by replacing the carbonate rock buffer in a high temperature fluid and the present 3-O isotope is a mixed up oxygen isotope of initial carbonate deposition and diagenetic fluid. The final value of 3-O isotope follows equation 5.1. As calculated above, in studied section chert has formed at F/R ratio of ~0.81 from around ~300°C temperature fluid. In understanding of this, revised the chert precipitation fluid (black star in Fig. 6.13) and we proposed that chert has

precipitated from around $\Delta'^{17}O \approx +0.01‰$ and $\delta'^{18}O \approx -7.25‰$ as soon as this silica supersaturated fluid cooled. Ultimate temperature of chert is around 40°C.

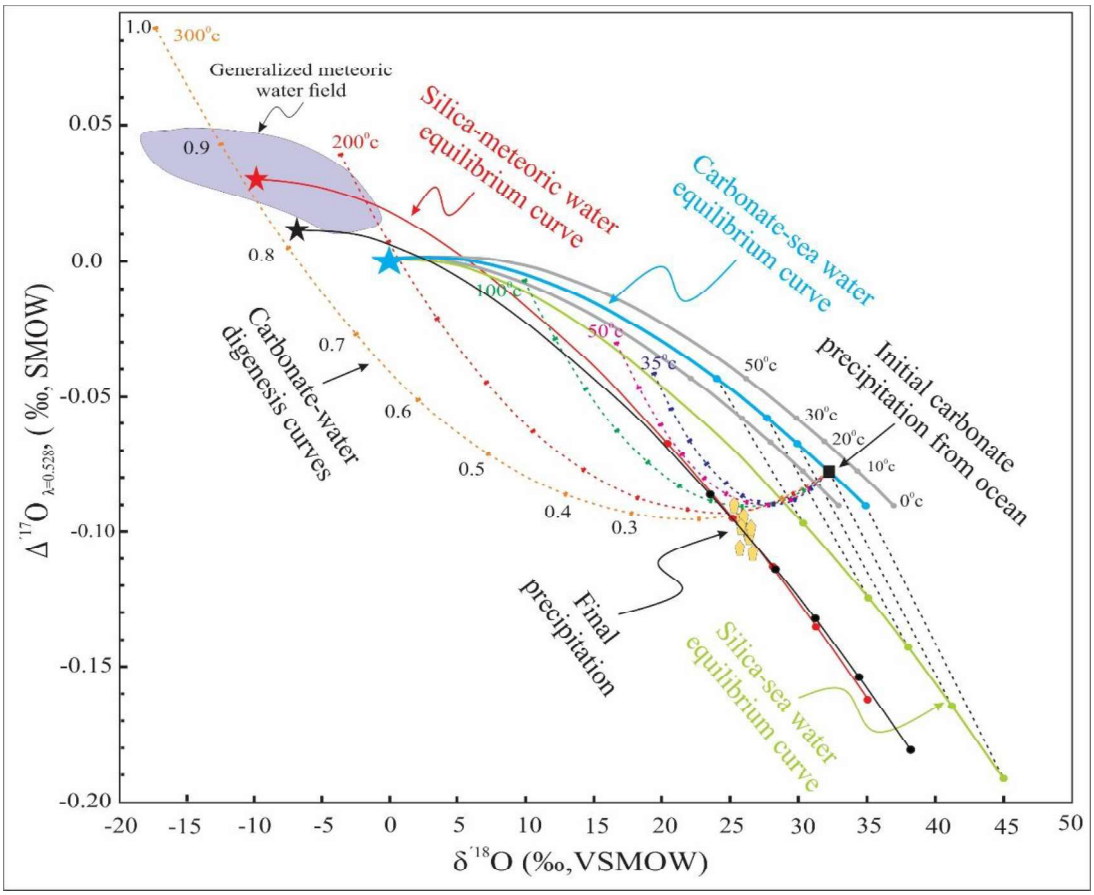


Fig. 6.13. Revised possible reaction sequence to explain the triple oxygen isotope value of carbonate replaced chert from the triple oxygen isotope data of present study. Carbonate was initially precipitating at $10^0$c temperature with equilibrium of SMOW (black diamond). 300°C hot silica rich pore fluid buffered the carbonate rock following the orange dotted line at black star. This fluid cooled and precipitated quartz at $40^0$c, in equilibrium of silica-fluid composition ($\delta^{18}O \approx -7.25‰$ and $\Delta'^{17}O \approx +0.01‰$; red solid line). Possible ancient triple oxygen isotopes are result of a long range temperature fluid (35°C to 300°C) interaction with initial sedimentary rock (may be carbonate, shale, iron minerals, phosphates) at different F/R ratio.

We extrapolate that carbonate was initially precipitated at 10°C in equilibrium with sea water at composition of $\Delta'^{17}O \approx +0.073‰$ and $\delta'^{18}O \approx 32.6‰$ (marked in Fig. 6.13). Carbonate interact with silica supersaturated hot fluid, equilibrate its oxygen isotope with at and around F/R≈0.81 (orange line in Fig. 6.13). This fluid then percolates through porous space in grains and/ or bed boundary and come at or near earth surface. With decreasing of temperature, quartz precipitate at or near 40°C (marked in Fig. 6.13). Ultimate cooling temperature of silica fluid is around 40°C. It is questanible wherether this colling temperture will be use as paleo-temperature and paleo-climate recordered.

## 6.5. Conclusion

Present model and measurements indicate that the chertification is not a simple process of sea water and meteoric water mixing. Further, show silica enrich fluid is depending on pH of fluid, temperature and pressure. Chert precipitate from a silica rich fluid of pH> 9.82 with a wide range of temperature and pressure. Precambrian chert may have formed from a hot temperature fluid form ($\geq 100^0$c) and these are the record direct hydrothermal fluid and wall rock interaction. The summary of present study outline as:

a) Studied chert has formed by replacement of dolostone, in an interaction of hot silica enrich fluid and meteoric water.
b) Chertification process has completed with constant volume. Chertification processes increase about 212% mass of dolostone.
c) 540-liter silica enrich fluid has precipitated total 1 kg of chert. In the present study, silica has enriched total 81%.
d) The source of silica was disordered silica present in the earlier deposit of Vindhyan succession. Dissolution of volcanic materials (porcellanite) enhance alkalinity. Burrial pressure increases the tempresure.
e) To form the chert pH of fluid must be >9.82 but temperature may be very high (>300ºC) as solubility of silica is not changed with high temperature (i.e. 100ºC to 300ºC) at constant pressure.
f) 3-O isotope preserved in studied chert is a modified version of F/R ratio of 0.81. Chert pecpitate at 40ºC from 300ºC hot silica fluid.
g) Composition of Mesoproterozoic ocean was equilibrated with modern ocean and carbonate was precipitated from a water composition of $\Delta'^{17}O \approx +0.073‰$ and $\delta'^{18}O \approx 32.6‰$ at temperature of 10ºC.

# CHAPTER 7

# Revisiting the boundary of the Upper and Lower Vindhyan Group in Son Valley Vindhyan, Central India

## 7.1. Introduction

The Paleo to Neoproterozoic Vindhyan Supergroup, largest 'Purana' basin in India and world's second largest Proterozoic basin, is one of the most well studied and focused Proterozoic successions in India (Fig. 1.1; Auden, 1933; Banerjee, 1974; Sastry and Moitry, 1984; Bhattacharyya, 1996; Rai et al., 1997; Seilacher et al., 1998; Bose et.al., 2001, 2015; Ray et al., 2002; Rasmussen et al., 2002; Sarkar et al., 2002a, 2004, 2006, 2014; Banerjee et al., 2006; Malone et al., 2008; Bengston et al., 2009, 2017; Kumar and Sharma, 2011; Chakraborty et al., 2012; Gopalan et al., 2013; Tripathy and Singh, 2015; Bickford et al., 2017; Gilleaudeau et al., 2018; Mishra et al., 2018; Sallstedt et al., 2018). The Vindhyan basin, exposed in the eastern part of central India is divisible into Bundelkhand sector and Son valley sector (Fig. 1.1, Chakraborty, 2006; Chakraborty et al., 2010; Sarkar and Banerjee, 2020). The basin-wide unconformity divides the Vindhyan succession into two parts, lower Vindhyan/ Semri Group and the upper Vindhyan (Table-1.1). However, the exact stratigraphic position of the unconformity is still controversial. Previous studies carried out in the Bundelkhand sector, the unconformity lying between the lower and the upper Vindhyan has been considered above the Rohtas Limestone (top most succession of the lower Vindhyan Group) and below the Sasaram Sandstone (equivalent to Lower Quartzite of the Kaimur Formation; Chakraborty, 2006; Fig. 7.1). In contrast to this, most of the previous studies in the Son valley sector noted that the top part of the Rohtas Limestone gradually passes upward into the Bhagwar Shale which is composed of sand-silt alternations with substantial amount of volcanic input (Fig.7.2; Banerjee, 1974; Sastry and Moitry, 1984; Chakraborty and Chaudhuri, 1990; Bhattacharyya, 1996; Chakraborty, 2006; Kumar and Sharma, 2011) and the unconformity between the lower and upper Vindhyan lies above this shale (Fig. 7.1). A claim has also been made that the arkosic/ pebbly sandstone of the Sasaram Sandstone (also known as Lower Quartzite) observed above the unconformity in the Bundelkhand sector is absent in the Son valley sector (Chakraborty, 2006).

Recent fieldwork in the Son valley sector along ~150 km stretch from Mohaniyain in East (24°25'34.06"N, 81°40'8.86"E) to Kymore (24°3'36.78"N, 80°36'31.53"E) in West (Fig. 1.5) reveals the presence of a sandstone having maximum thickness ~12 m immediately above the Rohtas Limestone with a sharp, undulating and erosional contact in between (Fig.

7.2). A thin (ca.15 cm), laterally persistent and sheet-like coarse-grained layer with chertified limestone clasts demarcate the erosional contact between the Rohtas Limestone and the sandstone (Fig. 3.2a). So far the sandstone had not been described and detail sedimentalogical study of this sandstone is non-existent. Possibly this is the reason why most of the previous workers considered the Bhagwar Shale within the lower Vindhyan/ Semri Group and placed the unconformity above it (Banerjee, 1974; Rao and Neelakantam, 1978; Sastry and Moitry, 1984; Bhattacharyya, 1996; Chakraborty, 2006; Valdiya, 2010; Kumar and Sharma, 2011).

The goal of the present paper is to revisit the boundary between the lower and upper Vindhyan in the Son valley sector and also to record the nature of this contact with the help of a detailed sedimentary facies analysis of this sandstone, hitherto undescribed.

## 7.2.Geological background

The Vindhyan basin, developed during the Palaeo to Neoproterozoic time (Bose et al., 2001; Chakraborty et al., 2010), rests unconformably on the Aravalli craton, the Bundelkhand granitic gneiss and the Mahakoshal Group of rocks. The Vindhyan rocks are distributed over ~1,00,000 sq km. The Vindhyan sediments are generally unmetamorphosed and only mildly deformed. The geophysical investigation has suggested the presence of E-W trending faults that initiated the formation of the Vindhyan basin (Naqvi and Rogers, 1987). The rifting was accompanied by a dextral shear which created some NW-SE elongated sub-basins where the sedimentation took place (Bose et al., 1997, 2001). As a result, strike-wise variations in both thicknesses of the constituting facies and sediment character change are rapid in the Lower Vindhyan/ Semri Group (Bose et al., 2001). Contrastingly the Upper Vindhyan Group is laterally persistent, likely to be deposited in a sag basin (Chanda and Bhattacharyya, 1982; Bose et al., 2001; Sarkar et al., 2002b). The beds are much steeper in the lower part compared to that of the upper part of the Vindhyan succession.

The Vindhyan sediments are exposed into three outcrop sectors viz., Bundelkhand sector, Son valley sector and Rajasthan sector (Chakraborty, 2006; Chakraborty et al., 2010). The Bundelkhand and Rajasthan sectors are dominated by carbonate sediments, the sediments in Son valley sector is also represented by both siliciclastic and carbonate in nearly equal volume (Chakraborty, 2006; Chakraborty et al., 2010). The Son valley Vindhyan has a maximum thickness of 4.5 km. They are constituted by two Groups- lower

Vindhyan/ Semri Group and upper Vindhyan Group separated by a basin-wide unconformity (Fig 7.1; Kumar 1978a, 1978b; McMenamin et al., 1983; Chakraborty and

| | | Fm. | Eastern part of Son valley sector (existing) | Western part of Son valley sector (existing) | Proposed stratigraphy of Son valley sector | Age (Ma) |
|---|---|---|---|---|---|---|
| VINDHYAN SUPERGROUP | UPPER VINDHYAN GROUP | BHENDER | Upper Bhander Sandstone | Upper Bhander Sandstone | Upper Bhander Sandstone | |
| | | | Sirbu Shale | Sirbu Shale | Sirbu Shale | 625±25[F-T]Srivastava and Rajagopalan, (1988) |
| | | | Lower Bhander Sandstone | Lower Bhander Sandstone | Lower Bhander Sandstone | |
| | | | Bhander Limestone | Bhander Limestone | Bhander Limestone | 908±72[Pb-Pb] Ray et al. (2002) 1075-900[Pb-Pb] Gopalan et al. (2013) |
| | | | Ganurgarh Shale | Ganurgarh Shale | Ganurgarh Shale | |
| | | REWA | Rewa Sandstone | Rewa Sandstone | Rewa Sandstone | |
| | | | Rewa Shale | Rewa Shale | Rewa Shale | 1100-700[Chauria-Tawuia] Rai et al. (1997) |
| | | KAIMUR | Dhandraul Sandstone | Dhandraul Sandstone | Dhandraul Sandstone | |
| | | | Scarp Sandstone/ Mangeswar Sandstone | Scarp Sandstone/ Mangeswar Sandstone | Scarp Sst./ Mangeswar Sst. | |
| | | | Bijaigarh Sh. | | Bhagwar Shale/Silicified Shale | 1210±52[Re-Os] Tripathy and Singh (2015) |
| | | | Ghaghar Sandstone Upper Sandstone/Quartzite | | | |
| | | | Susunia Breccia | | | |
| | | | Silicified Shale | | | |
| | | | Sasaram Sandstone (Lower Quartzite) | | Sasaram Sandstone (Lower Quartzite) | |
| | | UN | | | | |
| | LOWER VINDHYAN / SEMRI GROUP | ROHTAS | Rohtas Limestone | Bhagwar Shale / Rohtas Limestone | Rohtas Limestone | 1514±120[Pb-Pb] Chakraborti et al. (2007) 1599±48[Pb-Pb] Sarangi et al. (2004) 1601±130[Pb-Pb] Ray et al. (2003) |
| | | | Rampur Shale | Rampur Shale | Rampur Shale | 1599±8[SHRIMP] Rasmussen et al.( 2002) 1602±10[SHRIMP] Rasmussen et al.( 2002) |
| | | KHEINJUA | Chorhat Sandstone | Chorhat Sandstone | Chorhat Sandstone | |
| | | | Koldaha Shale | Koldaha Shale | Koldaha Shale | |
| | | | PORCELLANITE | | | 1628±8[SHRIMP] Rasmussen et al.(2002) 1630.7±0.4[U-Pb] Ray et al.(2002) 1631.7±5.4[SHRIMP] Ray et al.(2002) 1640±4[$^{206}$Pb/$^{207}$Pb] Bickford et al.(2017) |
| | | KAJRAHAT | Kajrahat Limestone | Kajrahat Limestone | Kajrahat Limestone | 1721±90 [Pb-Pb] Sarangi et al.(2004) |
| | | | Arangi Shale | Arangi Shale | Arangi Shale | |
| UN | | | DEOLAND / MAHAKOSHAL GROUP | | | |

UN-Unconformity; Fm.-Formation

Fig. 7.1. Stratigraphy of Vindhyan Supergroup, Son valley (modified after Auden, 1933; Banerjee, 1974; Rao and Neelakantam, 1978; Sastry and Maitry, 1984; Bhattacharyya, 1996; Chakraborty, 2006; Chakraborty et al., 2010; Kumar and Sharma, 2011).

Bose, 1992a, b; Chakraborty, 1993; Bose et al., 2001; Schieber et al., 2007; Paikaray et al., 2008; Pati et al., 2008; Raza et al., 2010; Sallstedt et al., 2018). Five formations are present (Deoland, Kajrahat, Porcellanite, Kheinjua, and Rohtas) within the Lower Vindhyan Group while there are three formations (Kaimur, Rewa and Bhander) present within the Upper Vindhyan (Kumar, 1978a, 1978b; McMenamin et al., 1983; Chakraborty and Bose, 1992a, b; Chakraborty, 1993; Bose et al., 2001; Schieber et al., 2007; Paikaray et al., 2008; Pati et al., 2008; Raza et al., 2010; Sallstedt et al., 2018). The age of the Vindhyan Supergroup ranges from 1721 Ma to 650 Ma (Chakraborty et al., 2010 and references there in; Gopalan et al., 2013; Tripathy and Singh, 2015; Bickford et al., 2017). Dominant lithologies of the Supergroup are mature sandstone, shale, carbonate, and conglomerate, mostly intra-formational. Dominance of shallow marine depositional regime has been considered mostly (Singh, 1973; Banerjee, 1974; Chanda and Bhattacharyya, 1982; Prasad and Verma, 1991) with a range of variation from barrier bar-lagoon, tidal and beach to relatively deeper part of Shelf (Chakraborty and Bose, 1992; Chakraborty, 1995; Bose et al., 2001; Sarkar et al., 1996, 2002a, b). On the other hand, subordinate amount of fluvial and aeolian deposits also have been reported from the Supergroup (Bhattacharyya and Morad, 1993; Bose and Chakraborty, 1994; Bose et al., 1999; Chakraborty and Chakraborty, 2001).

### 7.3. Stratigraphic Problem

The Bhagwar Shale is well exposed in parts of the Son valley sector (Fig. 7.2). The Bhagwar Shale composed of sand-silt alternations with a substantial amount of volcanic input (Chakraborty, 2006). The shale is well exposed along the studied stretch (Fig. 1.5). A persistent sandstone layer is present below the shale (Fig. 7.2). The upper contact of the sandstone with the Bhagwar shale is gradational while the lower contact of the sandstone is sharp and undulatory with the underlying Rohtas Limestone (Fig. 7.2). The contact of the Bhagwar shale is also gradational with the overlying Kaimur Formation. The color of the shale varies from grey to dark grey; even black at places, both vertically as well as laterally. The sand/silt stringers present within the shale are laterally continuous. Some laterally persistent sand layers with sole features at their bases are present within the shale. Very fine-grained tuff layers are also present within the Bhagwar Shale (see Fig. in Chakraborty et al., 1996). As discussed the sandstone below this Bhagwar Shale is directly overlying the Rohtas Limestone (Fig. 3.1, 3.2, 3.3, 3.4, 3.5) and here lies the problem of placing the boundary between lower and upper Vindhyan in this sector. So far in most of the studies, the boundary has been demarcated above the Bhagwar shale which is showing

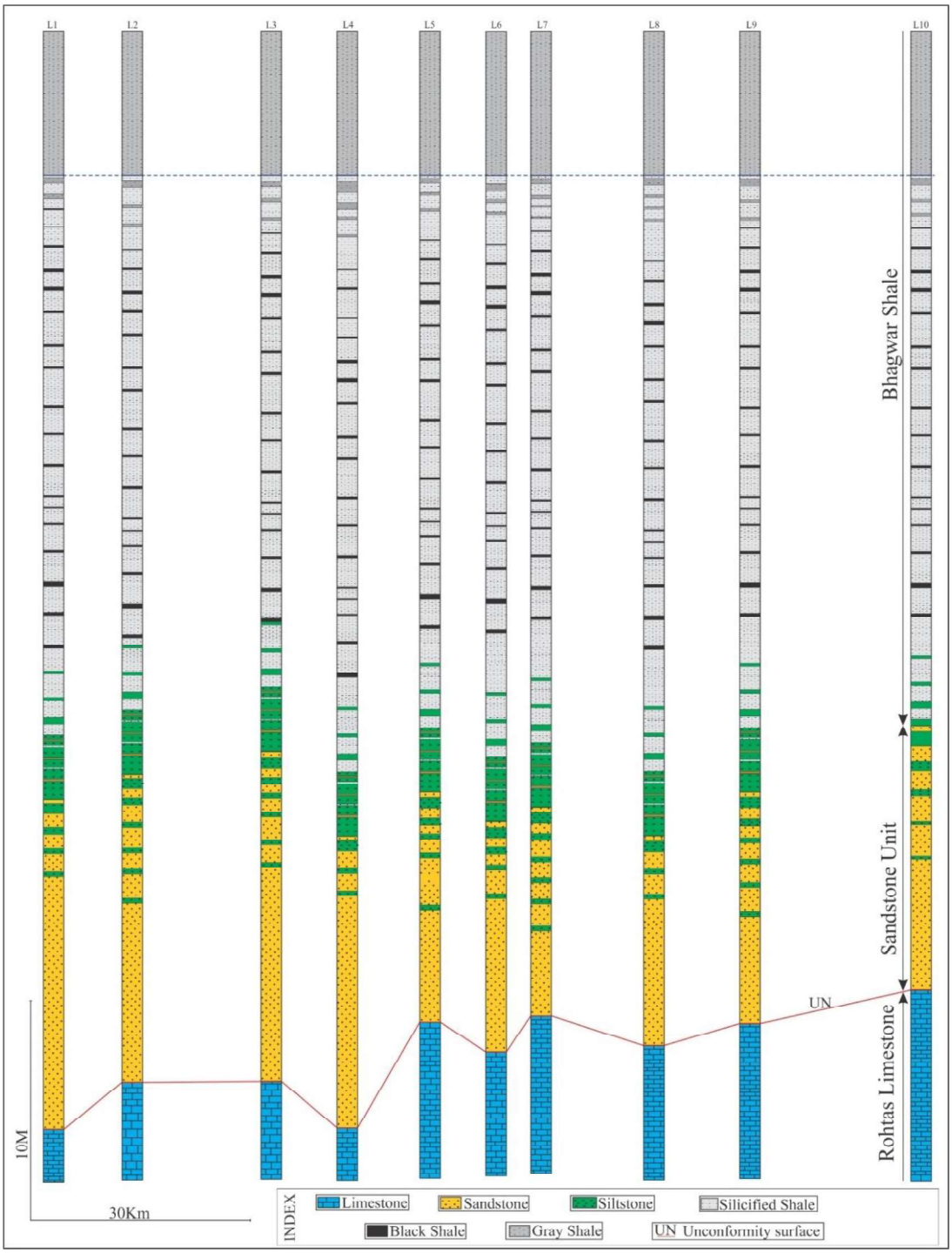


Fig. 7.2. Stratigraphic sections across the boundary between lower and upper Vindhyan along the studied stretch (marked in Fig.1.5). Note the unconformable relationship between the Rohtas limestone and the overlying sandstone unit. Also note the gradational relationship between the Sandstone and the overlying Bhagwar Shale.

a gradational boundary with the overlying Mangeswar/ Scrap Sandstone of Kaimur Formation. However, the sandstone lying below the Bhagwar Shale has not been reported earlier in the Son valley sector and hence, demands a detailed study before considering the contact between lower and upper Vindhyan.

### 7.4. Facies analysis of the sandstone present immediate above the Rohtas limestone

Deposition of the Semri/ lower Vindhyan Group ends with ca. 110m thick Rohtas Limestone (topmost part of the Rohtas Formation). The upper part of the Rohtas Limestone is chertified in many places (Fig. 7.2). The Rohtas limestone in the Son valley sector is overlain by ca. 12m thick sandstone unit (Fig. 7.2). The boundary between the Rohtas Limestone and the overlying Sandstone is sharp, erosional and demarcated by a thin (~10 cm) sheet-like unit containing pebbles of chertified limestone (av. clast size 5cm) at several places in the study area (Fig. 3.2a). Possibly these pebbles are derived from the upper part of the chertified Rohtas Limestone.

This sheet-like pebble bearing unit is followed upward by a laterally persistent sandstone unit (max thickness 12 meter) along ~ 150 Km East-West stretch of the study area (Fig. 1.5). The overall grain size of this sandstone varies from coarse to fine sand. Considering the primary sedimentary structures, sediment composition and bed geometry the sandstone can be subdivided into two facies associations - (a) Facies Association I and (b) Facies Association II (Fig. 3.1). The constituting facies of Facies Association I is in general of fine to medium size sandstone and also rich in mud compared to that of Facies Association II. As mentioned earlier the details regarding this sandstone unit are not available in the literature, so we thought it is pre-requisite to discuss this sandstone in detail before finalizing the boundary between the lower and the Upper Vindhyan in the Son valley. Following are the detailed description and interpretations for each Facies Association of the sandstone.

#### 7.4.1. Facies Association I

Facies Association I is distinctly different from the facies association II with respect to grain size (varying from medium to fine sand) and mud content. This Facies Association I is dominantly cross-stratified in nature and consists of four major facies. See the details description and interpretation of each facies in section 3.2.1.

### 7.4.2 Facies association II

This association occasionally interferes with the Facies Association I. However, Facies Association II, characteristically contains less mud compared to Facies Association I. Facies Association II primarily consists of coarse to fine-grained sandstone. Five facies comprising of the Facies Association II are discussed as described in section 3.2.2.

## 7.5. Discussion

The Rohtas Limestone is the topmost unit of Lower Vindhyan succession. The limestone is overlain by laterally persistent sandstone in the studied stretch of the Son valley (Fig. 7.2). The sandstone deposited on an undulating surface over a transgressive lag formed on the top surface of Rohtas Limestone. The majority of the clasts present within the lag derived from the Rohtas Limestone. The majority of the lime-clasts are chertified. The top most part of the Rohtas limestone is also chertified at places. The degree of chertification also varies laterally to a remarkable extent. The chertified layers thus often appear to have irregular geometry and boundaries difficult to trace. Often they appear laterally discontinuous. Only exposure or near-exposure on earth surface can account this much abundance of silica during post-depositional alteration or weathering of the limestone. It is likely that part of the Rohtas limestone was exposed for a long period of time which helps chertification (Kolodny et al., 1980). However, the transgressive lag indicates a fresh sedimentation event. The sedimentation started on a tide-dominated shelf. The presence of thick-thin alternation, double mud drape the cross-strata bear tell-tale evidence of tide domination. This tide-dominated environment layers, herringbone cross-stratification, reactivation surface and frequently mud lamina within intervened by storm is evidenced by the presence of hummocky cross-stratification, an amalgamation of sandstone beds, conglomerates/ massive beds with sole features. The presence of numerous sand-clasts within the facies association II supports the influence of microbiota that turned sand into a cohesive (Sarkar et al., 2014, 2018). The vertical transition of the facies assemblages rules out any major paleogeographic shift.

Some of them indicate clear evidence of subtidal deposition while a shallow marine depositional environment can be inferred from the sandstone in general. This sandstone unit is gradationally overlain by a shale unit known as Bhagwar Shale, also laterally persistent over the studied area (Fig. 7.1).

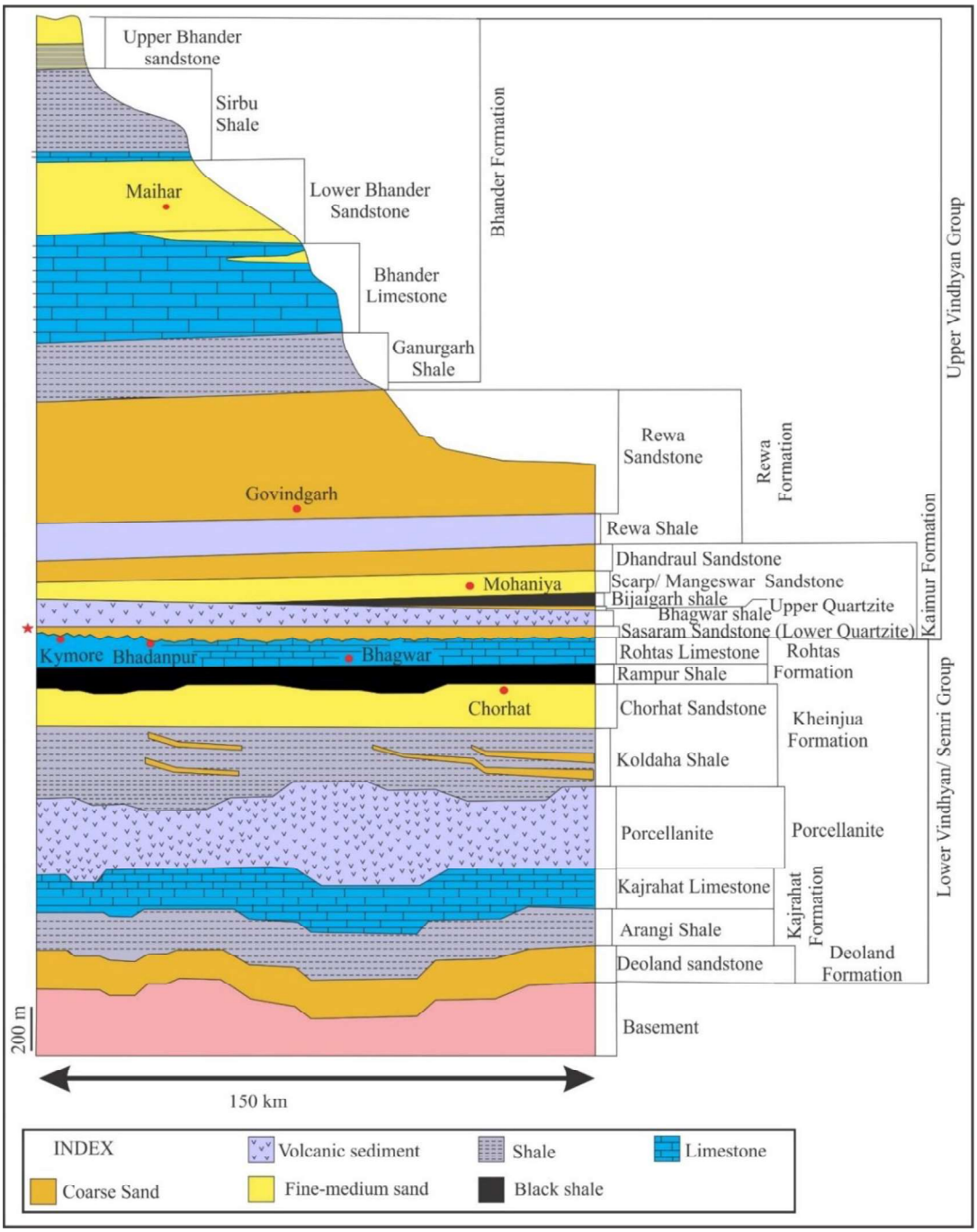


Fig. 7.3. Stratigraphic column of Vindhyan Supergroup present in the Son valley, Central India (modified after Chakraborty, 2006). Note the laterally persistent sandstone unit present above the Rohtas Limestone with an erosional surface in-between, traced from Mohaniya to Kymore.

The boundary between the Lower and the Upper Vindhyan should be placed below the sandstone unit that indicates a change from a carbonate depositional system of Rohtas Limestone to a siliciclastic regime. The presence of transgressive lag, consisting of pebbles of chertified limestone supports the initiation of a sedimentation event after a considerable gap. This sandstone deposited above the Rohtas Limestone is likely to be the equivalent of

Sasaram Sandstone (Lower Quartzite member of the Kaimur Formation) reported from the Bundelkhand sector of the Vindhyan basin (Chakraborty, 2006; Chakraborty et al., 2010). The depositional milieu of the newly studied sandstone resembles that of Sasaram Sandstone (Chakraborty and Bose, 1990). After considering the detailed study in this part of the Son valley sector it seems the boundary between the upper and the lower Vindhyan has not been placed properly (Fig. 7.3). Rather it will be more logical to put the boundary between the same at the base of the newly discovered sandstone which is equivalent of Sasaram Sandstone (Lower Quartzite).

## 7.6. Conclusions

Considering the facies distribution and sediment distribution in the studied streach, present study draws the following conclusion.

(a) Two-tier stratigraphic subdivision of the Vindhyan Supergroup viz. lower and upper Vindhyan is well entranced in literature. The unconformity separating the lower and upper Vindhyan is placed above the Rohtas Limestone Formation in the Bundelkhand sector. However, in the Son Valley sector it is placed above the Bhagwar Shale, a sandstone-shale heterolithic unit. Our study, therefore, contradicts the exiting view regarding a gradational transition between the Rohtas Limestone and overlying Bhagwar Shale

(b) Revisiting contact relationship between the Bhagwar Shale and Rohtas Limestone with the employment of process-based facies analysis, the present study documents a ~ 12m thick laterally persistent sandstone unit, hitherto undescribed, directly above the Rohtas Limestone with a sharp, erosional contact. The sandstone gradationally passes upward to the sensu-stricto Bhagwar Shale.

(c) The presence of transgressive lag dominantly consists of chertified lime clasts picked up from long-exposed Rohtas Limestone surface, at the basal part of the sandstone unit bears tell-tale evidence for initiation of a new sedimentation regime with transgression on unconformity surface.

(d) From the interpretation of depositional processes, a shallow-marine, subtidal environment is suggested for the sandstone unit. Possibly a tide-dominated shelf condition developed with transgression that is occasionally intervened by storm. Similar sedimentation history also recorded from the Sasaram Sandstone (i.e. Lower Quartzite

member of Kaimur Formation) that overlies the Rohtas Limestone in the Bundelkhand sector.

(e) The process-based appraisal indicates that sedimentation starts with laterally persistent sandstone above the unconformity surface of Rohtas Limestone. The sandstone, in turn, gives way upward to the Bhagwar Shale.

(f) The contact between the Lower and Upper Vindhyan in the Son Valley should be placed below the sandstone described in this work and not above the Bhagwar Shale

# CHAPTER 8

# Origin and sequence stratigraphic implication of high-alumina glauconite within the Lower Quartzite, Vindhyan Supergroup

## 8.1. Introduction

Fe-Mg-bearing dioctahedral glauconite originates by the active exchange of cations in seawater and pore-water in a marine condition (Odin and Matter, 1981; Velde, 2003; Meunier and El Albani, 2007), although it may form in other environments in rare occasions (Banerjee et al., 2016). Glauconite is poorly represented in the Precambrian as it contributes ~5% of the total record (Banerjee et al. op. cit.). The chemical composition of glauconite has possibly evolved through time as the Precambrian variety is found be enriched in $Al_2O_3$ and depleted in $Fe_2O_3$ compared to its Phanerozoic counterpart (Dasgupta et al., 1990; Deb and Fukuoka, 1998; Banerjee et al., 2016a, b; Tang et al., 2017a; Rudmin et al., 2017; Bansal et al., 2017, 2018). Ferruginous seawater facilitates the transformation of the Mesoproterozoic glauconite to chamosite, which is a Fe-Mg-rich, K-poor variety of authigenic green clay minerals (Tang et al., 2017b). Although, the modern glauconite forms primarily within a depth range between 200 and 500 m (Odin and Matter, 1981), during the Precambrian it possibly formed in shallow marine rocks (Banerjee et al., 2008, 2015; Tang et al., 2017a). The crystallo-chemical properties of the shallow marine glauconite are poorly addressed. Recent studies indicate that the composition of the Phanerozoic authigenic glauconite depends on factors like the chemical composition of the substrate, availability of Fe, depositional redox conditions and the stratigraphic condensation (Banerjee et al., 2016; Meunier and El Albani, 2007; Bansal et al., 2017,2018,2019; Rudmin et al., 2017, 2018). However, because of the lack of data, the influence of these factors on the composition of Precambrian glauconite is yet to be tested. The Precambrian glauconite often bears the signature of Mg-rich ocean (Banerjee et al., 2018). The Mg content of the glauconite is, however, overlooked as it does not depend on the compositional maturity. Amorosi (2013) attempted to relate the authigenic glauconite to 'simple omission surface', 'condensed section' and 'mega-condensed section' for sequence stratigraphic applications. However, the extrapolation of these concepts of stratigraphic condensation to Precambrian shallow marine succession needs detailed facies and paleogeographic analysis.

The present study envisages the origin and depositional implications of the glauconite in the Mesoproterozoic Lower Quartzite Member of the Kaimur Formation, Vindhyan Supergroup. The glauconite occurs at the top part of the member. Objectives of

the paper are as follows: a) to highlight the crytallo-chemical evolution of the Precambrian glauconite, b) to check the depositional and sequence stratigraphic implications of glauconite in Precambrian succession and c) to compare the glauconite with the Phanerozoic variety. We have carried out extensive facies and paleogeographic analysis to infer the depositional environment and to present the sequence stratigraphic framework of the glauconitic horizon within the Lower Quartzite Member of the Kaimur Formation. A thorough mineralogical and mineral chemical investigation highlights the crystallo-chemical characteristics of the Mesoproterozoic glauconite.

## 8.2. Geological setting

The studied glauconite belongs to the Lower Quartzite Member, of the Kaimur Formation in the Vindhyan basin in central India (Fig. 1.1). The Lower Quartzite occurs immediately above the Rohtas Limestone of the Semri group with an erosional unconformity in between.

### 8.2.1. Stratigraphy and age constraints

The entire Vindhyan sedimentary succession is mildly deformed and metamorphosed (Bose et al., 2001). It rests on the granitic basement or Mahakoshal Group of rocks in central India (Bose et al. op. cit.). The presence of an unconformity between the Kaimur and the Rohtas Limestone formations divides the Vindhyan succession into two, viz. Lower Vindhyan/ Semri Group and Upper Vindhyan (Fig. 1.3). The Rohtas Limestone, the uppermost member of the Semri Group was deposited c.a.1601-1514 Ma ago (Fig. 1.3; Ray et al., 2002; Sarangi et al., 2004; Chakraborti et al., 2007). While the age of the overlying Bijaigarh Shale of the Kaimur Formation is constrained to 1210 Ma (Tripathy and Singh, 2015). Therefore, the glauconite in the Lower Quartzite Member belongs to early Mesoproterozoic because of its occurrence in between the Rohtas Limestone and Bhagwar Shale.

The glauconitic sandstone beds occur at the top part of the Lower Quartzite Member (Fig. 8.1). The Lower quartzite succession gradationally passes over to the Bhagwar Shale. The Bhagwar Shale is dominated by the shaley sediments and it exhibits alternations between black shale and fine tuff, which in turn, gradationally passes upward to the pyritiferous, organic-rich Bijaigarh Shale (Fig. 8.2; Chakraborty, 2006; Banerjee et al., 2006).

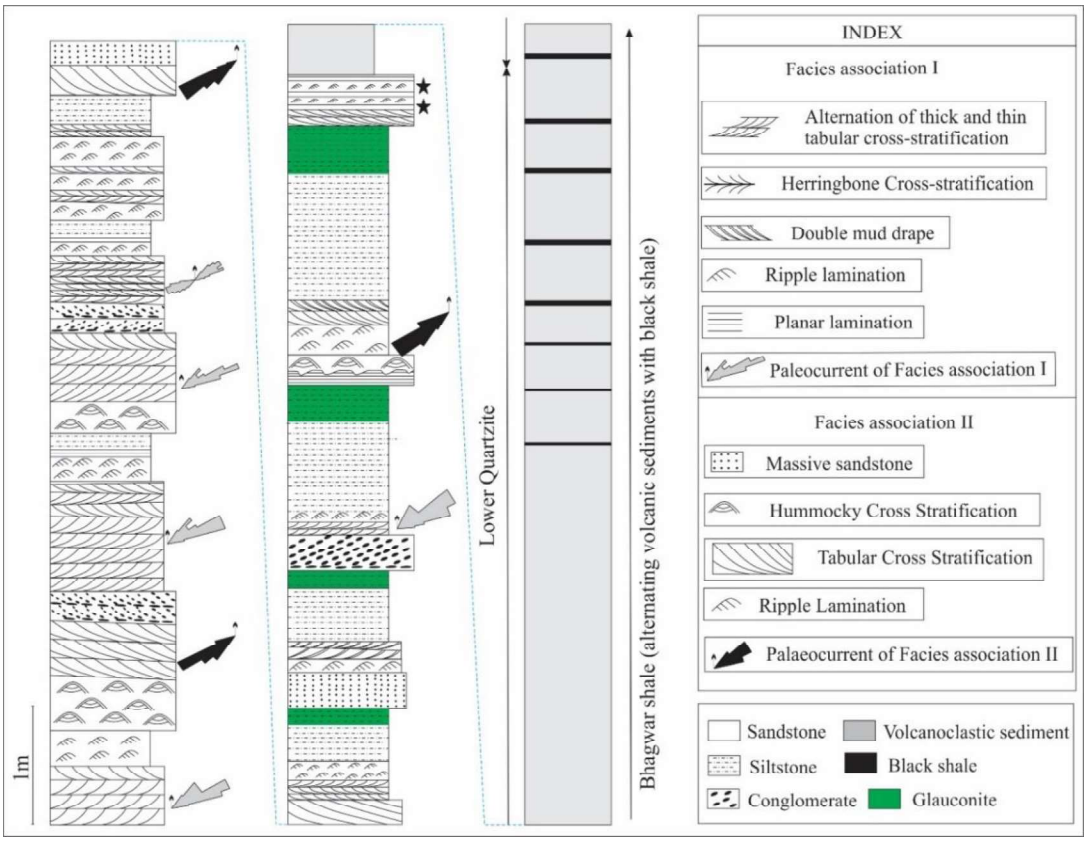


Fig. 8.1. Distribution of the facies associations along with palaeocurrent directions of two Facies associations of the Lower Quartzite Member in the studied area (occurrences of glauconite horizon is marked by green colour).

### 8.2.2. Depositional and sequence stratigraphic interpretation of the Lower Quartzite

The Lower Quartzite succession, occurring above the unconformity on Rohtas Limestone consists entirely of siliciclastic followed by Bhagwar Shale in turn overlies by Bijaigarh Shale (Fig. 8.1, 8.2). The sedimentation above the unconformity starts with a thin (ca. 10 cm) granular lag (Fig. 3.2a). The upper part of the Lower Quartzite Member is shaley, the thickness of shale increases upward (Fig. 8.1). The Lower Quartzite Member can be subdivided into two facies associations i.e. I and II, based on lithology, primary sedimentary structures and grain-size variability (Fig. 8.2). The description of each facies in is provided in Table-8.1. The Lower Quartzite Member is overlain gradationally by Bhagwar Shale, comprises of shale and sandstone intercalations. This fining upward interbedded shale- sandstone succession ascribed to predominant storm deposition (Bose et al., 2001). This shale gradationally overlies another shale unit which is black in colour, sand free at its top and pyrite rich known as Bijaigarh Shale (Fig. 8.3). Above this Bijaigarh Shale Upper Kaimur Sandstone is present. The lower part of the Upper Kaimur Sandstone

| Table-8.1. Description of facies in facies associations | |
|---|---|
| Facies association I | |
| Planar lamination | Intermittent mud lamina in sandstone has defined this facies with an average thickness 20 cm (Fig. 5f) in a sand mud alternation. Thickness of mud laminates 0.3 cm and 2 cm for sand lamina. |
| Small scale ripple lamination | Thicknesses of ripple laminations are c.a. 5 cm. Ripple crests are straight to sinusoidal. Crests are bifurcating on bedding surface. Mud is present at the foreset boundaries of ripples (Fig. 5e). Ripples are dominance in siltstone. |
| Herring bone cross-stratification | Two successive oppositely dipping cross-strata with a distinct erosional boundary in between characterize this facies (Fig. 5c). The orientation of herringbone cross-strata shows bimodal bipolar distribution. In places herring bone cross-stratified beds contain mud clasts. Double mud drape occurs in places within cross strata (Fig.5d). |
| Alternative thick thin tabular cross-stratification | This facies is characterized by abundant unidirectional cross-stratification with an average set thickness 15 cm. Internally cross-stratifications are alternate with thick thin planar cross stratum (Fig. 5b). Foreset boundaries of cross-strata are separated by thick mud parting. Thickness measurement show cyclic repetitions of foreset thickness. A maximum 28 laminae occur between two thick successive peaks. |
| Facies association II | |
| Wave ripple lamination | This facies is present on top of hummocky cross-stratified sandstone. Ripple crests are straight and bifurcated (Fig. 5k). Abundant syneresis cracks are present above this facies. |
| Amalgamated tabular cross-stratification | This facies is characterized by amalgamated sandstone bed with cross- stratification (Fig. 5j). Cross stratification is mainly tabular. Paleo-current direction of cross- stratification is directed towards WNW. It is commonly associated with massive sandstone and hummocky cross-stratification. |
| Hummocky cross-stratification | This facies is characterized by well-sorted sandstone with tabular to lenticular bed geometry and convex up top (Fig. 5i). Hummocky and swales are frequent with c.a. wavelength 35 cm and amplitude 10 cm. Abundant sole features occupy the basal part of this facies. |
| Massive sandstone | It consists of coarse-grained sandstone without any distinguish structures (Fig.5h). Gutters, flutes and tool marks are common at the basal part of the sandstone beds. It grades upward into non-cyclic cross-stratification with lateral transition. |
| Conglomerate | It consists of matrix-supported conglomerate with lenticular body geometry (Fig. 5g). Clasts are composed of chertified limestone and basement fragment, with minor sand clasts. Base of this facies is sharp and scoured (Fig. 5g). It is graded into massive sandstone. |

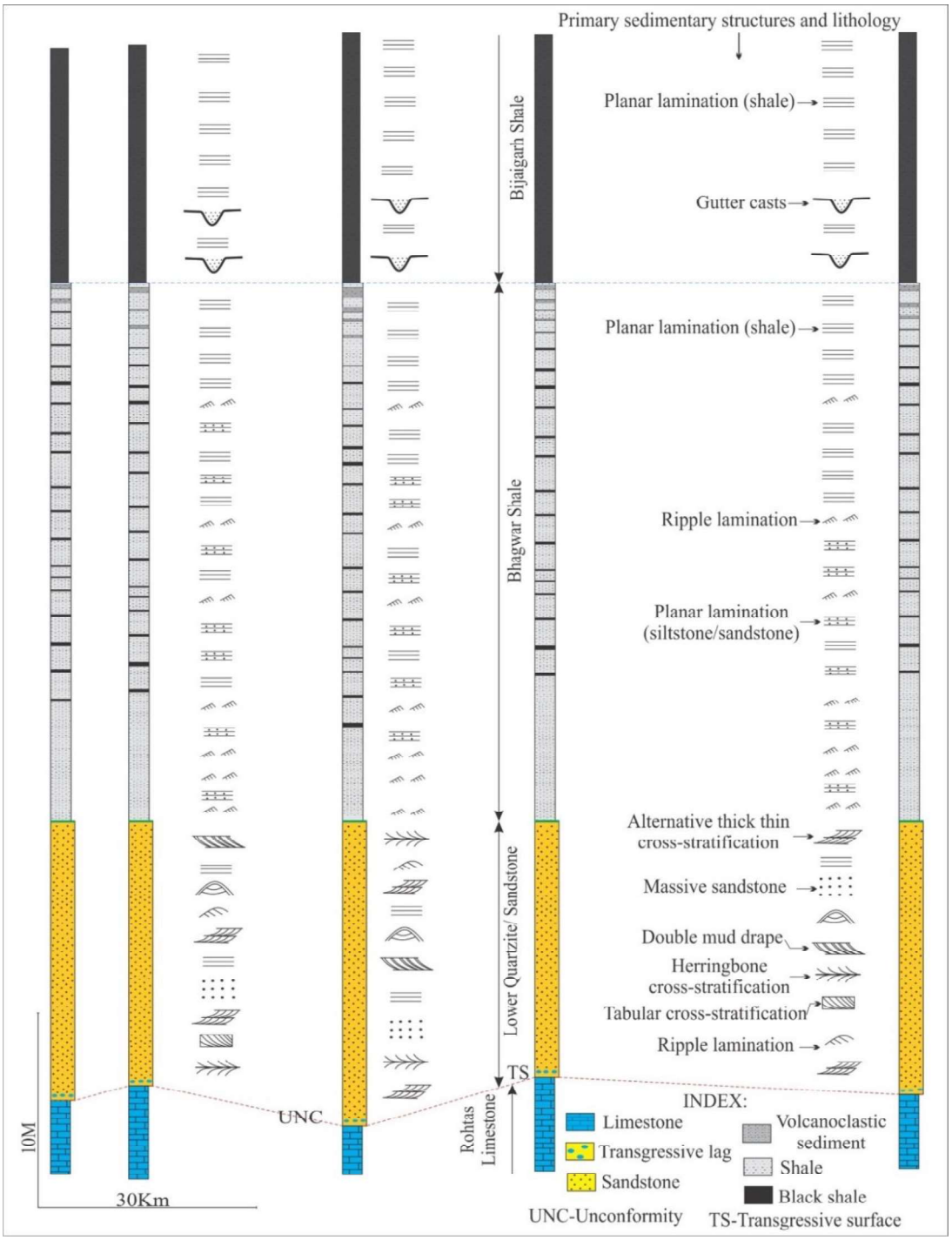


Fig. 8.2. Stratigraphy section across the boundary between Lower Vindhyan and Upper Vindhyan (modified after Mandal et al., 2019).

is composed of a shelf Sandstone gradually passes upward into fluvial and aeolian deposits in a coarsening upward succession (Chakraborty, 1993; Bose et al., 2001).

The presence of primary sedimentary structures such as alternating thick-thin laminae and abundant mud content within sandstone beds indicate the deposition of sediments in a tide-dominated environment (Bose et al., 1997). Unidirectional cross-stratification represents the bed load deposition. The conspicuous alternative thick-thin laminae indicate a bi-monthly tidal cycle with 28 foresets. Herringbone cross-stratification corroborates the deposition within a tidal regime. The presence of double mud drape in alternating thick-thin tabular cross-stratification facies indicates the subtidal depositional setting. Episodic storm events frequently interrupt the tide-dominated depositional condition. Coarse-grained sandstone and conglomerate indicate a high-energy product in a tidal setting. Conglomerate with a basal scour suggests turbulent flow that is high enough to pick up the chertified lime clasts from the underlying Rohtas Limestone. The massive sandstone beds represent quick deposition. Lateral and vertical transitions of the conglomerate to massive sandstone suggest deposits of a single flow. The sharp and scoured base of all facies within the facies association II, bearing flute casts, tool marks represent the deposition from a high energy flow, possibly related to a storm surge. The presence of hummocky cross-stratification with sole marks corroborates this interpretation. Wave ripples on hummocky cross-stratification facies form during the waning flow of storm. Therefore, the Lower Quartzite Member represents the deposition in a tide-dominated environment that is frequently affected by storms.

The thin granular lag between the Lower quartzite and the Rohtas Limestone represents a transgressive lag (cf. Catuneanu, 2009). The presence of a transgressive lag at the basal part of the Lower Quartzite indicates the commencement of sedimentation after a prolonged gap. The unconformity above the Rohtas Limestone represent a sequence boundary (Fig. 8.3). Increasing thickness of the shale at the expense of sandstone in the vertical succession of the Lower Quartzite indicates retrogradation of the shoreline. The transgression continued until the deposition of overlying Bhagwar Shale and Bijaigarh Shale (Bose et al., 2001). This continued transgression likely to represent a transgressive system tract (TST) followed by a Maximum flooding zone (MFZ, Fig. 8.3) within the Pyritiferous Bijaigarh Shale. Therefore, the transgressive systems tract (TST) deposits immediately overlying the granular lag consists of Lower Quartzite Member, Bhagwar

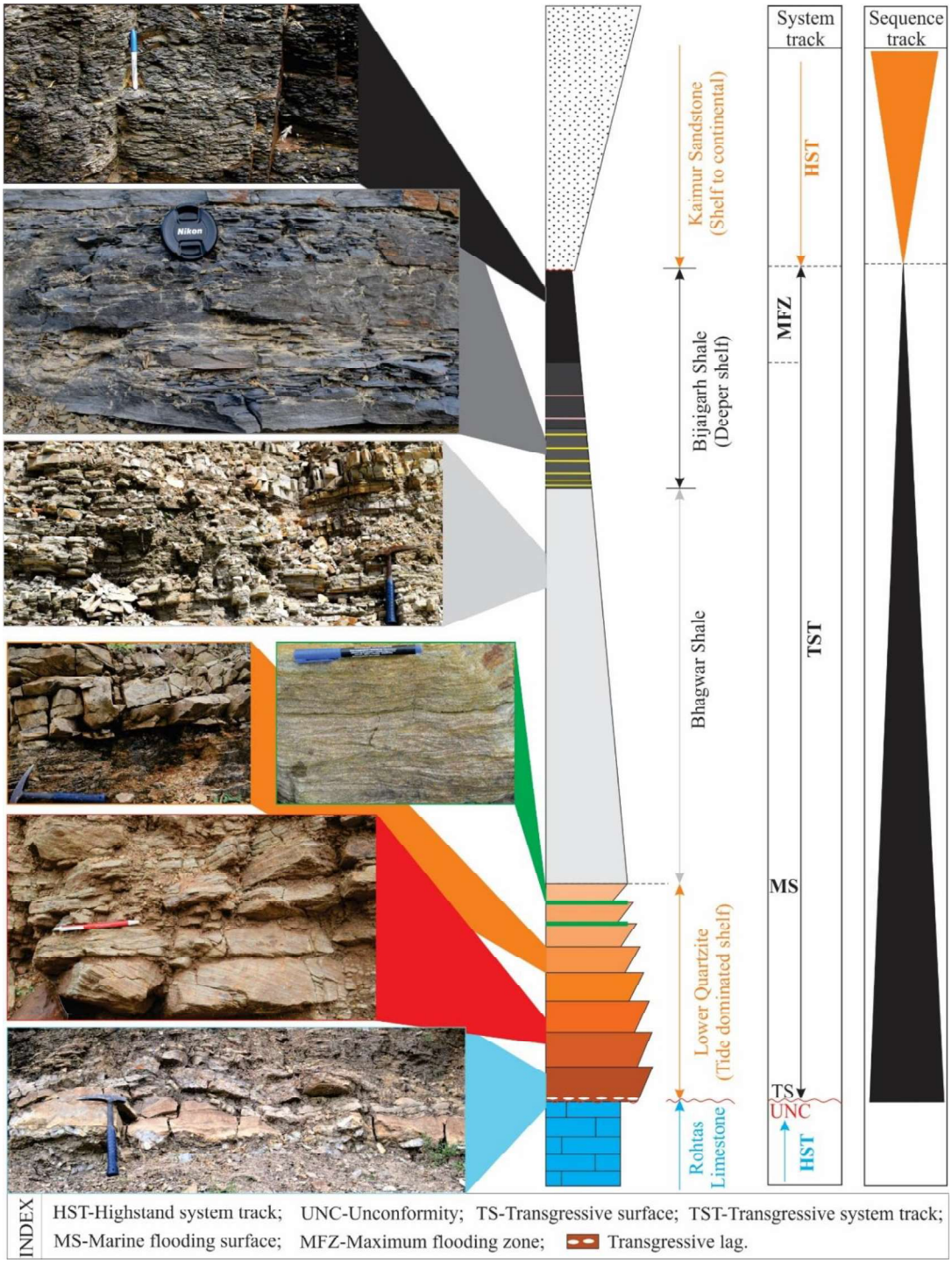


Fig. 8.3. Sequence stratigraphy system tract and sequence boundary in studied section.

Shale and Bijaigarh Shale with a MFZ at its top (cf. Bose et al., 2001; Banerjee et al., 2006). Within the overall TST the Lower Quartzite Member consists of no. of coarsening up individual para-sequences (Fig. 8.3). The thickness of the para-sequences present within the Member also decreases upward (Fig. 8.3). The TST is overlain by Kaimur Sandstone, possibly of shelf to continental origin (Chakraborty, 1993) represents another High stand

system tract (HST, Fig. 8.3). Glauconite exclusively occurs within the sandstone horizon of the topmost parasequence of the Lower Quartzite Member and is absent in the underlying sandstone and the overlying shale (Fig. 8.1, 8.3). This fact also disagrees the transportation of glauconites from the deep water during the deposition of the sand unit, a large part of which is a tidal deposit.

## 8.3. Samples and methods

The glauconite samples were collected from the Lower Quartzite Member of the Kaimur Formation in Kymore section (24°3'36.78"N, 80°36'31.53"E; Fig. 1.5). Thin sections prepared from the glauconitic sandstone samples were examined using Leica DM 4500P polarizing microscope attached to Leica DFC420 camera. Major element concentrations of glauconite were estimated in 8 thin sections on 75 points using a Camera SX 5 Electron Probe Micro Analyzer at Department of Earth Sciences, Indian Institute of Technology Bombay, with following specifications: accelerating voltage 15 kV, specimen current of 40 nA and beam diameter of 1µm (peak: 10–20s and background counting: 5-10s) and analytical error less than 1%. Standards include both synthetic and mineral phases. Glauconite pellets were separated from the lightly crushed rocks using Zeiss Stemi 2000 stereo zoom microscope for geochemical and mineralogical analysis. About 0.1 gm of glauconite pellets was powdered and ultrasonicated for the preparation of smear mounts. These smear mounts were scanned from 1° to 70° (step size–0.026° 2θ), using the nickel filter copper radiation at a scan speed of 96 sec/step in an Empyrean X-Ray Diffractometer with Pixel 3D detector at Department of Earth Sciences, Indian Institute of Technology Bombay. The $Fe^{+2}/Fe^{+3}$ ratio of glauconite pellets was measured by the titration process (cf. Kelly and Webb, 1999).

## 8.4. Results

### 8.4.1. Composition of glauconitic sandstone

The glauconitic sandstone primarily consists of quartz and feldspar grains. The feldspar frequently alters to glauconite. The rare minerals include zircon, tourmaline, rutile and apatite grains. The quartz and feldspar grains are sub-rounded to rounded, while glauconite pellets appear well rounded. The sandstone is moderate to well sorted. Both monoclinic and polycrystalline quartz occur within the sandstone, although the former type dominates (av. 65%) over polycrystalline quartz (av. 5%). The modal percentage of

unaltered feldspar grains is ~10% modal percentage. The feldspar includes both orthoclase and microcline variety. The content of glauconite within the sandstone is around 20%. The detailed petrographic investigation identifies the sandstone as sub-arkose. The sandstone is entirely devoid of ferromagnesium minerals. Glauconite represents the earliest authigenic phase, occurring within feldspar grains, which is surrounded by an extensive overgrowth of feldspar. The overgrowth around the feldspar grain indicates their early diagenetic origin (cf. Dasgupta et al., 1990).

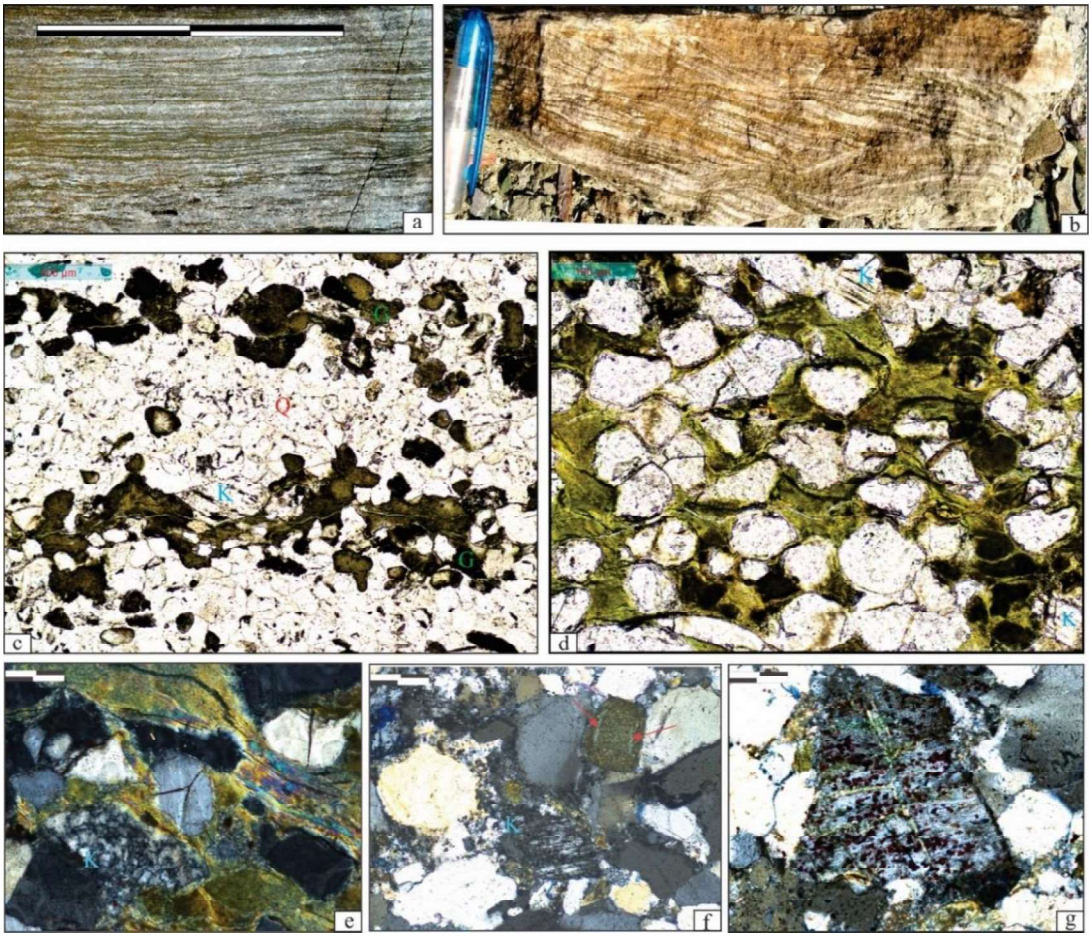


Fig. 8.4. Planar laminated glauconitic sandstone (a; bar length 15 cm). Cross stratified glauconitic sandstone (b; pen length 15 cm). Microscopic photograph of green sands (c; feldspar is marked by K, quartz is marked by Q, glauconite is marked by G). Replacement texture of glauconite (d). Glauconitization around feldspar grains (e, f, g; bar length 50 micrometer, feldspar is marked by K) Note their occurrences along fracture plane and cleavage of feldspar (fracture plane is marked by arrow).

### 8.4.2. Types of Glauconite

Glauconite occurs at the top part of the ca. 12 m thick Lower Quartzite Member (Fig. 8.1). It occupies the mid-level of the transgressive systems tract deposits of the Kaimur Formation. It concentrates along planar laminae and foresets of cross-stratified

sandstones (Fig. 8.4a, b). The glauconite commonly occurs as linear stringers along with fractures and cleavages of feldspar grains (Fig. 8.4c, d, e, f, g). In places, the glauconite largely replaces feldspar grains in the form of pellets, leaving tiny remnants of the original substrate (Fig. 8.4d). Occasionally, the glauconite surrounds feldspar grains as thick rims (Fig. 8.4e, f, g). Individual glauconite pellet has a long dimension of 2 mm. The glauconite appears light green under plane polarized light and third-order light green to dark green under cross-polar.

### 8.4.3. Mineralogy of glauconite

X-ray Diffraction studies on glauconite grains were carried out using both randomly oriented powder mount and oriented sample mounts. In random powder diffraction, sharp and symmetrical peaks of (001) at 10.31Å and (003) at 3.35Å respectively, are the most dominant peaks (Fig. 8.5a). Other peaks include (020) at 4.51Å, (060) at 1.51Å, (130) at 2.57Å, (112) and ($11\bar{2}$) at 3.10Å and 3.65Å, respectively (Fig. 8.5a). The diffraction patterns of the oriented sample show strong basal reflections of (001), (002), (003) and (005) at 10.31Å, 4.98Å, 3.34Å and 1.99Å respectively (Fig. 8.5b). The (060) reflection at 1.51Å confirms the presence of 'glauconite' and rules out illite. The glauconite peaks become more intense and appear symmetrical upon glycolation and heating (at 400°C for 1 hr), but the peaks do not shift position (Fig. 8.5b).

Quartz occurs as an impurity and interferes with the (003) peak of glauconite at 3.34 Å and ($11\bar{1}$) at 4.26Å, causing difficulty in identifying the glauconite polytype. The sharp and intense basal reflection of (001) at 10.31Å, which does not shift upon glycolation and heating, indicates the lack of interstratification of expandable and non-expandable layers (Thomson and Hower, 1975; Odin and Matter, 1981; Amorosi et al., 2007). The presence of sharp and symmetric peaks at 10.31Å, 4.51Å, 3.34Å and (112) and ($11\bar{2}$) reflections indicate a 'well ordered 1M mineral glauconite' (cf. Bentor and Kastner, 1965).

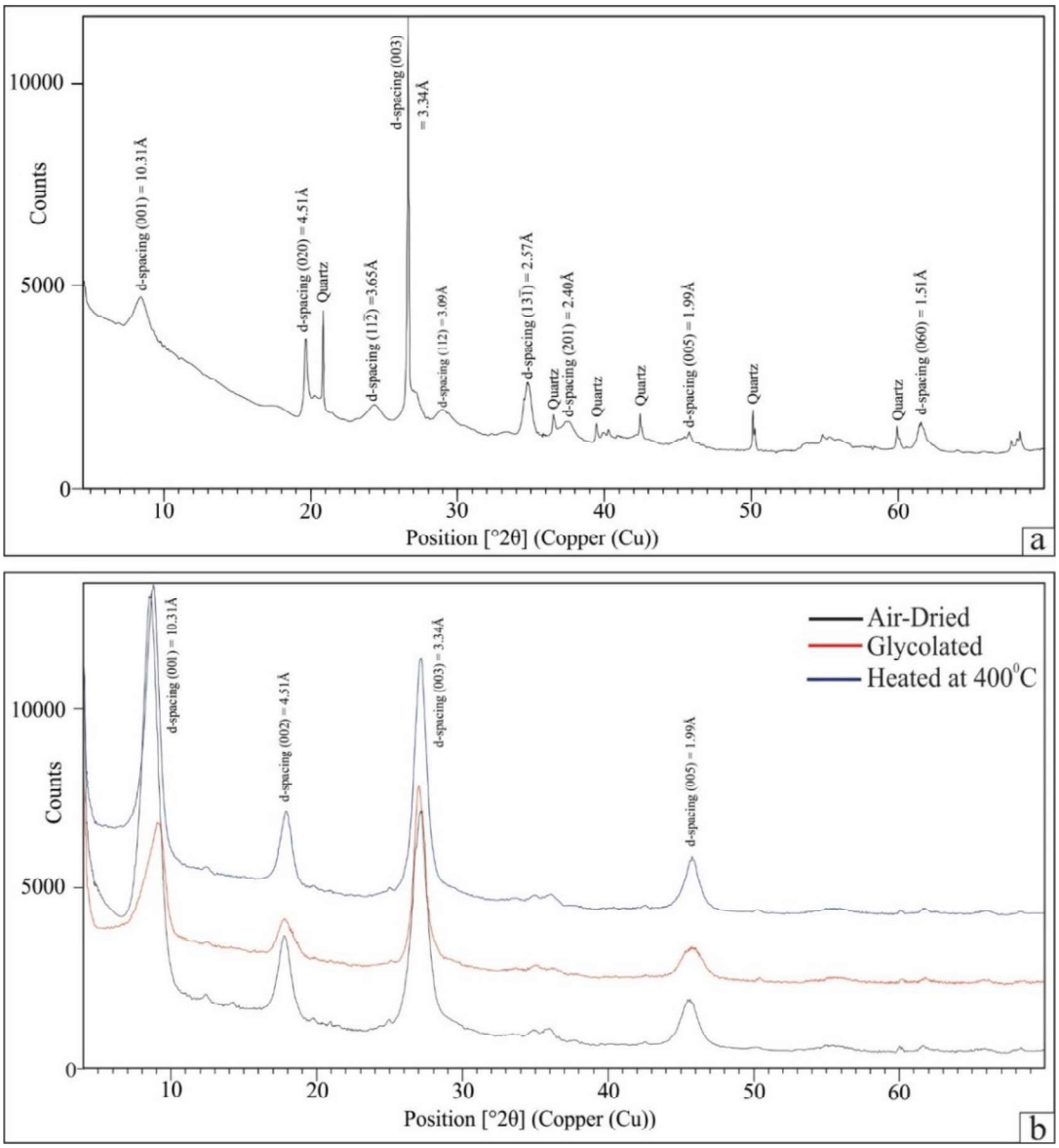


Fig. 8.5. X-ray diffractograms in random oriented glauconites (a). X-ray diffractograms of glauconite under different conditions i.e., air-dried, glycolated and heated at $400^0$c (b).

### 8.4.4. Major element composition

The $K_2O$ content of the glauconite varies from 6.69 wt% to 8.27 wt% (Table-8.2). The $Fe_2O_3$ (total) content of glauconite is low, varying from 4.50 to 9.60 wt% (Table-8.2). The $Al_2O_3$ content of the glauconite is high, varying from 15.98% to 27.68% (Table-8.2). The MgO content of the glauconite varies from 2.18% to 3.85% (Table-8.2). The $SiO_2$ content of the glauconite varies from 46.42 to 57.14 wt% (Table-8.2). The CaO content of the glauconite is negligible. The glauconite exhibits high contents of $K_2O$, $Al_2O_3$, $SiO_2$ and MgO. The $SiO_2$ content in the glauconite is comparable to those reported from the Vindhyan Supergroup (Banerjee et al., 2008; Sarkar et al., 2014) and other Proterozoic

basins (Guimaraes et al., 2000; Ivanovskaya et al., 2006; Banerjee et al., 2016a, b; Tang et al., 2017a).

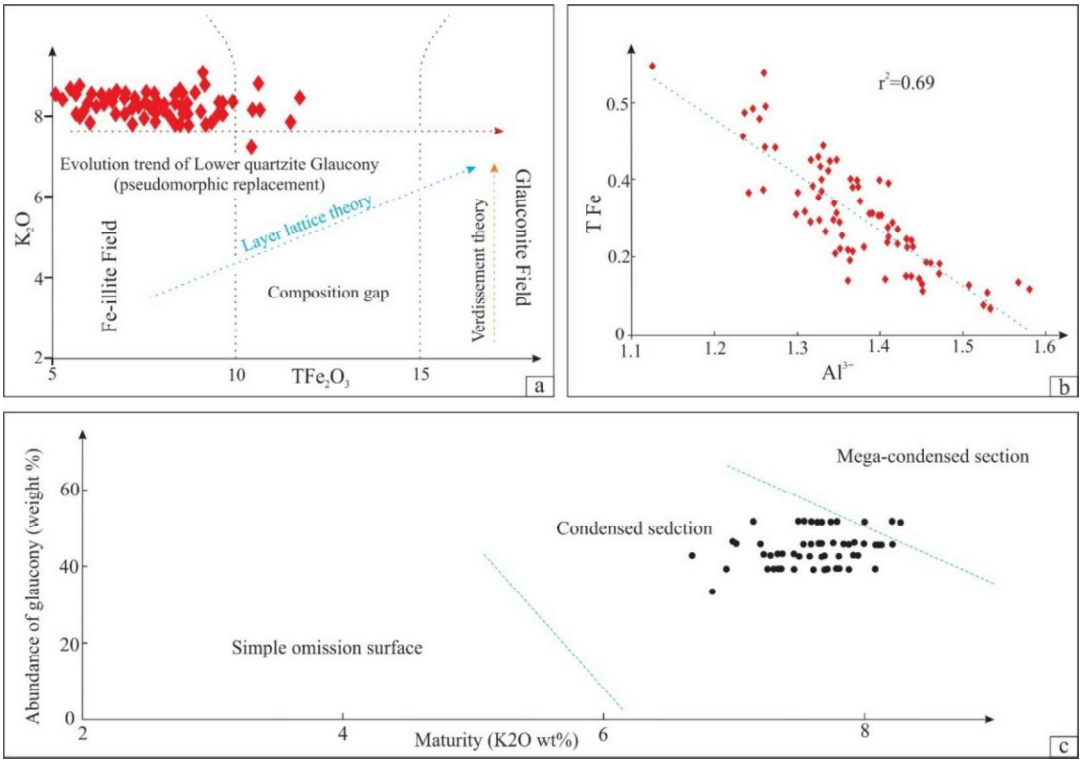


Fig. 8.6. Cross plot between $K_2O$ and $TFe_2O_3$ (a; field of illite minerals and glauconitic minerals are after Odin and Matter, 1981, note the evolution path of glauconite marked by arrow), Cross plot of between TFe and Al (b), Relation between maturity ($K_2O$ wt%) and abundance of glauconite. Note the abundance of glauconite within the condensed section (c).

Table-8.2. Oxide weight percentage within Lower Quartzite glaucony

| Sample No. | $Na_2O$ | MgO | $Al_2O_3$ | $SiO_2$ | $P_2O_5$ | $K_2O$ | CaO | $TiO_2$ | MnO | $Fe_2O_3$ | Total |
|---|---|---|---|---|---|---|---|---|---|---|---|
| Evolved ferric illites | | | | | | | | | | | |
| GK9 | 0.05 | 2.78 | 21.36 | 50.29 | 0.03 | 7.03 | 0.41 | 0.04 | 0.00 | 5.44 | 87.41 |
| | 0.05 | 3.25 | 20.38 | 53.03 | 0.03 | 7.32 | 0.41 | 0.03 | 0.01 | 4.85 | 89.36 |
| | 0.02 | 3.28 | 19.05 | 52.51 | 0.02 | 7.50 | 0.41 | 0.08 | 0.00 | 5.41 | 88.27 |
| | 0.10 | 3.07 | 18.34 | 51.81 | 0.00 | 6.93 | 0.36 | 0.04 | 0.01 | 5.29 | 85.95 |
| | 0.01 | 2.83 | 19.96 | 50.91 | 0.05 | 6.69 | 0.41 | 0.03 | 0.00 | 4.66 | 85.56 |
| | 0.06 | 3.47 | 18.90 | 55.39 | 0.00 | 7.92 | 0.41 | 0.05 | 0.00 | 6.51 | 92.71 |
| | 0.06 | 3.69 | 17.28 | 55.15 | 0.04 | 7.80 | 0.37 | 0.02 | 0.03 | 6.90 | 91.34 |
| | 0.03 | 3.54 | 18.91 | 51.14 | 0.00 | 7.27 | 0.32 | 0.04 | 0.00 | 5.23 | 86.47 |
| | 0.03 | 3.01 | 19.86 | 54.25 | 0.02 | 7.28 | 0.44 | 0.07 | 0.00 | 5.65 | 90.60 |
| | 0.05 | 3.78 | 19.63 | 54.05 | 0.01 | 7.49 | 0.40 | 0.03 | 0.00 | 4.87 | 90.30 |
| | 0.03 | 3.61 | 19.33 | 54.28 | 0.00 | 7.68 | 0.34 | 0.04 | 0.00 | 6.48 | 91.79 |
| | 0.03 | 2.96 | 21.25 | 53.51 | 0.03 | 7.25 | 0.31 | 0.03 | 0.00 | 4.65 | 90.02 |
| | 0.54 | 3.24 | 19.30 | 53.84 | 0.00 | 7.69 | 0.33 | 0.09 | 0.00 | 5.97 | 90.99 |
| | 0.00 | 2.97 | 20.93 | 51.93 | 0.01 | 7.03 | 0.34 | 0.08 | 0.00 | 4.56 | 87.86 |
| | 0.06 | 3.11 | 19.58 | 53.59 | 0.00 | 7.57 | 0.34 | 0.08 | 0.00 | 6.17 | 90.50 |

| | | | | | | | | | | | |
|---|---|---|---|---|---|---|---|---|---|---|---|
| | 0.03 | 3.39 | 18.75 | 55.20 | 0.09 | 7.36 | 0.15 | 0.10 | 0.04 | 6.30 | 91.40 |
| | 0.03 | 3.58 | 17.81 | 55.94 | 0.01 | 7.90 | 0.28 | 0.05 | 0.00 | 7.08 | 92.68 |
| | 0.03 | 3.12 | 19.24 | 53.58 | 0.01 | 7.65 | 0.32 | 0.12 | 0.00 | 5.46 | 89.52 |
| | 0.02 | 3.27 | 19.29 | 52.56 | 0.00 | 7.47 | 0.45 | 0.04 | 0.04 | 5.22 | 88.36 |
| | 0.04 | 3.32 | 18.47 | 53.43 | 0.02 | 7.64 | 0.32 | 0.00 | 0.00 | 6.10 | 89.35 |
| | 0.06 | 2.86 | 17.65 | 49.68 | 0.02 | 6.82 | 0.36 | 0.04 | 0.03 | 5.37 | 82.88 |
| | 0.06 | 2.80 | 20.27 | 51.01 | 0.03 | 7.67 | 0.44 | 0.01 | 0.01 | 7.20 | 89.50 |
| | 0.25 | 3.31 | 21.25 | 50.35 | 0.00 | 7.26 | 0.39 | 0.06 | 0.00 | 9.60 | 92.47 |
| | 0.10 | 2.90 | 20.86 | 50.95 | 0.00 | 7.28 | 0.46 | 0.07 | 0.00 | 7.83 | 90.45 |
| | 0.13 | 3.32 | 20.79 | 53.67 | 0.00 | 7.61 | 0.37 | 0.03 | 0.00 | 6.75 | 92.67 |
| | 0.13 | 2.63 | 27.14 | 47.33 | 0.03 | 7.69 | 0.32 | 0.02 | 0.00 | 4.62 | 89.91 |
| | 0.14 | 2.95 | 23.32 | 54.83 | 0.00 | 7.86 | 0.42 | 0.03 | 0.00 | 6.07 | 95.62 |
| GNS2 | 0.14 | 3.31 | 22.57 | 52.34 | 0.00 | 7.71 | 0.42 | 0.05 | 0.00 | 6.80 | 93.34 |
| | 0.17 | 3.11 | 22.06 | 54.43 | 0.03 | 7.45 | 0.39 | 0.11 | 0.01 | 7.99 | 95.74 |
| | 0.17 | 2.80 | 25.38 | 48.75 | 0.05 | 7.79 | 0.45 | 0.13 | 0.00 | 4.54 | 90.05 |
| | 0.21 | 2.83 | 19.89 | 49.15 | 0.02 | 7.67 | 0.48 | 0.02 | 0.00 | 7.25 | 87.51 |
| | 0.10 | 2.68 | 22.62 | 52.35 | 0.04 | 7.78 | 0.52 | 0.00 | 0.00 | 5.85 | 91.93 |
| | 0.04 | 2.55 | 19.45 | 53.27 | 0.08 | 7.35 | 0.56 | 0.00 | 0.00 | 7.43 | 90.74 |
| | 0.09 | 2.87 | 24.88 | 51.76 | 0.01 | 8.06 | 0.28 | 0.05 | 0.00 | 4.85 | 92.86 |
| | 0.08 | 3.27 | 19.23 | 57.14 | 0.02 | 6.93 | 0.63 | 0.03 | 0.00 | 9.07 | 96.39 |
| | 0.12 | 3.27 | 24.02 | 46.42 | 0.03 | 7.32 | 0.42 | 0.04 | 0.00 | 6.83 | 88.46 |
| | 0.14 | 3.42 | 19.76 | 55.55 | 0.00 | 7.80 | 0.16 | 0.01 | 0.00 | 9.20 | 96.03 |
| | 0.08 | 3.18 | 19.93 | 50.58 | 0.00 | 7.97 | 0.12 | 0.00 | 0.00 | 8.69 | 90.56 |
| | 0.12 | 3.38 | 23.26 | 55.40 | 0.01 | 7.92 | 0.16 | 0.02 | 0.00 | 5.16 | 95.41 |
| | 0.13 | 3.42 | 23.07 | 55.73 | 0.01 | 8.20 | 0.11 | 0.00 | 0.00 | 5.27 | 95.94 |
| | 0.11 | 3.08 | 21.68 | 56.60 | 0.00 | 7.54 | 0.10 | 0.00 | 0.00 | 6.76 | 95.86 |
| | 0.09 | 3.00 | 21.71 | 55.20 | 0.00 | 7.59 | 0.11 | 0.00 | 0.00 | 6.59 | 94.29 |
| | 0.15 | 3.29 | 21.18 | 55.88 | 0.02 | 7.53 | 0.10 | 0.05 | 0.00 | 8.14 | 96.33 |
| | 0.14 | 3.08 | 22.28 | 54.01 | 0.01 | 8.14 | 0.09 | 0.02 | 0.00 | 7.31 | 95.09 |
| | 0.09 | 3.57 | 21.04 | 55.17 | 0.01 | 7.93 | 0.11 | 0.00 | 0.00 | 6.66 | 94.56 |
| | 0.17 | 3.36 | 21.04 | 55.16 | 0.03 | 7.87 | 0.16 | 0.00 | 0.00 | 7.46 | 95.24 |
| | 0.13 | 3.85 | 20.54 | 55.81 | 0.00 | 7.99 | 0.16 | 0.00 | 0.00 | 7.23 | 95.71 |
| GNS4 | 0.09 | 3.76 | 21.23 | 55.36 | 0.01 | 7.91 | 0.09 | 0.00 | 0.00 | 6.57 | 95.04 |
| | 0.13 | 3.07 | 23.17 | 55.72 | 0.00 | 7.97 | 0.14 | 0.00 | 0.00 | 6.45 | 96.65 |
| | 0.11 | 3.26 | 23.25 | 54.62 | 0.01 | 8.08 | 0.16 | 0.00 | 0.00 | 5.99 | 95.47 |
| | 0.15 | 3.29 | 22.71 | 54.56 | 0.01 | 8.11 | 0.13 | 0.00 | 0.00 | 6.01 | 94.97 |
| | 0.15 | 2.97 | 24.21 | 54.82 | 0.00 | 8.14 | 0.06 | 0.00 | 0.00 | 5.53 | 95.90 |
| | 0.08 | 3.59 | 19.18 | 54.49 | 0.00 | 7.64 | 0.13 | 0.00 | 0.00 | 8.95 | 94.07 |
| | 0.10 | 3.15 | 22.09 | 54.86 | 0.00 | 7.76 | 0.16 | 0.02 | 0.00 | 6.66 | 94.80 |
| | 0.09 | 2.79 | 24.77 | 54.43 | 0.02 | 7.97 | 0.15 | 0.00 | 0.00 | 4.51 | 94.72 |
| | 0.06 | 2.69 | 21.48 | 51.58 | 0.01 | 7.01 | 0.13 | 0.00 | 0.00 | 7.08 | 90.04 |
| | 0.06 | 2.72 | 21.29 | 49.54 | 0.00 | 7.02 | 0.13 | 0.00 | 0.00 | 4.77 | 85.54 |
| | 0.05 | 2.83 | 20.31 | 52.08 | 0.00 | 7.19 | 0.01 | 0.02 | 0.00 | 6.99 | 89.46 |
| | 0.16 | 3.51 | 19.80 | 55.13 | 0.01 | 7.87 | 0.14 | 0.00 | 0.00 | 8.19 | 94.81 |
| | 0.13 | 2.96 | 22.47 | 56.18 | 0.01 | 7.65 | 0.13 | 0.00 | 0.00 | 6.51 | 96.04 |

| | | | | | | | | | | | |
|---|---|---|---|---|---|---|---|---|---|---|---|
| | 0.16 | 3.10 | 22.79 | 55.70 | 0.00 | 7.94 | 0.15 | 0.00 | 0.00 | 6.47 | 96.31 |
| GNS7 | 0.06 | 3.76 | 21.16 | 54.25 | 0.00 | 7.54 | 0.32 | 0.00 | 0.05 | 6.99 | 94.13 |
| | 0.01 | 3.83 | 20.43 | 55.84 | 0.00 | 8.00 | 0.32 | 0.06 | 0.00 | 8.40 | 96.88 |
| | 0.06 | 3.38 | 20.87 | 55.17 | 0.00 | 8.23 | 0.25 | 0.05 | 0.00 | 7.32 | 95.33 |
| | 0.01 | 3.49 | 23.41 | 53.67 | 0.00 | 7.77 | 0.38 | 0.04 | 0.02 | 7.53 | 96.32 |
| | 0.05 | 3.18 | 26.76 | 53.74 | 0.01 | 8.27 | 0.35 | 0.01 | 0.00 | 4.50 | 96.87 |
| | 0.08 | 2.90 | 16.94 | 56.17 | 0.01 | 7.68 | 0.36 | 0.08 | 0.00 | 8.26 | 92.48 |
| | 0.05 | 2.56 | 19.80 | 47.81 | 0.00 | 7.72 | 0.35 | 0.06 | 0.00 | 7.00 | 85.36 |
| | 0.03 | 2.88 | 27.68 | 50.33 | 0.00 | 7.64 | 0.26 | 0.00 | 0.00 | 4.99 | 93.80 |
| | 0.06 | 2.18 | 19.18 | 56.60 | 0.00 | 7.14 | 0.29 | 0.07 | 0.02 | 5.94 | 91.48 |
| | 0.07 | 3.68 | 15.98 | 52.65 | 0.08 | 7.59 | 0.29 | 0.05 | 0.00 | 9.52 | 89.91 |
| | 0.10 | 3.11 | 23.85 | 53.07 | 0.00 | 7.78 | 0.32 | 0.17 | 0.03 | 5.44 | 93.87 |
| | 0.03 | 3.71 | 21.19 | 56.24 | 0.00 | 7.49 | 0.28 | 0.09 | 0.01 | 7.35 | 96.39 |
| Max. | 0.54 | 3.85 | 27.68 | 57.14 | 0.09 | 8.27 | 0.63 | 0.17 | 0.05 | 9.60 | 96.88 |
| Min. | 0.00 | 2.18 | 15.98 | 46.42 | 0.00 | 6.69 | 0.01 | 0.00 | 0.00 | 4.50 | 82.88 |
| Mean | 0.27 | 3.02 | 21.83 | 51.78 | 0.04 | 7.48 | 0.32 | 0.09 | 0.03 | 7.05 | 89.88 |

The $K_2O$ content of the glauconite corresponds to 'evolved' and 'highly evolved' stages of maturity (Amorosi, 1997; Odin and Matter, 1981). However, the content of $Fe_2O_3$ (total) is low within the glauconite. Therefore, most data points of the glauconite occupy the field of ferric illite in the $K_2O$ vs. $Fe_2O_3$ cross plot of Odin and Matter (1981), although a few of these plot within the 'compositional gap' (Fig. 8.6a). Odin and Matter (1981) found a 'compositional gap' between ferric illite and glauconite, containing low and high contents of $Fe_2O_3$, respectively. However, the later workers ruled out the concept of 'compositional gap', as they reported a continuity in mineral chemistry between ferric illite and glauconite (Dasgupta et al., 1990; Banerjee et al., 2008, 2015, 2016; Tang et al., 2017a, b). For the glauconite with similar chemical composition, Berg-Madsen (1983) introduced the term high-alumina glauconite. The relationship between $Al^{3+}$ verses $Fe_2O_3$ (total) exhibits a moderate negative correlation ($r^2$=0.7) (Fig. 8.6b), indicating the substitution of Al ions by Fe in the octahedral site of glauconite, as reported in several studies (Odin and matter, 1981; Velde, 1985; Dasgupta et al., 1990; Amorosi et al., 2007; Banerjee et al., 2015, 2016a, b, 2019; Bansal et al., 2017, 2018; Tang et al., 2017a, b; Rudmin et al., 2017). The cross-plot of $Al_2O_3$ verses $K_2O$ with negligible correlation implies a simultaneous increase of Al during glauconitization.

### 8.4.5. Structural formula of glauconite

Major element oxide composition of glauconite was determined by EPMA on 75 points (Table-8.2). All data were normalized to 100% on an anhydrous basis for different

cross plots (Fig. 8.6a, b). The concentration of elements was calculated on an anion equivalent basis to the structural formulae per $O_{10}(OH)_2$. The $Fe^{2+}/Fe^{3+}$ ratio, calculated by the titration technique, is 0.8. Al is the dominant octahedral cation ranging from 1.12 to 1.58 atoms per formula unit. Total Fe content in the octahedral site ranges between 0.23 to 0.54 atoms per formula. $Fe^{2+}$ and $Fe^{3+}$ range between 0.11 to 0.25 and 0.12 to 0.28 atoms per formula unit, respectively. Mg varies from 0.22 to 0.39 atoms per formula unit. $Fe^{3+}$ cations in octahedral sites are low compared to $Fe^{2+}$. Total octahedral in $R^{3+}$ states vary from 1.86 to 1.22 atoms (average 1.54). The average Si and Al content in tetrahedral sites are 3.59 and 0.41 atoms. The formulae of glauconites are represented in Table-8.3. The average formula of the glauconite is as follows:

$(K_{0.66},Na_{0.04},Ca_{0.02})_{0.72}\ (Mg_{0.31},Fe^{+2}{}_{0.18},Fe^{+3}{}_{0.20},Al_{1.35})_{2.04}\ (Si_{3.59},Al_{0.41})_4\ O_{10}\ (OH)_2.nH_2O.$

Table-8.3. Structural formula of glaucony in Lower Quartzite

| Sample No. | Structural Formulae of Fully evolved ferric illites | Tetrahedral charge | Octahedral charge |
|---|---|---|---|
| GK9 | $(K_{0.65},Na_{0.01},Ca_{0.03})_{0.68}\ (Mg_{0.30},Fe^{+3}{}_{0.16},Fe^{+2}{}_{0.15},Al_{1.43})_{2.04}\ (Al_{0.38},Si_{3.62})_4\ O_{11}\ (OH)_2.nH_2O$ | 0.38 | 0.17 |
| | $(K_{0.65},Na_{0.01},Ca_{0.03})_{0.68}\ (Mg_{0.34},Fe^{+3}{}_{0.14},Fe^{+2}{}_{0.13},Al_{1.40})_{2.01}\ (Al_{0.28},Si_{3.72})_4\ O_{11}\ (OH)_2.nH_2O$ | 0.28 | 0.20 |
| | $(K_{0.68},Na_{0.00},Ca_{0.03})_{0.71}\ (Mg_{0.35},Fe^{+3}{}_{0.16},Fe^{+2}{}_{0.14},Al_{1.35})_{2.00}\ (Al_{0.25},Si_{3.7})_4\ O_{11}\ (OH)_2.nH_2O$ | 0.25 | 0.21 |
| | $(K_{0.64},Na_{0.01},Ca_{0.03})_{0.69}\ (Mg_{0.33},Fe^{+3}{}_{0.16},Fe^{+2}{}_{0.14},Al_{1.36})_{2.00}\ (Al_{0.22},Si_{3.78})_4\ O_{11}\ (OH)_2.nH_2O$ | 0.22 | 0.20 |
| | $(K_{0.62},Na_{0.00},Ca_{0.03})_{0.65}\ (Mg_{0.31},Fe^{+3}{}_{0.14},Fe^{+2}{}_{0.13},Al_{1.43})_{2.01}\ (Al_{0.28},Si_{3.72})_4\ O_{11}\ (OH)_2.nH_2O$ | 0.28 | 0.18 |
| | $(K_{0.69},Na_{0.01},Ca_{0.03})_{0.73}\ (Mg_{0.35},Fe^{+3}{}_{0.19},Fe^{+2}{}_{0.16},Al_{1.29})_{2.00}\ (Al_{0.22},Si_{3.78})_4\ O_{11}\ (OH)_2.nH_2O$ | 0.22 | 0.21 |
| | $(K_{0.69},Na_{0.01},Ca_{0.03})_{0.73}\ (Mg_{0.38},Fe^{+3}{}_{0.20},Fe^{+2}{}_{0.18},Al_{1.24})_{1.99}\ (Al_{0.18},Si_{3.82})_4\ O_{11}\ (OH)_2.nH_2O$ | 0.18 | 0.24 |
| | $(K_{0.67},Na_{0.00},Ca_{0.02})_{0.69}\ (Mg_{0.38},Fe^{+3}{}_{0.16},Fe^{+2}{}_{0.14},Al_{1.34})_{2.03}\ (Al_{0.28},Si_{3.72})_4\ O_{11}\ (OH)_2.nH_2O$ | 0.28 | 0.23 |
| | $(K_{0.64},Na_{0.00},Ca_{0.03})_{0.67}\ (Mg_{0.31},Fe^{+3}{}_{0.16},Fe^{+2}{}_{0.15},Al_{1.38})_{2.00}\ (Al_{0.24},Si_{3.76})_4\ O_{11}\ (OH)_2.nH_2O$ | 0.24 | 0.18 |
| | $(K_{0.66},Na_{0.01},Ca_{0.03})_{0.70}\ (Mg_{0.39},Fe^{+3}{}_{0.14},Fe^{+2}{}_{0.13},Al_{1.36})_{2.01}\ (Al_{0.25},Si_{3.75})_4\ O_{11}\ (OH)_2.nH_2O$ | 0.25 | 0.24 |
| | $(K_{0.67},Na_{0.00},Ca_{0.03})_{0.70}\ (Mg_{0.37},Fe^{+3}{}_{0.19},Fe^{+2}{}_{0.17},Al_{1.30})_{2.02}\ (Al_{0.27},Si_{3.73})_4\ O_{11}\ (OH)_2.nH_2O$ | 0.27 | 0.22 |
| | $(K_{0.64},Na_{0.00},Ca_{0.02})_{0.66}\ (Mg_{0.31},Fe^{+3}{}_{0.13},Fe^{+2}{}_{0.12},Al_{1.45})_{2.01}\ (Al_{0.29},Si_{3.71})_4\ O_{11}\ (OH)_2.nH_2O$ | 0.29 | 0.18 |
| | $(K_{0.68},Na_{0.07},Ca_{0.02})_{0.77}\ (Mg_{0.34},Fe^{+3}{}_{0.17},Fe^{+2}{}_{0.15},Al_{1.33})_{1.99}\ (Al_{0.25},Si_{3.75})_4\ O_{11}\ (OH)_2.nH_2O$ | 0.25 | 0.20 |
| | $(K_{0.64}Na_{0.00},Ca_{0.03})_{0.67}\ (Mg_{0.31},Fe^{+3}{}_{0.14},Fe^{+2}{}_{0.12},Al_{1.45})_{2.02}\ (Al_{0.31},Si_{3.69})_4\ O_{11}\ (OH)_2.nH_2O$ | 0.31 | 0.18 |
| | $(K_{0.67},Na_{0.01},Ca_{0.03})_{0.71}\ (Mg_{0.32},Fe^{+3}{}_{0.18},Fe^{+2}{}_{0.16},Al_{1.34})_{2.01}\ (Al_{0.26},Si_{3.74})_4\ O_{11}\ (OH)_2.nH_2O$ | 0.26 | 0.19 |
| | $(K_{0.65},Na_{0.00},Ca_{0.01})_{0.66}\ (Mg_{0.35},Fe^{+3}{}_{0.18},Fe^{+2}{}_{0.16},Al_{1.32})_{2.01}\ (Al_{0.20},Si_{3.80})_4\ O_{11}\ (OH)_2.nH_2O$ | 0.20 | 0.21 |

| | | | |
|---|---|---|---|
| | $(K_{0.69},Na_{0.00},Ca_{0.02})_{0.71}(Mg_{0.36},Fe^{+3}_{0.20},Fe^{+2}_{0.18},Al_{1.25})_{2.00}(Al_{0.18},Si_{3.82})_4O_{11}(OH)_2.nH_2O$ | 0.18 | 0.22 |
| | $(K_{0.69},Na_{0.00},Ca_{0.02})_{0.71}(Mg_{0.33},Fe^{+3}_{0.16},Fe^{+2}_{0.14},Al_{1.36})_{1.99}(Al_{0.23},Si_{3.77})_4O_{11}(OH)_2.nH_2O$ | 0.23 | 0.20 |
| | $(K_{0.68},Na_{0.00},Ca_{0.03})_{0.71}(Mg_{0.35},Fe^{+3}_{0.16},Fe^{+2}_{0.14},Al_{1.36})_{2.00}(Al_{0.26},Si_{3.74})_4O_{11}(OH)_2.nH_2O$ | 0.26 | 0.21 |
| | $(K_{0.69},Na_{0.01},Ca_{0.02})_{0.72}(Mg_{0.35},Fe^{+3}_{0.18},Fe^{+2}_{0.16},Al_{1.31})_{2.00}(Al_{0.23},Si_{3.77})_4O_{11}(OH)_2.nH_2O$ | 0.23 | 0.21 |
| | $(K_{0.66},Na_{0.01},Ca_{0.03})_{0.70}(Mg_{0.32},Fe^{+3}_{0.17},Fe^{+2}_{0.15},Al_{1.35})_{1.99}(Al_{0.23},Si_{3.77})_4O_{11}(OH)_2.nH_2O$ | 0.23 | 0.19 |
| | $(K_{0.70},Na_{0.01},Ca_{0.03})_{0.74}(Mg_{0.30},Fe^{+3}_{0.21},Fe^{+2}_{0.19},Al_{1.33})_{2.03}(Al_{0.37},Si_{3.63})_4O_{11}(OH)_2.nH_2O$ | 0.37 | 0.17 |
| GNS2 | $(K_{0.64},Na_{0.03},Ca_{0.03})_{0.70}(Mg_{0.34},Fe^{+3}_{0.28},Fe^{+2}_{0.25},Al_{1.25})_{2.12}(Al_{0.49},Si_{3.51})_4O_{11}(OH)_2.nH_2O$ | 0.49 | 0.19 |
| | $(K_{0.65},Na_{0.01},Ca_{0.03})_{0.69}(Mg_{0.30},Fe^{+3}_{0.23},Fe^{+2}_{0.21},Al_{1.32})_{2.06}(Al_{0.41},Si_{3.59})_4O_{11}(OH)_2.nH_2O$ | 0.41 | 0.17 |
| | $(K_{0.66},Na_{0.02},Ca_{0.03})_{0.71}(Mg_{0.34},Fe^{+3}_{0.19},Fe^{+2}_{0.17},Al_{1.34})_{2.04}(Al_{0.34},Si_{3.66})_4O_{11}(OH)_2.nH_2O$ | 0.34 | 0.20 |
| | $(K_{0.69},Na_{0.02},Ca_{0.02})_{0.73}(Mg_{0.28},Fe^{+3}_{0.14},Fe^{+2}_{0.12},Al_{1.58})_{2.11}(Al_{0.67},Si_{3.33})_4O_{11}(OH)_2.nH_2O$ | 0.67 | 0.15 |
| | $(K_{0.66},Na_{0.02},Ca_{0.03})_{0.71}(Mg_{0.29},Fe^{+3}_{0.17},Fe^{+2}_{0.15},Al_{1.43})_{2.03}(Al_{0.39},Si_{3.61})_4O_{11}(OH)_2.nH_2O$ | 0.39 | 0.17 |
| | $(K_{0.67},Na_{0.02},Ca_{0.03})_{0.72}(Mg_{0.34},Fe^{+3}_{0.19},Fe^{+2}_{0.17},Al_{1.37})_{2.07}(Al_{0.44},Si_{3.56})_4O_{11}(OH)_2.nH_2O$ | 0.44 | 0.19 |
| | $(K_{0.63},Na_{0.02},Ca_{0.03})_{0.68}(Mg_{0.31},Fe^{+3}_{0.22},Fe^{+2}_{0.20},Al_{1.34})_{2.06}(Al_{0.39},Si_{3.61})_4O_{11}(OH)_2.nH_2O$ | 0.39 | 0.17 |
| | $(K_{0.70},Na_{0.02},Ca_{0.03})_{0.75}(Mg_{0.29},Fe^{+3}_{0.13},Fe^{+2}_{0.12},Al_{1.53})_{2.07}(Al_{0.58},Si_{3.42})_4O_{11}(OH)_2.nH_2O$ | 0.58 | 0.16 |
| | $(K_{0.72},Na_{0.03},Ca_{0.04})_{0.79}(Mg_{0.31},Fe^{+3}_{0.22},Fe^{+2}_{0.20},Al_{1.31})_{2.04}(Al_{0.41},Si_{3.59})_4O_{11}(OH)_2.nH_2O$ | 0.41 | 0.18 |
| | $(K_{0.68},Na_{0.01},Ca_{0.04})_{0.74}(Mg_{0.27},Fe^{+3}_{0.17},Fe^{+2}_{0.15},Al_{1.43})_{2.02}(Al_{0.40},Si_{3.60})_4O_{11}(OH)_2.nH_2O$ | 0.40 | 0.16 |
| | $(K_{0.66},Na_{0.01},Ca_{0.04})_{0.71}(Mg_{0.27},Fe^{+3}_{0.22},Fe^{+2}_{0.19},Al_{1.32})_{2.00}(Al_{0.28},Si_{3.72})_4O_{11}(OH)_2.nH_2O$ | 0.28 | 0.15 |
| | $(K_{0.70},Na_{0.01},Ca_{0.02})_{0.73}(Mg_{0.29},Fe^{+3}_{0.14},Fe^{+2}_{0.12},Al_{1.50})_{2.05}(Al_{0.49},Si_{3.51})_4O_{11}(OH)_2.nH_2O$ | 0.49 | 0.16 |
| | $(K_{0.58},Na_{0.01},Ca_{0.04})_{0.63}(Mg_{0.32},Fe^{+3}_{0.25},Fe^{+2}_{0.22},Al_{1.25})_{2.04}(Al_{0.24},Si_{3.76})_4O_{11}(OH)_2.nH_2O$ | 0.24 | 0.19 |
| | $(K_{0.67},Na_{0.02},Ca_{0.03})_{0.72}(Mg_{0.35},Fe^{+3}_{0.21},Fe^{+2}_{0.18},Al_{1.40})_{2.14}(Al_{0.64},Si_{3.36})_4O_{11}(OH)_2.nH_2O$ | 0.64 | 0.20 |
| | $(K_{0.66},Na_{0.02},Ca_{0.01})_{0.69}(Mg_{0.34},Fe^{+3}_{0.26},Fe^{+2}_{0.23},Al_{1.24})_{2.06}(Al_{0.31},Si_{3.69})_4O_{11}(OH)_2.nH_2O$ | 0.31 | 0.20 |
| | $(K_{0.72},Na_{0.01},Ca_{0.01})_{0.74}(Mg_{0.34},Fe^{+3}_{0.26},Fe^{+2}_{0.23},Al_{1.25})_{2.08}(Al_{0.41},Si_{3.59})_4O_{11}(OH)_2.nH_2O$ | 0.41 | 0.19 |
| | $(K_{0.66},Na_{0.2},Ca_{0.01})_{0.69}(Mg_{0.33},Fe^{+3}_{0.14},Fe^{+2}_{0.13},Al_{1.44})_{2.04}(Al_{0.36},Si_{3.64})_4O_{11}(OH)_2.nH_2O$ | 0.36 | 0.19 |
| | $K_{0.69},Na_{0.02},Ca_{0.01})_{0.72}(Mg_{0.33},Fe^{+3}_{0.14},Fe^{+2}_{0.13},Al_{1.43})_{2.04}(Al_{0.35},Si_{3.65})_4O_{11}(OH)_2.nH_2O$ | 0.35 | 0.20 |
| | $(K_{0.63},Na_{0.01},Ca_{0.01})_{0.65}(Mg_{0.30},Fe^{+3}_{0.19},Fe^{+2}_{0.16},Al_{1.38})_{2.04}(Al_{0.29},Si_{3.71})_4O_{11}(OH)_2.nH_2O$ | 0.29 | 0.17 |
| | $(K_{0.65},Na_{0.01},Ca_{0.01})_{0.67}(Mg_{0.30},Fe^{+3}_{0.18},Fe^{+2}_{0.16},Al_{1.39})_{2.04}(Al_{0.32},Si_{3.68})_4O_{11}(OH)_2.nH_2O$ | 0.32 | 0.17 |
| | $(K_{0.63},Na_{0.02},Ca_{0.01})_{0.66}(Mg_{0.32},Fe^{+3}_{0.22},Fe^{+2}_{0.20},Al_{1.32})_{2.06}(Al_{0.32},Si_{3.68})_4O_{11}(OH)_2.nH_2O$ | 0.32 | 0.19 |

| | | | |
|---|---|---|---|
| GNS4 | $(K_{0.69},Na_{0.02},Ca_{0.01})_{0.72}(Mg_{0.31},Fe^{+3}_{0.20},Fe^{+2}_{0.18},Al_{1.36})_{2.05}(Al_{0.39},Si_{3.61})_4O_{11}(OH)_2.nH_2O$ | 0.39 | 0.18 |
| | $(K_{0.68},Na_{0.01},Ca_{0.01})_{0.70}(Mg_{0.36},Fe^{+3}_{0.19},Fe^{+2}_{0.17},Al_{1.34})_{2.05}(Al_{0.32},Si_{3.68})_4O_{11}(OH)_2.nH_2O$ | 0.32 | 0.21 |
| | $(K_{0.67},Na_{0.02},Ca_{0.03})_{0.72}(Mg_{0.33},Fe^{+3}_{0.21},Fe^{+2}_{0.18},Al_{1.32})_{2.05}(Al_{0.33},Si_{3.67})_4O_{11}(OH)_2.nH_2O$ | 0.33 | 0.19 |
| | $(K_{0.68},Na_{0.02},Ca_{0.01})_{0.71}(Mg_{0.38},Fe^{+3}_{0.20},Fe^{+2}_{0.18},Al_{1.30})_{2.05}(Al_{0.31},Si_{3.69})_4O_{11}(OH)_2.nH_2O$ | 0.31 | 0.23 |
| | $(K_{0.67},Na_{0.01},Ca_{0.01})_{0.69}(Mg_{0.37},Fe^{+3}_{0.18},Fe^{+2}_{0.16},Al_{1.34})_{2.06}(Al_{0.32},Si_{3.68})_4O_{11}(OH)_2.nH_2O$ | 0.32 | 0.22 |
| | $(K_{0.66},Na_{0.02},Ca_{0.01})_{0.69}(Mg_{0.30},Fe^{+3}_{0.18},Fe^{+2}_{0.16},Al_{1.41})_{2.04}(Al_{0.37},Si_{3.63})_4O_{11}(OH)_2.nH_2O$ | 0.37 | 0.17 |
| | $(K_{0.68},Na_{0.01},Ca_{0.01})_{0.70}(Mg_{0.32},Fe^{+3}_{0.17},Fe^{+2}_{0.15},Al_{1.42})_{2.05}(Al_{0.39},Si_{3.61})_4O_{11}(OH)_2.nH_2O$ | 0.39 | 0.19 |
| | $(K_{0.69},Na_{0.02},Ca_{0.01})_{0.72}(Mg_{0.33},Fe^{+3}_{0.17},Fe^{+2}_{0.15},Al_{1.40})_{2.04}(Al_{0.38},Si_{3.62})_4O_{11}(OH)_2.nH_2O$ | 0.38 | 0.19 |
| | $(K_{0.68},Na_{0.02},Ca_{0.00})_{0.70}(Mg_{0.29},Fe^{+3}_{0.15},Fe^{+2}_{0.13},Al_{1.47})_{2.04}(Al_{0.40},Si_{3.60})_4O_{11}(OH)_2.nH_2O$ | 0.40 | 0.17 |
| | $(K_{0.66},Na_{0.01},Ca_{0.01})_{0.68}(Mg_{0.36},Fe^{+3}_{0.25},Fe^{+2}_{0.23},Al_{1.23})_{2.07}(Al_{0.31},Si_{3.69})_4O_{11}(OH)_2.nH_2O$ | 0.31 | 0.21 |
| | $(K_{0.66},Na_{0.01},Ca_{0.01})_{0.68}(Mg_{0.31},Fe^{+3}_{0.19},Fe^{+2}_{0.16},Al_{1.38})_{2.05}(Al_{0.35},Si_{3.65})_4O_{11}(OH)_2.nH_2O$ | 0.35 | 0.18 |
| | $(K_{0.67},Na_{0.01},Ca_{0.01})_{0.69}(Mg_{0.27},Fe^{+3}_{0.12},Fe^{+2}_{0.11},Al_{1.52})_{2.03}(Al_{0.41},Si_{3.59})_4O_{11}(OH)_2.nH_2O$ | 0.41 | 0.16 |
| | $(K_{0.63},Na_{0.01},Ca_{0.01})_{0.65}(Mg_{0.28},Fe^{+3}_{0.21},Fe^{+2}_{0.18},Al_{1.39})_{2.07}(Al_{0.38},Si_{3.62})_4O_{11}(OH)_2.nH_2O$ | 0.38 | 0.16 |
| | $(K_{0.66},Na_{0.01},Ca_{0.01})_{0.68}(Mg_{0.30},Fe^{+3}_{0.15},Fe^{+2}_{0.13},Al_{1.47})_{2.04}(Al_{0.37},Si_{3.63})_4O_{11}(OH)_2.nH_2O$ | 0.37 | 0.17 |
| | $(K_{0.65},Na_{0.01},Ca_{0.00})_{0.66}(Mg_{0.30},Fe^{+3}_{0.21},Fe^{+2}_{0.18},Al_{1.36})_{2.05}(Al_{0.32},Si_{3.68})_4O_{11}(OH)_2.nH_2O$ | 0.32 | 0.17 |
| | $(K_{0.67},Na_{0.02},Ca_{0.01})_{0.70}(Mg_{0.35},Fe^{+3}_{0.23},Fe^{+2}_{0.20},Al_{1.27})_{2.05}(Al_{0.30},Si_{3.70})_4O_{11}(OH)_2.nH_2O$ | 0.30 | 0.21 |
| | $(K_{0.64},Na_{0.02},Ca_{0.01})_{0.67}(Mg_{0.29},Fe^{+3}_{0.18},Fe^{+2}_{0.16},Al_{1.41})_{2.03}(Al_{0.32},Si_{3.68})_4O_{11}(OH)_2.nH_2O$ | 0.32 | 0.17 |
| | $(K_{0.66},Na_{0.02},Ca_{0.01})_{0.69}(Mg_{0.30},Fe^{+3}_{0.18},Fe^{+2}_{0.16},Al_{1.40})_{2.04}(Al_{0.35}Si_{3.65})_4O_{11}(OH)_2.nH_2O$ | 0.35 | 0.17 |
| GNS7 | $(K_{0.65},Na_{0.01},Ca_{0.02})_{0.68}(Mg_{0.38},Fe^{+3}_{0.20},Fe^{+2}_{0.17},Al_{1.32})_{2.07}(Al_{0.35},Si_{3.65})_4O_{11}(OH)_2.nH_2O$ | 0.35 | 0.22 |
| | $(K_{0.67},Na_{0.00},Ca_{0.02})_{0.69}(Mg_{0.37},Fe^{+3}_{0.23},Fe^{+2}_{0.21},Al_{1.25})_{2.06}(Al_{0.33},Si_{3.67})_4O_{11}(OH)_2.nH_2O$ | 0.33 | 0.22 |
| | $(K_{0.70},Na_{0.01},Ca_{0.02})_{0.73}(Mg_{0.34},Fe^{+3}_{0.20},Fe^{+2}_{0.18},Al_{1.31})_{2.03}(Al_{0.32},Si_{3.68})_4O_{11}(OH)_2.nH_2O$ | 0.32 | 0.20 |
| | $(K_{0.65},Na_{0.00},Ca_{0.03})_{0.68}(Mg_{0.34},Fe^{+3}_{0.21},Fe^{+2}_{0.18},Al_{1.36})_{2.09}(Al_{0.46},Si_{3.54})_4O_{11}(OH)_2.nH_2O$ | 0.46 | 0.20 |
| | $(K_{0.68},Na_{0.01},Ca_{0.02})_{0.71}(Mg_{0.31},Fe^{+3}_{0.12},Fe^{+2}_{0.11},Al_{1.53})_{2.07}(Al_{0.52},Si_{3.48})_4O_{11}(OH)_2.nH_2O$ | 0.52 | 0.17 |
| | $(K_{0.67},Na_{0.01},Ca_{0.03})_{0.71}(Mg_{0.30},Fe^{+3}_{0.24},Fe^{+2}_{0.21},Al_{1.23})_{1.97}(Al_{0.14},Si_{3.86})_4O_{11}(OH)_2.nH_2O$ | 0.14 | 0.18 |
| | $(K_{0.74},Na_{0.01},Ca_{0.03})_{0.78}(Mg_{0.29},Fe^{+3}_{0.22},Fe^{+2}_{0.20},Al_{1.33})_{2.03}(Al_{0.42},Si_{3.58})_4O_{11}(OH)_2.nH_2O$ | 0.42 | 0.16 |
| | $(K_{0.65},Na_{0.00},Ca_{0.02})_{0.67}(Mg_{0.29},Fe^{+3}_{0.14},Fe^{+2}_{0.12},Al_{1.56})_{2.12}(Al_{0.63},Si_{3.37})_4O_{11}(OH)_2.nH_2O$ | 0.63 | 0.16 |
| | $(K_{0.62},Na_{0.01},Ca_{0.02})_{0.65}(Mg_{0.22},Fe^{+3}_{0.17},Fe^{+2}_{0.15},Al_{1.40})_{1.95}(Al_{0.14},Si_{3.86})_4O_{11}(OH)_2.nH_2O$ | 0.14 | 0.13 |

| | | | |
|---|---|---|---|
| | $(K_{0.69},Na_{0.01}, Ca_{0.02})_{0.72}$ $(Mg_{0.39},Fe^{+3}_{0.28},Fe^{+2}_{0.25}, Al_{1.12})_{2.05}$ $(Al_{0.23},Si_{3.77})_4$ $O_{11}$ $(OH)_2.nH_2O$ | 0.23 | 0.24 |
| | $(K_{0.67},Na_{0.01}, Ca_{0.02})_{0.70}$ $(Mg_{0.31},Fe^{+3}_{0.15},Fe^{+2}_{0.14}, Al_{1.45})_{2.05}$ $(Al_{0.43},Si_{3.57})_4$ $O_{11}$ $(OH)_2.nH_2O$ | 0.43 | 0.18 |
| | $(K_{0.63},Na_{0.00}, Ca_{0.02})_{0.71}$ $(Mg_{0.36},Fe^{+3}_{0.20},Fe^{+2}_{0.18}, Al_{1.32})_{2.06}$ $(Al_{0.32},Si_{3.68})_4$ $O_{11}$ $(OH)_2.nH_2O$ | 0.32 | 0.21 |

## 8.5. Discussion

### 8.5.1. Compositional evolution and environmental significance of glauconite

The formation of glauconite has explained by two popular theories viz. the 'layer lattice' (Burst, 1958a, b; Hower, 1961) and the 'verdissement' (Odin and Matter, 1981). The compositional evolution of glauconite supporting the 'verdissement' theory reflects an increase in the $K_2O$ content at a fixed $Fe_2O_3$ (total). While glauconite supporting the 'layer lattice' theory records a simultaneous rise in $K_2O$ content at a fixed $Fe_2O_3$(total) (Banerjee et al., 2016a). The consistently high $K_2O$ and variable $Fe_2O_3$ (total) contents of glauconite within the Lower Quartzite glauconite neither support 'layer lattice' nor 'verdissement' theories. The relationship between $K_2O$ and $Fe_2O_3$ (total) supports the 'pseudomorphic replacement' proposed in earlier works (Dasgupta et al., 1990; Banerjee et al., 2015, 2016a, b). Textural evidence indicates that replacement of K-feldspar by glauconite. The pseudomorphic replacement theory explains the origin of most glauconites within the Precambrian (Dasgupta et al., 1990; Banerjee et al., 2008, 2015; Tang et al., 2017a, b and many others). However, in recent years, the origin of a few Phanerozoic glauconites has been explained by this theory (cf. Banerjee et al., 2016; Bansal et al., 2017). However, the $Fe_2O_3$ (total) content of the Phanerozoic glauconite is higher than the Precambrian counterpart (Banerjee et al., 2016).

The 'pseudomorphic replacement' involves the supply of excess K and Si in the pore-water by the dissolution of K-feldspar. The availability of excess K, Fe, Si and Mg facilitates the formation of glauconite in laboratory experiments (Harder, 1980). However, Si and Fe contents of the seawater are too low to form glauconite. The absence of mafic minerals within the framework the Lower Quartzite sandstones suggests the seawater source for Fe and Mg contents in glauconite. The highly alkaline seawater favors the dissolution of feldspar, releasing excess K, Si and Al to the pore-water. Elevated concentrations of $H_3SiO_4$, Cl, K, Na, Mg and Fe required for the formation of glauconite may be related either to continental weathering or to volcanism. A large flux of continental weathering related products possibly results in highly alkaline conditions in the shallow

marine setting. However, the glauconitic sandstone of the Lower Quartzite Member is immediately overlain by volcanic-derived sediments. Therefore, the volcanic source of the relevant ions cannot be ruled out. A high MgO content in Precambrian seas possibly facilitated the formation of glauconite, as suggested by the experimental results of Harder (1980). The MgO content of the glauconite within the Lower Quartzite Member is higher than the average values (cf. Odin and Matter, 1981; Banerjee et al., 2016a, b; Bansal et al., 2018, 2019; Rudmin et al., 2017, 2019). The high content of MgO in glauconite may indicate inter-stratifications of glauconite with chlorite and smectite (Drits et al., 2010). However, the XRD parameters do not reveal any inerstratification of glauconite with chlorite or smectite. Mg-rich seawater during the Mesoproterozoic possibly caused the high Mg content of glauconite (Banerjee et al., 2008).

As the formation of glauconite is favoured in the modern ocean at a depth range between 200 and 500 m (Odin and Matter, 1981), the same environmental interpretation is often extrapolated for the ancient variety including Precambrian. However, the glauconite possibly formed in shallow marine environment during the Precambrian (Banerjee et al., 2016a). The only deep marine example of Precambrian glauconite is from the Penganga Group of the Pranhita-Godavari valley (Deb and Fukuoka, 1998). However, Bandopadhyay (2007) considered allogenic origin for the same glauconite. Several studies indicate that a sub-oxic depositional setting favours the formation of glauconite (Tang et al., 2017a; Rudmin et al., 2019; Bansal et al., 2019), while an anoxic condition facilitates the formation of pyrite (Berner, 1981). Recently, Bansal (2019) found that the formation of shallow marine hypoxia during the greenhouse climate of the Mesozoic facilitated the formation of glauconite. The $Fe^{2+}/Fe^{3+}$ ratio of the glauconite within the Lower Quartzite Member supports the hypoxic seawater in the shallow marine setting during the Mesoproterozoic (Tang et al., 2017a). The paucity of suitable substrates like fecal pellets and bioclasts may be the primary reasons for the rarity of glauconite in the Precambrian. The secondary alteration to chlorite by the low-grade metamorphism might have destroyed many records of glauconite. The formation of authigenic glauconite during the Precambrian took place by the alteration of sand-size substrate that may include quartz, feldspar, mica and mud clast, which are more common in shallow marine. Moreover, the shallow marine environment receives the continental weathering related supply of relevant ions

### 8.5.2. Sequence Stratigraphic context of the Precambrian glauconite

The presence of authigenic glauconite may be used to distinguish between 'simple omission surface', 'condensed section' and 'mega-condensed section' in Phanerozoic sedimentary sequences (Amorosi, 2013). While a thin (decimeter-scale) horizon with ~20% of nascent to slightly evolved glauconite (<6 wt% $K_2O$) characterizes the 'simple omission surface', the several cm-thick bed containing 50 wt% of the evolved variety (with 6 to 7.5 wt% $K_2O$) indicates a 'condensed surface' (Amorosi, 2013). A few m-thick horizons with a very high content of highly evolved glauconite ($K_2O$>7.5%) represents a "mega-condensed surface" (Amorosi op. cit.). The relationship between abundance and maturity of the glauconite in the Lower Quartzite Member suggests a condense zone (Fig. 8.6c). However, a major caveat is that the incipiently formed glauconite within the cleavages of the K-feldspar grains exhibits a high value of $K_2O$ within the Lower Quartzite Member. Therefore, only the pellets need to be considered for the sequence stratigraphic interpretations, while the incipient variety needs to be ignored.

The formation of glauconite within a condensed zone involves an extremely low rate of sedimentation for a prolonged period (Amorosi, 1995, 1997, 2013; Amorosi et al., 2007). TSTs are associated with major sediment starvation (Amorosi, 1995; Catuneanu et al., 2009). The studied glauconitic horizon occurs at the mid-level of a TST consisting of the stacking of Lower Quartzite, Bhagwar Shale and Bijaigarh Shale members (Fig. 8.2 and 8.3). The top of the glauconite horizon of the Lower Quartzite Member represents a major flooding surface, associated with a sharp change in lithology (Fig. 8.2). The Lower Quartzite is overlain by the Bhagwar Shale indicates a relatively sharp transition from a sandstone to shale depositional environments in response to a sharp rise in the relative sea level. The presence of black shale alternating with the volcanogenic shale indicates the continuity of the TST deposition. The overlying highly carbonaceous Bijaigarh Shale mark the top of the TST containing the MFZ (Banerjee et al., 2006). The glauconite neither occurs in the Bhagwar Shale, nor in the Bijaigarh Shale. The anoxic condition during the deposition of Bhagwar and Bijaigarh shales favored the formation of authigenic pyrite, rather than glauconite. A roughly 1 m-thick pyrite horizon marks the condensed deposit within the Bjiagarh shale (Sur et al., 2006; Singh et al., 2018). Therefore, we argue that the glauconite horizon in the Lower Quartzite, with evolved to highly evolved glauconite ($K_2O$ 6.7% to 8.3%) is associated with a marine flooding surface, but not the condensed deposit.

The anoxic seawater discourages the formation of glauconite, while the dys-oxic depositional condition facilitates its growth.

## 8.6. Conclusions

The study of the glauconite within the Lower Quartzite Member in the Kaimur Formation of the Vindhyan Supergroup leads to the following conclusions.

(a) A detailed facies and paleogeographic analysis establishes that the glauconite formed in a shallow, sub-tidal environment, unlike its Phanerozoic counterpart which forms in the deep marine condition.

(b) The chemical characteristics of the glauconite are unique, with high $K_2O$, MgO and $Al_2O_3$ and low $Fe_2O_3$. The X-Ray diffraction parameters confirm the evolved character of the glauconite with negligible interstratifications of expandable and non-expandable layers in the crystal.

(c) The glauconite forms by the pseudomorphic replacement of the K-feldspar. The glauconite evolves by the addition of $Fe_2O_3$ at consistently high content of $K_2O$. Similar compositional evolution has been recorded in most Precambrian glauconites, although this maturation trend is also known from the Phanerozoic.

(d) The formation of glauconite is facilitated by elevated concentrations of $H_3SiO_4$, Cl, K, Na, Mg and Fe, possibly derived by continental weathering and/or contemporary volcanism. The high Mg content of the glauconite is possibly related to the Mg-rich seawater during the Mesoproterozoic.

(e) The glauconite occurs at the mid-level of a TST, associated with a major marine flooding surface and dys-oxic depositional condition, and is absent in the condensed zone containing the MFZ. The establishment of anoxic depositional condition facilitates the deposition of carbonaceous and pyritiferous shale in the overlying condensed zone deposits.

# CHAPTER 9

# Shallow marine glauconitization during the Proterozoic in response to intrabasinal tectonics: a study from the Proterozoic Lower Bhander Sandstone, Central India

## 9.1. Introduction

Glauconite is an authigenic K- and Fe-rich di-octahedral clay mineral, typically formed by the active exchange of cation between sea water and sediment substrate (Odin and Matter, 1981; Velde, 2003; Meunier and El Albani, 2007; Tang et al., 2017). Although glauconite occurs in marine deposits ranging in age from Proterozoic to Recent, a close review of its temporal distribution reveals non-uniform distribution pattern across the stratigraphic column, with Proterozoic records contributing ~7% (Ivanovskaya., 2009; Banerjee et al., 2016, 2020; Bansal et al., 2020). A low rate of sedimentation and oxygen-depleted depositional condition allow the prolonged chemical interaction between incipient glauconite and the ambient sea water (Baldermann et al., 2013; Mandal et al., 2020; Roy Choudhury et al., 2021). Therefore, the maturation of glauconite is often used as a tool to identify stratigraphic 'condensed' and 'mega-condensed' sections associated with transgressive sediments (Amorosi, 2012; see Bansal et al., 2017 for more references). However, in a sharp contrast to modern glauconite preferably forming in the outer shelf and slope environments, it occurs within shallow marine deposits in the Precambrian (Banerjee et al., 2016; Bansal et al., 2020; Mandal et al., 2020). Several studies show low to moderate contents of $Fe_2O_3$ and higher content of MgO in Proterozoic glauconites compared to their Phanerozoic counterparts (Banerjee et al., 2008, 2015, 2016; Tang et al., 2017, Mandal et al., 2020; Algabri et al., 2020). However, Precambrian glauconites are prone to aluminization and/or chloritization (Ivanovskaya., 2009; Bansal et al., 2020). The widespread compositional variation in glauconite reflects a combination of factors, including seawater chemistry, initial composition of the substrate and the redox conditions (El Albani et al., 2005; Meunier and El Albani, 2007; Banerjee et al., 2016, 2020; Tang et al., 2017; Mandal et al., 2020; Bansal et al., 2020; Algabri et al., 2020; Roy Choudhury et al., 2021). Although, the controlling factors in modern and Phanerozoic deposits are well understood (Banerjee et al., 2016), the origin of Precambrian glauconites is enigmatic. Proterozoic epeiric seas are generally characterized by low-gradient, shallow seafloor, recording slow subsidence, albeit repetitive (Jackson, 1990; Eriksson et al., 1998; Sarkar et al.,

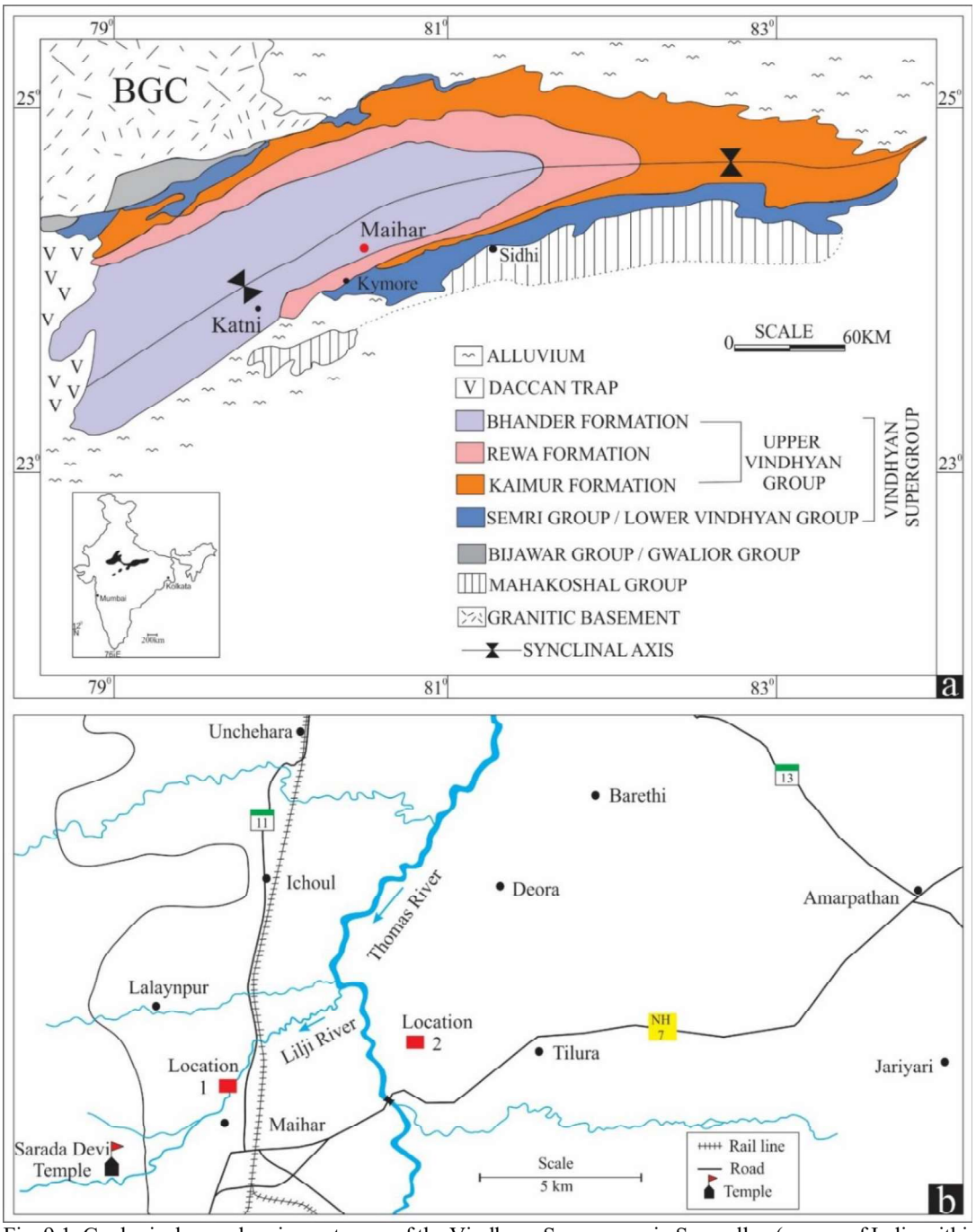


Fig. 9.1. Geological map showing outcrops of the Vindhyan Supergroup in Son valley (a, map of India within inset). Location map showing the studied sections of the Lower Bhander Sandstone (b, red rectangles).

2002). Dysoxic/ sub-oxic conditions prevail at shallow depth in these oceans (Canfield, 1998; Farquhar et al., 2000; Holland, 2002; Pavlov and Kasting, 2002; Bekker et al., 2004; Holland, 2006; Scott et al., 2008; Och and Shields-Zhou, 2012). A few studies have presented redox variations in Precambrian epeiric sea deposits based on proxies such as trace elements, including REE concentrations of glauconite and host sediments (Tang et al., 2017; Bansal et al., 2020; Algabri et al., 2020). The factors responsible for the variation

of paleo-redox variation in Proterozoic epeiric seas are yet to be addressed. Besides, the redox variation within the sedimentary sequence in relation to intrabasinal tectonics is yet to be investigated.

We have examined the Lower Bhander Sandstone of the Proterozoic Vindhyan basin to highlight the role of intrabasinal tectonics on glauconitization. The objectives of this study are (a) to highlight the geochemical and mineralogical characteristics and the evolution of Proterozoic glauconite and (b) to examine the influence of basinal tectonics on paleo-redox variation in an epeiric setting. Field, petrographical, geochemical and mineralogical information have been integrated to highlight the basic tenet of glauconitization in overall shallow Proterozoic epeiric seas.

## 9.2. Geology of study area

### 9.2.1. Stratigraphy and age constrain

The present investigation focuses on glauconite within the Lower Bhander Sandstone Member of the Bhander Formation, Vindhyan Supergroup in central India (Fig. 9.1). The mildly deformed, two-tiered Vindhyan Supergroup, separated by an unconformity, consists of the Lower Vindhyan (Semri Group) and the Upper Vindhyan Group (Fig. 9.2a; Bose et al., 2015, Mandal et al., 2019). The Bhander Formation of the Upper Vindhyan Group consists of Ganurgarh Shale, Bhander limestone, Lower Bhander Sandstone, Sirbu Shale and Upper Bhander Sandstone Members (Fig. 9.2a; Bose et al., 2001). The Lower Bhander Sandstone Member, hosting the glauconite, is bounded between Bhander Limestone and Sirbu Shale Member (Bose et al., 2001). The age of the Lower Vindhyan Group ranges from 1.7 to 1.5 Ga (Rasmussen et al., 2002, Ray et al., 2002; Sarangi et al., 2004; Bickford et al., 2017), while the age of the Upper Vindhyan Group is uncertain. The underlying Bhander Limestone yields 1.0-0.9 Ga age by Pb-Pb dating (Gopalan et al., 2013). Although, Lan et al. (2020) has reported detrital zircon within top part of Bhander formation around 548 Ma but, it needs confirmation by more geochronological data (Bickford and Basu, 2021).

### 9.2.2. Intrabasinal tectonics

Despite its origin in an overall stable intra-cratonic basin, the Vindhyan sediments record the tell-tale evidence of tectonic signatures (Bose et al., 1997, 2001; Sarkar et al.,

1995, 2002, 2014). Small-scale tectonic features and related sedimentary attributes highlight the

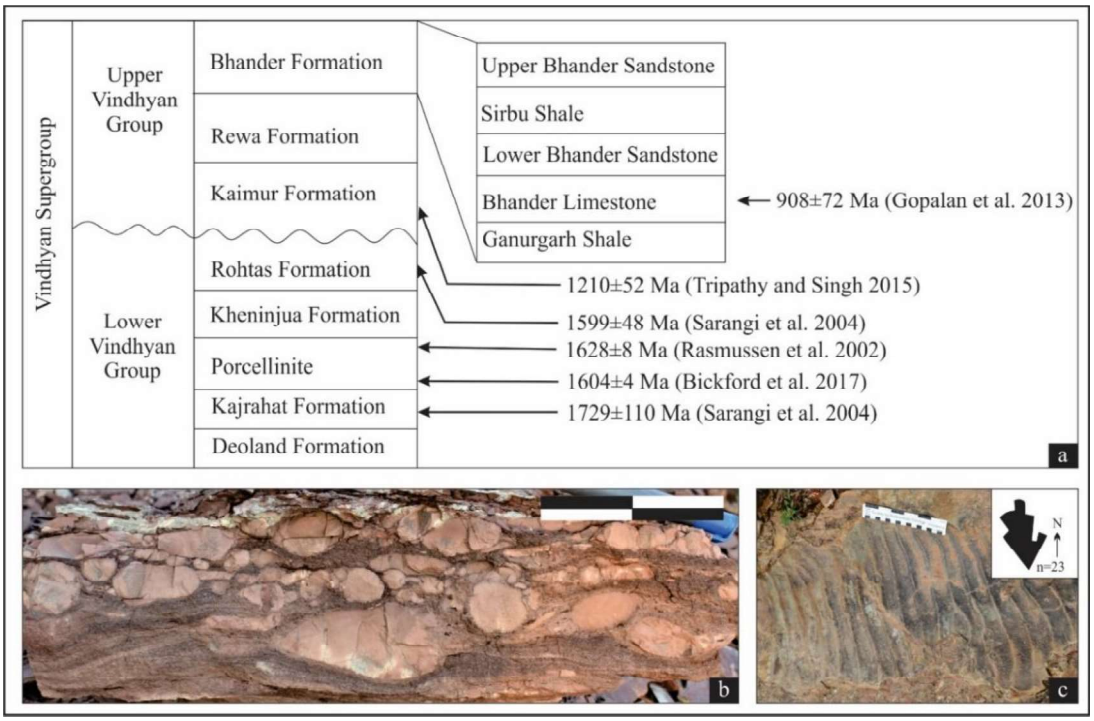


Fig. 9.2. Overall stratigraphy of the Vindhyan Supergroup, with necessary elaborations of the Bhander Formation(a), Wedge-shaped mud pebble conglomerate (b, length of the bar 15 cm), and asymmetric wave ripples on bed surface (c, scale length 15 cm, paleocurrent data within inset) within the Lower Bhander Sandstone.

evolution of the basin (Bose et al., 1997, 2001). The dominantly marine, lower Vindhyan sediments were deposited in an E-W elongated basin under the influence of N-S rifting (Bose et al., 2001). The Upper Vindhyan sediments, on the other hand, deposited in a sag basin after the cessation of rifting (Bose et al., 2001; Sarkar et al., 2002). The scale of tectonically induced deformation features reduced as the basin underwent a rift to sag transition. In the sag stage, the tectonic imprints were recorded in cm-scale slump folds and slide planes associated with deflection of paleocurrent patterns. Tectonically induced subsidence events induced small-scale soft sediment deformation structures (Sarkar et al., 2002, 2014; Singh and Chakraborty, 2021). Although the influence of tectonism was mild during the sag stage, depositional cycles of various orders developed.

Both Bhander Limestone and Sirbu Shale contain abundant syn-depositional soft-sedimentary deformation structures (SSDS) (Bose et al., 2001; Sarkar et al., 2002, 2014; Singh and Chakraborty, 2021). The related sedimentary packages bear the influence of intrabasinal tectonics during the deposition (Sarkar et al., 2002, 2014). The preservation of

laterally persistent convolute laminated horizons, small-scale folding, in-situ brecciation, tilted blocks and small-scale faults in the Bhander Limestone signify the presence of seismicity (Sarkar et al., 2014). The change of depositional packages in association with those of *seismites* horizon indicate tectonically induced subsidence during the sag stage (Sarkar et al., 2014). Similarly, the Lower Bhander Sandstone is composed of a number of repetitive cycles, constituted by mudstone, sandstone-siltstone and mud pebble conglomerate (Fig. 9.2b), affected by basinal tectonics (Bose et al., 2001). Strikingly, the slides planes (NW-SE) occur at certain intervals, exclusively associated with the wedge-shaped conglomerates. The paleocurrent patterns in this association are different than other parts of the LBS (Fig. 9.2c). Exhumed gullies locally occur in this association (maximum width and depth 45 cm and 9 cm respectively). The occurrence of wedge-shaped mud pebble conglomerate and the slide plane within these beds indicates sequential basin subsidence (Bose et al., 2001; Sarkar et al., 2002).

### 9.3. Material and methods

Detailed field study was carried out around Maihar area exposing the Lower Bhander Sandstone (Fig. 9.1b). A high-resolution facies analysis was carried out within the LBS based on detailed documentation of lithological variability and primary sedimentary structures. Graphic logs were prepared showing lateral and vertical facies variation. Fresh samples of mudstones and glauconitic rocks were collected. Sample positions were marked in the graphic log (Fig. 9.3). Petrographic investigation was carried out using Leica DM 4500P polarizing microscope attached to Leica DFC420 camera at Department of Geological Sciences, Jadavpur University. Major element concentrations of glauconite and its substrate were determined on 4 thin sections at 105 points, using a Camera SX 5 Electron Probe Micro Analyzer at Department of Earth sciences, Indian Institute of Technology Bombay, with following specifications: accelerating voltage 15 kV, specimen current of 40 nA and beam diameter of 1 μm (peak: 10-20s and background counting: 5-10s) and analytical error < 1%. Standards include both synthetic and mineral phases. The crushed glauconitic samples were washed with distilled water and then ultra-sonicated. The slurry was transferred in a glass cylinder for settling the silt particles. The silt-free slurry was centrifuged at 300 rpm for 15 min to recover the clay fraction. The residue was mixed with small quantity of distilled water for the preparation of smear mounts, which was scanned from $10^0$ to $70^0$ (step size – $0.026^0$ 2θ), using the nickel filter copper radiation at a scan

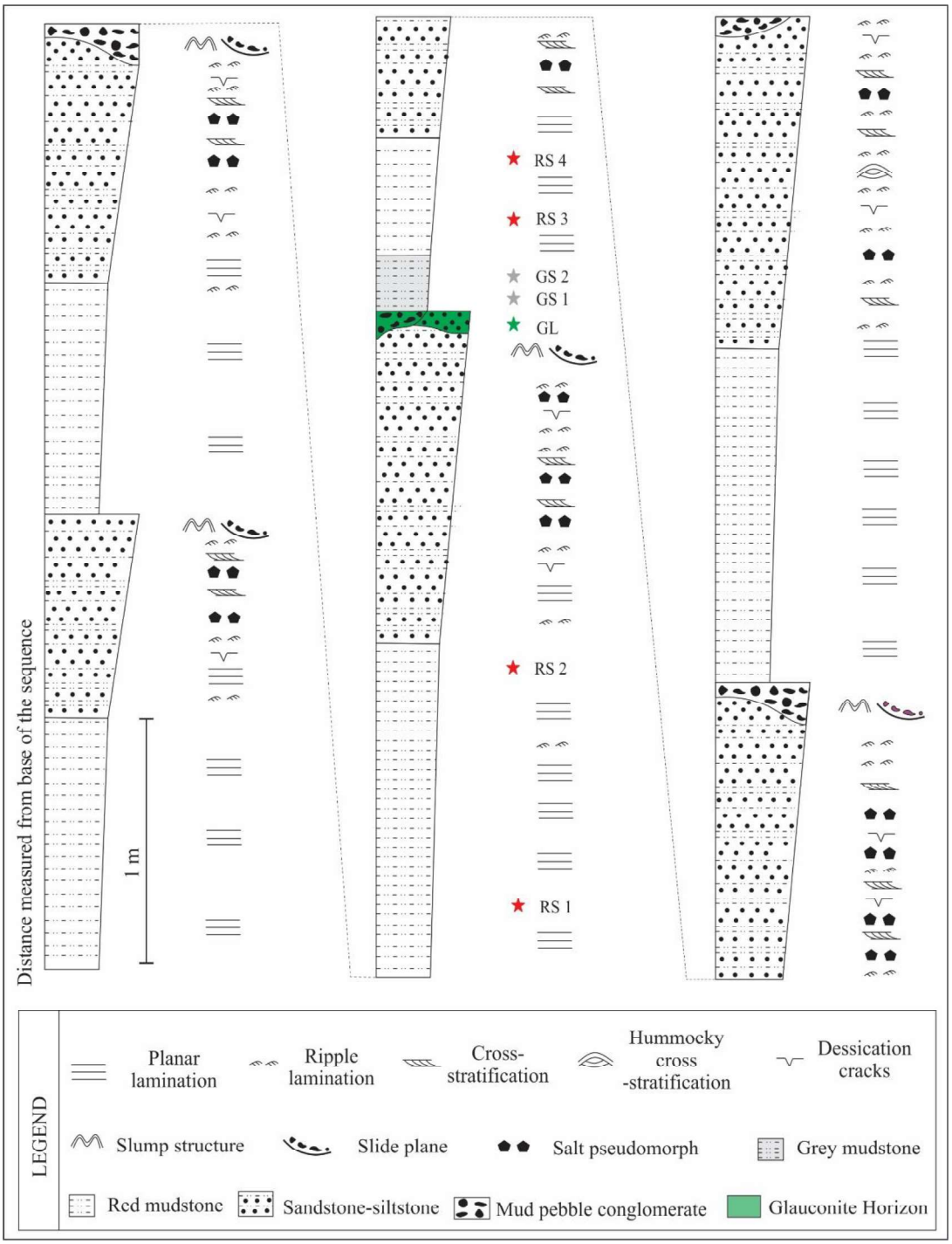


Fig. 9.3. Log showing facies comprising the Lower Bhander sandstone. Note the glauconitic horizon (marked by star, green colour) at the mid-level of the measured section. Also note the position of collected samples (RS- red mudstone, GS- grey mudstone, GL- glauconitic rock).

speed of 96 s/ step using an Empyrean X-Ray Diffractometer with pixel 3D detector at Department of Earth Sciences, Indian Institute of Technology Bombay.

Trace elements concentrations of mudstone and glauconitic rock were performed at the Department of Earth Sciences, Indian Institute of Technology Kanpur. For the determination of the trace elements concentrations, 7 samples were collected across the glauconitic interval. Sample lithology were noted down. Approximately 0.25 g of sample powder was digested in pre-cleaned Teflon beakers at 130 ± $5^0$C using a mixture of trace element grade HF (3 parts) and $HNO_3$ (1 part) for 48 hours. After the digestion, the samples were dried and re-dissolved in concentrated 2 ml of aqua regia. The steps were repeated to complete the digestion process. Trace element concentrations were determined at ~200 ppm total dissolved solid solutions. Three procedural blanks, Reference Materials SBC-1 and SCO-1 (shale), SRM-2704 (river sediment), and SRM 2709a (soil) from US Geological Survey (USGS) and WGB-1 (Gabbro) rock standard from Canadian Certified Reference Material Project were also digested following the same procedures. Multi elemental standard solution, diluted to 7 appropriate concentrations, was used to construct the calibration curve. Trace element concentrations were determined based on the calibration curve. Details of analytical procedures are provided in Mukherjee et al. (2018). The measured trace element concentration of reference materials agrees well with the USGS certified values.

Trace element "enrichment factors" (EFs) was calculated relative to the average upper continental crust (UCC; Rudnick and Gao, 2014) as follows.

$X_{EF}=[(X/Al)_{sample}/(X/Al)_{UCC}]$, where X and Al stand for the weight concentrations of trace elements X and Al respectively.

## 9.4. Results

### 9.4.1. Lithofacies analysis

The Lower Bhander Sandstone (LBS) is dominantly composed of mudstone and sandstone-siltstone with occasional mud pebble conglomerate (Fig. 9.3, 9.4a). The mudstone facies constitutes more than 50% of the rocks within the LBS succession (Fig. 9.3). The colour of the mudstone is generally red. However, a grey mudstone occurs in the studied section immediately above the glauconitic horizon (Fig. 9.3, 9.4b). The primary sedimentary structures are well preserved within the LBS (Fig. 9.4, 9.5, 9.6). A detailed

investigation of facies comprising the LBS was carried out for paleo-environmental interpretations (Table-9.1).

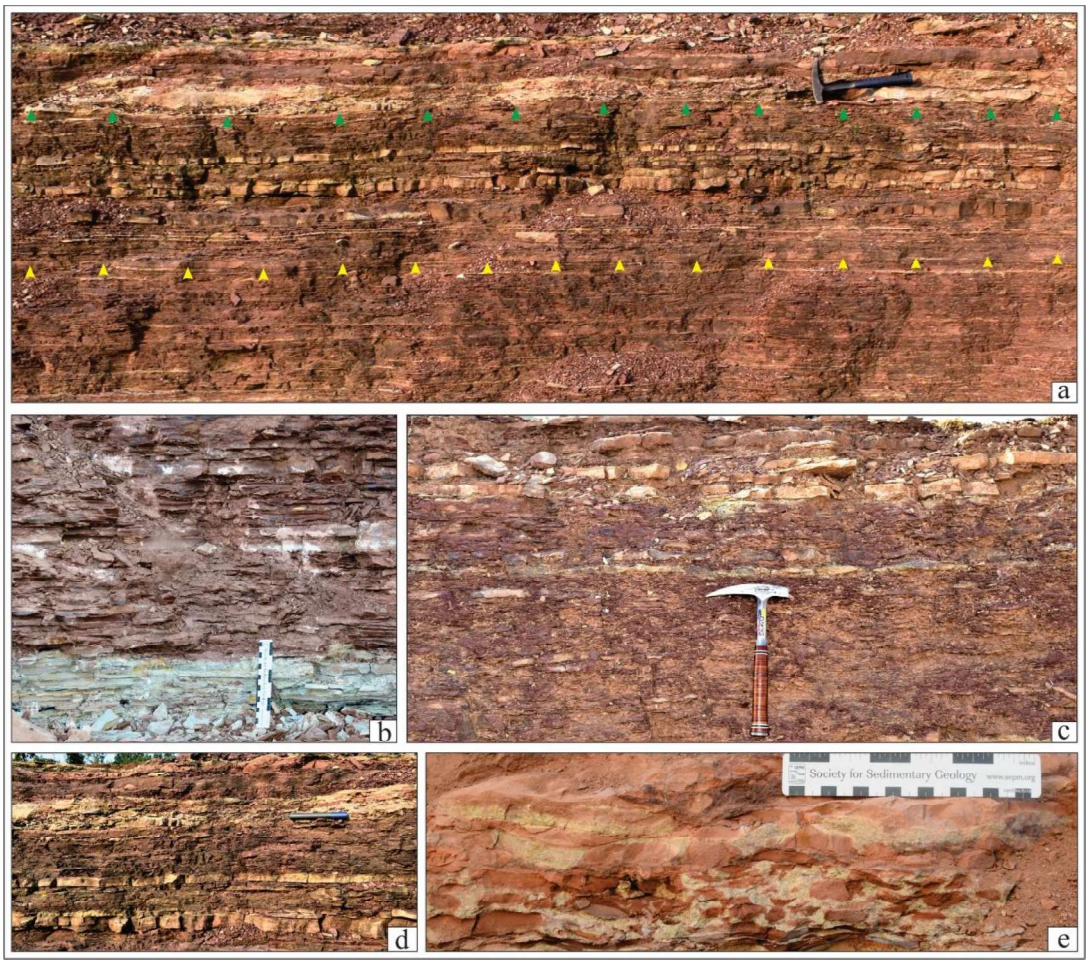


Fig. 9.4. Vertical facies variation within a complete cycle of mudstone, sandstone-siltstone and conglomerate in ascending order (a, yellow arrows are defining the boundary of mudstone and sandstone-siltstone facies, green arrows are separating sandstone-siltstone facies and conglomerate facies, hammer length 35 cm), grey and red mudstone (b, scale length 15 cm), gradational transition of sandstone-siltstone facies from mudstone facies (c, hammer length 35 cm), amalgamated conglomerate beds above sandstone-siltstone facies (d, marker length 15 cm), and clasts supported conglomerate (e, scale length 15 cm).

| Table-9.1. Description and interpretation of depositional facies in the Lower Bhander Sandstone | | |
|---|---|---|
| Facies | Description | Interpretation |
| Mudstone | This facies is characterized by monotonous, finely laminated reddish brown coloured mudstone (Fig. 9.4a, 4b), except one occasion, where the colour of the mudstone is grey (Fig.9. | Mudstone suggests a low-energy suspension fallout deposit in a relatively calm and quiet environment. However, the presence of some lenticular |

| | | |
|---|---|---|
| | 3). It occurs between sandstone-siltstone and conglomerate facies (Fig. 9.3). While the contact between conglomerate and red mudstone is very demarcated but the contact of mudstone and sandstone is gradational. Thickness of this tabular facies varies from 40 cm to 1 m. Cm-scale lenticular sandstone beds are occasionally present within this facies. These sandstone beds consist of small-scale cross-stratification, with occasional starved ripples. Under microscope, the mudstone shows alternation of laminae, marked by the appearance of quartz, mica grains. The characteristics of grey mudstone is compositionally similar to red mudstone (Fig. 9.4b). Thickness of bed is ca. 30 cm. This deposit is almost free of sand and emergence feature. Interestingly, it occurs between conglomerate and red mudstone. | sandstone bed within the red mudstone infers occasional high-energy input. The starved rippled bed suggests slow rate of sediment supply in the depositional site and formation during the high-energy (may be storm) events. On the other hand, grey mudstone suggests deeper paleogeography, below the wave base. The absence of sandstone-siltstone stringers and emergence features also support this contention. |
| Sandstone-siltstone | This facies is characterized by tabular fine-grained sandstone, siltstone beds with few mud interlaminae (Fig. 9.4a, 4c). The mud is generally red in colour. The sandstone beds are amalgamated. Maximum thicknesses of the amalgamated sandstone-siltstone body are ca. 1.7 m (Fig. 9.3). Maximum individual bed thickness is 30 cm. These sandstone beds have sharp base and gradational top with overlying red mudstone (Fig. 9.3). The basal part of these sandstone is | The abundance of cross laminations, different types of ripples and desiccation cracks on sandstone-siltstone bed surfaces infer shallow water deposition with occasional emergence. The alternation of mudstone with these sandstone beds signifies a steep change in energy gradient (Bose et al., 1997). The erosional base and abundant sole marks suggest high energy depositional conditions for their deposition (Bose and |

| | | |
|---|---|---|
| | massive or planar laminated with mud clasts at the base. They change into ripple laminated sandstone gradationally at the top part. Some of the beds contains hummocky cross-stratification (Fig. 5a). Most of the bed soles exhibit tool marks like flute casts, grooves, prods and brush marks at their bases (Fig. 5b, 5c). Most ripples show straight to sinuous and bifurcating crests (Fig. 5d). Superimposed and interference ripples are also present within on sandstone bed surfaces. Rain imprints (Fig. 5d) and desiccation cracks are also found. Halite pseudomorphs are abundant within these sandstone beds (Fig. 5e). | Choudhuri, 1990). The preservation of mudstone clasts at the base of some sand beds with undulatory base suggest erosion of underlying mudstone. The gradational change from massive/plane laminated to ripple cross laminations indicate the waning nature of the flow. The sharp base and the gradational upper contact support the interpretation. Salt pseudomorphs in combination with emergence features suggest deposition in a coastal playa (Bose and Chaudhuri, 1990; Bose et al., 2001). The occasional preservation of salt crystals on bedding surface indicates evaporative conditions. The emergence features including rain imprints, desiccations cracks indicate emergence. |
| Mud pebble conglomerate | This facies is characterized wedge-shaped conglomerate with non-erosional base (Fig. 4a, 4d). The conglomerate varies from matrix-supported (Fig. 6a) to clasts supported (Fig. 4e). In lateral continuity, it transits to sandstone (Fig. 6a, 7). The clasts are mainly composed of red mudstone. The sandy matrix contains glauconite at places. Mud clasts within conglomerate are generally platy to ellipsoidal with maximum length of 18 cm. (Fig. 4e, 6a). The mud pebbles are chaotically arranged. Thin planar | Abundance of red mudstone clasts suggests intra-formational conglomerate and sand associated with these conglomerates are also intra-formational. The matrix-supported conglomerate with chaotic alinement of mud clasts and non-erosional base indicates high-density mass flow (Lowe, 1982; Myrow and Hiscott, 1991; Mulder and Alexander, 2001). The wedge-shaped geometry of these conglomerate suggests debris flow deposition (Bose and Chaudhuri, |

| | | |
|---|---|---|
| | laminated sandstone beds alternate with these conglomerate beds (Fig. 4e). Slide planes and slump folds are essentially associated with these beds (Fig. 6a, 6c). The slide planes are directed along NW-SE direction (Fig. 6c). | 1990; Bose and Sarkar, 1991). The crude thin sandstone alternation with some debris flow conglomerate beds represents winnowing of flow or coarse tail behind debris flow (Fig. 6d). Association of slide planes suggests that the debris flow was triggered by the slide planes (Fig. 6d; Bose et al., 2001). |

### 9.4.2. Occurrence and type of glauconite

Glauconite occurs within sandy matrix of intra-formational mud pebble conglomerate and associated sub-arksoic sandstone (Fig. 9.6b, 9.7). The conglomerate occurs near the base of a slide plane, laterally transiting to clasts-free sandstone (Fig. 9.6a, b, 9.7). The sandstone consists of ca. 70% quartz and 15% feldspar besides rock fragments and glauconite (Fig. 9.8a, b). Glauconite occurs predominantly as laths and pellets besides a few showing dumbbell shape (Fig. 9.8b, c). The longest dimension of glauconite is 800 µm in laths and 250µm in pellets. Glauconite appears light green to olive green under plane polarized light and variegated interference colour under crossed polar. Although many of the glauconite occurs as pellets, incipient glauconite forms as green patches of alterations along fractures and cleavages of feldspars (Fig. 9.8d) and around rims of quartz grains (Fig. 9.8e). X-ray mapping shows enrichment of K, Al, Fe, Mg and Si within the altered zone and confirms the glauconite (Fig. 9.9, 9.10). Occasionally fractures, filled with carbonate cement cross-cut the lath-shaped glauconite grains (Fig. 9.8f).


Fig. 9.5. Hummocky cross-stratification in sandstone facies (a, marked by white arrows; bar length 20 cm), flute casts (b, marker length 10 cm), prod and brush marks (c, yellow arrows show prod, red arrows show brush marks, current direction of sole marks is within inset; scale length 15 cm) on the sole surface of LBS. Wave ripples on sandstone bed surface with rain imprints (d, length of scale 15 cm), and salt pseudomorphs at the base of sandstone bed (e, white arrows, diameter of the coin is 2.3cm).

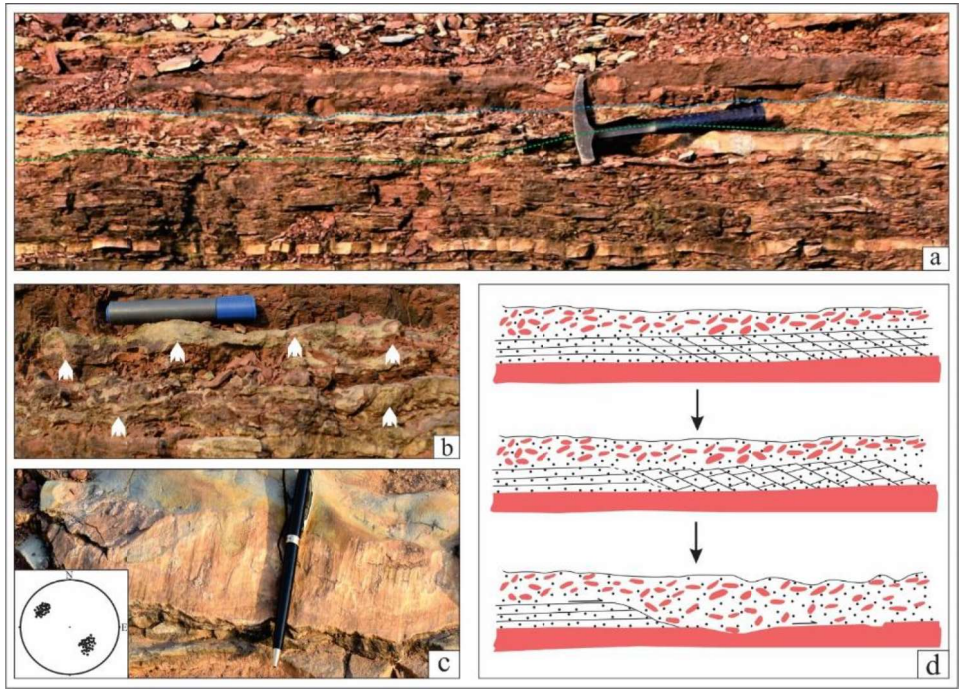


Fig. 9.6. Wedge-shaped conglomerate (a, thickness variations and lateral transition to siltstone-sandstone marked by dotted lines, hammer length 35 cm), glauconite- bearing conglomerate and sandstone (b, glauconitic sandstone indicated by arrows; marker length 15 cm), slide planes present at the contact of conglomerate bed (c, poles showing of dip direction of slide planes within the inset, pen length 15 cm) and schematic diagram showing stages of evolution of the slide plane and its associations. Note the contemporaneous mechanism for sediment gravity flow from sandstone unit intervened by thin mud layers (d).

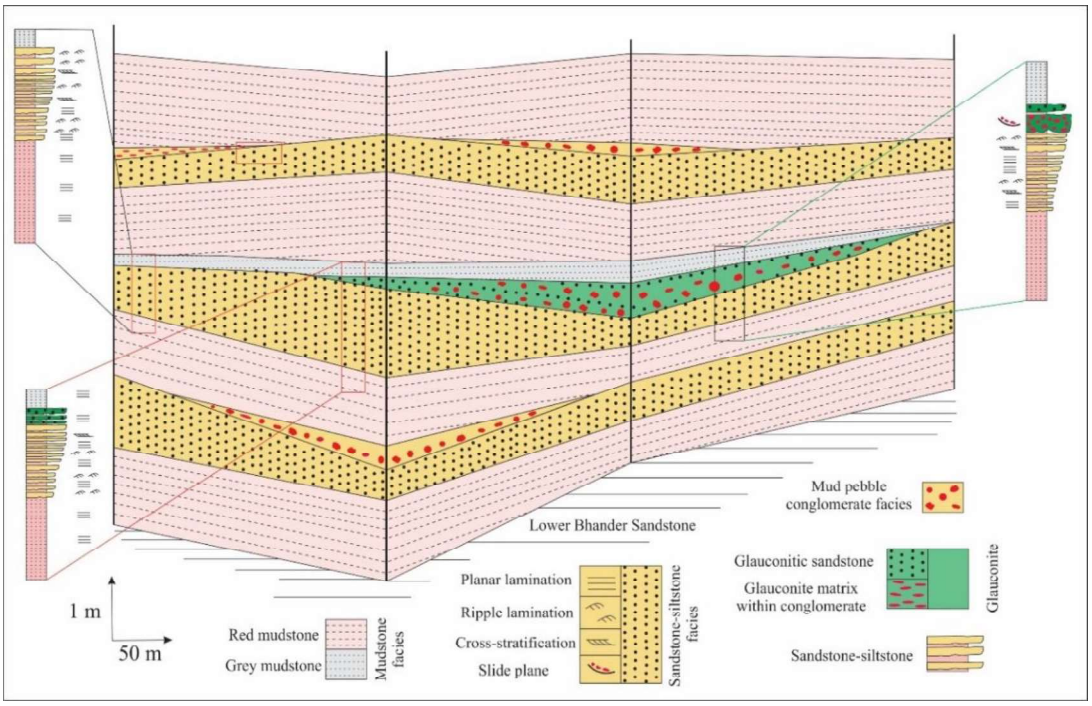


Fig. 9.7. Fence diagram showing lithological disposition of facies comprising the Lower Bhander Sandstone in close association of the glauconite horizon. Note the lateral termination of the conglomerate and lateral transition to sandstone.

### 9.4.3. Mineralogy of glauconite

The air-dried, smear-mounted samples of separated glauconite exhibit basal reflections of (001), (002), (003), (004) and (005) at 10.54 Å, 5.00 Å, 3.33 Å, 2.45 Å and 1.99 Å respectively (Fig. 9.11). The basal (001) reflections are asymmetric and broad-based. The intensity of (002) and (004) reflections are subdued. Apart from the basal (001) reflections, the glauconites also exhibit (020) reflection at 4.50 Å and (060) reflection at 1.51 Å. Other characteristic peaks include ($11\bar{2}$), (112), (130) and (240) at 3.50 Å, 3.24 Å, 2.58 Å and 1.67 Å (Fig. 11). Upon glycol solvation, the basal (001) reflections broaden and record a shift in position and d-spacing. The (001) reflection shifts to 10.10 Å with a broad hump at a lower diffraction angle. The (002) and (003) peaks shift to 5.06 Å and 3.35 Å respectively. The (004) and (005) reflections do not show noticeable shift in peak position. Other characteristic peaks record small shift in peak position. Upon heating at 550 °C for 1 hour, the basal (001) peak collapses to 10.17 Å with broad bases. The (002) and (003) peaks show broad bases and shift to 5.00 Å and 3.31 Å respectively in heated samples (Fig. 9.11).

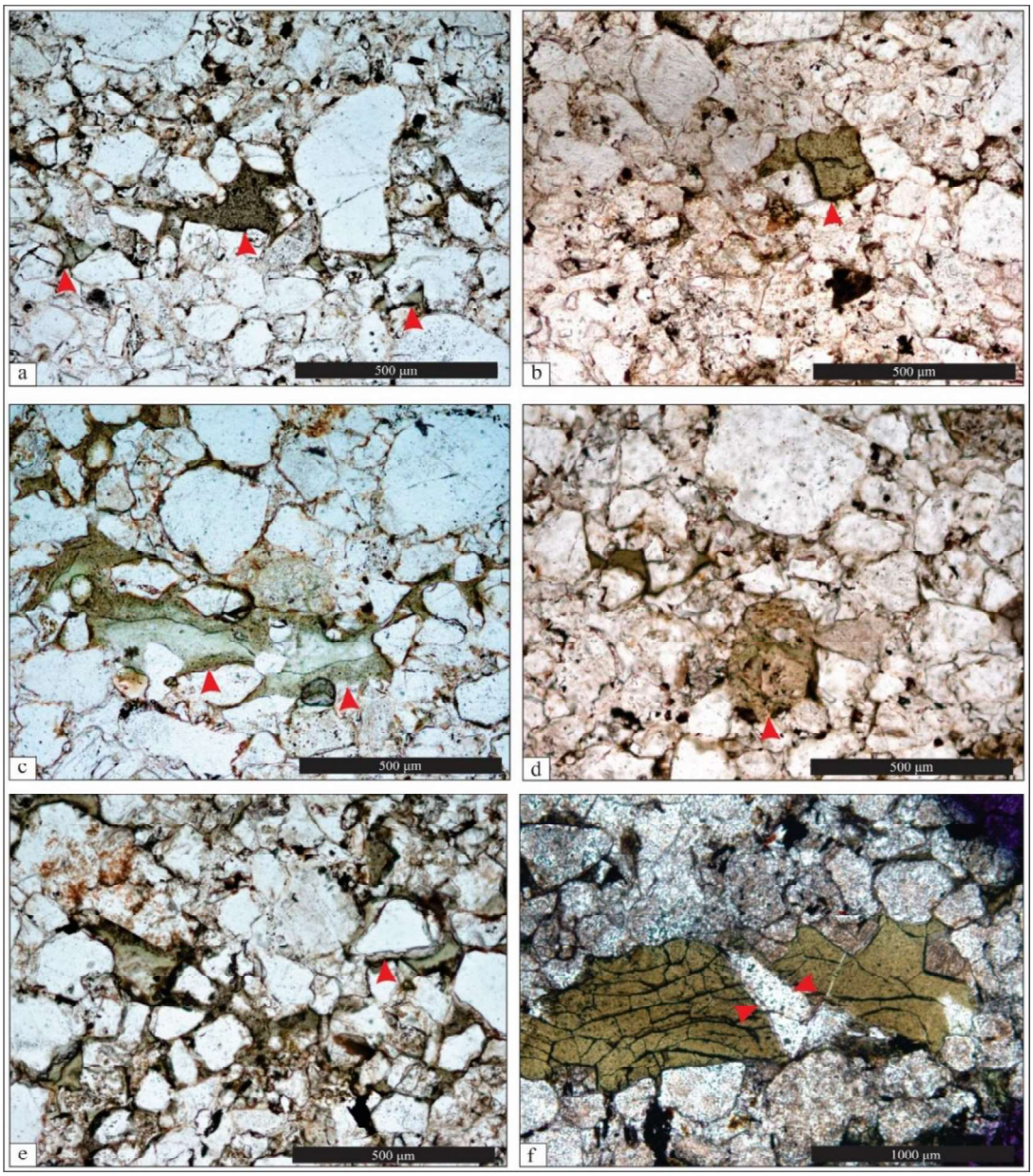


Fig. 9.8. Photomicrographs under plane polarized light: glauconitic quartz arenite (a, b), lath-shaped glauconite (c), glauconite pellet and partially replaced feldspar (d, partially replaced feldspar is marked by arrow), glauconite rim around a quartz grains (e, marked by arrow), and late diagenetic carbonate along fracture within glauconite (f, mark by arrows).

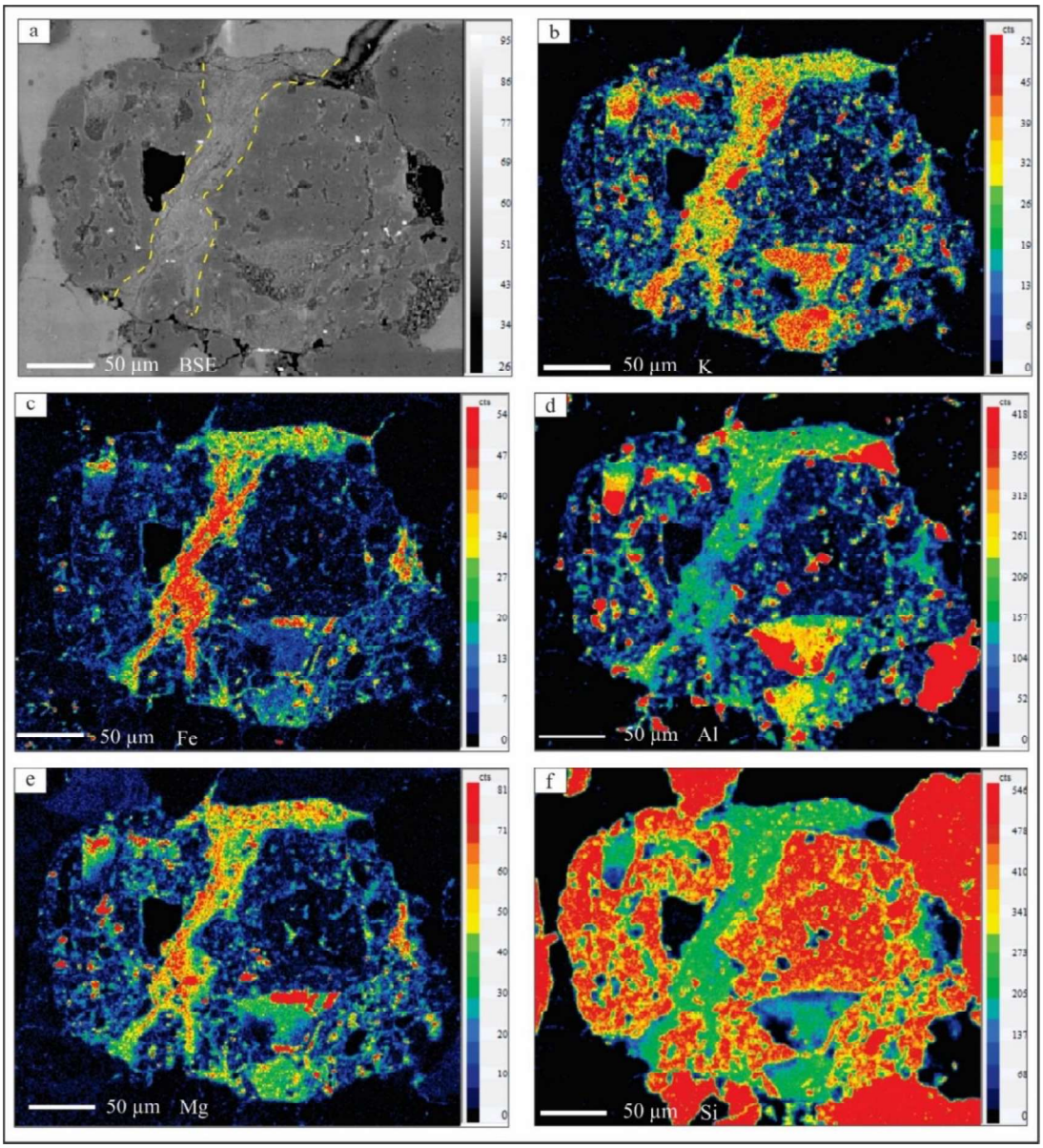


Fig. 9.9. EPMA backscattered image of glauconitization along the cleavage of feldspar (a, marked by yellow dotted lines). Elemental mapping showing abundance of K (b), Fe (c), Al (d), Mg (e), Si (f).

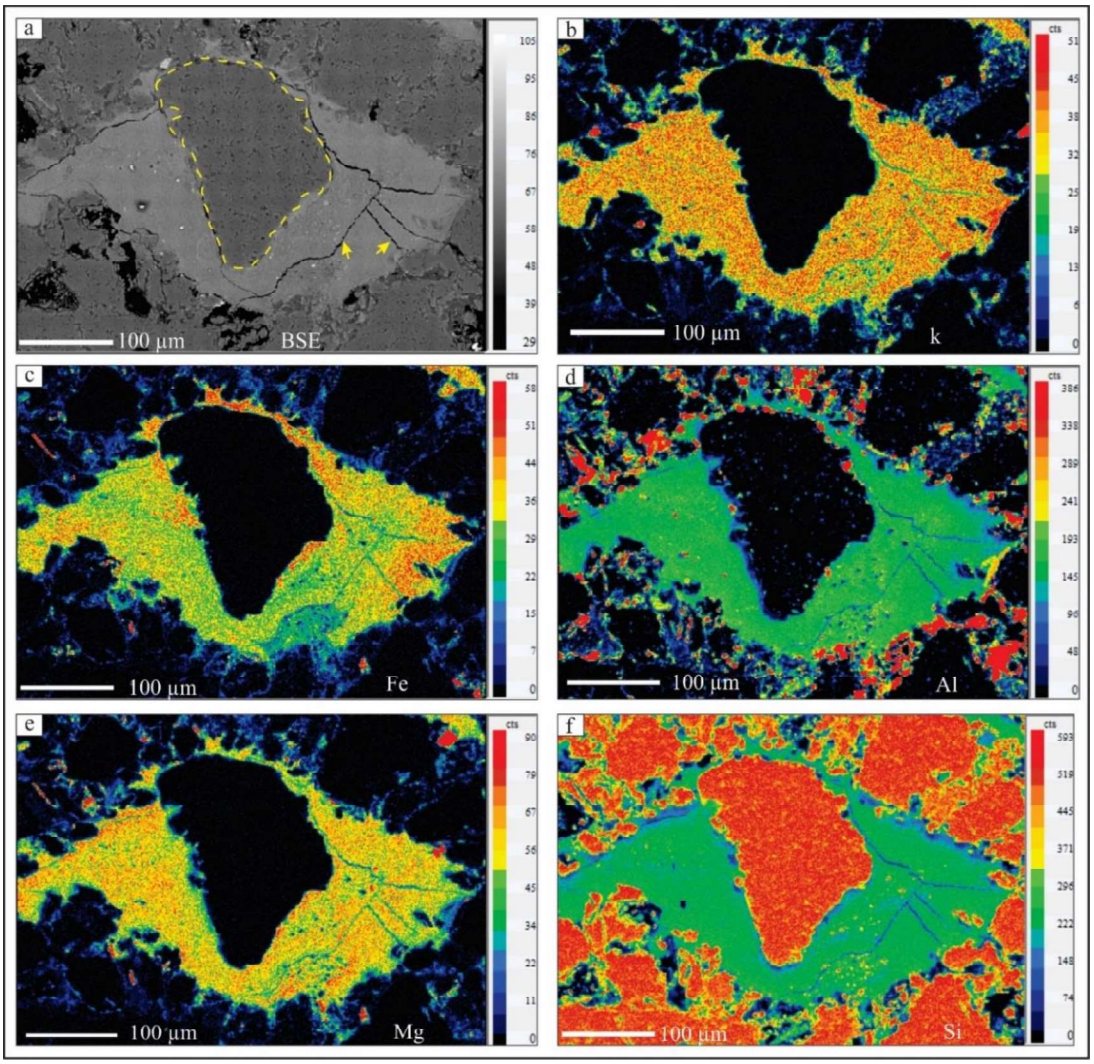


Fig. 9.10. EPMA backscattered image of glauconite formed by the replacement of quartz (a, marked by dotted line). Mapping showing elemental abundance of K (b), Fe (c), Al (d), Mg (e), Si (f).

The basal (001) reflection close to 10 Å is the characteristic of glauconite (Odin and Matter, 1981). The occurrence of (001) reflection at 10.54 Å (air-dried sample) signifies a glauconite structure with negligible interstratified smectite (Thompson and Hower, 1975; Odom, 1984; Xiang et al., 2012; Baldermann et al., 2013; Banerjee et al., 2019). Minor shifts in peak position upon glycolation and heating further attests to this possibility. The subdued intensity of (002) and (004) reflections at 5.00 Å and 2.45 Å respectively, indicates glauconite with high octahedral iron concentration. Both these peaks are not found in case of illite (Odom, 1984; Banerjee et al., 2015; Bansal et al., 2020). The reflections of $(11\overline{2})$ and (112) along with positions of the basal (001) reflection close to 10 Å signifies an ordered structure (Xiang et al., 2012). The X-ray diffractional parameters point towards a 'evolved' to 'highly-evolved' glauconite. The sharp and symmetrical peaks at 4.26 Å, 1.82

Å and at 1.54 Å correspond to quartz. The glauconite (003) reflection at 3.33 Å overlaps with that of quartz (011), resulting in a sharper reflection.

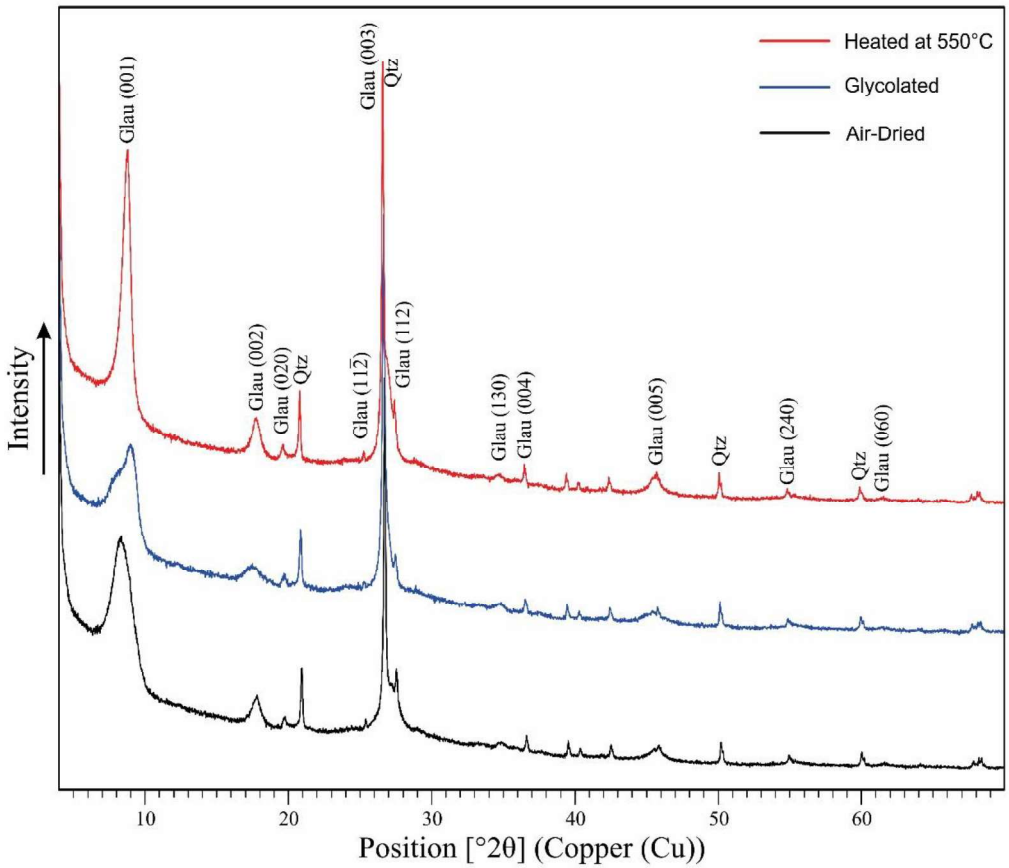


Figure 9.11: X-Ray diffractogram of separated glauconite after air-drying, glycolation and heating (550°C for 1 hour).

### 9.4.4. Major oxide concentration and Structural formula of Glauconite

Concentrations of major elements were determined at 105 points in 4 samples using Electron Probe Micro Analysis (EPMA) (Table-9.2). All analyses were normalized to 100 wt% on anhydrous basis for cross-plots. The $K_2O$ content of glauconites ranges from 7.1 to 8.6 wt% (avg. 8.0 wt%). The $Fe_2O_3$(total) content varies from 6.2 to 18.5 wt% (avg. 11.1 wt%). The $Al_2O_3$ content in the majority of the glauconite grains (>80%) exceed 15 wt%. The MgO content varies from 2.8 to 4.7 wt% (avg. 3.8 wt%). The $SiO_2$ content ranges from 47.9 to 58.3 wt% (avg. 53.1 wt%). Contents of CaO, $P_2O_5$, MnO, $TiO_2$ and $Na_2O$ are negligible. The major oxides composition provides the following crucial information regarding the compositional evolution of glauconites.

(a) The $K_2O$ content of glauconites in the LBS suggest 'evolved' to 'highly evolved' varieties (Odin and Matter, 1981; Amorosi, 1995; Amorosi, 1997). Further, the

$TFe_2O_3$ contents of glauconites show low to moderate values. The $K_2O$ vs. $TFe_2O_3$ cross-plot of the LBS glauconite exhibits widely varying chemical composition from 'ferric illite' to 'glauconite' (Fig. 12a) (Odin and Matter, 1981). The poor correlation between $K_2O$ and $TFe_2O_3$ suggests the addition of $Fe_2O_3$ into the glauconite structure at a constant $K_2O$ (Fig. 9.12a). The compositional ranges of $K_2O$ and $TFe_2O_3$ of LBS glauconites bear typical Proterozoic signature, as most of the data-points occupy the 'compositional gap' (Dasgupta et al., 1990, Deb and Fukuoka, 1998; Ivanovskaya et al., 2006; Mingxiang et al., 2008; Banerjee et al., 2008, 2015, 2016; Tang et al., 2017; Bansal et al., 2020; Mandal et al., 2020; Algabri et al., 2020).

(b) All glauconite grains contain a high amount of $Al_2O_3$, with an average of 18.9 wt%. The high $Al_2O_3$ content of the glauconite in the LBS relates them to the 'high-alumina' variety (Berg-Madsen, 1983; Lee and Paik, 1997; Jach and Starzec, 2003). Although the Proterozoic glauconite shows high $Al_2O_3$ content, recently Roy Choudhury et al. (2021) reported similar glauconite in Paleogene deposits. Further, the $Al_2O_3$ content shows a strong negative correlation with $TFe_2O_3$ ($r^2$=0.9, Fig. 9.12b). The negative relationship between $Al_2O_3$ and $TFe_2O_3$ construes the replacement of $Al^{3+}$ ions by Fe in octahedral site (Odin and Matter, 1981; Velde, 1985; Dasgupta et al., 1990; Amorosi et al., 2007; Banerjee et al., 2015, 2019; Rudmin et al., 2017).

The element concentration was constructed on an anion equivalent basis to structural formula per $O_{10}(OH)_2$ in glauconite. The $Fe^{2+/}Fe^{3+}$ ratio is assigned as 0.5, which is similar to other Proterozoic glauconite (Tang et al., 2017; Bansal et al., 2020). In octahedral site, $Al^{3+}$is the major cation, varying between 0.70 to 1.4 atoms per formula unit (a.p.f.u.). The $Mg^{2+}$cation ranges from 0.3 to 0.5 a.p.f.u. The octahedral $R^{3+}$ varies from 1.2 to 1.6 atoms with an average 1.4 a.p.f.u. The average of $Si^{4+}$ and $Al^{3+}$ in tetrahedral sites are 3.6 and 0.4 atoms, respectively (Table-9.2). The average structural formula of the glauconite is as follows.

$$K_{0.7}\,(Fe^{2+}_{0.3}Fe^{3+}_{0.3}Mg^{2+}_{0.4}Al^{3+}_{1.1})_{2.1}\,(Si_{3.6}Al_{0.4})_4\,O_{10}\,(OH)_2.\,nH_2O.$$

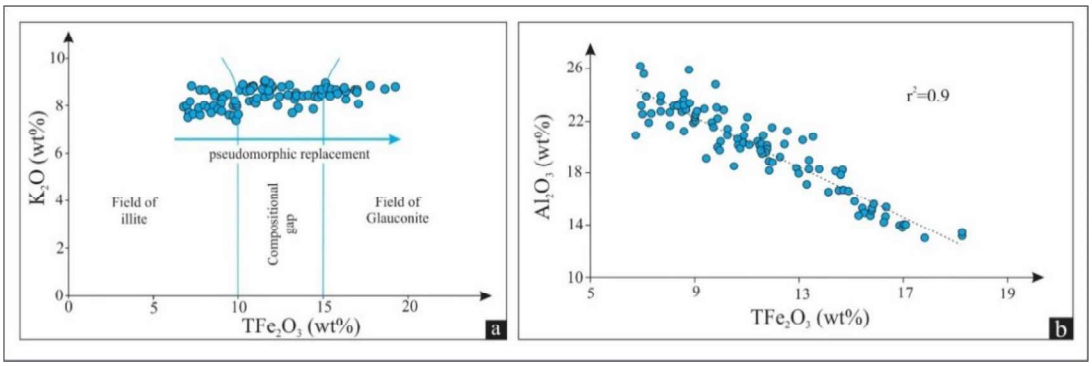


Fig. 9.12. Relationship between $K_2O$ vs. $TFe_2O_3$ (a, glauconite evolution path is represented by blue arrow), $Al_2O_3$ vs. $TFe_2O_3$ (b, $r^2$=0.9) invariant diagram of Lower Bhander Sandstone glauconite.

Table-9.2. Oxide weight percentage of glauconites and their structural formula

| Samples No | MgO | $Al_2O_3$ | $SiO_2$ | $TFe_2O_3$ | $K_2O$ | Total | $K^+$ | $Mg^{2+}$ | Al in oct. | $Fe^{3+}$ | $Fe^{2+}$ | $Si^{4+}$ | Al in tet. | $R^{3+}$ |
|---|---|---|---|---|---|---|---|---|---|---|---|---|---|---|
| | 3.9 | 21.1 | 53.5 | 8.7 | 7.9 | 95.9 | 0.7 | 0.4 | 1.2 | 0.2 | 0.2 | 3.6 | 0.4 | 1.5 |
| | 4.0 | 22.8 | 53.1 | 8.3 | 7.6 | 96.3 | 0.6 | 0.4 | 1.3 | 0.2 | 0.2 | 3.5 | 0.5 | 1.5 |
| | 3.5 | 20.9 | 52.5 | 9.3 | 7.6 | 94.5 | 0.7 | 0.4 | 1.2 | 0.2 | 0.3 | 3.6 | 0.4 | 1.5 |
| | 3.8 | 21.8 | 55.4 | 7.1 | 7.4 | 96.7 | 0.6 | 0.4 | 1.3 | 0.2 | 0.2 | 3.6 | 0.4 | 1.5 |
| | 3.9 | 21.0 | 49.9 | 10.4 | 7.6 | 94.3 | 0.7 | 0.4 | 1.1 | 0.3 | 0.3 | 3.4 | 0.6 | 1.4 |
| | 3.5 | 23.3 | 53.0 | 8.3 | 7.7 | 96.7 | 0.7 | 0.4 | 1.3 | 0.2 | 0.2 | 3.5 | 0.5 | 1.5 |
| | 3.0 | 24.6 | 51.4 | 6.5 | 7.4 | 93.8 | 0.6 | 0.3 | 1.4 | 0.2 | 0.2 | 3.5 | 0.5 | 1.6 |
| | 3.4 | 22.3 | 53.2 | 7.3 | 7.5 | 94.8 | 0.6 | 0.3 | 1.3 | 0.2 | 0.2 | 3.6 | 0.4 | 1.5 |
| | 3.4 | 19.3 | 47.9 | 10.8 | 7.9 | 89.8 | 0.7 | 0.4 | 1.1 | 0.3 | 0.3 | 3.5 | 0.5 | 1.4 |
| | 3.7 | 19.7 | 48.9 | 11.7 | 8.2 | 92.9 | 0.7 | 0.4 | 1.1 | 0.3 | 0.4 | 3.5 | 0.5 | 1.4 |
| | 4.3 | 23.0 | 52.9 | 7.4 | 7.3 | 96.2 | 0.6 | 0.4 | 1.3 | 0.2 | 0.2 | 3.5 | 0.5 | 1.5 |
| LBS 1 | 3.7 | 21.7 | 53.7 | 7.4 | 8.3 | 95.5 | 0.7 | 0.4 | 1.3 | 0.2 | 0.2 | 3.6 | 0.4 | 1.5 |
| | 3.5 | 24.4 | 49.5 | 8.3 | 7.4 | 94.2 | 0.6 | 0.4 | 1.3 | 0.2 | 0.2 | 3.4 | 0.6 | 1.5 |
| | 3.5 | 21.5 | 52.4 | 8.6 | 8.0 | 94.8 | 0.7 | 0.4 | 1.3 | 0.2 | 0.2 | 3.6 | 0.5 | 1.5 |
| | 3.5 | 21.5 | 52.9 | 8.2 | 7.4 | 94.0 | 0.6 | 0.4 | 1.3 | 0.2 | 0.2 | 3.6 | 0.4 | 1.5 |
| | 3.8 | 19.1 | 51.2 | 10.7 | 8.1 | 93.8 | 0.7 | 0.4 | 1.1 | 0.3 | 0.3 | 3.6 | 0.5 | 1.4 |
| | 3.9 | 21.9 | 51.8 | 9.7 | 8.3 | 96.1 | 0.7 | 0.4 | 1.2 | 0.3 | 0.3 | 3.5 | 0.5 | 1.5 |
| | 3.8 | 23.0 | 55.0 | 8.3 | 7.8 | 98.7 | 0.6 | 0.4 | 1.3 | 0.2 | 0.2 | 3.6 | 0.5 | 1.5 |
| | 3.8 | 21.7 | 53.0 | 8.8 | 7.9 | 97.5 | 0.7 | 0.4 | 1.2 | 0.2 | 0.2 | 3.5 | 0.5 | 1.4 |
| | 3.3 | 22.2 | 53.8 | 8.2 | 7.7 | 96.0 | 0.7 | 0.3 | 1.3 | 0.2 | 0.2 | 3.6 | 0.4 | 1.5 |
| | 3.7 | 24.7 | 53.3 | 6.8 | 7.4 | 96.5 | 0.6 | 0.4 | 1.4 | 0.2 | 0.2 | 3.5 | 0.5 | 1.6 |
| | 3.0 | 22.3 | 54.0 | 8.4 | 7.5 | 95.7 | 0.6 | 0.3 | 1.3 | 0.2 | 0.2 | 3.6 | 0.4 | 1.6 |
| | 3.6 | 21.5 | 54.2 | 8.7 | 7.4 | 96.0 | 0.6 | 0.4 | 1.3 | 0.2 | 0.2 | 3.6 | 0.4 | 1.5 |
| | 4.3 | 22.9 | 55.4 | 8.4 | 7.6 | 99.3 | 0.6 | 0.4 | 1.3 | 0.2 | 0.2 | 3.6 | 0.5 | 1.5 |
| | 3.2 | 19.1 | 56.6 | 9.6 | 7.7 | 96.7 | 0.7 | 0.3 | 1.2 | 0.2 | 0.3 | 3.7 | 0.3 | 1.5 |
| | 4.2 | 22.1 | 52.3 | 9.5 | 7.1 | 96.3 | 0.6 | 0.4 | 1.2 | 0.2 | 0.3 | 3.5 | 0.5 | 1.5 |
| | 4.0 | 17.7 | 53.6 | 14.1 | 7.6 | 97.6 | 0.7 | 0.4 | 1.0 | 0.4 | 0.4 | 3.6 | 0.4 | 1.4 |
| | 2.8 | 22.0 | 58.3 | 6.9 | 7.3 | 98.0 | 0.6 | 0.3 | 1.4 | 0.2 | 0.2 | 3.7 | 0.3 | 1.6 |
| | 4.0 | 19.2 | 52.8 | 11.3 | 8.1 | 95.9 | 0.7 | 0.4 | 1.1 | 0.3 | 0.3 | 3.6 | 0.4 | 1.4 |
| | 3.7 | 22.5 | 55.1 | 8.0 | 7.7 | 97.5 | 0.6 | 0.4 | 1.3 | 0.2 | 0.2 | 3.6 | 0.4 | 1.5 |
| LBS 2 | 3.9 | 21.0 | 53.4 | 10.7 | 8.0 | 97.6 | 0.7 | 0.4 | 1.2 | 0.3 | 0.3 | 3.5 | 0.5 | 1.4 |
| | 3.6 | 18.4 | 57.6 | 9.1 | 7.3 | 96.5 | 0.6 | 0.4 | 1.2 | 0.2 | 0.3 | 3.8 | 0.2 | 1.4 |
| | 3.9 | 23.0 | 53.5 | 6.9 | 7.8 | 96.1 | 0.7 | 0.4 | 1.3 | 0.2 | 0.2 | 3.5 | 0.5 | 1.5 |
| | 3.8 | 21.5 | 52.4 | 8.1 | 8.1 | 95.1 | 0.7 | 0.4 | 1.3 | 0.2 | 0.2 | 3.5 | 0.5 | 1.5 |
| | 3.2 | 20.2 | 53.1 | 6.7 | 8.2 | 92.6 | 0.7 | 0.3 | 1.3 | 0.2 | 0.2 | 3.7 | 0.4 | 1.5 |
| | 4.0 | 19.8 | 54.6 | 10.5 | 8.5 | 98.0 | 0.7 | 0.4 | 1.2 | 0.3 | 0.3 | 3.6 | 0.4 | 1.4 |
| | 3.6 | 19.3 | 52.3 | 11.1 | 8.6 | 95.5 | 0.8 | 0.4 | 1.1 | 0.3 | 0.3 | 3.6 | 0.4 | 1.4 |
| | 3.6 | 20.1 | 52.9 | 10.5 | 8.4 | 96.0 | 0.7 | 0.4 | 1.2 | 0.3 | 0.3 | 3.6 | 0.4 | 1.4 |
| | 3.8 | 20.8 | 52.9 | 9.2 | 7.6 | 95.0 | 0.7 | 0.4 | 1.2 | 0.2 | 0.3 | 3.6 | 0.4 | 1.5 |
| | 3.6 | 21.7 | 53.2 | 7.7 | 8.3 | 95.8 | 0.7 | 0.4 | 1.3 | 0.2 | 0.2 | 3.6 | 0.5 | 1.5 |
| | 3.1 | 19.1 | 55.3 | 6.2 | 7.3 | 91.6 | 0.6 | 0.3 | 1.3 | 0.2 | 0.2 | 3.8 | 0.2 | 1.5 |
| | 3.7 | 20.0 | 51.5 | 9.6 | 8.3 | 93.8 | 0.7 | 0.4 | 1.2 | 0.3 | 0.3 | 3.6 | 0.5 | 1.4 |

| | | | | | | | | | | | | | | |
|---|---|---|---|---|---|---|---|---|---|---|---|---|---|---|
| | 3.6 | 20.8 | 55.6 | 7.8 | 7.7 | 96.0 | 0.7 | 0.4 | 1.3 | 0.2 | 0.2 | 3.7 | 0.3 | 1.5 |
| | 3.8 | 17.5 | 52.6 | 13.2 | 8.0 | 95.6 | 0.7 | 0.4 | 1.0 | 0.3 | 0.4 | 3.6 | 0.4 | 1.4 |
| | 3.8 | 19.1 | 53.6 | 10.3 | 8.4 | 95.7 | 0.7 | 0.4 | 1.1 | 0.3 | 0.3 | 3.6 | 0.4 | 1.4 |
| | 3.6 | 16.9 | 51.8 | 13.9 | 8.2 | 94.8 | 0.7 | 0.4 | 1.0 | 0.4 | 0.4 | 3.6 | 0.4 | 1.4 |
| | 4.0 | 20.8 | 54.7 | 9.4 | 7.3 | 96.7 | 0.6 | 0.4 | 1.2 | 0.2 | 0.3 | 3.6 | 0.4 | 1.5 |
| | 4.0 | 18.6 | 51.7 | 10.9 | 8.4 | 94.0 | 0.8 | 0.4 | 1.1 | 0.3 | 0.3 | 3.6 | 0.4 | 1.4 |
| | 3.6 | 23.8 | 51.0 | 9.4 | 7.9 | 96.1 | 0.7 | 0.4 | 1.3 | 0.2 | 0.3 | 3.4 | 0.6 | 1.5 |
| | 3.7 | 19.8 | 52.0 | 11.1 | 8.1 | 95.1 | 0.7 | 0.4 | 1.2 | 0.3 | 0.3 | 3.6 | 0.5 | 1.4 |
| | 3.6 | 19.2 | 52.5 | 10.3 | 8.3 | 94.7 | 0.7 | 0.4 | 1.1 | 0.3 | 0.3 | 3.6 | 0.4 | 1.4 |
| | 3.5 | 17.1 | 50.0 | 10.9 | 8.0 | 91.0 | 0.7 | 0.4 | 1.0 | 0.3 | 0.3 | 3.6 | 0.4 | 1.3 |
| | 4.0 | 17.5 | 53.8 | 11.4 | 8.1 | 96.3 | 0.7 | 0.4 | 1.0 | 0.3 | 0.3 | 3.6 | 0.4 | 1.3 |
| | 4.0 | 17.4 | 52.6 | 12.8 | 8.1 | 95.3 | 0.7 | 0.4 | 1.0 | 0.3 | 0.4 | 3.6 | 0.4 | 1.4 |
| | 3.8 | 18.0 | 51.9 | 12.7 | 8.0 | 94.8 | 0.7 | 0.4 | 1.1 | 0.3 | 0.4 | 3.6 | 0.4 | 1.4 |
| | 3.9 | 15.8 | 52.7 | 14.2 | 8.3 | 95.3 | 0.7 | 0.4 | 0.9 | 0.4 | 0.4 | 3.7 | 0.4 | 1.3 |
| | 3.9 | 16.1 | 53.8 | 14.2 | 8.3 | 96.9 | 0.7 | 0.4 | 1.0 | 0.4 | 0.4 | 3.7 | 0.3 | 1.3 |
| | 3.4 | 19.4 | 52.6 | 12.0 | 8.1 | 96.3 | 0.7 | 0.4 | 1.1 | 0.3 | 0.3 | 3.6 | 0.4 | 1.4 |
| | 3.4 | 17.5 | 51.5 | 11.0 | 8.3 | 92.4 | 0.7 | 0.4 | 1.1 | 0.3 | 0.3 | 3.6 | 0.4 | 1.4 |
| | 3.1 | 19.8 | 54.4 | 9.7 | 7.4 | 97.0 | 0.6 | 0.3 | 1.1 | 0.2 | 0.3 | 3.6 | 0.4 | 1.4 |
| | 4.0 | 17.5 | 51.9 | 14.1 | 8.0 | 95.9 | 0.7 | 0.4 | 1.0 | 0.4 | 0.4 | 3.6 | 0.4 | 1.3 |
| | 3.5 | 16.3 | 54.3 | 12.7 | 7.8 | 95.2 | 0.7 | 0.4 | 1.0 | 0.3 | 0.4 | 3.7 | 0.3 | 1.4 |
| LBS 3 | 3.7 | 17.7 | 53.9 | 12.5 | 8.1 | 96.5 | 0.7 | 0.4 | 1.1 | 0.3 | 0.4 | 3.7 | 0.4 | 1.4 |
| | 3.6 | 17.0 | 52.6 | 12.3 | 8.3 | 94.4 | 0.7 | 0.4 | 1.0 | 0.3 | 0.4 | 3.7 | 0.4 | 1.4 |
| | 4.3 | 13.4 | 53.2 | 16.3 | 8.2 | 95.8 | 0.7 | 0.4 | 0.8 | 0.4 | 0.5 | 3.7 | 0.3 | 1.2 |
| | 4.3 | 13.4 | 53.8 | 16.4 | 8.4 | 96.7 | 0.7 | 0.5 | 0.8 | 0.4 | 0.5 | 3.7 | 0.3 | 1.2 |
| | 4.3 | 13.3 | 53.1 | 16.1 | 8.3 | 95.5 | 0.7 | 0.4 | 0.8 | 0.4 | 0.5 | 3.7 | 0.3 | 1.2 |
| | 4.3 | 13.5 | 54.0 | 16.5 | 7.8 | 96.6 | 0.7 | 0.4 | 0.8 | 0.4 | 0.5 | 3.7 | 0.3 | 1.2 |
| | 4.4 | 12.4 | 52.8 | 17.0 | 8.4 | 95.2 | 0.8 | 0.5 | 0.7 | 0.5 | 0.5 | 3.7 | 0.3 | 1.2 |
| | 3.3 | 18.4 | 54.0 | 11.8 | 7.7 | 95.6 | 0.7 | 0.3 | 1.1 | 0.3 | 0.3 | 3.7 | 0.3 | 1.4 |
| | 4.0 | 19.2 | 52.1 | 11.3 | 8.1 | 95.3 | 0.7 | 0.4 | 1.1 | 0.3 | 0.3 | 3.6 | 0.4 | 1.4 |
| | 4.4 | 14.0 | 53.1 | 15.0 | 8.2 | 95.1 | 0.7 | 0.5 | 0.9 | 0.4 | 0.4 | 3.7 | 0.3 | 1.2 |
| | 4.7 | 14.0 | 53.5 | 14.6 | 8.3 | 95.6 | 0.7 | 0.5 | 0.9 | 0.4 | 0.4 | 3.7 | 0.3 | 1.2 |
| | 4.5 | 13.6 | 52.9 | 15.5 | 8.3 | 95.1 | 0.7 | 0.5 | 0.8 | 0.4 | 0.5 | 3.7 | 0.3 | 1.2 |
| | 3.6 | 19.0 | 55.2 | 9.4 | 7.6 | 95.4 | 0.7 | 0.4 | 1.2 | 0.2 | 0.3 | 3.7 | 0.3 | 1.4 |
| | 4.2 | 19.6 | 49.8 | 12.8 | 7.4 | 94.5 | 0.7 | 0.4 | 1.1 | 0.3 | 0.4 | 3.5 | 0.5 | 1.4 |
| | 3.8 | 19.1 | 52.0 | 11.1 | 8.5 | 95.2 | 0.8 | 0.4 | 1.1 | 0.3 | 0.3 | 3.6 | 0.4 | 1.4 |
| | 3.6 | 20.9 | 53.9 | 8.6 | 7.9 | 95.9 | 0.7 | 0.4 | 1.2 | 0.2 | 0.2 | 3.6 | 0.4 | 1.5 |
| | 4.0 | 20.3 | 54.2 | 10.0 | 8.5 | 97.4 | 0.7 | 0.4 | 1.2 | 0.3 | 0.3 | 3.6 | 0.4 | 1.4 |
| | 4.3 | 14.5 | 54.1 | 15.0 | 8.4 | 96.6 | 0.7 | 0.4 | 0.9 | 0.4 | 0.4 | 3.7 | 0.3 | 1.3 |
| | 4.3 | 15.0 | 54.5 | 15.1 | 8.2 | 97.7 | 0.7 | 0.4 | 0.9 | 0.4 | 0.4 | 3.7 | 0.3 | 1.3 |
| | 4.3 | 16.0 | 53.0 | 14.4 | 8.2 | 96.5 | 0.7 | 0.4 | 0.9 | 0.4 | 0.4 | 3.6 | 0.4 | 1.3 |
| | 4.3 | 15.8 | 52.6 | 13.8 | 8.0 | 94.9 | 0.7 | 0.4 | 0.9 | 0.4 | 0.4 | 3.6 | 0.4 | 1.3 |
| | 3.9 | 22.5 | 55.5 | 6.8 | 7.8 | 97.3 | 0.7 | 0.4 | 1.3 | 0.2 | 0.2 | 3.6 | 0.4 | 1.5 |
| | 4.3 | 14.6 | 52.8 | 15.1 | 8.1 | 95.3 | 0.7 | 0.4 | 0.9 | 0.4 | 0.4 | 3.7 | 0.3 | 1.3 |
| | 4.5 | 14.3 | 54.3 | 15.9 | 8.0 | 97.4 | 0.7 | 0.5 | 0.8 | 0.4 | 0.5 | 3.7 | 0.3 | 1.2 |
| | 4.2 | 14.7 | 52.1 | 15.6 | 8.2 | 95.5 | 0.7 | 0.4 | 0.8 | 0.4 | 0.5 | 3.6 | 0.4 | 1.3 |
| | 4.2 | 12.8 | 51.7 | 18.5 | 8.4 | 96.0 | 0.8 | 0.4 | 0.7 | 0.5 | 0.6 | 3.6 | 0.4 | 1.2 |
| | 3.6 | 18.5 | 53.1 | 11.0 | 8.0 | 94.8 | 0.7 | 0.4 | 1.1 | 0.3 | 0.3 | 3.6 | 0.4 | 1.4 |
| | 4.4 | 20.0 | 52.2 | 12.9 | 7.5 | 97.5 | 0.6 | 0.4 | 1.1 | 0.3 | 0.4 | 3.5 | 0.5 | 1.4 |
| | 3.4 | 20.1 | 54.6 | 8.2 | 8.0 | 94.6 | 0.7 | 0.3 | 1.3 | 0.2 | 0.2 | 3.7 | 0.3 | 1.5 |
| LBS 4 | 3.7 | 21.7 | 52.1 | 8.9 | 8.0 | 95.1 | 0.7 | 0.4 | 1.3 | 0.2 | 0.3 | 3.5 | 0.5 | 1.5 |
| | 4.1 | 16.0 | 53.7 | 13.7 | 8.2 | 96.8 | 0.7 | 0.4 | 0.9 | 0.4 | 0.4 | 3.7 | 0.4 | 1.3 |
| | 3.8 | 12.6 | 52.0 | 18.4 | 8.4 | 95.6 | 0.8 | 0.4 | 0.7 | 0.5 | 0.5 | 3.7 | 0.3 | 1.2 |
| | 3.9 | 18.9 | 53.5 | 11.4 | 8.3 | 96.5 | 0.7 | 0.4 | 1.1 | 0.3 | 0.3 | 3.6 | 0.4 | 1.4 |
| | 3.8 | 19.9 | 53.9 | 10.3 | 8.4 | 96.7 | 0.7 | 0.4 | 1.2 | 0.3 | 0.3 | 3.6 | 0.4 | 1.4 |
| | 3.4 | 17.9 | 56.2 | 10.2 | 8.3 | 96.5 | 0.7 | 0.3 | 1.2 | 0.3 | 0.3 | 3.8 | 0.3 | 1.4 |
| | 3.9 | 19.6 | 54.3 | 10.8 | 8.1 | 97.4 | 0.7 | 0.4 | 1.1 | 0.3 | 0.3 | 3.6 | 0.4 | 1.4 |
| | 3.9 | 19.4 | 53.5 | 11.1 | 8.1 | 96.6 | 0.7 | 0.4 | 1.1 | 0.3 | 0.3 | 3.6 | 0.4 | 1.4 |
| | 3.8 | 19.2 | 54.1 | 10.2 | 7.8 | 95.5 | 0.7 | 0.4 | 1.2 | 0.3 | 0.3 | 3.7 | 0.4 | 1.4 |
| | 3.9 | 19.9 | 53.7 | 10.3 | 8.4 | 96.5 | 0.7 | 0.4 | 1.2 | 0.3 | 0.3 | 3.6 | 0.4 | 1.4 |
| | 3.9 | 18.6 | 51.8 | 11.1 | 8.1 | 94.2 | 0.7 | 0.4 | 1.1 | 0.3 | 0.3 | 3.6 | 0.4 | 1.4 |

| | | | | | | | | | | | | | | |
|---|---|---|---|---|---|---|---|---|---|---|---|---|---|---|
| | 4.3 | 14.8 | 52.3 | 15.1 | 8.1 | 95.0 | 0.7 | 0.5 | 0.9 | 0.4 | 0.4 | 3.7 | 0.4 | 1.3 |
| | 4.2 | 15.2 | 53.1 | 14.5 | 8.6 | 96.1 | 0.8 | 0.4 | 0.9 | 0.4 | 0.4 | 3.7 | 0.3 | 1.3 |
| | 4.2 | 14.4 | 52.9 | 15.0 | 8.1 | 95.1 | 0.7 | 0.4 | 0.9 | 0.4 | 0.4 | 3.7 | 0.3 | 1.3 |
| Min | 2.8 | 12.4 | 47.9 | 6.2 | 7.1 | 89.8 | 0.6 | 0.3 | 0.7 | 0.2 | 0.2 | 3.4 | 0.2 | 1.2 |
| Max | 4.7 | 24.7 | 58.3 | 18.5 | 8.6 | 99.3 | 0.8 | 0.5 | 1.4 | 0.5 | 0.6 | 3.8 | 0.6 | 1.6 |
| Average | 3.8 | 18.9 | 53.1 | 11.1 | 8.0 | 95.7 | 0.7 | 0.4 | 1.1 | 0.3 | 0.3 | 3.6 | 0.4 | 1.4 |

### 9.4.5. Redox-sensitive trace elements chemistry

The concentration of redox-sensitive trace metals was determined for the red mudstone, grey mudstone and glauconitic rock of the LBS (Table-9.3). Although, a number of redox-sensitive elements can be used to infer the paleo-redox conditions of basin but, for the present study, we have used V, Sc and Cr. Besides, we have calculated the enrichment factors (EFs) of these redox sensitive elements relative to UCC and ratios of V/Cr and V/Sc (Table-9.3). The glauconitic interval records the highest enrichment factors (EFs) for all the elements (Fig. 9.13). The ratios of redox-sensitive trace metals V/Cr and V/Sc also vary within the same interval, showing the highest values (V/Cr= 2.0 and V/Sc= 10.22) within the glauconitic interval followed by grey mudstone (V/Cr= 1.38–1.6 and V/Sc= 6.25–7.21) and red mudstone (V/Cr= 0.88–1.13 and V/Sc= 5.26–5.47) (Fig. 9.13). The V/Cr values of 2 and V/Sc value of 9.1 in rocks demarcate the boundary between oxic and sub-oxic environments (Jones and Manning, 1994; MaKirdy, 2011). The high EFs for the glauconitic rock along with high V/Cr and V/Sc values indicates sub-oxic condition in glauconite horizon while, the red and grey mudstones represent oxic depositional conditions (Jones and Manning, 1994; MaKirdy, 2011).

Table-9.3. Redox-sensitive trace elements concentration of different facies consisting in the Lower Bhander Sandstone (Note RS1, RS2, RS3, RS4 are red mudstone; GS1, GS2 are grey shale and GL is glauconite rock)

| Sample No | RS1 | RS2 | GL | GS1 | GS2 | RS3 | RS4 |
|---|---|---|---|---|---|---|---|
| V (ppm) | 113.17 | 113.42 | 47.87 | 166.95 | 155.75 | 108.24 | 84.82 |
| Sc (ppm) | 21.51 | 20.80 | 4.68 | 26.73 | 21.60 | 20.48 | 15.51 |
| Cr (ppm) | 100.37 | 102.77 | 24.06 | 121.05 | 97.47 | 102.23 | 95.94 |
| $V_{(EF)}$ | 10.03 | 10.11 | 24.68 | 12.67 | 15.58 | 10.76 | 11.25 |
| $Sc_{(EF)}$ | 13.21 | 12.85 | 16.73 | 14.06 | 14.97 | 14.11 | 14.26 |
| $Cr_{(EF)}$ | 9.38 | 9.66 | 13.08 | 9.69 | 10.28 | 10.72 | 13.42 |
| V/Cr | 1.13 | 1.10 | 2.0 | 1.38 | 1.60 | 1.06 | 0.88 |
| V/Sc | 5.26 | 5.45 | 10.22 | 6.25 | 7.21 | 5.28 | 5.47 |
| Al (wt%) | 9.4 | 9.4 | 1.6 | 11.0 | 8.4 | 8.5 | 6.3 |

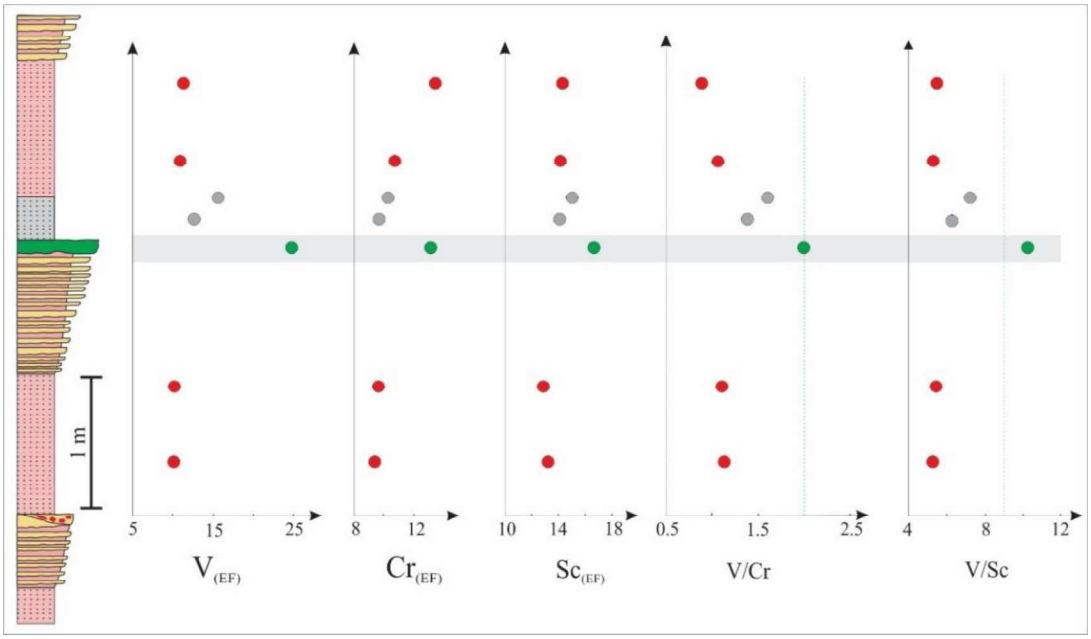


Fig. 9.13. Distribution of redox-sensitive elements enrichment factors with lithological facies of LBS section and redox-sensitive element ratios of V/Cr and V/Sc across the studied section (dotted green line separating the oxic and suboxic condition, right side and left side infer sub-oxic zone and oxic condition respectively). Note grey band along glauconite horizon shows highest value for both enrichment factor and element ratios. The red and grey dot represent red and grey mudstone, and green dot represents glauconitic sediment respectively.

## 9.5. Discussion

### 9.5.1. Depositional environment and paleogeography

The studied section of the LBS consists of repetitive alternation of laminated mudstone and siltstone-sandstone with occasional intra-formational mud pebble conglomerate. The red mudstone shows fine lamination with a few intercalations of lenticular siltstone beds and it occurs directly on the intra-formational mud pebble conglomerate. The sandstones above the mudstone (red and grey) are mostly amalgamated. The base of the sandstone beds is sharp and erosional, showing abundant tool marks and flute casts. The sandstones are planar laminated and cross-stratified, showing ripples on bed surfaces. Hummocky cross-stratifications characterize the vertical sections of the sandstone beds (Fig. 9.5a). Desiccation cracks and rain imprints are abundant on red mudstones. Wedge-shaped conglomerate laterally grades to sandstone-siltstone beds (Fig. 9.6a, 9.6d, 9.7). Thickness of the conglomerate varies from 15 to 25 cm. Glauconite occurs within the matrix of these wedge-shaped mud pebble conglomerates besides its laterally continuous sandstone (Fig. 9.7). Slide planes and slump folds are associated within these conglomerate beds.

The sharp lower contacts of sandstone beds encased within muddy deposits suggests allogenic origin of sandstone. The amalgamated sandstones with aforementioned structures represent high-energy event deposits. Alignments of clasts along the cross-stratification also support the contention. The transition from planar lamination to ripple lamination through cross-stratification within a single bed infers the waning nature of the flow. Erosional bases of sandstone beds, flute casts and bidirectional tool marks at the undersurface and the sheet-like geometry of sandstones supports their storm origin. The straight and bifurcated ripple crests infer the wave domination in the depositional site. The mudstone deposit, with alignment of mica grains along the laminae, suggests suspension fall out in a quiet water condition (O'Brien et al, 1980; Postma et al., 2009) though micas may orient randomly in microbial mat originated sediments (Sarkar et al., 2008). The lenticular geometry, lateral transition of mud pebble bearing conglomerate to sandstone-siltstone and mudstone suggests intra-basinal origin of the mud pebble conglomerate. Association of slide planes with massive conglomerate beds supports sediment gravity flow origin of the deposits (Fig. 9.6d). The grey mudstone and associated glauconitic rock appear once in the studied sequence, otherwise dominated by red mudstones. The absence of emergence features within the grey mudstone suggests the greater depth in the depositional setting. Desiccation cracks in within mudstone and siltstone indicate periodic exposure of the basin. The abundance of salt pseudomorphs at the undersurface of siltstone beds suggests a high rate of evaporation in shallow marine environment and overall arid condition. The LBS is also replete with tidal bedform implies that the basin had connection with open ocean (Chanda et al., 1974, Bhattacharyya and Chanda, 1976., Bose and Chaudhury, 1990, Sarkar and Banerjee, 2019). The presence of flat top, double-crested, interference, superimposed and ladder back ripples corroborates the contention. Millimeter to centimeter-scale sand -mud alternation cycle within the tidal bedforms, with storm intervention, has also been reported from the Member (Bhattacharyya et al., 1980; Bose and Chaudhury, 1990; Bose et al., 2001). The depositional facies study, therefore, confirms that the LBS was broadly deposited in the marginal marine environment. The sand-free grey mudstone suggests relatively deeper condition, while red mudstone in association with sandstone-siltstone beds with desiccation cracks, salt pseudomorphs represent the emergence of the shallow seafloor.

### 9.5.2. Origin and chemical evolution of glauconite

The glauconite geochemistry varies significantly across geological time (Banerjee et al., 2016). The Proterozoic glauconites are enriched in $K_2O$, MgO and $Al_2O_3$ and depleted in $TFe_2O_3$, while the Phanerozoic counterparts exhibits high $TFe_2O_3$ and low $Al_2O_3$ (Banerjee et al., 2016). Occasionally, Phanerozoic glauconite may show high $TFe_2O_3$ and $Al_2O_3$ contents (cf. Roy Choudhury et al., 2021). The LBS glauconite exhibits high $K_2O$, MgO and $Al_2O_3$ and low to moderate $TFe_2O_3$ concentration. Three models viz. 'layer lattice theory', 'verdissement theory', 'pseudomorphic theory' explains the evolution of glauconite. The 'layer lattice theory' suggests simultaneous incorporation of K and Fe (Brust, 1958). The 'verdissement theory' proposes continuous intake of K at constant Fe in Fe-smectite or Fe-Al smectite (Odin and Matter, 1981). The 'pseudomorphic theory' explains the glauconitization process by the continuous incorporation of Fe at a constant K within in the K-feldspar substrate (Dasgupta et al., 1990; Banerjee et a., 2015, 2016).

The dominance of dumbbell-spheroidal glauconite grain suggests the authigenic origin of glauconite. The complete absence of broken glauconites in LBS corroborates the authigenic origin (Deb and Fukuoka, 1998; Bandopadhyay, 2007; Banerjee et al., 2008, 2016). The incipient glauconitization remains confined along the fractures of feldspar and around the quartz grains and never cross-cuts grain boundaries, further attesting to autochthonous origin of glauconites (Dasgupta et al., 1990; Banerjee et al., 2008, 2015, 2016; Bansal et al., 2020; Mandal et al., 2020). Thin section studies using light microscopy and X-ray imaging reveals the formation of glauconite exclusively by the replacement of feldspar and quartz grains (Fig. 9.8, 9.9, 9.10). The increase in $TFe_2O_3$ of glauconites at a constant $K_2O$ characterizes the pseudomorphic replacement process (Fig. 9.12a; Dasgupta et al., 1990; Banerjee et al., 2008, 2015; Tang et al., 2017; Bansal et al., 2020; Mandal et al., 2020). The dissolution of K-feldspar during the pseudomorphic replacement turned the pore water into a high $K^+$ environment (Banerjee et al., 2015; Mandal et al., 2020). The highly alkaline Proterozoic seawater and pore water might have enhanced this process (Banerjee et al., 2015). The high Mg content of the glauconite in the absence of ferruginous minerals in the glauconitic rocks relates to Mg-rich Proterozoic ocean (Banerjee et al., 2008; 2016). As the iron content of the seawater is negligible and hydrothermal activity is absent in vicinity, it is reasonable to consider that iron has been supplied into the shallow marine depositional environment by continental weathering (Banerjee et al., 2015; Tang et al., 2017; Mandal et al., 2020).

### 9.5.3. Role of intrabasinal tectonics on the development of coarsening-up cycles

The overall increase of mudstone from the bottom to the top of the LBS succession suggest a fining upward trend with the intervention of a number of repetitive coarsening-up cycles in-between (Fig. 9.4a, 9.14). The fining upward trend is maintained from the Ganurgarh Shale to the lower part of the Sirbu Shale (Fig. 9.14a) (Bose et al., 2001; Sarkar and Banerjee, 2020). The overall fining upward segment of the Sirbu Shale represents a transgressive system tract (TST) while the overlying coarsening upward part is a highstand system tract (HST, Bose et al., 2001; Sarkar and Banerjee, 2020), with a maximum flooding surface (MFS) in between (Fig. 9.14a).

The fining up LBS succession, consisting of small coarsening up packages, are composed of red and/ or grey mudstone and sandstone-siltstone with occasional mud pebble conglomerate (Fig. 9.4a, 9.14b). Each package starts with red and/ or grey mudstone and terminates in sandstone-siltstone with the wedge-shaped conglomerate (Fig. 9.7, 9.14b). The sandstone-siltstone alternations lie in-between red mudstone and the wedge-shaped mud pebble conglomerates (Fig. 9.7). The presence of these conglomerates along with slide planes possibly indicates the subsidence of the basin and creation of new accommodation space (Sarkar et al., 2002), where mudstone deposition succeeds upward to sand-silt sedimentation with shallowing (Fig. 9.7). Infact the sedimentation of a new cycle starts with mudstone after the subsidence of the basin floor and it continues till another conglomerate horizon appear at the base of the next cycle. The repeated occurrences of these packages indicate recurrent episodes of slow subsidence. The presence of conglomerate beds in each cycle defines the bottom bounding surface (Fig. 9.14b). The small-scale cycles correlate with sea level changes (Fig. 9.14b). Although, in most of the cycles the mudstone is red, however, grey mudstone appears on top of glauconite horizon (Fig. 9.14b). The glauconite in the sandy matrix of this mud pebble conglomerate and laterally associated sandstone represent the subsidence of the basin during the deposition of the LBS. The association of slide planes, related soft sediment deformation structures, and the grey colour of the mudstone corroborate the greater depth of the basin during the formation of glauconite.

### 9.5.4. Paleoredox influence on glauconitization

The EFs of redox-sensitive elements such as V, Cr, and Sc have been widely used as a proxy for the depositional redox conditions as these trace elements readily remobilize,

incorporates/adsorbs into sediments and precipitates in marine (Jones and Manning, 1994; Tribovillard et al., 2006; MaKirdy, 2011; Boidin et al., 2007; Baioumy and Lemann, 2017; Tang et al., 2016; Cole et al., 2017; Algabri et al., 2020). Although, a number of factors are responsible for the shift in redoxcline (the boundary separating oxygenated water at top with the oxygen-depleted bottom water), the depositional paleogeography also plays a major role (Pi et al., 2014; Baioumy and Lemann, 2017). Variation of EFs in the LBS is a result of remobilization of redox-sensitive elements, and corresponds to the redox condition governed by paleogeographic changes (Pi et al., 2014). Higher EFs of the glauconitic rock indicates maximum remobilization with reducing condition compared to other lithological variety. The redox profiles V/Cr and V/Sc support the glauconitization below the redoxcline, in sub-oxic environment (Jones and Manning, 1994; Bau and Dulski, 1996; MaKirdy, 2011). Differential value of V/Cr and V/Sc is a consequence of depositional facies varies with depositional depth and redox condition also. The paleoredox proxies of the LBS suggest the sub-oxic condition for the deeper glauconitic rock. Grey and red mudstone, forming in shallower environment represent oxic condition. Therefore, the progradational cycles possibly reflect repetitive redox cycles. The recurrent subsidence during the sedimentation influences the oxygen saturation of the then depositional milieu of the seawater because of the increasing water depth. With an appropriate decrease in oxygen saturation of seawater, the glauconitic interval formed below the redoxcline. The ferric iron ($Fe^{3+}$) was partially reduced at this depth and was converted to $Fe^{2+}$. The $Fe^{2+}$ was incorporated into K-feldspar and quartz substrates during the early diagenesis, facilitating the glauconitization (Meunier and El Albani, 2007; Tang et al., 2017). The initial sedimentation for each coarsening upward cycle took place under oxygen-depleted condition soon after the tectonic subsidence. Each coarsening upward cycle recorded a shift from a low to slightly high oxygen saturation of seawater. Repetitive cycles with similar paleo-redox fluctuation suggests slow subsidence and sediment accumulation, which characterizes the epeiric seas. The sub-oxic redox condition of glauconitic sediments and its appearance in the LBS succession supports the maximum depth of deposition for the glauconitic interval. The present study, demonstrating the correlation of intrabasinal tectonic-induced subsidence to glauconitization, is significant for understanding the variations in paleoredox conditions of Proterozoic epeiric seas.

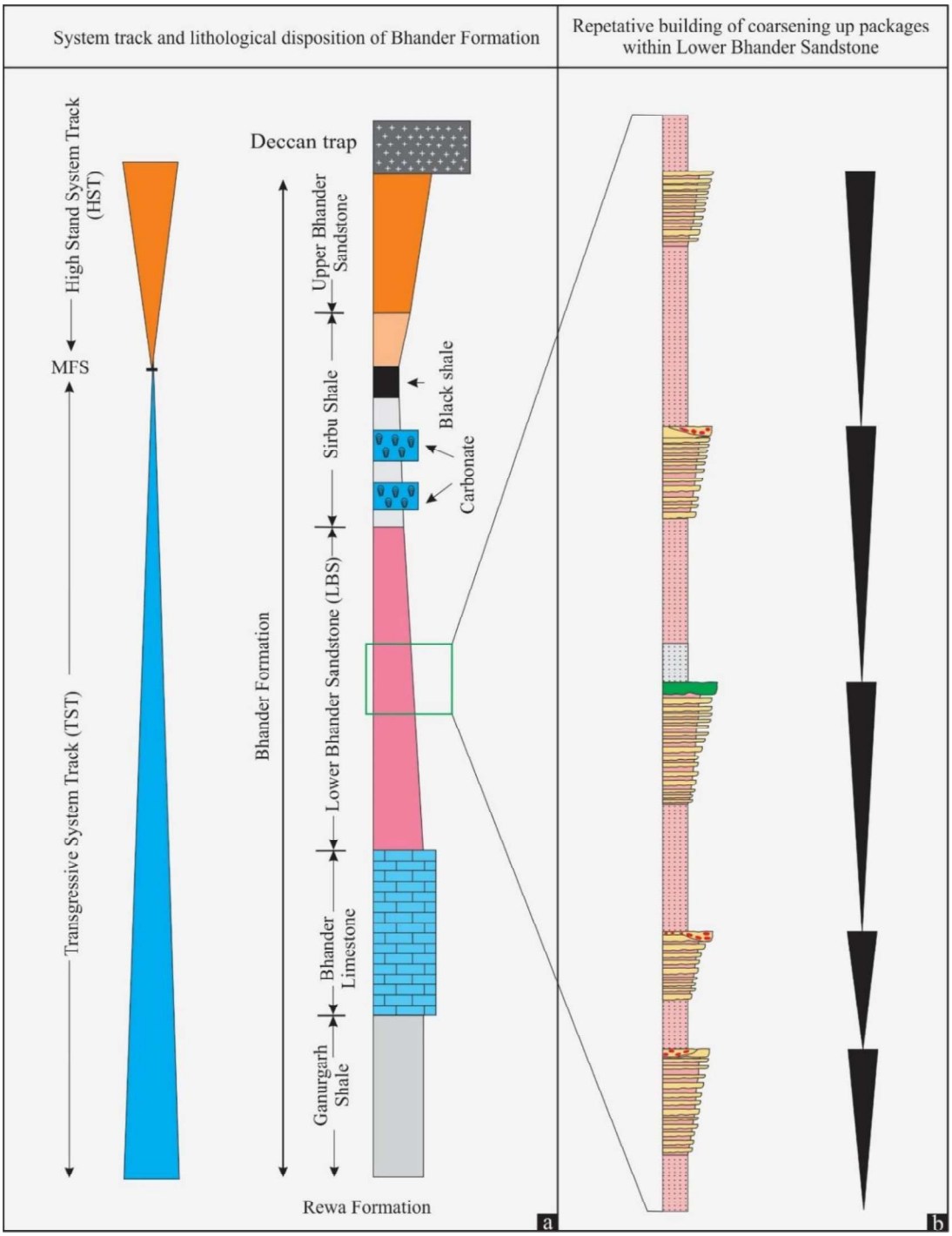


Fig. 9.14. Overall sequence stratigraphic architecture of the Bhander Formation (a), and the enlarged portion of overall finning up Lower Bhander Sandstone (b). Note, the shallowing up packages marked by black triangles within the finning up succession of LBS. Also, note the presence of glauconite at the base of a shallowing up cycle.

## 9.6. Conclusions

Considering the sediment dynamics, related intrabasinal tectonics and geochemistry of authigenic sediments, present study draws the following conclusions to explain the glauconitization within the LBS.

(a) Although the Lower Bhander Sandstone is overall fining upward, it is constituted by small-scale progradation cycles related to intrabasinal tectonics. The marginal marine deposits of the LBS consists of repetitive cycles representing sequential accommodation space creation, and filling in response to the intrabasinal tectonics.

(b) The glauconite within the LBS formed by the replacement of feldspar and quartz. The glauconite evolved by the addition of Fe at a constant K. Fe, Mg contents in the glauconite derives by the weathering of continent.

(c) The paleoredox proxies of each progradation cycle records increase of oxygen saturation with the shallowing of the depositional environment. The repetition of this paleo-redox profile within the coarsening up cycles reflect sequential basin tectonics. The glauconitic interval at base of a progradation cycle represents the suboxic depositional condition.

(d) Prevailing intrabasinal tectonics induces the local dysoxic conditions on Proterozoic epeiric seafloor, and facilitates glauconitization.

# PART III

# CHAPTER 10

# Summary and Conclusion

An integration of the depositional and climatic scenario of the Meso-to Neoproterozoic Rohtas Limestone, Lower Quartzite/ Sasaram Sandstone and Lower Bhander Sandstone unfurled in piecemeal in the preceding chapters, is attempted to summarize in this chapter. Besides state of art facies analysis, a forward projection of glauconite enable the present author to reconstruct a more holistic scenario, to estimate deeper implications of glauconite formation in shallow marine setup. Observations of chert formation by replacing carbonate rock (dolostone) made a revised model for silicification and open a new window of silicification (chert formation) and estimation of paleotemperature. A collage of snapshots taken through space and time would probably allow a vision of deep time (Proterozoic) regarding the paleoclimate and paleoenvironment.

The sedimentary facies analysis throws a new light on the studied section over 120 km stretch of Vindhyan succession, below and above the unconformity namely the Rohtas Limestone and Lower Quartzite Members that so long eschewed. The limestone deposition of Rohtas Formation resting on the maximum flooding surface of a transgressive system track (Rampur Shale) has been divided into two major associations. The lower part, association I has been inferred as restricted shelf environment while the association II overlying on association I likely to be deposited in an open marine shelf. A zone of soft sediment deformation structures with lateral continuity over ca.57 km has separated these associations. The characters of the SSDS present in these horizons suggests seismicity related deformation, but similar characteristics has also been reported in case of endogenic trigger (e.g., storm pounding, floods, tidal shearing, rapid sedimentation etc.). Present study proposes a thorough facies analysis may be an effective tool to identify *seismites*(exogenic) from endogenic triggering agent. The change of depositional setting imprinted in the deformed zone, separated two associations, has been inferred as seismicity related shocks responsible for liquefaction-fluidization of the sediment. SSDS in association I was formed possibly due to the influence of micro-seismicity while in association II those related to storm pounding.

A thick sandstone of LQ (~12 m) deposited directly above the unconformity present in all the studied sections. Facies analysis help to identify two facies associations. Association I inferred tidal depositional setting while association II indicate occasional storm intervention within the overall tidal setting. The LQ so far reported from the eastern

sector of the Son valley only, but the present study recognizes this sandstone from the western part as well. The study also confirms that the direct contact of this sandstone above the unconformity present between lower and Upper Vindhyan are continuous rather than a localized body, claimed earlier.

The triple oxygen isotope compositions of chert provide better constraint on the paleoclimate that was in equilibrium with the chert. Compilation of triple oxygen data of chert from the published information show variation of the $\delta^{18}O$ and $\delta^{17}O$ compositions from Archaean to recent time. It is likely that the variation of triple oxygen compositions of the cherts result from high and low temperature alternation, diagenetic modification or replacement of earlier rock by meteoric water/ high temperature fluid. Diagenetic alteration by various fluid of different composition and temperature shows a best fit curve with 3-O of chert over time. The elevated seawater temperature of Archean and/ or Proterozoic cherts are likely the results of high temperature alteration in presence of high hydrothermal flux. Initially sediments might have precipitated from a range of temperature between 30$^{o}$C to 10$^{o}$C in equilibrium with marine water as carbonate, phosphate, iron mineral etc., except mid oceanic ridge and subduction zones. Shale, sandstone, iron mineral, phosphate, carbonate may change with the interaction of silica rich fluid of 300$^{o}$C to 25$^{o}$C temperature at different fluid rock ratio. Depending on F/R ratio and temperature of fluid, the triple oxygen isotope might have modified. Present study interprets that ocean water composition may have evolved but there is no such fixed path which we can trace by $\lambda$ (alternation rate) of silica-water equilibrium curvature. Present study also reveals that triple oxygen data sets in Precambrian are likely to be an overestimation. Ancient ocean composition was seeming to be similar as that of modern equivalent, except in active tectonic regions and the temperature may range from 30$^{o}$C -10$^{o}$C. Although the present dataset indicate that the Mesoproterozoic earth surface's temperature was around 25$^{o}$C and initial carbonate sea ca. 10$^{o}$C in equilibrium of modern ocean but the mass balance calculation (considering source of silica, temperature, pressure and pH of silica bearing fluid, cooling process to precipitate chert) and 3-O isotope altogether may answer properly about ancient ocean and temperature.

A chert layer of ~1m thickness is present on top of the Rohtas Limestone, below the unconformity surface. The chert layer has formed by replacing the carbonate rock lying at or below the unconformity surface. Various models that are proposed so far for the chertification of limestone, contains gaps in understanding of the certification process of

dolomite/limestone from meteoric water. Alternatively, involvement of a hot siliceous fluid has assumed responsible for the formation of these chert layer. Detailed Study shows that the chert in RLM has formed by the replacement of dolostone with an interaction of hot silica enrich fluid and meteoric water. Meteoric water percolated through the available porosity of the sediments and intake silica from disordered silica of porcellanite beds available in the nearby areas. The breakdown of minerals, e.g. sanidine, pumice, glass etc. increase the pH of fluid, may reach around ~9.82. Burial temperature help to intake silica as temperature has proportional relation with solubility. In this process the temperature of fluid may reach upto 300ºC (critical point of water). Mass balance calculation show chertification process has completed at constant volume with increase mass about 212%. A general calculation shows that 540-liter silica enriched fluid is required to precipitate 1 kg of chert. In this silicification processes silica enrichment may reach upto 81%. It is likely that the 3-O isotope preserved in the studied chert might have been modified due to high Fluid/Rock ratio of 0.81. It is also likely that the composition of the Mesoproterozoic Ocean was equilibrated with modern ocean where carbonate precipitated from a water composition of $\Delta'^{17}O \approx +0.073‰$ and $\delta'^{18}O \approx 32.6‰$ at a temperature of 10ºC. Chert precipitated by replacing of pre-existing rock from a secondary fluid at a temperature of 40ºC.

Glauconite present in Lower Quartzite sandstone has formed in pseudomorphic replacement with increasing of Fe at constant K. Fe was supplied from the volcanic beds distributed in Vindhyan succession. Mg was supplied possibly from Mg-rich Ocean. Maturity vs. abundance diagram infer that glauconite horizon is not always an indicator of maximum flooding surface. Glauconite can also represent marine flooding surface with its suitable oxygen saturation environment i.e. sub-oxic condition. Here, transgressive system tract continued from LQ to Bijaigarh shale and this shale is likely to be the maximum flooding surface.

Lower Bhander Sandstone was deposited in shallow water marginal marine condition. The overall fining upward sequences constitute by small-scale repeatating progradation cycles related to intrabasinal tectonics. Repetitive cycles representing sequential accommodation space creation, and filling in response to the intrabasinal tectonics. Glauconite is present in the matrix of mud pebble conglomerate and sandstone has formed in pseudomorphic replacement with increase of Fe at constant K. Fe was possibly supplied from the volcanic beds distributed in Vindhyan succession. Mg was likely

to be supplied from Mg-rich Ocean, an inherited character of Precambrian Ocean. Paleoredox measurement infer that each progradation cycle representation of increase of oxygen saturation with the shallowing of the depositional environment. The repetition of this paleo-redox profile within the coarsening up cycles reflect sequential basin subsidence. Glauconite has formed at the base of progradation cycle represents the suboxic depositional condition. This suboxic condition prevailed only in glauconitic interval whereas entire oxic (through there had different oxygen satuaration) condition is because of maximum subsidence compare to surrounding. As soon as suboxic condition formed iron transfer its redox state from $Fe^{3+}$ to $Fe^{2+}$ and starts to pseudomorphic replacement of feldspar, quartz. The glauconitic interval at base of a Prevailing intrabasinal tectonics induces the local dysoxic conditions on Proterozoic epeiric seafloor, and facilitates glauconitization.

# References

Abd El-Hameed, A.T., Abdel-Wahab, A.A., El-Shishtawy, A.M., Abu Shama, A.M., 1997. Petrogenesis of some Lower Eocene siliceous rocks from Egypt. Egyptian Mineralogists 9, 215-250.

Acharyya, S.K., 2003. The nature of Mesoproterozoic Central Indian Tectonic Zone with exhumed and reworked older granulites. Gond Res 6, 197-214.

Adachi, M., Yamamoto, K., Sugisaki, R., 1986. Hydrothermal chert and associated siliceous rocks from the northern Pacific: Their geological significance as indication of ocean ridge activity. Sedimentary Geology, 47, 125–148.

Ague, J.J., 1994a. Mass transfer during Barrovian Metamorphism of Pelites, south-central Connecticut, I: Evidence for composition and volume change. American Journal of Science 294, 989-1057.

Ague, J.J., 1994b, Mass transfer during Barrovian Metamorphism of Pelites, south-central Connecticut, II: Channelized fluid flow and the growth of staurolite and kyanite. American Journal of Science, 294, 1061-1134.

Ahmad, F., 1958. Palaeogeography of central India. Geol. Sur. of Ind. Rec. 87, 513-548.

Ahmad, F., 1971. Geology of the Vindhyan System in the eastern part of the Son valley in Mirzapur District, U.P. Rec. Geol. Surv. India 96, 1-41.

Ahmad, K., 1955. Glaciation in the Vindhyan System. Curr. Sci. 24, 231.

Aitchison, J.C., Flood, P.G., 1990. Geochemical constraints on the depositional setting of Palaeozoic cherts from the New England orogen, NSW, eastern Australia. Marine Geology 94, 79-95. https://doi.org/10.1016/0025-3227(90)90104-R

Akhtar, K., 1996. Facies, sedimentation processes and environments in the Proterozoic Vindhyan Basin, India. Mem. Geol. Soc. India 36, 127–136.

Alexander, A., Meunier, J.D., Llorens, E., Hill, S.M., Savin, S.M., 2004. Methodological improvements for investigating silcrete formation: petrology, FT-IR and oxygen isotope ratio of silcrete quartz cement, Lake Eyre Basin (Australia). Chemical Geology, v. 211, p. 261–274.

Algabri, M., She, Z., Jiao, L., Papineau, D., Wang, G., Zhang, C., Tang, D., Ouyang, G., Zhang, Y., Chen, G., Li, C., 2020. Apatite-glaucony association in the Ediacaran Doushantuo Formation, South China and implications for marine redox conditions. Precambr. Res. 347, 105842.

Allen, J.R.L., 1988. Reworking of muddy intertidal sediments in the Sevem Estuary, southwestern UK - a preliminary survey. Sedim. Geol. 50, 1-23.

Altermann, W., 2002. The evolution of life and its impact on sedimentation. In: Altermann W, Corcoran PL (eds) Precambrian Sedimentary Environments: a Modern Approach to Ancient Depositional Systems, vol 33. Spec Publ Int Ass Sed, Blackwell, Oxford, pp 15-32.

Altermann, W., 2004. Precambrian stromatolites: problems in definition, classification, morphology and stratigraphy. In: Eriksson PG, Altermann W, Nelson DR, Muller WU, Catuneanu O (eds) The precambrian Earth: Tempos and Events. Elsevier, Amsterdam, pp 639-670.

Amorosi, A., 1995. Glaucony and sequence stratigraphy: A conceptual framework of distribution in siliciclastic sequences. J. Sed. Res. 65, 419-425.

Amorosi, A., 1997. Detecting compositional, spatial, and temporal attributes of glaucony: a tool for provenance research. Sed. Geol. 109, 135-153.

Amorosi, A., 2012. The occurrence of glaucony in the stratigraphic record: Distribution patterns and sequence-stratigraphic significance. International Association of Sedimentologists Special Publications 45, 37–54.

Amorosi, A., 2013. The occurrence of glaucony in the stratigraphic record: distribution patterns and sequence stratigraphic significance. In: Morad, S., Ketzer, M. de Ros, L.F. (Eds.), Linking Diagenesis to Sequence Stratigraphy, Int. Ass. Sed. Spec. Publ. 45, pp. 37-53.

Amorosi, A., Sammartino, I., Tateo, F., 2007. Evolution patterns of glaucony maturity: a mineralogical and geochemical approach. Deep Sea Research Part II: Topical Studies in Ocean. 54, 1364-1374.

Anand, A., Jain, A.K., 1987. Earthquakes magnitude–frequency, epicentral distance, and soft-sediment deformation in sedimentary basins. Sedimentary Geology 46, 67-75.

Anketell, J.M., Cegła, J., Dżułyński, S., 1970. On the deformational structures in systems with reversed density gradients. Annales Societatis Geologorum Poloniae 1, 3-30.

Auden J B 1933 Vindhyan sedimentation in Son valley, Mirzapur District. Geol. Surv. India Memoir 62, 141-250.

Baioumy H., Lehmann B., 2017. Anomalous enrichment of redox-sensitive trace elements in the marine black shales from the Duwi Formation, Egypt: Evidence for the late Cretaceous Tethys anoxia. J Afr Earth Sci 113, 7-14.

Baldermann, A., L.N. Warr, G.H., Grathoff, M. Dietzel., 2013. The rate and Mechanism of deep-sea glauconite formation at the Ivory Coast–Ghana Marginal ridge. Clays and Clay Miner. 61, 258–276.

Bandopadhyay, P.C., 2007. Interpretation of authigenic vs. allogenic green peloids of ferric clay in Proterozoic Penganga Group, southern India. Clay Min. 42, 471-485.

Bandyopadhyay, B., Roy, A., Huin, A.K., 1995. Structure and tectonics of a part of central Indian Shield. In: Sinha Roy S, Gupta KR (eds) Continental crust of the Northwestern and Central India, vol 3. Mem Geol Soc India, pp 433-467.

Banerjee, I., 1964. On some broader aspects of Vindhyan Sedimentation: Sedimentary Geology and Tectonics. Proceeding 22nd of Int. Geol. Cong., New Delhi, India, pp. 189-204.

Banerjee, I., 1974. Barrier coast-line sedimentation model and the Vindhyan example. In: Dey, A. (Ed.), Contributions to the Earth and Planetory Sciences. Geol. Min. Metall. Soc. India, Golden Jubilee Vol., pp. 101-127.

Banerjee, S., 1997. Facets of the Mesoproterozoic Semri Sedimentation in Son valley, India. Unpubl. Ph.D. thesis,
Jadavpur University, Kolkata, pp. 137.

Banerjee, S., Jeevankumar, S., 2005. Microbially originated wrinkle structures on sandstones and their stratigraphic context: Paleoproterozoic Koldaha Shale, Central India. Sedimentary Geology 176, 211-224.

Banerjee, S., Dutta, S., Paikaray, S., Mann, U., 2006. Stratigraphy, sedimentology and bulk organic geochemistry of black shales from the Proterozoic Vindhyan Supergroup (central India). J. Earth Sys. Sci. 115, 37-48.

Banerjee, S., Bhattacharya, S.K., and Sarkar, S., 2007. Carbon and oxygen isotopic variations in peritidal stromatolite cycles, Paleoproterozoic Kajrahat Limestone, Vindhyan basin of central India. J. Asian Earth Sci., 29, 823-831

Banerjee, S., Jeevankumar, S., Eriksson, P.G., 2008. Mg-rich ferric illite in marine transgressive and highstand systems tracts: examples from the Paleoproterozoic Semri Group, central India. Precambrian Res. 162, 212-226.

Banerjee, S., Bhattacharya, S. K., Sarkar, S., 2009. Facies, dissolution seams and stable isotope compositions of the Rohtas Limestone (Vindhyan Supergroup) in the Son valley area, Central India. Journal of Earth System Science, 114, 87-96.

Banerjee, S., Sarkar, S., Eriksson, P.G., Samanta, P., 2010. Microbially related structures in siliciclastic sediment resembling Ediacaran fossils: examples from India, ancient and modern. In: Seckbach J, Oren A (eds) Microbial Mats: Modern and Ancient Microorganisms in Stratified System. Springer, Berlin, pp 111-129.

Banerjee, S., Chattoraj, S.L., Saraswati, P.K., Dasgupta, S., Sarkar, U., 2012a. Substrate control on formation and maturation of glauconites in the Middle Eocene Harudi Formation, western Kutch, India. Mar. Pet. Geol. 30, 144–160.

Banerjee, S., Chattoraj, S.L., Saraswati, P.K., Dasgupta, S., Sarkar, U., Bumby, A., 2012b. The origin and maturation of lagoonal glauconites: A case study from the Oligocene Maniyara Fort Formation, western Kutch, India. Geol. J. 47, 357–371.

Banerjee, S., Mondal, S., Chakraborty, P.P., Meena, S.S., 2015. Distinctive compositional characteristics and evolutionary trend of Precambrian glaucony: example from Bhalukona Formation, Chhattisgarh basin, India. Precam. Res. 271, 33-48.

Banerjee, S., Bansal, U., Thorat, A.V., 2016a. A review on palaeogeographic implications and temporal variation in glaucony composition. J. Palaeo. 43-71.

Banerjee, S., Bansal, U., Pande, K., Meena, S.S., 2016b. Compositional variability of glauconites within the Upper Cretaceous Karai Shale Formation, Cauvery Basin, India: implications for evaluation of stratigraphic condensation. Sed. Geol. 331, 12-29.

Banerjee, S., Khanolkar, S., Saraswati, P.K., 2018. Facies and depositional settings of the Middle Eocene-Oligocene carbonates in Kutch. Geodin. Acta 30, 119-136.

Banerjee, S., Farouk, S., Nagm, E., Roy Choudhury, T., Meena, S.S., 2019. High Mg-glauconite in Campanian Duwi Formation of Abu Tartur Plateau, Egypt and its implications. J. African Earth Sci.156, 12-25.

Banerjee, S., Choudhury, T.R., Saraswati, P.K., Khanolkar, S., 2020. The formation of authigenic deposits during Paleogene warm climatic intervals: a review. J. Palaeo. 9(1), 1-27.

Banks, N. G., 1970. Nature and origin of early and late cherts in the Lead- Ville limestone, Colorado. Geological Society of America Bulletin 81, 3033-3048.

Bansal, U., Banerjee, S., Pande, K., Arora, A., Meena, S.S., 2017. The distinctive compositional evolution of glauconite in the Cretaceous Ukra Hill Member (Kutch basin, India) and its implications. Mar. Petrol. Geol. 82, 97-117

Bansal, U., Banerjee, S., Ruidas, D.K., Pande, K., 2018. Origin and geochemical characterization of the glauconites in the Upper Cretaceous Lameta Formation, Narmada Basin, central India. J. Palaeogeogr. 7, 99-116.

Bansal, U., Banerjee, S., Pande, K., Das, D.K., 2019. Unusual seawater composition of the Late Cretaceous Tethys imprinted in glauconite of Narmada basin, central India. Geol. Mag. https://doi.org/10.1017/S0016756819000621 .

Bansal, U., Banerjee, S., Nagendra, R., 2020. Is the rarity of glauconite in Precambrian Bhima Basin in India related to its chloritization? Precambr. Res. 336, 105509.

Basu, A., Bickford, M.E., 2014. Contributions of zircon U-Pb geochronology to understanding the volcanic and sedimentary history of some Purana basins, India.

Basu, P., Banerjee, A., Chakrabarti, R., 2021. A combined geochemical, Nd, and stable Ca isotopic investigation of provenance, paleo-depositional setting and subbasin connectivity of the Proterozoic Vindhyan Basin, India. Lithos 388: 106059.

Basu, S., Verchovsky, A.B., Bogush, A., Jones, A.P., Jourdan, A.L., 2019. Stability of organic carbon components in shale: implications for carbon cycle. Front. Earth Sci. 7, 297.

Bau, M., Dulski, P., 1996. Distribution of yttrium and rare-earth elements in the Penge and Kuruman iron formations, Transvaal Supergroup, South Africa. Precamb. Res. 79, 37–55.

Beer, E.J., 1919. Note on spiral impression on Lower Vindhyan limestone. Rec Geol Surv India 50:139.

Bekker, A., Holland, H., Wang, PL., 2004. Dating the rise of atmospheric Oxygen. Nature 427, 117–120.

Bengtson, S., Belivanova, V., Rasmussen, B., Whitehouse, M., 2009. The controversial 'Cambrian' fossils of the Vindhyan are real but more than a billion years older; Proc. Nat. Acad. Sci. USA 106, 7729-7734.

Bengston, S., Sallstedt, T., Belivanova, V., Whitehouse, M., 2017. Three-dimensional preservation of cellular and subcellular structures 1.6 billion-year-old crowd-group red algae; PLoS Biol., https://doi.org/10.1371/journal.pbio.2000735

Bentor, K., Kastner, M., 1965. Notes on the mineralogy and origin of glauconite. J. Sed. Petrol. 35, 155-166.

Berg-Madsen, V., 1983. High-alumina glaucony from the Middle Cambrian of Orland and Bornholm, southern Baltoscandia. J. Sed. Petrol. 53, 875-893.

Berner, R.A., 1981. A new geochemical classification of sedimentary environments. J. Sed. Res. 51, 339-365.

Bhattacharyya, A., 1996. Recent advances in Vindhyan geology. Geol. Soc. India.

Bhattachryya, A., Chanda, S. K., 1976. Tidal ripple drift cross-lamination and related lamination types: Indian Jour. Earth-Sciences 3, 173-177.

Bhattacharyya, A., Sarkar, s., Chanda, S.K., 1980. Storm deposits in the late Proterozoic Lower Bhader Sandstone of Vindhyan Supergroup around Maihar, Stana distric, Madhya Pradesh, India. Journal of sedimentary Petrology 50, 1327-1336.

Bickford, M.E., Mishra, M., Mueller, P.A., Kamenov, G.D., Schieber, J., Basu, A., 2017. U-Pb Age and Hf isotopic composition of Magmatic Zircon from A Rhyolite Flow in Porcellanite Formation I the Vindhyan Supergroup, Son Valley (India): Implications for its Tectonic Significance. The Journal of Geology, 125(3), 367-379.

Bickford, M.E., Basu, A., 2021. Towards resolving the'jigsaw puzzle'and age-fossil inconsistency within east Gondwana: A comment. Precamb. Res. 352,105881.

Bindeman, I.N., Zakharov, D.O., Palandri, J., Greber, N.D., Dauphas, N., Retallack, G.J., Hofmann, A., Lackey, J.S., Bekker, A. 2018. Rapid emergence of subaerial landmasses and onset of a modern hydrologic cycle 2.5 billion years ago. Nature 557, 545-548.

Bolhar, R., Kamber, B.S., Moorbath, S., Fedo, C.M., Whitehouse, M.J., 2004. Characterisation of early Archaean chemical sediments by trace element signatures. Earth. Planet. Sc. Lett. 222, 43–60.

Bora, S., Kumar, S., Yi, K., Kim, N., Lee, T.H., 2013. Geochemistry and U-Pb SHRIMP zircon chronology of granitoids and microgranular enclaves from Jhirgadandi pluton of Mahakoshal Belt, Central India Tectonic Zone, India. J. Asian Earth Sci. 70, 99-114.

Bose, P. K., Chaudhuri, A. K., 1990. Tide versus storm in epeiric costal deposition: two Proterozoic sequence, India. Geol. Jour. 25, 81-100.

Bose, P. K., Sarkar, S., 1991. Basinal autoclastic mass flow regime in the Precambrian Chanda limestone formation, Adilabad, India. Sedim. Geol. 73, 299–315.

Bose, P.K., Banerjee, S., Sarkar, S., 1997. Slope-controlled seismic deformation and tectonic framework of deposition: Koldaha Shale, India. Tectonophys. 269, 151-169.

Bose, P.K., Chakraborty, P.P., 1994. Marine to fluvial transition: Proterozoic Upper Rewa Sandstone, Maihar, India. Sed. Geol. 89, 285-302.

Bose, P.K., Chakrabarty, S., Sarkar, S., 1999. Recognition of ancient eolian longitudinal dunes: a case study in Upper Bhander Sandstone, Son valley, India. J. Sed. Res. 69, 86-95.

Bose, P.K., Sarkar S., Chakrabarty, S., Banerjee, S., 2001. Overview of Meso- to Neoproterozoic evolution of Vindhyan Basin, central India. Sed. Geol. 141/142, 395-419.

Bose, P.K., Sarkar, S., Das, N.G., Banerjee, S., Mandal, A., Chakraborty, N., 2015. Proterozoic Vindhyan Basin: configuration and evolution. Geol. Soc. London. Memoirs. 43, 85-102.

Bottjer, D., and Hangardon, J.W., 2007. Mat Growth Features. In: Schieber, J., Bose, P.K., Eriksson, P.G., Banerjee, S., Sarkar, S., Altermann, W., and Catuneanu, O., (Eds.), Atlas of Microbial Mat Features Preserved Within The Siliciclastic Rock Record. Atlases in Geoscience, pp. 53-71.

Bouougri, E., Gerdes, G., and Porada, H., 2007. Inherent Problems of Terminology: Definition Of Terms Frequently Used In Connection With Microbial Mats. In: Schieber, J., Bose, P.K., Eriksson, P.G., Banerjee, S., Sarkar, S., Altermann, W., and Catuneanu, O., (Eds.), Atlas of Microbial Mat Features Preserved Within The Siliciclastic Rock Record, Atlases in Geoscience, pp. 145-152.

Burst, J.F., 1958a. "Glauconite" pellets: Their mineral nature and applications to stratigraphic interpretations. AAPG Bull. 42, 310-327.

Burst, J.F., 1958b. Mineral heterogeneity in glauconite pellets. Am. Mineral. 43, 481-497.

Bustillo, M.A., 2010. Carbonates in Continental Settings: processes, facies and applications (Eds.: Alonso-Zarza A. and Tanner L. H.) Developments in Sedimentology Series (Ed: Van Loon A.J). 62, 153-174.

Bustillo, M.A., Castañeda, N., Capote, M., Consuegra, S., Criado, C., Díaz- Del-Río, P., Terradas, X., 2009. Is the macroscopic classification of flint useful? A petroarchaeological analysis and characterization of flint raw materials from the Iberian Neolithic Mine OF Casa Montero. Archaeometry 51(2), 175-196.

Canfield, D., 1998. A new model for Proterozoic ocean chemistry. Nature 396, 450–453.

Catuneanu O 2006 Principles of sequence stratigraphy; Elsevier, Amsterdam, 375p.

Catuneanu, O., Abreu, V., Bhattacharya, J. P., Blum, M. D., Dalrymple, R.W., Eriksson, P.G., Fielding, C. R., Fisher, W. L., Galloway, W. E., Gibling, M. R., Giles, K. A., Holbrook, J. M., Jordan, R., Kendall, C. G.St. C., Macurda, A. Amorosi, B., Martinsen, O.J., Miall, A.D., Neal, J.E., Nummedal, D., Pomar, L., Posamentier, H.W., Pratt, B.R., Sarg, J.F., Shanley, K.W., Steel, R.J., Strasser, A., Tucker, M. E.,Winker, C., 2009. Towards the standardization of sequence stratigraphy. Earth-Sci. Rev. 92, 1-33.

Chakrabarti, R., Basu, A.R., Chakrabarti, A., 2007. Trace and Nd-isotope evidence for sediments sources in the mid-Proterozoic Vindhyan Basin, central India. Precambrian Res. 159, 260-274.

Chakraborty, C., 1993. Morphology, internal structure and mechanics of small longitudinal (seif) dune in an aeolian horizon of the Proterozoic Dhandraul Quartzite, India. Sedimentology 40, 79-85.

Chakraborty, C., 1995. Gutter casts from the Proterozoic Bijaygarh Shale formation, India: Their implication for storm-induced circulation in shelf settings. Geol. J. 30, 69-78.

Chakraborty, C., 2006. Proterozoic intracontinental basin: the Vindhyan example. J. Earth Sys. Sci. 115, 3-22.

Chakraborty, C., Bose, P. K., 1990. Internal structures of sand waves in a tide-storm interactive system: Proterozoic lower quartzite formation, India. Sedim. Geol. 67, 133-142.

Chakraborty, C., Bose, P.K., 1992a. Rhythmic shelf storm beds: Proterozoic Kaimur formation, India. Sedim. Geol. 77, 259-268.

Chakraborty, C., Bose, P.K., 1992b. Ripple/dune to upper stage plane bed transition: Some observations from the ancient record. Geol. J. 27, 349-359.

Chakraborty, C., Bhattacharyya, A., 1996. Fan delta sedimentation in a foreland moat: Deoland Formation. Geol Soc India Mem 36, 27-48.

Chakraborty, P. P., Dey, S., Mohanty, S. P., 2010 Proterozoic platform sequences of Peninsular India: Implications towards basin evolution and supercontinent assembly; J. Asian Earth Sci. 39 589-607.

Chakraborty, P.P., 1996. Facies and sequence development in some late Proterozoic Formations in Son valley, India with some clues for basin evolution. Unpublished Ph.D. thesis, Jadavpur University (Calcutta).

Chakraborty, P.P., Banerjee, S., Das, N.G., Sarkar, S., Bose, P.K., 1996. Volcaniclastics and their sedimentological bearing in Proterozoic Kaimur and Rewa groups in central India. In: Bhattacharya, A., (Ed.), Recent advances in Vindhyan Geology, Geol. Soc. Ind., Mem. 36, 59-76.

Chakraborty, P.P., Sarkar, S., Bose, P.K., 1998. A viewpoint on intracratonic chenier evolution: clue from a reappraisal of the Proterozoic Ganurgarh Shale, central India. In: B.S. Palliwal (Ed.) The Indian Precambrians, Scientific Publishers, India, Jodhpur, p. 61-72.

Chakraborty, P.P., Sarkar, S., 2005. Episodic emergence of offshore shale and its implications: Late Proterozoic Rewa Shale, Son valley, central India. J. Geol. Soc. India 66, 699-712.

Chakraborty, P.P., Sarkar, S., Patranabis Deb, S., 2012. Tectonics and sedimentation of Proterozoic basins of Peninsular India. Proc Ind Nat Sci Acad 78, 393-400.

Chakraborty, T., Chaudhuri, A.K., 1990. Stratigraphy of Proterozoic Rewa group and palaeogeography of the Vindhyan Basin in central India during Rewa sedimentation. J. Geol. Soc. India 36 383-402.

Chanda, S. K., Bhattacharyya, A., 1974, Ripple drift cross-lamination in tidal deposits: Examples from the Precambrian Bhander Formation of Maihar, Satna district, Madhya Pradesh, India: Geol. Soc. America Bull. 85, 1117-1122.

Chanda, S.K., Bhattacharyya, A., 1982. Vindhyan sedimentation and Paleogeography: Post-Auden developments. In: Valdiya, K.S., Bhatia, S.B., Gaur, V.K. (Eds.), Geol. of Vindh: Prof. Misra Volume. Hind. Publ. Corp., Delhi, pp. 88-101.

Chapmann, F., 1935. Primitive fossils, possibly Atrematous and Neotrematous brachiopod from the Vindhyans of India. Rec Geol Surv India 69, 109-120.

Chaudhuri, A.K., Chanda, S.K., 1991. The Proterozoic basin of the Pranhita–Godavari valley: an overview. In: Tandon SK, Pant CC, Casshyap SM (eds) Sedimentary Basins of India, Tectonic Context. Gyanodayan Prakashan, Nainital, pp 13-29.

Chen, D. F., Dong, W. Q., Qi, L., Chen, G. Q., Chen, X. P., 2003. Possible REE constraints on the depositional and diagenetic environment of Doushantuo Formation phosphorites containing the 27 earliest metazoan fauna. Chem. Geol. 201, 103–118.

Chen, J., Chough, S.K., Chun, S.S., and Han, Z., 2009. Limestone pseudoconglomerates in the Late Cambrian Gushan and Chaomidian Formations (Shandong Province, China): soft-sediment deformation induced by storm-wave loading. Sedimentology, 56, 1174–1195.

Chen, J., Han, Z., Zhang, X., Fan, A., and Yang, R., 2010. Early diagenetic deformation structures of the Furongian ribbon rocks (Shandong Province, China) – a new perspective of the genesis of limestone conglomerates. Science China Earth Sciences, 53, 241-252.

Choubey VD (1971) Narmada–Son Lineament. Nature 232:38–40.

Choudhuri, A., 2020. Implications of microbial mat induced sedimentary structures (MISS) in carbonate rocks: An insight from Proterozoic Rohtas Limestone and Bhander Limestone, India. Journal of Earth System sciences 129, 1-18.

Choudhuri, A., Schiber, J., Sarkar, S., Bickford, M.E., Basu, A., 2020. The "Lower Kaimur Porcellanite" (Vindhyan Supergroup) is of Sedimentary Origin and not Tuff. Journal Geological Society of India 95, 17-24.

Choudhuri, A., Sarkar, S., Banerjee, S., 2020. A review of biotic signatures within the Precambrian Vindhyan Supergroup: Implications on evolution of microbial and metazoan life on Earth. Journal of Mineralogical and Petrological Sciences, doi:10.2465/jmps.190827a.

Chowdhury, P., Talukdar, M., Sengupta, P., Sanyal, S., Mukhopadhyay, D., 2013. Controls of P-T path and element mobility on the formation of corundum pseudomorphs in Paleoproterozoic high-pressure anorthosite from Sittampundi, Tamil Nadu, India. Am. Mineral. 98, 1725–1737. http://dx.doi.org/10.2138/am.2013.4350

Clayton, R.N., 2003. Oxygen isotopes in meteorites. In Treatise on Geochemistry (eds. H. D. Holland and K. K. Turekian), pp. 129-142.

Cole, D.B., Zhang, S. and Planavsky, N.J., 2017. A new estimate of detrital redox-sensitive metal concentrations and variability in fluxes to marine sediments. Geochim. Cosmochim. Ac. 215, 337-353.

Cowan, C.A., James, N.P., 1992. Diastasis cracks: Mechanically generated synaeresis-like cracks in upper Cambrian shallow water oolite and ribbon carbonates; Sedimentology 39, 1101-1118.

Craig, H., 1957. Isotopic standards for carbon and oxygen and correction factors for mass-spectrometric analysis of carbon dioxide. Geochim. Cosmochim. Acta 12, 133-149.

Crawford, A. R., Compston, W., 1970. The age of the Vindhyan system of peninsular India. Q. J. Geol. Soc. Lond. 125, 351-371.

Crawford, A.R., 1978. Narmada-Son lineament of India traced into Madagascar. J Geol Soc India 19, 14-153.

Crundwell, F.K., 2017. On the Mechanism of the Dissolution of Quartz and Silica in Aqueous Solutions. American Chemical Society 2, 1116-1127.

Das, L.K., Misra, D.C., Ghosh, D., Banerjee, B., 1990. Geomorphotectonics of the basement in a part of Upper Son Valley of the Vindhyan basin. J Geol Soc India 35, 445-458.

Dasgupta, S., Chaudhuri, A.K., Fukuoka, M., 1990. Compositional Characteristics of Glauconitic Alterations of K-Feldspar from India and their Implications. J. Sediment. Petrol. 60, 277–287.

Davaud, E., Strasser, A., Jedoui, Y., 1994. Stromatolite and serpulid bioherms in a Holocene restricted lagoon (Sabkha el Melah, southeastern Tunisia). In: Bertrand-Sarfati J, Monty C (eds) Phanerozoic Stromatolites II. Kluwer Acad Publ, Dordrecht, pp 131-151.

Davis, J.K., Meert, J.G., Pandit, M.K., Kamenov, G.D., 2011. Initial paleomagnetic analysis of the Marwar Basin, Rajasthan, India. Geological Society of America Abstracts with Programs 43, 319.

De Boer, P.L., Oost, A.P., Visser, M.J., 1989. The diurnal inequality of the tide as parameter for recognizing tidal influences. J. Sediment. Res. 59, 912-921.

De Ronde, C.E.J., Channer, D.M.D., Faure, K., Bray, C.J., Spooner, E.T.C., 1997. Fluid chemistry of Archean seafloor hydrothermal vents: Implications for the composition of circa 3.2 Ga seawater. Geochim Cosmochim Acta 61, 4025-4042.

Deb, S.P., Fukuoka, M., 1998. Fe-Illites in a Proterozoic Deep Marine Slope Deposit in the Penganga Group of the Pranhita Godavari Valley: Their Origin and Environmental Significance. J. Geol. 106, 741–749.

Degens, E.T., Epstein, S., 1962. Relationship between $O^{18}/O^{16}$ ratios in coexisting carbonates, cherts, and diatomites: geological notes. AAPG Bull. 46, 534-542.

Demoulin, A., 1996. Clastic dykes in east Belgium: evidence for Upper Pleistocene strong earthquakes west of the Lower Rhine rift segment. J. Geol. Soc. 153, 803-810.

Derry, L.A., Jacobsen, S.B., 1990. The chemical evolution of Precambrian seawater: Evidence from REEs in banded iron formations. Geochimica et Cosmochimica Acta 54, 2965-2977.

Dhuime, B., Hawkesworth, C. J., Delavault, H., and Cawood, P. A., 2017. Continental growth seen through the sedimentary record. Sedimentary Geology 357,16–32. doi: 10.1016/j.sedgeo.2017.06.001

Dhuime, B., Hawkesworth, C.J., Cawood, P.A., and Storey, C.D., 2012. A change in the geodynamics of continental growth 3 billion years ago. Science 335, 1334-1336. doi: 10.1126/science.1216066

Drits, V.A., Ivanovskaya, T.A., Sakharov, B.A., Zvyagina, B.B., Derkowski, A., Gońkova N.V., Pokrovskaya, E.V., Savichev, A.T., Zaitseva, T.S., 2010. Nature of the structural and crystal- chemical heterogeneity of the Mg-rich glauconite (Riphean, Anabar Uplift). Lith. Min. Res. 45, 555- 576.

Dubey, V.S., Chaudhary, M.S., 1952. Late Precambrian glaciation in central India. Curr. Sci. 21, 331-352.

El Albani, A., Meunier, A., Fursich, F., 2005. Unusual occurrence of glauconite in a shallow lagoonal environment (Lower Cretaceous, northern Aquitaine Basin, SW France). Terra Nova 17, 537–544.

Erikson, J.P., Pindell, J.L., Karner, G.D., Sonder, L.J., Fuller, E., Dent, L., 1998. Neogene sedimentation and tectonics in the Cibao Basin and northern Hispaniola: an example of basin evolution near a strike-slip-dominated plate boundary. J. Geol. 106 (4),473-494.

Eriksson K A and Simpson E L 2004. Precambrian tidalites: Recognition and significance; In: Tempos and events in Precambrian time: Amsterdam, (Eds.), Eriksson PG, Elsevier Sci., pp. 631-642.

Eriksson, K.A., Simpson, E.L., 2004. Precambrian tidalites: Recognition and significance; In: Tempos and events in Precambrian time: Amsterdam (ed.) Eriksson P G, Elsevier Science, pp. 631-642.

Eriksson, P.G., Mazumder, R., Sarkar, S., Bose, P.K., Alterman, W., Vander-Merwee, R., 1999. The 2.7-2 Ga volcano–sedimentary record of Africa, India and Australia: Evidence for global and local changes in sea–level and continental freeboard. Precam Res 97, 269-302.

Eriksson, P.G., Sarkar, S., Banerjee, S., Porada, H., Catuneanu, O., Samanta, P., 2010. Paleoenvironmental context of microbial mat–related structures in siliciclastic rocks: examples from the Proterozoic of India and South Africa. In: Seckbach J, Oren A (eds) Microbial Mats: Modern and Ancient Microorganisms in Stratified Systems. Springer, Berlin, p 73.

Farber, K., Dziggel, A., Meyer, F.M., Prochaska, W., Hofmann, A., Harris, C., 2015. Fluid inclusion analysis of silicified Palaeoarchaean oceanic crust–A record of Archaean seawater? Precambrian Research 266, 150-164.

Farquhar, J., Bao, H., Thiemens, M., 2000. Atmospheric influence of Earth's earliest sulfur cycle. Science 289, 756–758.

Feulner, G., 2012. The faint young Sun problem. Rev. Geophys. 50, RG2006.

Fleming, B.A., Crerar, D.A., 1982. Silicic acid ionization and calculation of silica solubility at elevated temperature and pH application to geothermal fluid processing and reinjection. Geothermic 11(1), 15-29.

Froelich, P.N., Mortlock, R.A., Shemesh, A., 1989. Inorganic germanium and silica in the Indian Ocean: biological fractionation during (Ge/Si) opal Formation. Glob. Biogeochem. Cycl. 3.

Galili, N., Shemesh, A., Yam, R., Brailovsky, I., Sela-Adler, M., Schuster, E.M., Collom, C., Bekker, A., Planavsky, N., Macdonald, F.A., Préat, A., 2019. The geologic history of seawater oxygen isotopes from marine iron oxides. Science 365, 469-473.

Gao, G., Land, L. S. 1991. Nodular chert from the Arbuckle Group, Slick Hills, SW Oklahoma: A combined field, petrographic and isotopic study. Sedimentology, 38, 857–870. https://doi.org/10.1111/j.1365-3091.

Genedi, A., 1998. Formation of the Upper Cretaceous cherts in northeastern Sinai. Journal of African Earth Sciences 26(2), 297-311.

Georg, F., 2012.The faint young Sun problem. Reviews of Geophysics 50(2).

Gilleaudeau, G.J., Sahoo, S.P., Kah, L.C., Henderson, M.A., Kaufman, J., 2018. Proterozoic carbonates of the Vindhyan Basin, India: Chemostratigraphy and diagenesis. Gondwana Res. 57, 10-25.

Gopalan, K., Kumar, A., Kumar, S., Vijayagopal, B., 2013. Depositional history of the Upper Vindhyan succession, central India: Time constraints from Pb–Pb isochron ages of its carbonate components. Precamb. Res. 233, 108-117.

Grant, J.A., 1986. The isocon diagram: a simple solution to Gresen's equation for metasomatic alteration. Economic Geology 81, 1976-1982.

Grant, J.A., 2005. Isocon analysis: a brief review of the method and applications. Physics and Chemistry of the Earth 30, 997-1004.

Gregory, R.T. 2003. Ophiolites and global geochemical cycles: Implications for the isotopic evolution of seawater. Geol. Soc. Lond. Spec. Publ. 218, 353-368.

Guimaraes, E.M., Velde, B., Hillier, S., Nicot, E., 2000. Diagenetic/anchimetamorphic changes on the Proterozoic glauconite and glaucony from the Paranoá Group, mid-western Brazil. Rev. Brasil. de Geo. 30, 363-366.

Gummarsson, I., Arnorsson, S., 1999. New data on the Standsard Gibbs energy of H4SO4 and its effect on slisification solubility. In Geochemistry of the Earth's Surface (ed. H. Armannson), pp. 449-452. Balkema, Rotterdam.

Gummarsson, I., Arnorsson, S., 2000. Amorphous silica solubility and the thermodynamic properties of H4SiO°4 in the range of 0° to 350°C at Psat. Geochimica et Cosmochimica Acta 64(13), 2295-2307.

Harazim, D., Callow, R.H., McIlroy, D., 2013. Microbial mats implicated in the generation of intrastratal shrinkage ('synaeresis') cracks. Sedimentology 60, 1621-1638.

Hardardottir, V., 2011. Metal-rich Scales in the Reykjanes Geothermal System, SW Iceland: sulfide minerals in a seawater-dominated hydrothermal environment. PhD thesis, University of Ottawa, Canada.

Harder, H., 1980. Syntheses of Glauconite at surface temperatures Clays and clay Minerals 28(3), 217-222.

Harms, J.C., Southard, J.B., Spearing, D.R., Walker, R.G., 1975. Depositional environments as interpreted from primary sedimentary structures and stratification sequences, Dallas. SEPM Short course, 2, pp.161

Hawkesworth, C., Cawood, P.A., Dhuime, B., 2019. Rates of generation and growth of the continental crust. Geoscience Frontier 10, 165-173.

Hawkesworth, C., Cawood, P.A., Dhuime, B., 2020. The Evolution of the Continental Crust and the Onset of Plate Tectonics. Frontier in Earth Sciences 8, doi: 10.3389/feart.2020.00326.

Hayles, J.A., Gao, C., Cao, X., Liu, Y., Bao, H. 2018. Theoretical calibration of the triple oxygen isotope thermometer. Geochim Cosmochim Acta 235,237-245.

Hayles, J.A., Yeung, L.Y., Homann, M., Banerjee, A., Jiang, H., Shen, B., Lee, C-TA., 2019. Three-billion-year secular evolution of the triple oxygen isotope composition of marine chert. preprint, https://eartharxiv.org/n2p5q/download?format=pdf .

Herwartz, D., Pack, A., Krylov, D., Xiao, Y., Muehlenbachs, K., Sengupta, S., Di Rocco, T., 2015. Revealing the climate of snowball Earth from $\Delta^{17}O$ systematics of hydrothermal rocks. Proceedings of the National Academy of Sciences 112, 5337-5341.

Hesse, R., 1987. Selective and reversible carbonate–silica replacements in Lower Cretaceous carbonate-bearing turbidites of the Eastern Alps. Sedimentology 34, 1055-1077.

Hesse, R., 1989. Silica diagenesis: origin of inorganic and replacement cherts.: Earth Science Reviews 26, 253-284.

Hofmann, A., Harris, C. 2008. Silica alteration zones in the Barberton greenstone belt: A window into subsea floor processes 3.5–3.3 Ga ago. Chemical Geology 257, 221-239.

Hofmann, A., Harris, C., 2012. Silica alteration zones in the Barberton greenstone belt: A window into subseafloor processes 3.5–3.3 Ga ago. Chemical Geology 257, 221-229.

Holland, H.D., 2002. Volcanic gases, black smokers, and the Great oxidation event. Geochim. Cosmochim. Acta 66, 3811–3826.

Holland, H.D., 2006. The oxygenation of the atmosphere and oceans. Philos. Trans. R. Soc. B 361, 903–915.

Hövelmann, J., Putnis, A., Geisler, T., Schmidt, B.C., Golla-Schindler, U., 2010. The replacement of plagioclase feldspars by albite: observations from hydrothermal experiments. Contrib. Miner. Petrol. 159, 43-59. http://dx.doi.org/10.1007/s00410-009-0415-4

Hower, J., 1961. Some factors concerning the nature and origin of glauconite. Am. Mineral. 46, 313-334.

Ivanovskaya, T.A., 2009. Glauconitites in Terrigenous Rocks of the Khaipakh Formation (Middle Riphean, Olenek Uplift). Lithol Miner Resour 44, 348-366.

Ivanovskaya, T.A., Gor'kova, N.V., Karpova, G.V., Pokrovskaya, E.V., 2006. Phyllosilicates (glauconite, illite, and chlorite) in terrigenous sediments of the Arymas Formation (Olenek High). Litho. & Min. Res. 41(6), 547-569.

Ivanovskaya, T.A., Zviagina, B.B., Zaitseva, T.S., 2017. Secondary alterations of globular and platy phyllosilicates of the glauconite-illite series in the Precambrian and Vendian-Cambrian rocks. Lithol Miner Resour 52, 369-391.

Jach, R., Starzec, K., 2003. Glaucony from the condensed Lower-Middle Jurassic deposits of the Krizna Unit, Western Tatra Mountains, Poland. Annales Societatis Geologorum Poloniae 73, 183-192.

Jackson, S.E., Fryer, B.J., Gosse, W., Healey, D.C., Longerich, H.P. and Strong, D.F., 1990. Determination of the precious metals in geological materials by inductively coupled plasma-mass spectrometry (ICP-

MS) with nickel sulphide fire-assay collection and tellurium coprecipitation. Chem. Geol. 83(1-2), 119-132.

Jacobsen, S.B., Pimentel-Klose, M.R., 1988a. A Nd isotopic study of the Hamersley and Michipicoten banded iron formations: The source of REE and Fe in Archean oceans. Earth and Planetary Science Letters, 87, 29-44.

Jacobsen, S.B., Pimentel-Klose, M.R., 1988b. Nd isotopic variations in Precambrian banded iron formations. Geophysical Research Letters 15, 393-396.

Jafar, S.A., Akhtar, K., Srivastava, V.K., 1966. Vindhyan Palaeocurrents and their bearing on the Northern limits of Vindhyan sedimentatuion - A preliminary note. Bulletin of Geological Society of India 3, 82-84.

Jaffrés, J.B.D., Shields, G.A., Wallmann, K., 2007. The oxygen isotope evolution of seawater: a critical review of a long-standing controversy and an improved geological water cycle model for the past 3.4 billion years. Earth Sci. Rev. 83, 83-122.

James, V., Canerot, J., Meyer, A., Biteau, J.J., 2000. Growth and destruction of Bathonian silica nodules in the western Pyrenees (France). Sedimentary Geology 132, 5-23.

Jean-Baptiste, P., Charlou, J.L., Stievenard, M., 1997. Oxygen isotope study of mid-ocean ridge hydrothermal fluids: Implication for the oxygen-18 budget of the oceans. Geochim. Cosmochim. Acta 61, 2669-2677, https://doi.org/10.1016/S0016-7037(97)00090-2.

Johnson, B.W., Wing, B.A., 2020. Limited Archaean continental emergence reflected in an early Archaean 18O-enriched ocean. Nature Geoscience 13, 243-248.

Jones, A.P., Omoto, K., 2000. Towards establishing criteria for identifying trigger mechanisms for soft-sediment deformation: case study of Late Pleistocene lacustrine sands and clays, Onokobe and Nakayamadaira Basins, northeastern Japan. Sedimentology 47, 1211-1226

Jones, B., Manning, D.C., 1994, Comparison of geochemical indices used for the interpretation of paleo–redox conditions in Ancient mudstones: Chem. Geol. 111(1–4), 111–129.

Jones, H.J., 1909. In: General Report. Rec Geol Surv India 3, 66.

Kaila, K.L., Reddy, P.R., Dixit, M.M., Rao, P.K., 1985. Crustal structure across the Narmada–Son lineament, central India, from deep seismic soundings. J Geol Soc India 26, 465-480.

Kaila, K.L., Murthy, P.R.K., Mall, D.M., 1989. The evolution of the Vindhyan Basin vis–à–vis the Narmada–Son lineament, Central India, from deep seismic soundings. Tectonophys 162, 277-289.

Karhu, J., Epstein, S., 1986. The implication of the oxygen isotope records in coexisting cherts and phosphates. Geochim Cosmochim Acta 50, 1745-1756.

Kasting, J.F., 1987.Theoretical constraints on oxygen and carbon dioxide concentrations in the Precambrian atmosphere. Precambrian Res. 34, 205-229.

Kasting, J.F., Howard, M.T., Wallmann, K., Veizer, J., Shields, G., Jaffrés, J., 2006. Paleoclimates, ocean depth, and the oxygen isotopic composition of seawater. Earth Planet. Sci. Lett. 252, 82-93.

Keheila, E. A., El-Ayyat, A., 1992. Silicification and dolomitization of Lower Eocene carbonates in the Eastern Desert between Sohag and Qena, Egypt. Journal of African Earth Sciences 14(3), 341–349.

Keheila, E.A., 2000. Carbonate facies, sequential analysis and sedimentary cycles of the Lower Eocene Thebes Formation at Gebel Duwi (Red Sea Coast) and south Wadi Qena, Egypt: Chert breccia tempestites as evidence for synsedimentary silicification. Bulletin Faculty of Science, Assiut University, 29(2-E), 51-76.

Kelly, J.C., Webb, J.A., 1999. The genesis of glaucony in the Oligo-Miocene Torquay Group, southeastern Australia: petrographic and geochemical evidence. Sediment. Geol. 125, 99-114.

Kenny, R., Knauth, L.P. 1992. Continental paleoclimates from δD and $\delta^{18}O$ of secondary silica in paleokarst chert lags. Geology 20, 219-222.

Khalef, F.I., Thiry, M., Milnes, A., Alnaqi, R., 2020. Characterization of chert in the Damman Formation (Eocene), Kuwait: clues to geoundwater silisification processes. Journal of Sedimentary Research 90, 297-312.

Kidder, D.L., 1990. Facies-controlled shrinkage-crack assemblages in middle Proterozoic mudstones from Montana, USA. Sedimentology 37, 943-951.

Kidder, D.L., Erwin, H., 2001. Secular distribution of biogenic silica through the Phanerozoic: Comparison of silica-replaced fossils and bedded cherts at a series level. Journal of Geology 109, 509-522.

Kidder, D.L., Mumma, S.A., 2003. Silica-replaced oolites, bedded shelf cherts and Paleozoic changes in the silica cycle. Sedimentary Geology 162, 159-166.

Klein, C., Beukes, N.J., 1992. Time distribution, stratigraphy, sedimentologic setting, and geochemistry of Precambrian iron-formations, *in* Schopf, J.W., and Klein, C., eds., The Proterozoic biospher.: New York, Cambridge University Press, p. 139-146.

Knauth, L. P., Epstein, S., 1976. Hydrogen and oxygen isotope ratios in nodular and bedded cherts. Geochim. Cosmochim. Acta 40, 1095–1108.

Knauth, L. P.,1994. Petrogenesis of chert: Reviews in Mineralogy and Geochemistry 29, 233-258.

Knauth, L.P. 1979. A model for the origin of chert in limestone. Geology 7, 274-277.

Knauth, L.P., Lowe, D.R., 1978. Oxygen isotope geochemistry of cherts from the Onverwacht Group (3.4 billion years), Transvaal, South Africa, with implications for secular variations in the isotopic composition of cherts. Earth Planet. Sci. Lett. 41, 209-222.

Knauth, L.P., Lowe, D.R., 2003. High Archean climatic temperature inferred from oxygen isotope geochemistry of cherts in the 3.5 Ga Swaziland Supergroup, South Africa. Bull. Geol. Soc. Am. 115, 566-580.

Knauth, L.P., Lowe, D.R., 2003. High Archean climatic temperature inferred from oxygen isotope geochemistry of cherts in the 3.5 Ga Swaziland Supergroup, South Africa. Geol. Soc. Am. Bull. 115, 566-580.

Kneller, B.C., Branney, M.J., 1995. Sustained high-density turbidity currents and the deposition of thick massive sands. Sedimentalogy 42, 607-616.

Kohsiek, L.H.M., Terwindt, I.H.I., 1981. Characteristics of foreset and topset bedding in megaripples related to hydrodynamic conditions on an intertidal shoal; In: Holocene marine sedimentation in the North Sea basin (eds) Nio S D, Schllttenhelm R L E and Van Weering T J C E, IAS Spec. Publ. 5, 27-37.

Kolodny, Y., Taraboulos, A., Frieslander, U., 1980. Participation of fresh water in chert diagenesis: Evidence from oxygen isotopes and boron a-track mapping. Sedimentology 27, 305-316.

Krishnan, M.S., Swaminath, J., 1959. The great Vindhyan Basin of Northern India. Journal of Geological Society of India 1, 10-30.

Kulkarni, K.G., Borkar, V.D., 1996b. Occurrence of Cochlichnus hitchcock in the Vindhyan Supergroup (Proterozoic) of Madhya Pradesh. J Geol Soc India 47, 725-729.

Kumar, S., 1976a. Stromatolites from the Vindhyan rocks of the Son Valley-Maihar area, district Mirzapur (UP) and Satna (MP). J Palaeontol Soc India 18, 13-21.

Kumar, S., 1976b. Significance of stromatolites in the correlation of Semri Series (Lower Vindhyan) of Son Valley and Chitrakut area. UP. J Palaeontol Soc India 19, 24-27.

Kumar, S., 1978. Discovery of microorganisms from the black cherts of the Fawn limestone (Late Precambrian) Semri Group, Son Valley, Mirzapur district, UP. Curr Sci 47, 461.

Kumar, S., 1980. Stromatolites and Indian biostratigraphy. J Palaeotol Soc India 23, 166-183.

Kumar, S., 1982. Vindhyan stromatolites and their stratigraphic testimony. In: Valdia KS, Bhatia SB, Gaur VK (eds) Geology of Vindhyanchal, pp 102-112.

Kumar, S., 1984. Present status of stromatolites biostratigraphy in India. Geophytology 14, 96-110.

Kumar, S., 1995. Megafossils from the Mesoproterozoic Rohtas Formation (the Vindhyan Supergroup), Katni area, central India. Precam Res 72, 171-184.

Kumar, S., Srivastava, P., 1995. Microfossils from the Kheinjua Formation, Mesoproterozoic Semri Group, Newari area, central India. Precam Res 74, 91-117.

Kumar, S., Srivastava, P., 1997. A note on the carbonaceous megafossils from the Neoproterozoic Bhander Group, Maihar area, Madhya Pradesh. J Palaeontol Soc India 42, 141-146.

Kumar, S., Gupta, S., 2002. International Field Workshop on the Vindhyan Basin, central India. Field Guide Book, Pal Soc India, Lucknow.

Kumar, S., Schidlowski, M., Joachimski, M.M., 2005. Carbon isotope stratigraphy of the Paleo–Neoproterozoic Vindhyan Supergroup, central India: implications for basin evolution and intrabasinal correlation. J Palaeontol Soc India 50, 65-81.

Kumar, S., Sharma, M., 2011. Vindhyan Basin, Son Valley Area, central India; The Palaeol. Soc. of India, Field Guide.

Kumar, S., Sharma, M., 2011. Vindhyan Basin, Son Valley Area, central India; The Palaeol. Soc. of India, Field Guide.

Kwiatkowski, S., 2005. Origin of chert nodules from the Polish Muschelkalk, Middle Triassic. Annales. Societatis Geologorum Poloniae 75, 287-308.

Lan, Z., Zhang, S., Li, X.-H., Pandey, S.K., Sharma, M., Shukla, Y., Ahmad, S., Sarkar, S., Zhai, M., 2020. Towards resolving the 'jigsaw puzzle' and age-fossil inconsistency within East Gondwana. Precambr. Res. 345, 105775.

Laura, C.G., Meert, J.G., Pradhan, V., Pandit, M., Tamrat, E., Malone, S. J., 2006. A Paleomagnetic and Geochronologic study of the Majhgawan Kimberlite, India: implications for the Age of the Upper Vindhyan Supergroup. Precamb. Res. 149, 65-75.

Lawrence, M. J. F. 1993. Sedimentology and petrography of early diagenetic chert and dolomite in the Late Cretaceous–Early Tertiary Amuri Limestone Group, eastern Marlborough, New Zealand. Journal of Geology and Geophysics, 36, 9–25. https://doi.org/10.1080/00288306.1993.9514550 .

Lee, Y.I., Paik, I.S., 1997. High alumina glaucony from the Early Ordovician Mungok Formation, Korea. Geolog. J. 1(2), 108–114.

Levin, N.E., Raub, T.D., Dauphas, N., Eiler, J.M., 2014. Triple oxygen isotope variations in sedimentary rocks. Geochim. Cosmochim. Acta 139, 173-189.

Li, C., Jin, C., Planavsky, N.J., Algeo, T.J., Cheng, M., Yang, X., Zhao, Y., Xie, S., 2017. Coupled oceanic oxygenation and metazoan diversification during the early–middle Cambrian? Geology 45(8), 743-746.

Liljestrand, F.L., Knoll, A.H., Tosca, N.J., Cohen, P.A., Macdonald, F.A., Peng, Y., Johnston, D.T. 2020. The triple oxygen isotope composition of Precambrian chert. Earth Planet Sci Lett 537:116167.

Lindgreen, H., Jakobsen, F., 2012. Marine sedimentation of nano-quartz forming flint in North Sea Danian chalk. Marine and Petroleum Geology, 38, 73-82.

Logan, B.H., 1961. Cryptozoon and associate stromatolites from the Recent, Shark Bay, Western Australia. J Geol 69, 517-533.

Loucaides, S., Koning, E., Cappellen, V.C., 2012. Effect of pressure on silica solubility of diatom frustules in the oceans: Results from long-term laboratory and field incubations. Marine Chemistry 136/137, 1-6.

Lowe, D. R., 1982. Sediment gravity flows; II, Depositional models with special reference to the deposits of high-density turbidity currents. J. sedi. Res. 52(1), 279-297.

Lowe, D.R., 1975. Water-escape structures in coarse-grained sediments. Sedimentology 22, 157-204.

Lowe, D.R., 1976. Subaqueous liquefied and fluidized sediment flows and their deposits. Sedimentology 23, 285-308.

Lowe, D.R., Tice, M.M., 2004.Geologic evidence for Archean atmospheric and climatic evolution: Fluctuating levels of CO2, CH4, and O2 with an overriding tectonic control. Geology 32, 493.

Lowe, D.R., Ibarra, D.E., Drabon, N., and Chamberlain, C.P., 2020, Constraints on surface temperature 3.4 billion years ago based on triple oxygen isotopes of cherts from the Barberton Greenstone Belt, South Africa, and the problem of sample selection: American Journal of Science 320, 790–814, https://doi.org/10.2475/11.2020.02

Madsen, H.B., Stemmerik, L., 2010. Diagenesis of flint and porcellanite in the Maastrichtian chalk at Stevns Klint, Denmark. Journal of Sedimentary Research 80, 578–588. https://doi.org/10.2110/jsr.2010.052

Magalha˜es, A.J.C., Gabaglia, G.P., Scherer, C.M.S., Ballico, M.B., Guadagnia, F., Bento Freeire, E., Silva Born, L.R., Octavian, C., 2015. Sequence hierarchy in a Mesoproterozoic interior sag basin: From basin fill to reservoir scale, the Tombador formation, Chapada Diamantina Basin, Brazil. Basin Res. 28, 393-342.

Mageswarii G., Pal, S., Mishra, M., Shrivastava, J.P., 2019. Evidences of felsic volcanism and hydrothermal activities from clays associated with the Palaeoproterozoic Porcellanite Formation of the Vindhyan Supergroup, Central India. Geochemistry 79, 408-420.

Maithy, P.K., 1991. On *Krishnania* Sahni and Shrivastava, a Mid-Proterozoic macrofossil. J Palaeontol Soc India 36, 59-6.

Maithy, P.K., Gupta, S., 1983. Biota and organosedimentary structures from the Vindhyan Supergroup around Chandrehi, Madhya Pradesh. Palaeobotan 31, 154-164.

Maithy, P.K., Mandal, J., 1983. Microbiota from Vindhyan Supergroup of Karauli-Sapotra region of northeast Rajasthan, India. Palaeobolan 31, 129-142.

Maithy, P.K., Shukla, M., 1984. Biological remains from the Suket Shale formation, Vindhyan Supergroup. Geophytol 14, 212-215.

Maithy, P.K., Babu, R., 1988. The mid–Proterozoic Vindhyan Microbiota from Chopan, Southeast Uttar Pradesh. J Geol Soc India 31, 584-590.

Maithy, P.K., Meena, K.L., 1989. Organic-walled microfossils from the Proterozoic succession of Vindhyan Supergroup exposed around Satna, Madhya Pradesh, India. Indian J Earth Sci 16, 178-188.

Maliva, R.G., Siever, R., 1989. Nodular chert formation in carbonate rocks. Journal of Geology 97, 421-433.

Maliva, R.G., Knoll, A.H., Siever, R. 1989. Secular change in chert distribution; a reflection of evolving biological participation in the silica cycle. PALAIOS 4, 519-532.

Maliva, R.G., Knoll, A.H., Simonson, B.M. 2003. Secular change in the Precambrian silica cycle: Insights from chert petrology. GSA Bulleti 117 (7/8), 835-845.

Maliva, R.G., Knoll, A.H., Simonson, B.M., 2005. Secular change in the Precambrian silica cycle: insights from chert petrology. Geol. Soc. Am. Bull. 117 (7/8), 835-845.

Mallet, F.R., 1869. On the Vindhyan series in Northwestern and central provinces of India. Mem. Geol. Sur. of Ind. 7, 1-129.

Mallone, S.J., Meert, J.G., Banerjee, D.M., Pandit, M.K., Tamrat, E., Kamenov, G.D., Pradhan. V.R., Sohl, L.E., 2008. Paleomagnetism and detrital zircon geochronology of the Upper Vindhyan sequence, Son Valley and Rajasthan, India: A ca. 1000 Ma closure age for the Purana basins? Precambrian Research 164, 137-159.

Mandal, A., Koner, A., Sarkar, S., Tawfik, H.A., Chakraborty, N., Bhakta, S., Bose, P.K., 2016. Physico-chemical tuning of palaeogeographic shifts: Bhuj formation, Kutch, India. Mar. Pet. Geol. 78 474–492

Mandal, S., Banerjee, S., Sarkar, S., Mondal, I. And Choudhury, T.R., 2020. Origin and sequence stratigraphic implications of high-alumina glauconite within the Lower Quartzite, Vindhyan Supergroup. Mar. Pet. Geol. 112, 104040.

Mandal, S., Choudhuri, A., Mondal, I., Sarkar, S., Chakraborty, P.P. and Banerjee, S., 2019. Revisiting the boundary between the Lower and Upper Vindhyan, Son valley, India. J. Earth Syst. Sci. 128 (8),1-16.

Mandal, S., Banerjee, S., Sarkar, S., Mondal, I., Choudhury, T.R., 2020. Origin and sequence stratigraphic implications of high-alumina glauconite within the Lower Quartzite, Vindhyan Supergroup. Mar. Pet. Geol. 112, 104040.

Mandal, S., Roy Choudhuri, T., Das, A., Sarkar, S., Banerjee, S., 2022. Shallow marine glauconitization during the Proterozoic in response to intrabasinal tectonics: a study from the Proterozoic Lower Bhander Sandstone, Central India. Precambrian Research 372, https://doi.org/10.1016/j.precamres.2022.106596.

Marin-Carbonne, J., Faure, F., Chaussidon, M., Jacob, D., Robert, F., 2013. A petrographic and isotopic criterion of the state of preservation of Precambrian cherts based on the characterization of the quartz veins. Precambrian Research 231, 290-300.

Marin-Carbonne, J., Robert, F., Chaussidon M., 2014. The silicon and oxygen isotope compositions of Precambrian cherts: A record of oceanic paleo-temperatures? Precambrian Res 247, 223-234.

Marshall, W.L., Warakomski, J.M., 1980, Amorphous silica solubilities. II Effect of aqueous salt solutions at $25^0$C: Geochimica et Cosmochimica Acta. 44, 915-924.

Mathur, S.M., 1954. Late Pre-cambrian glaciation in central India - a rejoinder. Curr. Sci., 23, 7-8.

Mathur, S.M., 1960. A note on the Bijawar series in the eastern part of the type area. Rec. Geol. Surv. Ind., 86, 539-544

Mathur, S.M., 1981. The middle Proterozoic Gangua tillite, Bijawar Group, central India. Earth's pre-Pleistocene
Glacial record, Cambridge University Press, Cambridge, pp. 424-427.

Mathur, S.M., 1982. Organic materials in the Precambrian Vindhyan Supergroup. In: Valdiya KS, Bhatia SB, Gaur VK (eds) Geology of Vindhyanchal. Hindustan Publ Corp, India, pp 125-131.

Matyszkiewicz, J., 1989. Sedimentation and diagenesis of the Upper Oxfordian limestones in Piekary near Kraków. Ann. Soc. Geol. Pol. 59 (1-2), 201–230.

Matyszkiewicz, J., 1996. The significance of Saccocoma-calciturbidites for the analysis of the Polish epicontinental Late Jurassic Basin: an example from the Southern Cracow-Wielun Upland (Poland). Facies 34, 23-40

Mazumder, R., Bose, P.K., Sarkar, S., 2000 A commentary on the tectonic-sedimentary record of the Pre–2.0 Ga evolution of Indian craton vis-à-vis Pre-Gondwana Afro–Indian Supercontinent. J African Earth Sci 30, 201-217.

McBride, E.F., 1988. Silicification of carbonate pebbles in a fuvial conglomerate by groundwater. J. Sedim. Petrol. 58, 862-867.

McBride, E.F., Abdel Wahab, A., El Younsy, A.R., 1999. Origin of spheroidal chert nodules, Drunka Formation (Lower Eocene), Egypt. Sedimentology 46(4), 733-755. https://doi.org/10.1046/j.1365-3091.1999.00253.x

McCave, I.N., 1985. Recent shelf elastic sediments; In: Sedimentology: Recent developments and applied aspects (eds) Brenchley P J and Williams B P S, Geol. Soc. of London, Spec. Publ. 18, 49-65.

McKinney, C.R., McCrea, J.M., Epstein, S., Allen, H.A., Urey, H.C., 1950. Improvements in mass spectrometers for the measurement of small differences in isotope abundance ratios. Rev. Sci. Instrum. 21, 724-730. https://doi.org/10.1063/1.174569

McKirdy, D.M., Hall, P.A., Nedin, C., Halverson, G.P., Michaelsen, B.H., Jago, J.B., Gehling, J.G. and Jenkins, R.J.F., 2011. Paleoredox status and thermal alteration of the lower Cambrian (series 2) Emu Bay Shale Lagerstätte, South Australia. Aust. J. Earth Sci. 58 (3), 259-272.

Mclennan, S.M., 1989. Rare earth elements in sedimentary rocks: influence of provenance and sedimentary processes. In: Lipin, B.R., mckay, G.A. Eds., Geochemistry and Mineralogy of Rare Earth Elements. Min. Soc. Am. Rev. Mineral. 21, 169–200.

Mclennan, S.M., 2001. Relationships between the trace element composition of sedimentary rocks and upper continental crust. Geochem. Geophy. 2(4), 1021.

McMenamin, O.S., Kumar, S., Awramik, S.M., 1983. Microbial fossils from the Kheinjua Formation, Middle Proterozoic, Semri Group (Lower Vindhyan), Son Valley area, central India. Precam Res 34, 247-272.

Medlicott, H.B., 1859. On the Vindhyan rocks and their associates in Bundelkhand. Mem. Geol. Surv. India 2, 30-45.

Meert, J.G., Pandit, M.K., Pradhan, V.R., Banks, J., Sirianni, R., Stroud, M., Newstead, B., Gifford, J., 2010. Precambrian crustal evolution of Peninsular India: a 3.0 billion year odyssey. J. of Asian Earth Sci., 39, 483-515.

Meunier, A., El Albani, A., 2007. The glauconite–Fe–illite–Fe–smectite problem: a critical review. Terra Nova 19, 95–104.

Meyers, W.J., 1977. Chertification in the Mississippian Lake Valley Formation, Sacramento Mountains, New Mexico. Sedimentology 24, 75-105.

Miller, M.F., 2002. Isotopic fractionation and the quantification of $^{17}O$ anomalies in the oxygen three-isotope system: an appraisal and geochemical significance. Geochim. Cosmochim. Acta 66, 1881-1889.

Miller, M.F., Pack, A., 2021. Why Measure $^{17}O$? Historical Perspective, Triple-Isotope Systematics and Selected Applications. Reviews in Mineralogy & Geochemistry 86, 1-34.

Miller, M.F., Pack, A., Bindeman, I.N. Greenwood, R.C., 2020. Standardizing the reporting of $\Delta'^{17}O$ data from high precision oxygen triple-isotope ratio measurements of silicate rocks and minerals. Chem. Geol. 532:119332.

Mills, P.C., 1983. Genesis and diagnostic value of softsediment deformation structures d a review. Sedimentary Geology, 35, 83-104.

Mingxiang, M., Fengjie, Y., Jinhan, G., Qingfen, M., 2008. Glauconites formed in the high-energy shallow-marine environment of the Late Mesoproterozoic: case study from Tieling Formation at Jixian Section in Tianjin, North China. Earth Sci. Front. 15(4),146-158.

Mishra, M., Sen, S., Kumari, K., 2017a. Explosive felsic volcanism at PalaeoMesoproterozoic boundary from Vindhyan Supergroup, Son valley, Central Indiaevidences of crustal contamination. Geochem. Int. 55, 474-488.

Mishra, M., Srivastava, V., Sinha, P.K., Srivastava, H.B., 2017b. Geochemistry of Mesoproterozoic Deonar pyroclastics from Vindhyan Supergroup of central Indiaevidences of felsic magmatism in the Son Valley. J. Geol. Soc. India. 89, 375-385.

Mishra, M., Srivastava, V., Srivastava, H.B., 2017c. A report on the occurrence of ferruginous breccia in Chopan porcellanite formation from semri group, sonbhadra district, (u.p.). J. Sci. Res. 61, 1-11.

Mishra, M., Bickford, M.E., Basu, A., 2018. U-Pb age and chemical composition of an ash bed in the Chopan Porcellanite formation, Vindhyan Supergroup, India. J Geol 126, 553-560.

Mishra, R.C., 1969. The Vindhyan System. Presidential Address. Proc. Ind. Sci. Congr. Assoc., 56th session, Bombay, 2, pp. 111-142.

Misra, K, C., 2012. Introduction to Geochemistry Principle and Applications. Wiley-Blackwell, UK.

Misra, R.C., Bhatnagar, G.S., 1950. On carbonaceous discs and 'algal dust' from the Vindhyan Pre-Cambrian. Curr Sci 19, 88-89.

Misra, R.C., Dube, S.N., 1952. A new collection and restudy of the organic remains from the Suket shales (Vindhyans) Rampura, Madhya Bharat. Sci Cult 18, 46-48.

Misra, R.C., Awasthi, N., 1962. Sedimentary markings and other structures in the rocks of Vindhyan formation of the Son valley and Maihar-Rewa area, India. J Sed Petrol 32, 764-775.

Mohindra, R., Bagati, T.N., 1996. Seismically induced softsediment structures (seismites) around Sumdo in the lower Spiti valley (Tethys Himalaya). Sedimentary Geology 101, 69-83

Moretti, M., Sabato, L., 2007. Recognition of trigger mechanisms for soft-sediment deformation in the Pleistocene lacustrine deposits of the Sant Arcangelo Basin (southern Italy): seismic shock vs. overloading. Sedimentary Geology 196, 31-45.

Moretti, M., Ronchi, A., 2011. Liquefaction features interpreted as seismites in the Pleistocene fluvio-lacustrine deposits of the Neuquén Basin (Northern Patagonia). Sedimentary Geology 235, 200-209.

Moretti, M., Van Loon, A.J., 2014. Restrictions to the application of 'diagnostic' criteria for recognizing ancient seismites. Journal of Palaeogeography 3, 162-173.

Mount, J.F., Kidder, D., 1993. Combined flow origin of edgewise intraclast conglomerates: Sellick Hill Formation (Lower Cambrian), South Australia. Sedimentology, 40, 315-329.

Muehlenbachs, K., 1998. The oxygen isotopic composition of the oceans, sediments and the seafloor. Chem Geol 145, 263-273.

Muehlenbachs, K., Clayton, R.N., 1976. Oxygen isotope composition of the oceanic crust and its bearing on seawater. J. Geophys. Res. 81:4365. https://doi.org/10.1029/JB081i023p04365

Mukherjee, S., Dey, A., Ibanez-Mejia, M., Sanyal, S., Sengupta, P., 2018. Geochemistry, U-Pb geochronology and Lu-Hf isotope systematics of a suite of ferroan (A-type) granitoids from the CGGC: Evidence for Mesoproterozoic crustal extension in the east Indian shield. Precamb. Res. 305, 40-63.

Mulder, T., Alexander, J., 2001. The physical character of subaqueous sedimentary density flows and their deposits. Sedimentology https://doi.org/10.1046/j.1365-3091.2001.00360.x

Murray, R.W., Buchholtz ten Brink, M.R., Gerlach, D.C., Russ III, G.P., Jones, D.L., 1992. Rare earth, major, and trace element composition of Monterey and DSDP chert and associated host sediment: assessing the influence of chemical fractionation during diagenesis. Geochim. Cosmochim. Acta 56, 2657-2671.

Myrow, P. M., Hiscott, R. N., 1991. Shallow-water gravity-flow deposits, Chapel Island Formation, southeast Newfoundland, Canada. Sedimentalogy. https://doi.org/10.1111/j.1365-3091.1991.tb01880.x

Myrow, P. M., Tice, L., Archuleta, B., Clark, B., Taylor, J.F. and Ripperdan, R.L., 2004. Flat-pebble conglomerate: its multiple origins and relationship to metre-scale depositional cycles. Sedimentology, 51, 973-996.

Nair, K.K.K., Jain, S.C., Yedekar, D.B., 1995. Stratigraphy, structure and geochemistry of the Mahakoshal greenstone belt. Mem Geol Soc India 31, 403-432.

Naqvi, S.M., Rogers, J.J.W., 1987. Precambrian Geology of India. Clarendron Press, Oxford.

Narain, H., 1987. Geophysical constraints on the evolution of Purana basins of India with special reference to Cuddapah, Godavari and Vindhyan basins. Mem Geol Soc India 6, 5-12.

Nautiyal, A.C., 1983. Algonkian (Upper to Middle) micro-organisms from the Semri Group of Son Valley (Mirzapur District), India. Geoscience 4, 169-198.

Nautiyal, A.C., 1986. Lower Vindhyan (Algonkian) microflora (microbiota) and biostratigraphy of Sangrampur hill, Banda district, Northern India. Geos J 7, 1-22.

Nichols, R.J., 1995. The liquification and remobilization of sandy sediments. In: Hartley, A.J., Prosser, D.J. (Eds.), Characterization of Deep Marine Clastic Systems: Geological Society, London, Special Publication, 94, pp. 61-74.

Nichols, R.J., Sparks, R.S.J., Wilson, C.J.N., 1994. Experimental studies of the fluidization of layered sediments and the formation of fluid escape structures. Sedimentology 41, 233-253.

Nio, S.D., Yang, C.S., 1991. Diagnostic attributes of clastic tidal deposits: A review; In: Clastic tidal sedimentology:
Calgary (eds) Smith D G, Zaitlin B A, Reinson G E and Rahmani R A, Can. Soc. Pet. Geol., pp. 3-27.

Nozaki, Y., Yamamoto, Y., 2001. Radium 228 based nitrate fluxes in the eastern Indian Ocean and the South China Sea and a silicon-induced "alkalinity pump" hypothesis. Global Biogeochemical Cycles 15(3), 555-567.

Nutman, A.P., Mojzsis, S.J., Friend, C.R.L., 1997. Recognition of ≥3850 Ma water-lain sediments in West Greenland and their significance for the early Archaean Earth. Geochim. Cosmochim. Acta 61, 2475–2484.

O'Brien, N.R., Nakazawa, K., Toukuhashi S., 1980. Use of clay fabric to distinguish turbiditic and hemipelagic siltstones and silts. Sedimentology 27, 47-61.

Och, L.M., Shields-Zhou, G.A., 2012. The Neoproterozoic Oxygenation Event: Environmental perturbations and biogeochemical cycling. Earth-Sci. Rev. 110, 26–57.

Odin, G.S., Matter, A., 1981. De glauconiarum origine. Sedimentology 28, 611–641.

Odom, I. E., 1984. Glauconite and celadonite minerals. In Micas Reviews in Mineralogy and Geochemistry, vol. 13 (ed. SW Bailey), 554–72. Washington, DC: Mineralogical Society of America.

Oldham, R. D., Datta, R. N., Vredenburg, E., 1901. Geology of the Son Valley in the Rewa state and parts of the adjoining districts of Jabalpur and Mirzapur. Mem. Geol. Surv. Ind. 31, 1-178.

Owen, G., 1996. Experimental soft-sediment deformation: structures formed by the liquefaction of unconsolidated sands and some ancient examples. Sedimentology 43, 279-293.

Owen, G., 2003. Load structures: gravity-driven sediment mobilization in the shallow subsurface. In: Van Rensbergen, P., Hillis, R.R., Maltman, A.J., Morley, C.K. (Eds.), Subsurface Sediment Mobilization: Geological Society, London, Special Publications 216, pp. 21-34.

Owen, G., Moretti, M., 2011. Identifying triggers for liquefaction-induced soft-sediment deformation in sands. Sedimentary Geology 235, 141-147.

Owen, G., Moretti, M., Alfaro, P., 2011. Recognising triggers for soft-sediment deformation: current understanding and future directions. Sedimentary Geology 235, 133-140.

Pack, A., Herwartz, D., 2014. The triple oxygen isotope composition of the Earth mantle and Δ17O variations in terrestrial rocks. Earth and Planetary Science Letters 390, 138-145.

Pack, A., Herwartz, D., 2015. Observation and interpretation of $\Delta^{17}O$ variations in terrestrial rocks-response to the comment by Miller et al. on the paper by Pack & Herwartz (2014). Earth Planet. Sci. Lett. 418, 184–186.

Pack, A., Tanaka, R., Hering, M., Sengupta, S., Peters, S., Nakamura, E., 2016. The oxygen isotope composition of San Carlos olivine on the VSMOW2-SLAP2 scale. Rapid Commun. Mass Spectrom. 30, 1495-1504. https://doi.org/10.1002/rcm.7582

Paikaray, S., Banerjee, S., Mukherji, S., 2008. Geochemistry of Shales from the Paleoproterozoic to Neoproterozoic Vindhyan Supergroup: Implications on Provenance, Tectonics and Paleoweathering. Jour. Asian Earth Sci. 32(1), 34-48.

Paikaray, S., Banerjee, S., Mukherji, S., 2008. Geochemistry of shales from the Paleoproterozoic to Neoproterozoic Vindhyan Supergroup: Implications on provenance tectonics and paleoweathering. J. Asian Earth Sci. 32, 34-48.

Pati, J.K., Reimold, W.U., Koeberl, C., Pati, P., 2008. The Dhala structure, Bundhelkhand craton, central India-eroded remnant of large Paleoproterozoic impact structure. Meteor. Planet. Sci. 43(8), 1383-1398.

Pavlov, A. A., Kasting, J. F., 2002. Mass-independent fractionation of sulfur isotopes in Archean sediments: Strong evidence for an anoxic Archean atmosphere. Astrobiology 2, 27–41.

Peck, W.H., Valley, J.W., Wilde, S.A., Graham, C.M., 2001. Oxygen isotope ratios and rare Earth elements in 3.3 to 4.4 Ga zircons: ion microprobe evidence for high $\delta^{18}O$ continental crust and oceans in the early Archean. Geochim. Cosmochim. Acta 65, 4215–4229.

Perry, E.C., 1967. The oxygen isotope chemistry of ancient cherts. Earth Planet Sci Lett 3, 62-66.

Philpotts, A., Ague, J., 2009. Principles of Igneous and Metamorphic Petrology. Cambridge University Press, Cambridge, UK.

Pi, D.H., Jiang, S.Y., Luo, L., Yang, J.H., Hong-Fei Ling, H.F., 2014. Depositional environments for stratiformwitherite deposits in the Lower Cambrian black shale sequence of the Yangtze Platform, southern Qinling region, SW China: evidence from redox-sensitive trace element geochemistry. Palaeogeogr. Palaeoclimatol. Palaeoecol. 398, 125-131.

Postma, G., Cartigny, M., Kleverlaan, K., 2009. Structureless, coarse-tail graded Bouma Ta formed by internal hydraulic jump of the turbidity current? Sediment. Geol. 219, 1-6.

Potter, P.E., Pettijohn, F.J., 1977. Paleocurrents and Basin Analysis. Springer-Verlag, New York.

Pradhan, V.R., Meert, J.G., Pandit, M.K., Kamenov, G., Gregory, L.C., Malone, S.J., 2010. India's changing place in global Proterozoic reconstructions: a review of geochronologic constraints and paleomagnetic poles from the Dharwar, Bundelkhand and Marwar cratons. J. of Geodynamics, 50, 224-242.

Prakash, R., Dalela, I.K., 1982. Stratigraphy of the Vindhyans in Uttar Pradesh: A brief review. In: Valdiya, K.S., Bhatia, S.B., Gaur, V.K. (Eds.), Geol. of Vindh. Prof. Misra Volume. Hindu. Publ. Corp. Delhi, pp. 55-79.

Prasad, B., 1980. Vindhyan stromatolite biostratigraphy. Geol Surv India Misc Publ 44, 201-2016.

Prasad, B., 1980. Vindhyan stromatolite stratigraphy in south-eastern Rajasthan. Misc. Publ. Geol. Surv. Ind. 44, 201-206.

Prasad, B., 1984. Geology, sedimentation and paleogeography of the Vindhyan Supergroup, S.E. Rajasthan. Mem. Geol. Surv. Ind. 116, pp. 1-107.

Prasad, B., Ramaswamy, S.M., 1980. Stromatolites in Upper Vindhyan from Bundi, Kota and Sawai Madhopur District, Rajasthan: Stromatolites characteristic and utility. Geol Surv India Misc Publ 44, 275-277.

Prasad, B., Verma, K.K., 1991. Vindhyan basin- a review. In: Tandon, S.K., Pant, C.C., and Casshyap, S.M., (Eds.), Sedimentary basins of India: Tectonic Context. Gyanodayan Prakashan, Nainital pp. 13-29.

Pratt, B.R., 2002. Syneresis cracks: Subaqueous shrinkage inargillaceous sediments caused by earthquake-induced dewatering; Sedim. Geol. 117(1), 1-10.

Pujol, M., Marty, B., Burgess, R., Turner, G., Philippot, P., 2013. Argon isotopic composition of Archaean atmosphere probes early Earth geodynamics. Nature 498, 87-90. doi: 10.1038/nature12152

Putnis, A. 2009. Mineral replacement reactions. In: Oelkers, E.H., Schott, J. (Eds.), Thermo- Dynamics and Kinetics of Watererock Interaction. Reviews in Mineralogy & Geochemistry 30, 87-124.

Putnis, A., 2002. Mineral replacement reactions: from macroscopic observations to microscopic mechanisms. Mineral. Mag. 66, 689-708. http://dx.doi.org/10.1180/0026461026650056

Putnis, A., Putnis, C.V., 2007. The mechanism of reequilibration of solids in the presence of a fluid phase. J. Solid State Chem. 180, 1783-1786. http://dx.doi.org/10.1016/j.jssc.2007.03.023

Putnis, C.V., Ruiz-Agudo, E. 2013. The mineral-water interface: where minerals react with the environment. Elements 9, 177-182.

Quasim, M.A., Ghosh, S.K., Ahmad, A.H.M., 2019. Petrography and Diagenetic Evolution of the Proterozoic Kaimur Group Sandstones, Son Valley, India: Implication Towards Reservoir Quality. Geological Evolution of the Precambrian Indian Shild, 515-550.

Raaben, M.E., 1969. Columnar stromatolites and late Precambrian stratigraphy. Am J Sci 261, 1-18.

Raaben, M.E., 2005. On subdivisions of the Upper Riphean. Strat Geol Corr 13, 143-158.

Racki, G., Cordey, F., 2000. Radiolarian palaeoecology and radiolarites: is the present the key to the past? Earth Sci. Rev. 52, 83-120.

Raha, P.K., Sastri, M.V.A., 1982. Stromatolites and Precambrian stratigraphy in India. Precam Res 18, 292-318.

Rai, V., Gautam, R., 1998. New occurrence of carbonaceous megafossils from the Meso- to Neoproterozoic horizons of the Vindhya Supergroup, Kaimur–Katni area, Madhya Pradesh, India. Geophytol 26, 13-25.

Rai, V., Shukla, M., Gautam, R., 1997. Discovery of carbonaceous megafossils (*Chuaria–Tawuia* assemblage) from the Neoproterozoic Vindhyan succession (Rewa Group), Allahabad–Rewa area, India. Curr Sci 73, 783-788.

Ram, J., Shukla, S.N., Pramanik, A.G., Verma, B.K., Chandra, G., Murthy, M.S.N., 1996. Recent investigations in the Vindhyan Basin: implications for the basin tectonics. In: Bhattacharyya A (ed) Recent Advances in Vindhyan Geology, vol 36. Mem Geol Soc India, pp 267-286.

Rao, K.S., Ghosh, D.B., 1978. Stratigraphy and sedimentation of Vindhyans in parts of Son valley area, Madhya Pradesh. Rec. Geol. Surv. India. 110, 180-193.

Rao, K.S., Neelakantam, S., 1978. Stratigraphy and sedimentation of Vindhyans in parts of Son valley area, Madhya Pradesh. Rec. Geol. Surv. India 110,180-193.

Rao, K.S., Lal, C., Ghosh, D.B., 1977. Algal stromatolites in the Bhander Group, Vindhyan Supergroup, Satna district, Madhya Pradesh. Rec Geol Surv India 109, 38-47.

Rasmussen, B., Bose, P.K., Sarkar, S., Banerjee, S., Fletcher, I. R., Mcnaughton, N.J., 2002. 1.6 Ga U-Pb zircon age for the Chorhat Sandstone, Lower Vindhyan, India: possible implications for early evolution of animals. Geology 30, 103–106.

Rasmussen, B., Fletcher, I.R., Bengtson, S., McNaughton, N.J., 2004. SHRIMP U–Pb dating of diagenetic xenotime in the Stirling Range Formation, Western Australia: 1.8-billion-year minimum age for the Stirling biota. Precam Res 133, 329-337.

Rasmussen, B., Krapež, B., Muhling, J.R., Suvorova, A., 2019. Precipitation of iron silicate nanoparticles in early Precambrian oceans marks Earth's first iron age. Geology, 43(4), 303-306.

Rasmussen, B., Muhling, J.R., Fischer, W.W., 2019. Evidence from laminated chert in banded iron formations for deposition by gravitational settling of iron-silicate muds. Geology 47, 167-170.

Ray, J. S., Veizer, J., Davis, W.J., 2003. C, O, Sr and Pb isotope systematics of carbonate sequences of the Vindhyan Supergroup, India: age, diagenesis, correlation and implications for global events. Precamb. Res. 121, 103-140.

Ray, J. S., Veizer, J., Davis, W.J., 2003. C, O, Sr and Pb isotope systematics of carbonate sequences of the Vindhyan Supergroup, India: age, diagenesis, correlation and implications for global events. Precamb. Res. 121, 103-140.

Ray, J.S., Martin, M.W., Veizer, J., 2002. U-Pb Zircon dating and Sr isotope systematics of the Vindhyan Super Group, India. Geology 30, 131-134.

Raza, M., Casshyap, S.M., 1996. A tectonic-sedimentary model of evolution of middle Proterozoic Vindhyan Basin. In: Bhattacharyya A (ed) Recent Advances in Vindhyan Geology, vol 36. Mem Geol Soc India, pp 286–300.

Raza, M., Dayal, A.M., Khan, A., Bhardwaj, V.R., Rais, S., 2010. Geochemistry of lower Vindhyan clastic sedimentary rocks of Northwestern Indian shield: implications for composition and weathering history of Proterozoic continental crust. J. Asian Earth Sci. 39, 51-61.

Renard, F., Putnis, C.V., Montes-Hernandez, G., King, H.E., Breedveld, G.D., Okkenhaug, G., 2018. Sequestration of antimony on calcite observed by timeresolved nanoscale imaging. Environmental Science & Technology 52, 107-113.

Rigby, J.K., 1991. Evolution of Paleozoic heteractinellid calcareous sponges and demosponges: Patterns and records. In: Reitner, J., Keupp, H. (Eds.), Fossil and Recent Sponges. Springer-Verlag, Berlin, pp. 83-101.

Rimstidt, J. D.; Barnes, H. L., 1980. The kinetics of silica-water reactions. Geochim. Cosmochim. Acta 44, 1683-1699.

Rimstidt, J.D., 1997. Quartz solubility at low temperatures. Geochimica et Cosmochimica Acta 61, 2553-2558.

Robert, F., Chaussidon, M., 2006. A palaeotemperature curve for the Precambrian oceans based on silicon isotopes in cherts. Nature 443, 969.

Rogers, J.J.W., 1986. The Dharwar craton and assembly of peninsular India. J Geol 94, 129-144.

Rossetti, D.F., 1999. Soft-sediment deformation structures in late Albian to Cenomanian deposits, San Luìs Basin, northern Brazil: evidence for paleoseismicity. Sedimentology 46, 1065-1081.

Rouse, R., 1961. Fluid mechanics for hydralic engineers; Dover, New York.

Roy Choudhury, T., Banerjee, S., Khanolkar, S., Saraswati, P. K. and Meena, S.S., 2021. Glauconite authigenesis during the onset of the Paleocene-Eocene Thermal Maximum: A case study from the Khuiala Formation in Jaisalmer Basin, India. Palaeo3. 571, 110388.

Roy, A., Bandyopadhyay, B.K., 1990. Tectonics and structural pattern of the Mahakoshal belt of central India. Spec Publ Geol Surv India 28, 226-240.

Rudmin, M., Banerjee, S., Mazurov, A., 2017. Compositional variation of glauconites in Upper Cretaceous-Paleogene sedimentary iron-ore deposits in South-eastern Western Siberia. Sed. Geol. 355, 20–30.

Rudmin, M., Oskina, Y., Banerjee, S., Mazurov, A., Soktoev, B., Shaldybin, M., 2018. Roasting-leaching experiments on glauconitic rocks of Bakchar ironstone deposit (Western Siberia) for evaluation their fertilizer potential. Applied Clay Science 162, 121-128.

Rudmin, M., Mazurov, A., Banerjee, S., 2019. Origin of ooidal ironstones in relation to warming events: Cretaceous-Eocene Bakchar deposit, south-east Western Siberia. Mar. Petrol. Geol. 100, 309-325.

Rudnick, R.L., Gao, S., 2003. Composition of the continental crust. Treatise Geochem. 3, 1-64.

Ruiz-Agudo, E., Putnis, C.V., Putnis, A., 2014. Coupled dissolution and precipitation at mineral–fluid interfaces. Chemical Geology 383, 132-146.

Rumble, D., Miller, M.F., Franchi, I.A., Greenwood, R.C., 2007. Oxygen three-isotope fractionation lines in terrestrial silicate minerals: an inter-laboratory comparison of hydrothermal quartz and eclogitic garnet. Geochim. Cosmochim. Acta 71, 3592-3600.

Sahni, M.R., 1936. *Fermeria minima*: a revised classification of the organic remains from the Vindhyan of India. Rec Geol Surv India 69, 458-468.

Sallstedt, T., Bengtson, S., Broman, C., Crill, P.M., Canfield, D.E., 2018. Evidence of oxygenic phototrophy in ancient phosphatic stromatolites from the Paleoproterozoic Vindhyan and Aravalli Supergroups, India; Geobiology 16, 139-159.

Sarangi, S., Gopalan K., Kumar, S., 2004. Pb-Pb of earliest megascopic, eukaryotic alga bearing Rohtas Formation, Vindhyan Supergroup, India: Implication for Precambrian atmospheric oxygen evolution. Precam. Res. 132, 107-121.

Sarkar, S., Banerjee, S., Chakraborty, S., 1995. Synsedimentary seismic signature in Mesoproterozoic Koldaha Shale, Kheinjua Formation, central India. Ind. J. Ear. Sci. 22, 158-164.

Sarkar, S., Banerjee, S., and Bose, P.K., 1996. Trace fossils in MesoProterozoic Koldaha Shale, central India and their implications. N. Jb. Palaont. Mh. 7, 425-438.

Sarkar, S., Chakraborty, S., Banerjee, S., Bose, P.K., 2002a. Facies sequence and cryptic imprint of sag tectonics in the late Proterozoic Sirbu Shale, central India. Precambrian sedimentary environments: A modern approach to ancient depositional systems, 369-381.

Sarkar, S., Banerjee, S., Chakraborty, S., Bose, P.K., 2002b. Shelf storm flow dynamics: insight from the Mesoproterozoic Rampur Shale, central India. Sed. Geol. 147, 89-104.

Sarkar, S., Banerjee, S., Eriksson, P.G., 2004. Microbial mat features in sandstones illustrated. In: Eriksson, P. G., Altermann, W., Nelson, D.R., Mueller, W.U., and Catuneanu. O., (Eds.), The Precambrian Earth: Tempos and Events. Elsevier: Amsterdam, pp. 673-675.

Sarkar, S., Eriksson, P.G., Chakraborty, S., 2004. Epeiric sea formation on Neoproterozoic supercontinent break-up: A distinctive signature in coastal storm bed amalgamation. Gondwana Res. 7(2), 313-322.

Sarkar, S., Banerjee, S., Samanta, P., Jeevankumar, S., 2006. Microbial mat-induced sedimentary structures in siliciclastic sediments: Examples from the 1.6 Ga Chorhat Sandstone, Vindhyan Supergroup, M.P., India. J. of Earth System Science, 115, 49-60.

Sarkar, S., Bose, P. K., Samanta P., Sengupta P., Eriksson, P. G., 2008. Microbial mat mediated structures in the Ediacaran Sonia Sandstone, Rajasthan, India, and their implications for proterozoic sedimentation. Precmbr. Res. 162, 248-263.

Sarkar, S., Samanta, P., Altermann, W., 2011. Setulfs, modern and ancient: Formative mechanism, preservation bias and palaeoenvironmental implications. Sed. Geol. 238, 71-78.

Sarkar, S., Banerjee, S., Mukhopadhyay, S., Bose, P.K., 2012. Stratigraphic architecture of the Sonia Fluvial interval, India in its Precambrian context. Precamb. Res. 214/215, 210-226.

Sarkar, S., Choudhuri, A., Banerjee, S., Van Loon, A.T., Bose, P.K., 2014. Seismic and non-seismic soft-sediment deformation structures in the Proterozoic Bhander Limestone, central India. Geologos 20, 89-103.

Sarkar, S, Choudhuri, A., Mandal, S., Bose, P.K., 2019. Flat pebbles and their edge-wise fabric in relation to 2-D microbial mat. Geol. J., https://doi.org/10.1002/gj.3312.

Sarkar, S., Banerjee, S., 2020. A Synthesis of Depositional Sequence of the Proterozoic Vindhyan Supergroup in Son Valley: A Field Guide. Springer Nature.

Sastry, M.V.A., Moitra, A.K., 1984. Vindhyan stratigraphy: A review. Geol. Surv. India Memoir 116, 109-148.

Schieber, J., 1986. The possible role of benthic microbial mats during the formation of carbonaceous shales in shallow MidProterozoic basins. Sedimentology 33, 521-536.

Schieber, J., 2004. Microbial mats in the siliciclastic rock record: a summary of the diagnostic features. In: Eriksson PG, Altermann W, Nelson DR, Muller WU, Catuneanu O (eds) The Precambrian Earth: Tempos and Events. Elsevier, Amsterdam, pp 663-673.

Schieber, J., Sur, S., Banerjee, S., 2007. Benthic Microbial Mat in Black Shale Units from the Vindhyan Supergroup, Middle Proterozoic of India: The Challenges of Recognising the Genuine Article. In: Schieber, J., Bose, P. K., Eriksson, P. G., Banerjee, S., Sarkar, S., Altermann, W., Catuneanu, O., (Eds.), Atlas of Microbial Mat Features Preserved Within the Siliciclastic Rock Record, Atlases in Geoscience 2, pp. 189-197.

Scott, A.C., Sparks, R.S.J., Bull, I.D., Knicker, H., Evershed, R.P., 2008. Temperature proxy data and their significance for the understanding of pyroclastic density currents. Geology 36 (2), 143-146.

Scott, B., Price, S., 1988. Earthquake-induced structures in young sediments. Tectonophysics 147, 165-170.

Seilacher, A., 1969. Fault-graded beds interpreted as seismites. Sedimentology 13, 155-159.

Seilacher, A., 1997. Fossil Art. The royal tyrell museum of paleontology, Drumheller, Canada.

Seilacher, A., Bose, P.K., Pflüger, F., 1998. Triploblastic animals more than 1 billion years ago: trace fossil evidence from India. Science 282, 80-83.

Sengupta, S., Pack, A. 2018. Triple oxygen isotope mass balance for the Earth′s oceans with application to Archean cherts. Chem. Geol. 495,18-26.

Sengupta, S., Peters, S.T.M., Reitner, J., Duda, J.P., Pack, A. 2020. Triple oxygen isotopes of cherts through time. Chem. Geol. 554:119789.

Sepkoski, J.J., 1982. Flat-pebble conglomerates, storm deposits, and the Cambrian bottom fauna. In: Einsele, G., and Seilacher, A., (Eds.), Cyclic and Event Stratification. Springer-Verlag, pp. 371-386. Siringan & Anderson, 1994

Shaaban, M.N., 2004. Diagenesis of the Lower Eocene Thebes Formation, Gebel Rewagen area, Eastern Desert, Egypt. Sedimentary Geology 165, 53-65. https://doi.org/10.1016/j.sedgeo.2003.11.004

Shanks, W.C., 2001. Stable isotopes in seafloor hydrothermal systems: vent fluids, hydrothermal deposits, hydrothermal alteration, and microbial processes. Rev. Mineral. Geochem. 43, 469–525.

Shanmugam, G., 2016. The seismite problem. Journal of Paleogeography 5(4), 318-362.

Sharma, M., 1996. Microbiolites (stromatolites) from the Mesoproterozoic Salkhan Limestone, Semri Group, Rohtas, Bihar: their systematics and significance. Geol Soc India Mem 36, 167-196.

Sharp, Z.D., 1990. A laser-based microanalytical method for the in situ determination of oxygen isotope ratios of silicates and oxides. Geochim. Cosmochim. Acta 54, 1353-1357.

Sharp, Z.D., Gibbons, J.A., Maltsev, O., Atudorei, V., Pack, A., Sengupta, S., Shock, E.L., Knauth, L.P. 2016. A calibration of the triple oxygen isotope fractionation in the $SiO_2$-$H_2O$ system and applications to natural samples. Geochim Cosmochim Acta 186,105-119.

Sharp, Z.D., Wostbrock, J.A.G., Pack, A. 2018. Mass-dependent triple oxygen isotope variations in terrestrial materials. Geochem Perspect. Lett. 7, 27-31.

Shemesh, A., Charles, C.D., Fairbanks, R.G., 1992. Oxygen isotopes in biogenic silica: global changes in ocean temperature and isotopic composition. Science 256, 1434-1436.

Shemesh, A., Kolodny, Y., Luz, B., 1983. Oxygen isotope variations in phosphate of biogenic apatites, II. Phosphorite rocks. Earth Planet. Sci. Lett. 64, 405–416.

Shemesh, A., Kolodny, Y., Luz, B., 1988. Isotope geochemistry of oxygen and carbon in phosphate and carbonate of phosphorite francolite. Geochim. Cosmochim. Acta 52, 2565-2572, https://doi.org/10.1016/0016-7037(88)90027-0.

Shen, B., Ma, H., Ye, H., Lang, X., Pei, H., Zhou, C., Zhang, S., Yang, R., 2018. Hydrothermal origin of syndepositional chert bands and nodules in the Mesoproterozoic Wumishan Formation: Implications for the evolution of Mesoproterozoic cratonic basin, North China. Precambrian Res. 310, 213-228.

Shukla, M., Sharma, M., 1990. Palaeobiology of Suket Shale, Vindhyan Supergroup; age implications. Geol Surv India Spec Publ 28, 411-434.

Singh, A. K., Chakraborty, P. P., Sarkar, S., 2018. Redox structure of Vindhyan hydrosphere: clues from total organic carbon, transition metal (Mo, Cr) concentrations and stable isotope (delta C-13) chemistry. Curr. Sci. 115, 1334-1341.

Singh, A.K., Chakraborty, P.P., 2020. Shales of Palaeo-Mesoproterozoic Vindhyan Basin, central India: insight into sedimentation dynamics of Proterozoic shelf. Geol. Mag. 1-22.

Singh, A.K., Chakraborty, P.P., 2021. Geochemistry and hydrocarbon source rock potential of shales from the Palaeo-Mesoproterozoic Vindhyan Supergroup, central India. Energy Geoscience https://doi.org/10.1016/j.engeos.2021.10.007.

Singh, A.K., Chakraborty, P.P., Sarkar, S., 2018. Redox structure of Vindhyan hydrosphere: clues from total organic carbon, transition metal (Mo, Cr) concentrations and stable isotope (delta C-13) chemistry. Curr. Sci. 115, 1334-1341.

Singh, H.J.M., Banerjee, A.K., 1980. Stromatolites in the Vindhyan Group of Northeastern Rajasthan. Misc Publ Geol Surv India 44, 278-283.

Singh, I.B., 1973. Depositional environments of the Vindhyans in Son valley area. In: Verma, V.K., and others (Eds.), Recent Researches in Geology. Jhingran Comm. 1, 146-152.

Singh, I.B., 1980. Precambrian sedimentary sequences of India: their peculiarities and comparison with modern
sediments. Precambrian Res., 12, 411-436.

Singh, I.B., 1985. Paleogeography of Vindhyan Basin and its relationship with other Late Proterozoic Basins of India. Jour. Palaeont. Soc. India 30, 35-41.

Singh, S.P., Sinha, P.K., 2001. Vindhyan Supergroup of Bihar–an overview. In: Singh SP (ed) Precambrian Crustal Evolution and Metallogeny of India. South Asian Ass of Econ Geol Patna, pp 107-126.

Singh, S.P., Thakur, L.K., Sinha, A.K., 2001. Stratigraphy of the Semri Group in the Bhaunathpur area, Garwah District, Jharkhand. In: Singh SP (ed) Precambrian Crustal Evolution and Metallogeny of India. South Asian Ass of Econ Geol Patna, Patna, pp 95-106.

Snavely, P.D., Garrison, R.E., Meguid, A.A., 1979. Stratigraphy and regional depositional history of the Thebes Formation (Lower Eocene), Egypt. Annals. Geological Survey of Egypt 8, 344-362.

Soni, M.K., Chakraborty, S., Jain, V.K., 1987. Vindhyan Supergroup- A review in Purana Basins of Peninsular India. Memoir. Geol. Soc. India 32, 87-138.

Srivastava, A. P., Rajagopalan, G., 1988. F-T ages of Vindhyan Glauconitic sandstone beds exposed around Rewatbhata area, Rajasthan. J. Geol. Soc. Ind. 32, 527-529.

Srivastava, D.C., Sahay, A., 2003. Brittle tectonics and pore–fluid conditions in the evolution of the Great Boundary Fault around Chittaurgarh, Northwestern India. J Struc Geol 25, 1713-1733.

Srivastava, P., 2004. Carbonaceous fossils from the Panna Shale, Rewa Group (Upper Vindhyans), central India: a possible link between evolution of micro-megascopic life. Curr Sci 86:644-646.

Srivastava, R.N., Srivastava, A.K., Singh, K.N., Redcliffe, R.P., 2003. Sedimentation and depositional environment of the chopan porcellanite formation, semri group, vindhyan supergroup in parts of Sonbhadra District, Uttar Pradesh. J. Paleontol. Soc. India. 48, 167-179.

Sur, S., Schieber, S. and Banerjee, S., 2006. Petrographic observations suggestive of microbial mats from Rampur Shale and Bijaigarh Shale, Vindhyan basin, India. Journal of Earth Systems Science 115, 61-66.

Talukdar, M., Sanyal, S., Sengupta, p. 2017. Metasomatic alteration of chromite from parts of the late Archaean Sittampundi Layered Magmatic Complex (SLC), Tamil Nadu, India. Ore Geology Review 90, 148-165.

Tandon, K.K., Kumar, S., 1977. Discovery of annelid and arthropod remains from Lower Vindhyan rocks (Precambrian) of central India. Geophytol 7, 126-128.

Tang, D., Shi, X., Ma, J., Jiang, G., Zhou, X., Shi, Q., 2017a. Formation of Shallow water glaucony in weakly oxygenated Precambrian Ocean: An example from the Mesoprterozoic Tieling Formation in North China. Precam. Res. 294, 214-229.

Tang, D., Shi, X., Jiang, G., Zhon, X., Shi, Q., 2017b. Ferruginous seawater facilitates the transformation of glauconite to chamosite: An example from the Mesoproterozoic Xiamaling Formation of North China. Am. Mineral. 102, 2317-2332.

Taşgin, C.K., Orhan, H., Türkmen, I., Aksoy, E., 2011. Soft-sediment deformation structures in the late Miocene Şelmo Formation around Adıyaman area, Southeastern Turkey. Sedimentary Geology 235, 277-291.

Taylor, H.P., 1978. Oxygen and hydrogen isotope studies of plutonic granitic rocks. Earth Planet. Sci. Lett. 38, 177-210.

Tewari, A.P., 1968. A new concept of the paleotectonic set-up of a part of northern peninsular India with special reference to the Great Boundary Faults. Geol en Mijnb 47, 21-27

Thiry, M., Milens, A., 2017. Silcretes: insights into the occurrences and formation of materials sourced for stone tool making. Journal of Archaeological Sciences: Reports 15, 500-513.

Thiry, M., Milnes, A.R., Rayot, V., Simon-Coincon, R., 2006. Interpretation of palaeoweathering features and successive silicifications in the Tertiary regolith of Inland Australia: Geological Society of London 163, 723-736.

Thiry, M., Millot, R., Innocent, C., Franke, C., 2015a. The Fontainebleau Sandstone: bleaching, silicification and calcite precipitation under periglacial conditions: Orl´ eans, France, Applied Isotope Geochemistry Conference, Field Trip Guide. Scientific Report RS150901MTHI, 26.

Thiry, M., Milens, A., Ben-Brahim, M., 2015b. Pleistocene cold climate groundwater silicification, Jbel Ghassoul region, Missour Basin, Morocco. Geological Society of London, Journal 172, 125-137.

Thompson, G.R., Hower, J., 1975. The mineralogy of glauconite. Clays and Clay Miner. 23, 289-300.

Tréguer, P., Nelson, D.M., Van Bennekom, A.J., DeMaster, D.J., Leynaert, A., Quéguiner, B., 1995. The silica balance in the world ocean: A reestimate. Science 268, 375-379.

Tréguer, P.J., Rocha, C.L.D.L., 2013. The world ocean silica cycle. Ann. Rev. Marine Sci. 5, 477-501.

Tribovillard, N., Algeo, T.J., Lyons, T., Riboulleau, A., 2006. Trace metals as paleoredox and paleoproductivity proxies: an update. Chem. geol. 232, 12-32.

Tripathy, G.S., Singh, S.K., 2015. Re-Os depositional age for black shale from the Kaimur Group, Upper Vindhyan, India. Chemical Geology 413, 63-72.

Tucker, M.E., 1983. Diagenesis, geochemistry and origin of a Precambrian dolomite: The Beck Spring Dolomite of eastern California. Journal of Sedimentary Petrology 53, 1097-1119.

Tucker, M.E., and Wright, V.P., 1990. Carbonate Sedimentology. Blackwell Science, Blackwell Publishing Ltd., pp. 419.

Turner, C.C., Meert, J.G., Kamenov, G.D., Pandit, M.K., 2010. A detrital zircon transect across the Son valley sector of the Vindhyan basin, India: further constraints on basin evolution. Geological Society of America Annual Meeting Abstracts, 42, 195.

Urey, H. C., 1947. The thermodynamic properties of isotopic substances. J. Chem. Soc., 562-581.

Valdiya, K.S., 1982. Tectonic perspectives of the Vindhyachal region. In: Valdiya KS, Bhatia SB, Gaur VK (eds) Geology of Vindhyanchal. Hindustan Publishing Corporation, New Delhi, pp 23-29.

Valdiya, K.S., 2010. The Making of India Geodynamics Evolution; pp. 191-193.

Valley, J.W., Kitchen, N., Kohn, M.J., Niendorf, C.R., Spicuzza, M.J., 1995. UWG-2, a garnet standard for oxygen isotope ratios: Strategies for high precision and accuracy with laser heating 59, 5223-5231.

Van Loon, A.J., Han, Z. and Han, Y., 2013. Origin of the vertically orientated clasts in brecciated shallow-marine limestones of the Chaomidian Formation (Furongian, Shandong Province, China). Sedimentology, 60, 1059–1070.

Velde, B., 1985. Possible chemical controls of illite/smectite composition during diagenesis. Mineral. Mag. 49, 387–391.

Velde, B., 1985. Clay Minerals: A Physico-Chemical Explanation of their Occurrence. Developments in Sedimentology 40, pp. 1-427.

Velde, B., 2003. Green clay minerals. In: M5ackenzie, F.T. (Ed.), Treatise on Geochemistry, Elsevier Amsterdam, Vol 7, 309–324.

Venkateshwarlu, M., Rao, J.M., 2013. Palaeomagnetism of Bhander sediments from Bhopal inlier, Vindhyan Supergroup. J. of the Geol. Soc. of India 81, 330-336.

Vérard, C., Veizer, J., 2019. On plate tectonics and ocean temperatures. Geology 47, 881–885. https://doi.org/10.1130/g46376.1

Verma, P.K., 1991. Geodynamics of the Indian Peninsula and the Indian Plate Margin. Oxford and IBH, 357.

Verma, P.K., Banerjee, P., 1992. Nature of continental crust along the Narmada–Son Lineament inferred from gravity and deep seismic sounding data. Tectonophys 202, 375-397.

Vernon, H.R., 2004. A Practical Guide To Rock Microstructure. Cambridge University Press. http://dx.doi.org/10.1017/CBO9780511807206

Putnis, C.V., Tsukamoto, K., Nishimura, Y. 2005. Direct observations of pseudomorphism: compositional and textural evolution at a fluid-solid interface. American Mineralogist 90, 1909-1912.

Vredenburg, E.W., 1910. A summary of Geology of India. Calcutta.

Walker, R. G., and Plint, A.G., 1992. Wave- and storm-Dominated Shallow Marine Systems. In: Walker, R.G., and Jame, N.P., (Eds.), Facies Models: Response to Sea Level Change. Geol. Asso. Can., St. John's, NF, Canada, pp. 219-238.

Wallmann, K., 2001. The geological water cycle and the evolution of marine δ18O values. Geochim. Cosmochim. Acta 65, 2469-2485.

Walther, J.H., 2009. Application of geochemistry. John and Bartlett publication, Sudbury, Massachusetts.

West, W.D., 1962. The line of the Narmada and Son valleys. Cur Sci 31, 143-144.

Wilde, S.A., Valley, J.W., Peck, W.H., Graham, C.M., 2001. Evidence from detrital zircons for the existence of continental crust and oceans on the Earth 4.4 Gyr ago. Nature 409, 175-178.

Willams, L.A., Parks, G.A., Crerar, D.A., 1985. Silica diagenesis, I. Solubility controls: Journal of Sedimentary Petrology 55, 301-311.

Wostbrock J.A.G., Sharp, Z.D. 2021. Triple Oxygen Isotopes in Silica–Water and Carbonate-Water Systems. Reviews in Mineralogy & Geochemistry 86, 367-400.

Wostbrock, J.A.G., Brand, U., Coplen, T.B., Swart, P.K., Carlson, S.J., Sharp, Z.D., 2020. Calibration of carbonate-water triple oxygen isotope fractionation: seeing through diagenesis in ancient carbonates. Geochim Cosmochim Acta 288, 369-388.

Wostbrock, J.A.G., Brand, U., Coplen, T.B., Swart, P.K., Carlson, S.J., Sharp, Z.D., 2020. Calibration of carbonate-water triple oxygen isotope fractionation: seeing through diagenesis in ancient carbonates. Geochim Cosmochim Acta 288, 369-388.

Wostbrock, J.A.G., Sharp, Z. D., 2021. Triple Oxygen Isotopes in Silica-Water and Carbonate-Water Systems. Reviews in Mineralogy & Geochemistry 86, 367-400.

Wright J., Schrader H., Holser W., 1987. Paleoredox variations in ancient oceans recorded by rare earth elements in fossil apatite. Geochim. Cosmochim. Acta. 51, 631–44.

Yamamoto, K. 1987. Geochemical characteristics and depositional environment of cherts and associated rocks in the Franciscan and Shimanto terranes. Sedimentary Geology 52, 65-108.

Yang, G.M., 2018. Chapter 2-Precambrian Glacial Deposits: Their Origin, Tectonic Setting, and Key Role in Earth Evolution. Past Glaciation event (2nd edition)17-45.

Zakharov, D.O., Bindeman, I.N., 2019. Triple oxygen and hydrogen isotopic study of hydrothermally altered rocks from the 2.43-2.41 Ga Vetreny belt, Russia: An insight into the early Paleoproterozoic seawater. Geochim Cosmochim Acta 248, 185-209.

Zakharov, D.O., Marin-Carbonne, J., Alleon, J. 2021. Triple Oxygen Isotope Trend Recorded by Precambrian Cherts: A Perspective from Combined Bulk and in situ Secondary Ion Probe Measurements. Reviews in Mineralogy & Geochemistry 86, 323-365.